Production de forces par le cytosquelette d'actine : mécanismes et régulation par le micro-environnement

Timothée Vignaud

UNIVERSITÉ DE GRENOBLE

THÈSE

Pour obtenir le grade de

DOCTEUR DE L'UNIVERSITÉ DE GRENOBLE

Spécialité : **Physique pour les sciences du vivant**

Arrêté ministériel : 7 août 2006

Présentée par

Timothée VIGNAUD

Thèse dirigée par **Manuel THERY** et **Laurent BLANCHOIN**

préparée au sein du **Laboratoire de Physiologie Cellulaire et Végétale, équipe « Physique du Cytosquelette et de la Morphogenèse** »

dans **l'Ecole Doctorale de Physique**

Production de forces par le cytosquelette d'actine : mécanismes et régulation par le micro-environnement

Thèse soutenue publiquement le **« 15 novembre 2013»**,
devant le jury composé de :

M. Bertrand FOURCADE
Professeur de Physique à l'Université Joseph Fourier – Institut Albert Bonniot - Grenoble (Président du Jury)
Mme. Ewa PALUCH
Group Leader at University College of London (Rapporteur)
M Atef ASNACIOS
Professeur à l'Université Paris Diderot - Laboratoire Matière et Systèmes Complexes - Paris (Rapporteur)
M. Sanjay KUMAR
Associate professor at University of California - Berkeley (Membre)
M. Ulrich S. SCHWARZ
Full professor for the physics of complex systems at the University of Heidelberg (Membre)
M. Pekka LAPPALAINEN
Professor and research director at the Institute of Biotechnology – Helsinki (Membre)
M. Manuel THERY
Chercheur CEA, Laboratoire de Physiologie Cellulaire et Végétale - Grenoble (Membre)

Université Joseph Fourier / Université Pierre Mendès France /
Université Stendhal / Université de Savoie / Grenoble INP

A mes parents, mon frère et ma sœur.
Ils ont su m'armer pour cette vie et éveiller
ma curiosité pour tout ce qui m'entoure.
Sans eux, je n'en serais sans doute jamais arriver là.

« Auch aus Steinen, die einem in den Weg gelegt werden,
kann man Shönes bauen »

« On peut aussi construire quelque chose de beau avec les
pierres qui entravent le chemin »

Goethe

REMERCIEMENTS

J'aimerais remercier Manuel Théry et Laurent Blanchoin pour leur encadrement collectif tout au long de ma thèse. Manuel a su me laisser trouver mes marques au sein de l'équipe, me guider dans mes travaux et me transmettre un peu de son enthousiasme débordant, de sa rigueur, de son sens aigu de l'observation et de son goût pour l'esthétisme en matière d'iconographie. Laurent de son côté a toujours été d'un soutien indéfectible tout au long de ces 3 ans. Son dynamisme de tous les instants et le rythme qu'il parvient à insuffler à l'équipe, sont pour beaucoup dans la réussite des travaux entrepris. Savoir sa porte toujours ouverte en cas de besoin a été d'un grand réconfort tout au long de ma thèse. Merci également à Jean-Louis Martiel, qui aurait initialement dû être mon directeur de thèse. Les choses se sont arrangées autrement au moment de mon arrivée et il a néanmoins su m'accueillir lui aussi et ne pas m'en tenir rigueur.

Mes remerciements vont à Qingzong Tseng. C'est en suivant ses pas que j'ai pu apprendre à observer les cellules, à les manipuler, à mesurer les forces qu'elles exercent, … Il a su développer au sein de l'équipe un grand nombre d'outils qui ont été d'une utilité quotidienne tout au long de ma thèse.

Merci à Cristian Suarez, Didier Portran, Anne-Cécile Reymann et Théo Cambier. Leur accueil chaleureux au moment de mon arrivée, leur enthousiasme et leur bonne humeur permanente, leur gentillesse, ont fait de ces 3 ans un véritable bonheur.

Mes pensées vont également à Christophe Guérin (« CryCry ») et Jérémie Gaillard. Ces deux hommes à tout faire sont toujours disponibles et accueillants. Les pauses « cacao-skittles » au milieu d'une longue manip' ont toujours été d'un grand réconfort. Merci à Fabrice Senger. Ses phrases et ses airs énigmatiques ont souvent permis de détendre l'atmosphère pendant les heures passées en pièce de culture.

Laëtitia Kurzawa (« Leua ») et Jonathan Arnaud (« Johnny ») ont été d'un grand soutien au cours de ma 3ème année. Leur fraicheur, leur enthousiasme et tout le travail qu'ils ont fournis sont pour beaucoup dans l'avancée des travaux présentés. Leur arrivée à su me donner un élan nouveau à un moment où je m'essoufflais un peu.

Andreas Christ et Aldo Leal ont quant à eux su me transmettre une rigueur, un esprit critique aiguisé et une capacité de remise en question, qualités indispensables au raisonnement scientifique.

Merci à Mithila Burute (« Mit »), Hajer Ennomani (« Haj2haj »), Gaëlle Letort (« Boss Box »), Laura Schaedel et Laurène Gressin. Ces nouvelles recrues ont su apporter une cohésion et un esprit de groupe incroyable au sein des étudiants de l'équipe.

Enfin j'aimerais remercier les membres de l'équipe que je n'ai pas encore cités (Rémi Galland, Virginie Stoppin-Mellet, Francesca Farina, Alphée Michelot, Agnieszka Kawska, Rajaa Boujemaa Paterski, Tobias Klar, James Sillibourne, Magalie Prioux, Odile Filhol-Cochet et Marylin Vantard). La place me manque pour m'exprimer individuellement pour chacun d'entre eux mais je pense qu'ils savent combien ils m'ont apporté chacun à leur manière et combien j'ai apprécié travailler à leur côté pendant ces trois ans.

Il est toujours plus agréable d'entretenir des bonnes relations de voisinages. J'aimerai remercier toutes l'équipe de Biomics avec laquelle les choses se sont très bien passées et en particulier Patricia Obeid, Stéphanie Porte, Monika Pyzalska et Amandine Pitaval. Ce fut un vrai plaisir de travailler à leur côtés dans la bonne humeur.

Une petite note particulière à Sophie Mistri, Sylvianne Flammier et Danielle Adelaide qui ont toujours été disponibles, accueillantes et souriantes pour mes demandes de dernière minute et mes soucis administratifs. Je leur suis très reconnaissant de cette aide précieuse.

Une thèse est une expérience éprouvante par laquelle on peut se laisser emporter. Anne-Laure a toujours été là. Sans son oreille attentive, son attention et ses précieux conseils, certaines difficultés m'auraient sans doute parues insurmontables.

I. Introduction

1. INTRODUCTION GENERALE / MOTIVATIONS

Nous sommes en perpétuel renouvellement. Notre corps est en quelque sorte constamment remis à neuf. Au cours de notre vie, la grande majorité de nos organes, de nos tissus, de nos cellules va être complètement renouvelée plusieurs fois, à une fréquence plus ou moins élevée en fonction des cellules. Au bout du compte, l'écrasante majorité de nos cellules et de nos organes sont plus jeunes que nous. Seules exceptions à cette règle, les neurones et les cellules cardiaques dont le renouvellement est très lent ou quasi-inexistant.

Les cellules ont des durées de vie variables. Une cellule de peau a ainsi une durée de vie de 3 à 4 semaines avant d'être renouvelée. Un globule rouge vit lui quelque 120 jours. Une cellule de la rétine ne dépasse pas la dizaine de jours. Une cellule de foie ou de poumon vit de 400 à 500 jours tandis que les cellules tapissant la surface de l'intestin ne subsistent que 5 jours. Comment faisons-nous alors pour rester en vie et conserver une quantité suffisante de cellules fonctionnelles? Comment nos organes conservent-ils leur forme malgré cette perte constante de cellules?

De nouvelles cellules voient évidemment le jour. Des millions de cellules se divisent en deux cellules filles chaque seconde. Au cours de ce processus, la cellule « mère » s'arrondit pour pouvoir ensuite se scinder en deux. Mais cela ne suffit pas : imaginez un mur auquel on retire et on ajoute des pierres ça et là, la situation devient très vite instable ! Pour maintenir une intégrité au sein des tissus, les cellules sont capables de percevoir les modifications de leur environnement et de s'y adapter. Lorsqu'une cellule meurt, sa place est immédiatement comblée par une autre pour maintenir l'intégrité mécanique du tissu. Comment les cellules savent-elles la place qui est disponible autour d'elles ? Elles le sentent ! Nos cellules sont dotées d'un arsenal d'outils sensoriels qui vont leur permettre de sonder leur environnement pour pouvoir produire une réponse adaptée. Elles sont notamment capable de titrer des composés chimiques solubles générés par l'organisme pour stimuler ou inhiber leur croissance mais aussi de « palper » les propriétés physico-chimiques de l'environnement (rigidité, molécule d'adhésion, force exercée par leurs voisines, contact avec leurs voisines…), d'évaluer l'espace dont elles disposent au sein du tissu et d'intégrer l'ensemble de ces signaux pour produire une réponse adaptée.

Cette adaptation implique également la régulation des forces générées par la cellule sur son environnement. Ces forces de cohésions sont extrêmement importantes pour l'intégrité mécanique de nos tissus et pour le maintien de leur forme. Pour adapter ses forces à l'environnement mécanique, la cellule est capable de le « titiller » à travers des senseurs biomécaniques, les adhésions. Il s'agit de complexes protéiques qui jouent un double rôle : assurer une continuité physique entre la cellule et son

environnement, et réguler les voies de signalisation cellulaire qui vont permettre d'adapter les forces générées par la cellule sur ces adhésions.

Pour produire les forces, la cellule s'appuie le plus souvent sur son cytosquelette d'actine et sur des moteurs moléculaires, les myosines. Pour moduler les forces qu'elles génèrent et ses propriétés mécaniques, la cellule va pouvoir modifier l'architecture de son cytosquelette en régulant la quantité de protéines accessoires qui vont s'y associer (myosines, alpha-actinine, protéines de coiffe, de fragmentation, …). Les proportions différentes de ces protéines accessoires vont permettre la formation de modules différents dont l'organisation particulière génère des propriétés mécaniques spécifiques (lamellipode, filopode, fibres de stress, cortex d'actine).

Mes travaux se sont intéressés à ces deux niveaux de régulation des forces générées par les cellules en réponse à leur environnement physique : la signalisation au niveau des adhésions et le rôle de la forme de la cellule dans la régulation de la contractilité cellulaire.

Pour mettre en perspectives mes résultats, j'ai consacré mon premier chapitre à la description du cytosquelette d'actine, et à ce que l'on sait de la régulation de la contractilité cellulaire par les adhésions. Je passe également en revue le rôle primordial des contraintes environnementales imposées au cytosquelette et à la cellule, dans la régulation de l'architecture cellulaire et par extension de sa contractilité.

Pour estimer les forces ainsi produites, plusieurs solutions sont possibles. Mon deuxième chapitre décrit les solutions existantes permettant la mesure des forces générées par la cellule et justifie la méthode de travail utilisée.

Le troisième chapitre est consacré au rôle de la composition des adhésions dans la transmission et la régulation de la contractilité cellulaire.

Le dernier chapitre identifie la fibre de stress d'actine comme structure privilégiée de production de forces par la cellule et décrit comment la tension générée au sein de cette structure varie avec sa longueur.

2. FORME CELLULAIRE ET CYTOSQUELETTE : UNE FASCINANTE DIVERSITE

A. DIVERSITE DES FORMES CELLULAIRES

Ce qui frappe lorsqu'on observe différents tissus de notre organisme, c'est la diversité des formes que sont capables d'adopter nos cellules (voir figure 1). Elles utilisent pourtant toutes les

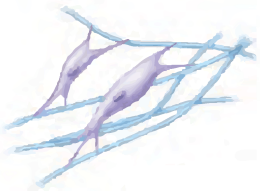

Fibroblaste

Erythrocyte

Macrophage

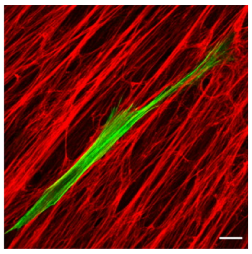

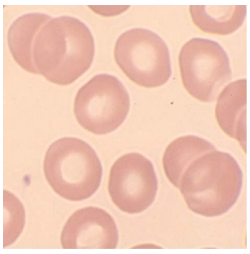

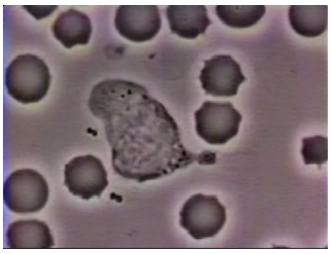

Cellule musculaire striée

Cellule musculaire lisse

Adipocyte

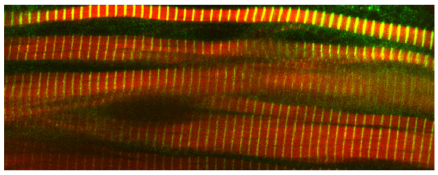

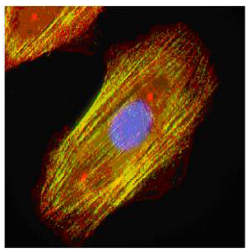

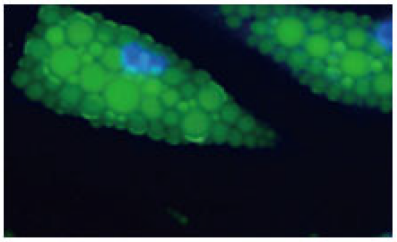

Cellule epithéliale

Neurone

Spermatozoïde

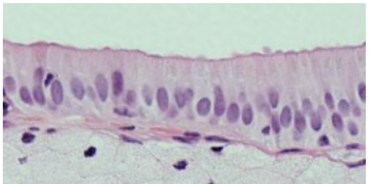

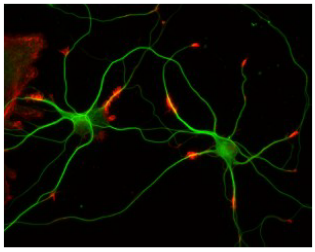

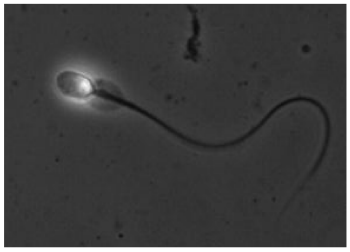

Figure 1 - Diversité des formes cellulaires

(Adapté de Marieb, Hoehn, Human Anatomy & Physiology)

de gauche à droite et de haut au bas

Fibroblaste (cellule du tissu conjonctif) migrant au sein d'une matrice fibrillaire. Son cytosquelette d'actine apparaît en vert, en rouge il s'agit de la matrice fibrillaire (fibronectine) sur laquelle il se déplace.

Erythrocyte (=globule rouge : cellule sanguine responsable du transport d'oxygène dans la circulation sanguine) marqué à l'hématoxyline. Sa forme caractéristique biconcave lui permet de se déformer pour passer dans les vaisseaux de très faibles calibres sans les boucher.

Macrophage (cellule du système immunitaire). Cette cellule est capable de migrer très rapidement en réponse à un gradient chimique. Cette faculté lui permet de « poursuivre » des agents pathogènes au sein de l'organisme.

Cellule musculaire striée. La cellule musculaire striée est le résultat de la fusion de plusieurs cellules. Cette forme hautement différenciée lui permet une contraction rapide et synchronisée sur une grande distance. En vert est représentée l'alpha-actinine (une protéine qui, en s'associant à l'actine, génère une organisation particulière sous forme de bande avec une alternance entre alpha-actinine et myosine) et en rouge l'actine.

Cellule musculaire lisse. Il s'agit également d'une cellule musculaire mais moins spécialisée que la cellule musculaire striée. Son architecture est également organisée autour de l'actine (rouge) mais l'organisation en bandes n'est pas retrouvée ici (myosine en vert). Ces cellules permettent également des contractions mais plus lentes que le muscle squelettique. On les retrouve notamment dans la paroi des vaisseaux pour leur permettre d'adapter leur calibre et de réguler le flux sanguin.

Adipocyte. Il s'agit de la cellule spécialisée dans le stockage énergétique sous forme de lipides (vert). Son cytoplasme est rempli de vésicules de stockage contenant les lipides qui pourront être utilisés pour produire de l'énergie en cas de besoin. (en bleu le noyau)

Cellule épithéliale. C'est une des cellules les plus abondantes de notre organisme. Les tissus épithéliaux assurent le recouvrement et la protection d'une grande partie des organes, vis à vis du milieu extérieur à l'organisme mais également intérieur. Ils peuvent prendre de nombreuses formes, souvent adaptée à leur emplacement (épais et plat pour un épithélium de protection (épiderme), fin et ondulé pour un épithélium d'absorption (épithélium intestinal)). Il s'agit d'un marquage éosine hématoxyline (noyau en violet, cytoplasme en rose).

Neurone. Il s'agit d'un des types cellulaires du système nerveux. Il permet le transport rapide d'une information d'un bout à l'autre de l'organisme et joue un rôle prépondérant dans les fonctions cognitives supérieures. Son cytosquelette est également très différencié avec peu d'actine (rouge) et des ramifications cellulaires (neurites) sous tendues par un coeur de microtubules (vert).

Spermatozoïde. Gamète mâle permettant le transport de l'information génétique paternelle jusqu'à l'ovocyte. Cette cellule est optimisée pour la migration en milieu liquide avec un long flagelle constitué d'une organisation particulière de microtubules permettant un mouvement ondulatoire.

mêmes bio-polymères (filaments d'actine, microtubules et filaments intermédiaires) pour générer leur forme et la maintenir. Seules sont modifiées la quantité de ces éléments et les protéines qui s'y associent pour générer des architectures particulières. Ces architectures jouent généralement un rôle important dans la fonction de la cellule. Le cytosquelette d'actine des fibroblastes leur permet de migrer au sein d'environnements fibrillaires. La migration amoeboïde des macrophages les rend capables de « traquer » des agents pathogènes, y compris en solution. Les filaments intermédiaires des érythrocytes leur donnent une forme biconcave idéale pour optimiser les surfaces d'échange avec le sang et nécessaire à la bonne circulation de ces cellules dans des vaisseaux sanguins de petit calibre. L'organisation sarcomérique de l'actine avec l'alpha-actinine et la myosine au sein des cellules musculaires squelettiques autorise une contraction rapide et orientée de la cellule, …

Pour bien comprendre l'enjeu de l'organisation du cytosquelette d'actine, je vais maintenant décrire les différentes organisations possibles et les propriétés mécaniques de ces différents modules. Pour notre étude, j'ai utilisé des cellules épithéliales. Je ne décrirai donc que les architectures que l'on peut retrouver au sein de ces cellules, en dehors du processus de division cellulaire. Il s'agit d'un modèle pertinent car les épithelia sont les tissus les plus dynamiques de notre organisme. L'importance des mécanismes d'adaptation cellulaire y est donc primordiale. La dérégulation de ces mécanismes peut conduire à l'apparition de lésions plus ou moins sévères, dont le cancer est l'un des exemples. En effet, le développement anormal d'une masse cellulaire au sein d'un organe suppose que les mécanismes de régulation du comportement cellulaire par son environnement sont perturbés

B. LE CYTOSQUELETTE D'ACTINE

Le cytosquelette cellulaire est un réseau enchevêtré de bio-polymères de différentes natures. Ce réseau est en perpétuel renouvellement et confère à la cellule une grande partie de ses propriétés mécaniques. Les 3 bio-polymères de base qui le constituent sont les filaments d'actine, les microtubules et les filaments intermédiaires.

Les microtubules jouent un rôle important dans l'orchestration de l'organisation du cytosquelette dans son ensemble et dans la séparation du matériel génétique au moment de la division cellulaire. Leur contribution directe aux propriétés mécaniques de la cellule et à la production de forces est secondaire, comparée au cytosquelette d'actine.

Les filaments intermédiaires sont encore mal connus, en particulier du fait de leur hétérogénéité qui rend un marquage fluorescent délicat. Leur rôle dans la mécanique cellulaire commence seulement à être compris. Ils participent d'avantage aux propriétés mécaniques passives de la cellule qu'à la production de forces actives par la cellule sur son environnement.

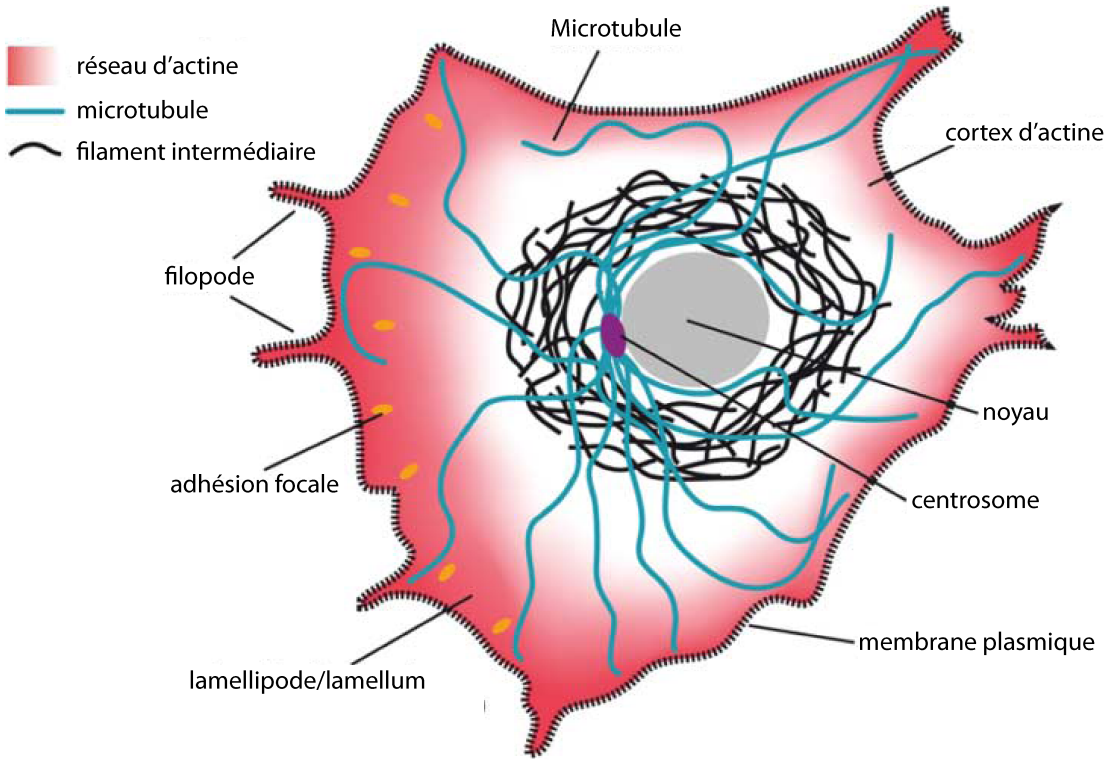

Figure 2 – Les trois principaux composants du cytosquelette

(Adapté de Huber, Advances in Physics, 2013)

Schéma d'une cellule étalée sur un support en 2D montrant la localisation principale des 3 composants majoritaires du cytosquelette. Les **microtubules** sont généralement nucléés au niveau du centrosome et s'étendent à travers la majeure partie du cytoplasme. Les **filaments intermédiaires** sont typiquement proches du noyau tandis que les **filaments d'actine** forment un réseau dense et dynamique à partir de la périphérie de la cellule au contact de la membrane plasmique.

Microtubules et filaments intermédiaires forment deux réseaux d'importance mais n'ont pas été au centre de mes travaux. Un lecteur souhaitant de plus amples informations pourra se reporter aux articles de revues suivants: F Huber, Advances in Physics, 2013 (microtubules), Eriksson, Journal of Clinical Investigation, 2009 et Herrmann, Journal of Clinical Investigation, 2009 (filaments intermédiaires).

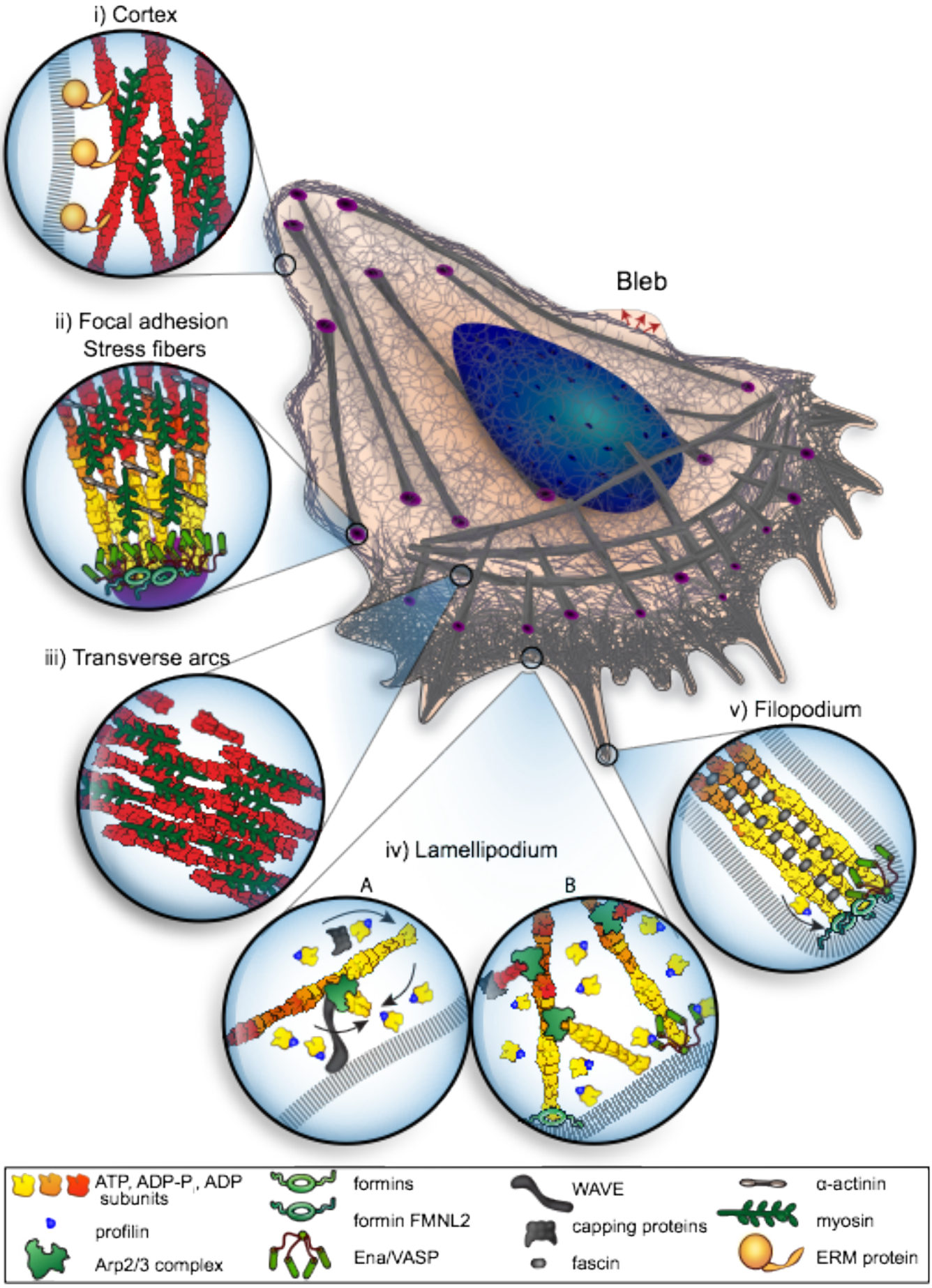
i) Cortex
Bleb
ii) Focal adhesion
Stress fibers
iii) Transverse arcs
v) Filopodium
iv) Lamellipodium
A
B
ATP, ADP-P$_i$, ADP subunits
profilin
Arp2/3 complex
formins
formin FMNL2
Ena/VASP
WAVE
capping proteins
fascin
α-actinin
myosin
ERM protein

Figure 3 : Les différents modules du cytosquelette d'actine

(Blanchoin, Physiological Reviews, 2013)

(i) – le **cortex d'actine** : il s'agit d'un fin réseau d'actine pontée sur lequel des myosines exercent des forces contractiles. Il est situé immédiatement sous la membrane à laquelle il est attaché. Ses mécanismes de formation sont encore mal connus à ce jour. Il joue un rôle central dans le contrôle de la forme de la cellule. Par exemple, il va être capable de résorber une bulle formée à sa surface (bleb). Le cortex d'actine va s'assembler à l'intérieur du bleb sous la membrane et va permettre de ramener la membrane à sa position d'origine, sous l'effet des myosines.

(ii) et (iii) – les **fibres de stress ventrales et les arcs transverses**: ces structures sont composées de filaments d'actine organisés en fagot de façon antiparallèles. Ces fagots sont connectés à leurs extrémités à des adhésions. Les filaments y sont pontés et la myosine permet de générer une force contractile. Les arcs transverses sont des structures intermédiaires également composées de filaments antiparallèles. Cependant ces arcs ne sont pas (encore) connectés à leurs extrémités à des adhésions. C'est en y parvenant qu'ils deviendront des fibres de stress.

(iv) – **le lamellipode** : il s'agit d'un réseau arborescent d'actine formé sous la membrane de la cellule. Des filaments d'actine naissent les uns des autres à une orientation de 70°. Les deux protagonistes majeurs de l'assemblage de ce réseau sont le complexe Arp2/3 activé et la capping protein. Il est plus épais que le cortex d'actine et aura un rôle important dans la formation de protrusion membranaire. Il sera effectivement capable de pousser la membrane au cours de sa formation.

(v) – **les filopodes** : il s'agit également de structures d'actine qui seront présentes préférentiellement sous la membrane plasmique. Il s'agit de fagots de filaments pontés organisés de façon parallèle, qui forment une sorte de doigts cellulaires. Ces structures sont capables de se projeter vers l'extérieur de la cellule. Ils contiennent des récepteurs qui leur permettent de sonder l'environnement. S'ils interagissent avec des molécules d'adhésions, ils pourront être stabilisés et générer une force de traction importante. Ils jouent un rôle important lorsque deux épithélia se rencontrent pour tirer les deux berges l'une vers l'autre et combler l'espace qui les séparent.

L'actine est capable de s'organiser sous diverses formes au sein de la cellule. Des architectures typiques, ou modules, ont été progressivement identifiées. Ils se caractérisent par une organisation particulière des filaments d'actine (voir figure 3).

Ces différentes architectures se mettent en place grâce à des protéines bien particulières pour chaque module. Je vais tout d'abord vous présenter les règles d'assemblage de l'actine seule et la suite s'emploiera à montrer comment différentes protéines vont permettre la formation de ces architectures originales et distinctes.

Une brique fondamentale, le filament d'actine

L'unité de base du cytosquelette est la protéine d'actine. Il s'agit d'une protéine de 43 kDa constituée de quatre sous-domaines. Elle est majoritairement associée, dans sa forme monomérique, à une molécule d'ATP.

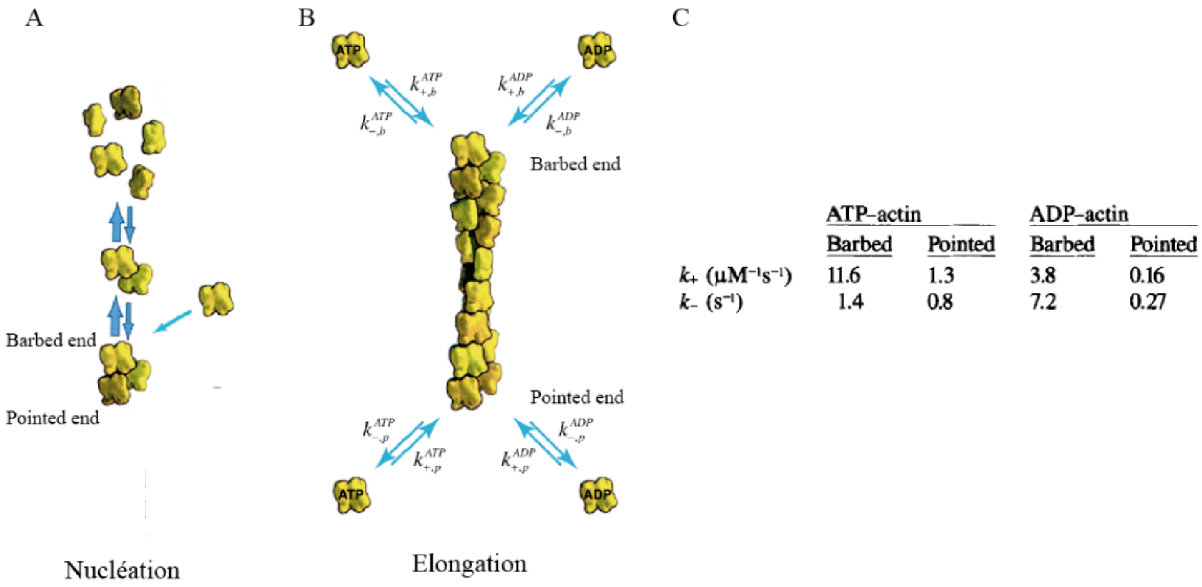

	ATP-actin		ADP-actin	
	Barbed	Pointed	Barbed	Pointed
k_+ ($\mu M^{-1}s^{-1}$)	11.6	1.3	3.8	0.16
k_- (s^{-1})	1.4	0.8	7.2	0.27

Figure 4: Cinétique de polymérisation du filament d'actine.

(A) Formation d'un nucléus composé d'un trimère hélicoïdal d'actine. (B) Elongation du filament par association de sous-unités d'actine à l'état ATP ou ADP aux extrémités du filament. Les constantes cinétiques d'association et de dissociation sont indiquées par des double-flèches (Pollard, Cell, 2003), (C) les valeurs des constantes cinétiques présentes en (B) sont résumées dans le tableau (Pollard, J. Cell. Biol., 1986).

Pour former un filament, les monomères d'actine s'assemblent en deux brins enroulés l'un autour de l'autre. L'étape d'initiation de la polymérisation à partir de monomères est thermodynamiquement défavorable ce qui interdit la polymérisation en dessous d'une concentration critique, de l'ordre de 0.1 µM (Pollard, J. Cell. Biol., 1986). L'élongation du filament, ou polymérisation, a ensuite lieu aux deux extrémités mais selon des cinétiques différentes (Figure 4). Le filament est en effet polarisé avec une extrémité plus dynamique (extrémité barbée) que l'autre (extrémité pointue). L'actine monomérique est présente en très grande concentration dans le cytoplasme de la cellule, à des concentrations comprises entre 10 et 100 µM. Au cours de l'élongation des filaments, les monomères d'actine vont s'ajouter rapidement à l'extrémité barbée du filament. Une fois incorporé, le monomère hydrolysera son nucléotide et libérera le phosphate généré pour être finalement associé à de l'ADP. Un filament dynamique se trouvera donc dans une situation où

l'extrémité barbée est composée de monomères liés à l'ATP et l'extrémité pointue de monomères liés à l'ADP. Ce détail a son importance car la dissociation des monomères au niveau de l'extrémité barbée est plus favorable pour les monomères-ADP que pour les monomères-ATP. La coiffe d'actine-ATP à l'extrémité barbée du filament le protège donc de la dépolymérisation, contrairement à l'extrémité pointue. A l'équilibre, cette situation conduit à un processus de tapis-roulant au sein d'un filament, avec une addition de monomères-ATP à l'extrémité barbée et le retrait de monomères-ADP à l'extrémité pointue, la longueur du filament restant constante. (Figure 5)

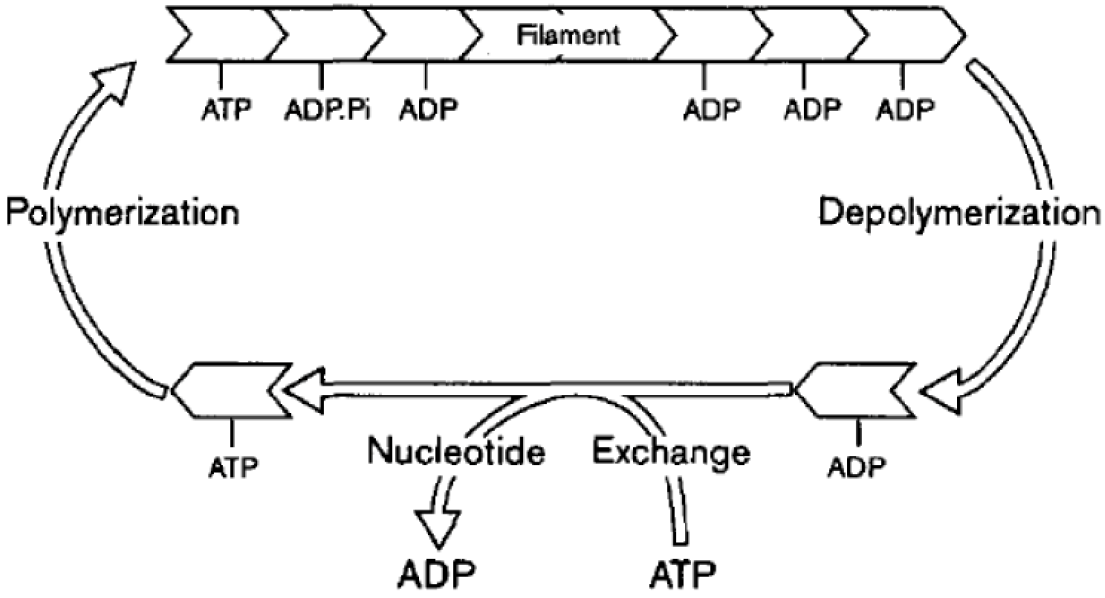

Figure 5: Treadmilling du filament d'actine à l'équilibre.

Les sous-unités d'actine à l'état ATP s'additionnent à l'extrémité barbée des filaments d'actine. L'hydrolyse ainsi que la dissociation du Pi intervient au sein du filament. La dissociation des sous-unités ADP intervient à l'extrémité pointue du filament. Les monomères ainsi libérés voient leur nucléotide ADP échangé contre une molécule d'ATP. Les monomères ATP peuvent de nouveau être utilisés pour l'élongation du filament à l'extrémité barbée (Carlier, Cur. Opin. Cell. Biol., 1998).

Le maintien d'une concentration élevée de monomères d'actine disponibles dans le cytoplasme est un élément fondamental de la dynamique du cytosquelette d'actine. Cette haute concentration permet de déclencher une polymérisation massive d'actine si la situation le demande. Pour maintenir ce pool d'actine libre, des protéines sont capables de s'associer à l'actine pour réguler sa polymérisation. Ces protéines vont également pouvoir jouer un rôle dans l'organisation du réseau du fait de leur mode d'interaction avec le filament.

Une polymérisation sous haute surveillance

Pour réguler de façon efficace la polymérisation, deux paramètres doivent être contrôlés. Ils apparaissent de façon évidente quand on regarde l'équation de polymérisation de l'actine dans la cellule (en ne tenant compte que de l'extrémité barbée) :

$$V_{polymérisation} = \boldsymbol{N_{extrémités\ barbées\ libres}} \cdot \left(k_+ . \left[\boldsymbol{actine_{monomérique}}\right] - k_-\right)$$

Il s'agit de la quantité d'extrémités barbées disponibles pour la polymérisation et de la concentration de monomères d'actine disponibles.

Pour réguler la concentration de monomères disponibles pour la polymérisation, deux protéines jouent un rôle important : la profiline et la thymosine-Béta4. Ces deux protéines, en s'associant à l'actine-ATP de façon très éphémère vont permettre de générer des stocks d'actine-monomérique-ATP non polymérisables mais rapidement mobilisables. (figure 6)

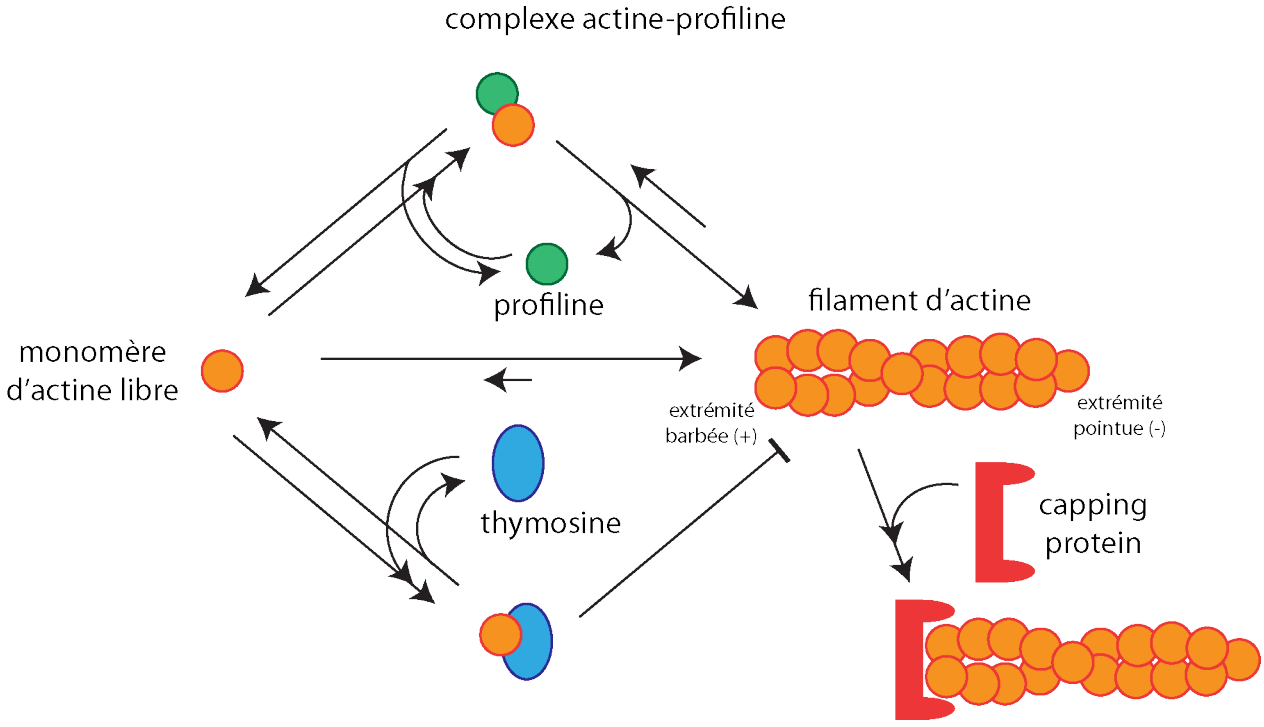

Figure 6 : Schéma du mode d'action de la profiline, la thymosine et la capping protein dans la régulation de la polymérisation des filaments d'actine.

Ces deux protéines sont présentes en quantité importante dans le cytoplasme (10-100 µM). La thymosine-Béta4 se fixe à l'actine-monomérique ATP avec une affinité inférieure à la profiline. L'actine présente sous cette forme n'est pas capable de polymériser. La profiline est en compétition avec la thymosine-béta4 pour l'association avec les monomères d'actine-ATP. Le caractère éphémère

des interactions avec ces protéines permet un transfert rapide d'un monomère de la thymosine vers l'actine.

La profiline ne modifie pas les propriétés cinétiques du monomère d'actine-ATP qui lui est associée, pour ce qui concerne l'extrémité barbée d'un filament existant. En revanche, elle augmente la concentration critique qui permet l'initiation d'un filament, empêche la formation spontanée d'extrémités barbées dans le cytoplasme et inhibe la polymérisation par l'extrémité pointue. Ces deux protéines agissent donc de concert pour diminuer la concentration de monomères d'actine-ATP disponibles pour la polymérisation et limiter la formation spontanée de filaments.

Une autre protéine joue un rôle primordial dans la régulation de la quantité d'extrémités barbées libres. Il s'agit de la protéine de coiffe (Capping Protein). Cette protéine a une très forte affinité pour les extrémités barbées libres (Kd = 0.1 nM) (Schafer, J. Cell. Biol, 1996) et permet de les bloquer rapidement après leur formation. Les extrémités barbés ne restent donc libres que pendant une très courte durée ce qui permet de limiter la polymérisation dans le temps et participe donc au maintien du pool d'actine monomérique.

Formation de modules de novo : différentes protéines pour différentes architectures

Du fait de la très forte répression de la nucléation spontanée, la formation de nouveaux filaments doit avoir lieu par d'autres mécanismes. Différentes protéines jouent ce rôle. Leur mode de nucléation particulier va mener à la génération de modules dont l'organisation conditionnera les propriétés mécaniques.

Le lamellipode(figure 7A)

Le complexe Arp2/3 est un complexe protéique stable composé de 7 protéines. Il est présent en solution sous forme inactive et doit interagir avec son activateur, un des représentants de la famille de protéines WASP/WAVE. Ce dernier doit lui-même être activé par des protéines interagissant avec la membrane. C'est à cette contrainte que l'on doit la localisation sub-membranaire du lamellipode. Le complexe Arp2/3 est capable de nucléer des filaments de novo, cependant son rôle principal consiste en la formation de nouveaux filaments d'actine, à partir d'un filament préexistant. Il est en effet capable

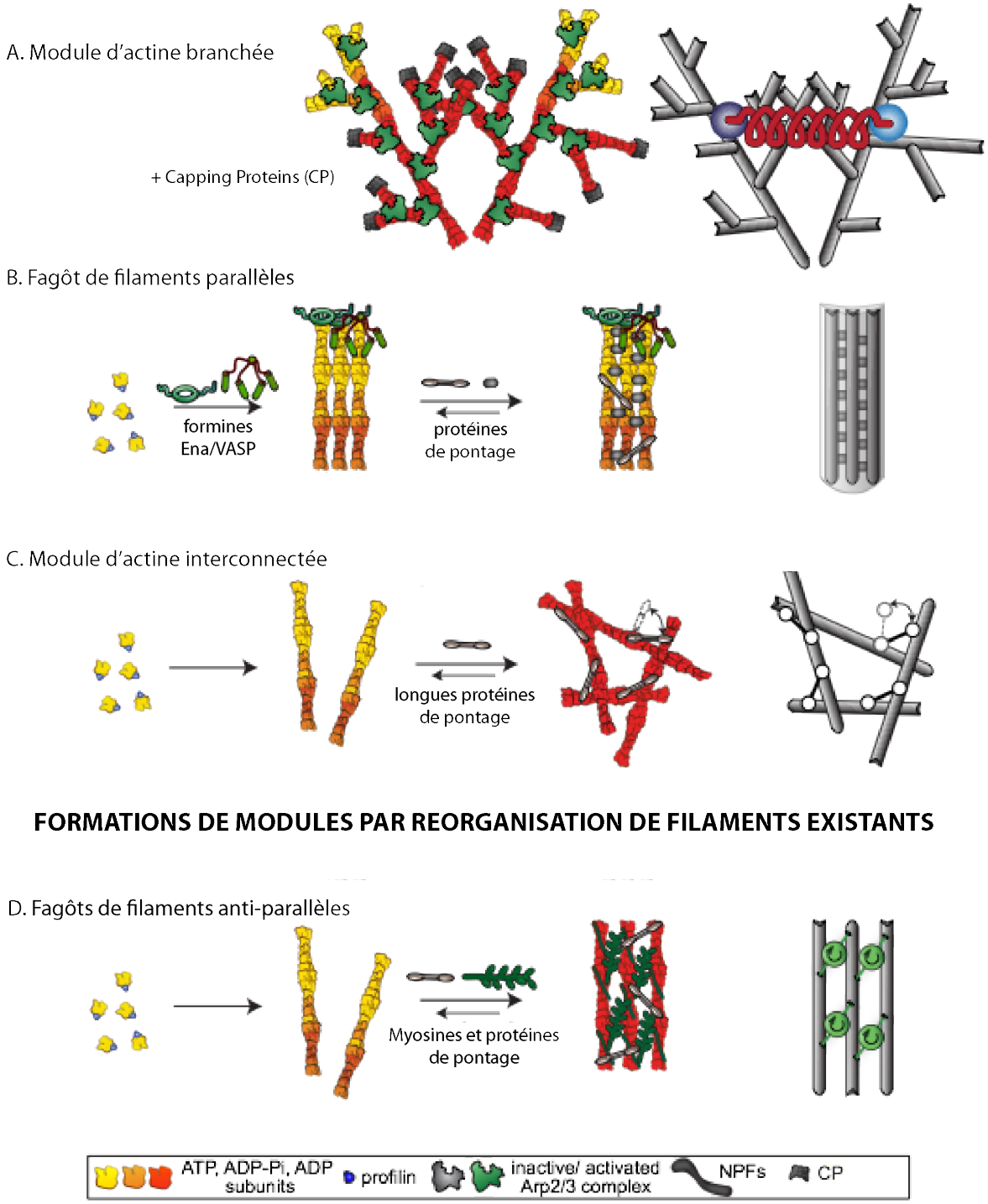

Figure 7 : Présentation des différents modules formés en fonction des protéines interagissant avec l'actine

Adapté de Blanchoin, Nature Reviews, 2013

de s'associer sur le côté du filament et de générer un nouveau filament (orienté à 70° par rapport au filament initial) auquel il reste associé par l'extrémité pointue. Ce complexe permet donc de générer des extrémités barbées libres qui seront bloquées rapidement par la capping protein. L'interaction entre ces deux mécanismes conduit à la génération de réseaux branchés dont la taille des branches peut être régulée par la concentration d'actine, la concentration de capping protein et la concentration d'Arp2/3 (Achard, Current Biology, 2010). Le renouvellement (« turnover ») de l'actine dans ces structures se compte en secondes et dizaine de secondes (Smith, Biophysical Journal, 2013). La régulation de ces paramètres va conditionner les propriétés mécaniques du réseau. Macroscopiquement, ce réseau possède des propriétés élastiques qui sont conditionnées par la taille du maillon du réseau (distance entre les filaments ou entre les complexes Arp2/3). Plus le réseau est dense, plus il est rigide (van der Gucht, PNAS, 2005). Ce réseau est également capable de générer des forces liées à sa polymérisation. Ces forces seront capables de pousser sur la membrane plasmique ce qui permettra de la déplacer mais également en réaction de pousser le réseau vers l'intérieur de la cellule (flux rétrograde d'actine). Ces phénomènes sont également utilisés par des pathogènes pour se déplacer dans le cytoplasme de la cellule (listeria, plasmodium, …) (Loisel, Nature, 1999)

Les filopodes (Figure 7B)

Le mécanisme de formation de ces structures est encore débattu aujourd'hui. Il implique la génération d'actine par le complexe Arp2/3 (à la base de la structure), par des formines et par Ena/VASP (au sommet de la structure, sous la membrane).

Les formines s'assemblent sous forme de dimères et sont capables de nucléer des filaments et de les allonger (plus rapidement que s'ils étaient libres) tout en maintenant l'extrémité barbée protégée de la capping protein. Les protéines Ena/VASP ont un mode de fonctionnement encore mal connu aujourd'hui. Elles protègent les filaments de la capping protein et augmentent la vitesse d'élongation des filaments d'actine à leur extrémité barbée, mais pourraient aussi jouer un rôle comme protéines de pontage. Les formines et Ena/VASP sont, comme le complexe Arp2/3, des protéines souvent régulées à proximité de la membrane plasmique ce qui limite leur champ d'action au sein de la cellule.

La structure générée par ces mécanismes est un doigt à la surface de la membrane dont le corps est constitué d'un fagot de filaments d'actine organisés de façon parallèle et pontés les uns aux autres. Les formines et Ena/VASP se localisent à l'extrémité du doigt, au contact de la membrane.

Le turnover des protéines associées à ces filaments se compte en secondes (Aratyn, Molecular Biology of the Cell, 2007) alors que le turnover de l'actine y est extrêmement lent (minutes). Ceci peut s'expliquer car les filaments se renouvellent par leurs extrémités. Dans ce type de structure, du fait de

la polymérisation par les formines et Ena/VASP, on s'attend à un faible ratio (nombres d'extrémités)/quantité d'actine polymérisée ce qui donne très peu ou pas de turnover de l'actine.

Cette structure linéaire possède elle aussi une rigidité qui dépendra de la quantité de protéines de pontage et de leur mode d'interaction avec les filaments (pontage fixe ou autorisant le coulissage des filaments les uns par rapport aux autres). La longueur de persistance de ces fagots est proportionnelle au nombre de filaments dans le cas du coulissement, et varie comme le carré du nombre de filaments si le coulissement n'est pas possible.

Le cortex d'actine (Figure 7C)

Il s'agit d'un fin réseau de filaments d'actine pontés, de façon isotrope, sur lequel des myosines exercent des forces contractiles. Il est intimement lié à la membrane cellulaire. Son mécanisme de formation est encore mal connu aujourd'hui en partie du fait de la difficulté à l'observer en microscopie. Certains de ses composants ont pu être identifiés : des protéines de pontage (alpha-actinine, filamine, fimbrine), des protéines liées à la contractilité (myosine, tropomyosine, tropomoduline) et des protéines de fixation à la membrane (famille ezrine-radixine-moesine (ERM), myosine 1, filamine). Le turnover des ces structures se compte en secondes ou dizaines de secondes selon les composants.

Le cortex d'actine se caractérise par ses propriétés viscoélastiques mais également par la tension corticale qui y est générée: il se comporte de façon élastique pour des déformations de courtes durées et de façon visqueuse pour des déformations plus longues (Howard, 2001), du fait du réarrangement des liens entre les filaments d'actine au cours du temps. Il est difficile de mesurer la tension corticale uniquement car toute déformation de la cellule implique potentiellement une réponse liée à la fois à sa tension mais également à ses propriétés élastiques.

Remodelage du cytosquelette d'actine et désassemblage : un module peut en cacher un autre.

Les fibres de stress (Figure 7 D)

Les fibres de stress (fagots d'actine antiparallèles) vont émerger de la réorganisation de filaments préexistants (lamellipode, filopode, cortex d'actine) sous l'effet de la myosine et d'autres protéines capables de réorganiser les réseaux d'actine (ADF/cofiline et alpha-actinine).

Leur existence in vivo a pu être remise en question lorsqu'on a montré que les fibroblastes ne produisaient pas de fibres de stress dans un tissu conjonctif normal (Byers , Cell. Muscle Motil., 1984 ; Ehrlich, Am. J. Pathol., 1984). Cependant, il existe de nombreuses situations dans lesquelles les

cellules forment des fibres de stress au sein de notre organisme. Il s'agit de situations particulières dans lesquelles les cellules produisent des forces importantes. C'est notamment le cas des fibroblastes au sein des blessures (Gabbiani, Experientia, 1971), des cellules épithéliales sur le bord d'une blessure (Bement, J. Cell Biol., 1993), des cellules endothéliales exposées à un flux (Franke, Nature, 1984), …

L'ADF/cofiline est une protéine qui s'associe préférentiellement à la partie ADP des filaments d'actine. Cette fixation modifie localement les propriétés mécaniques du filament. Son attachement focal sur un filament crée des zones de cisaillement qui vont permettre la fragmentation des filaments (Suarez, Current Biology, 2011).

Les myosines forment une grande famille de protéines (Berg, Molecular Biology of the Cell, 2001). Celles qui sont au centre des mécanismes qui m'intéressent sont les myosines non-musculaires de type 2 (NM 2). Elles partagent la même structure que les myosines musculaire de type 2 : elles sont

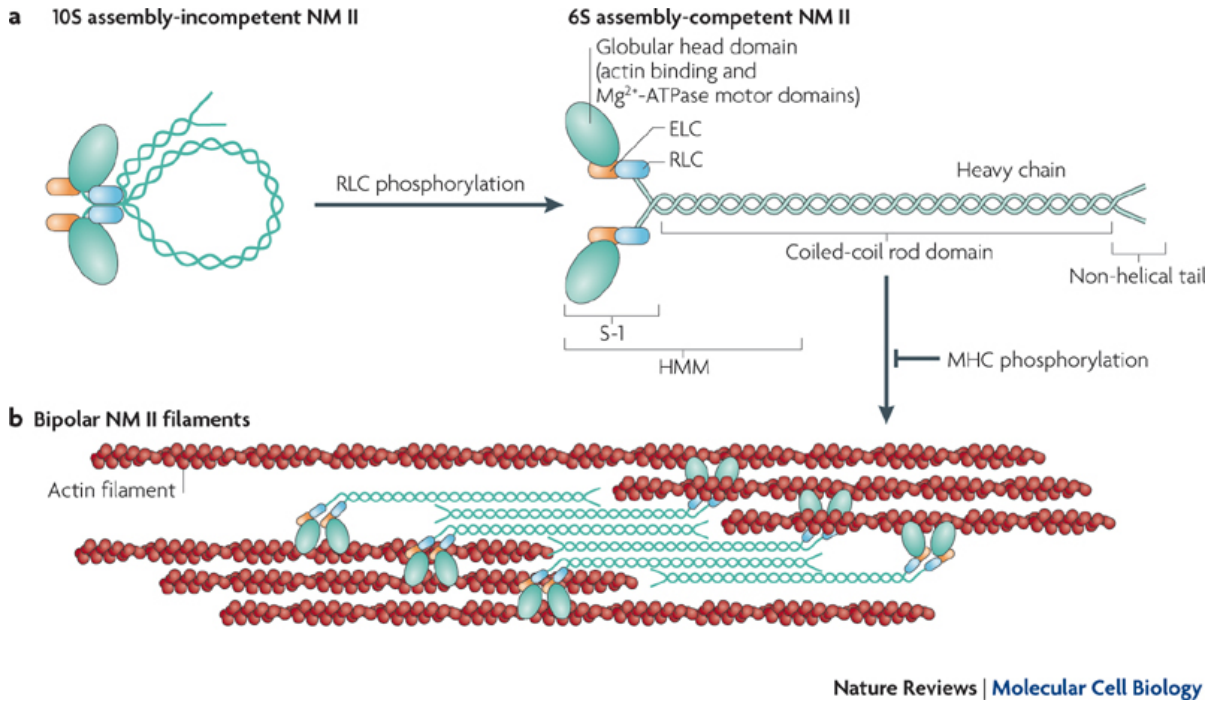

Figure 8 : Structure et action des myosines non-musculaire de type 2 (NM 2)

Vincente-Manzanares, Nature Reviews, 2009

(a) – conformations repliée (gauche) et activée de la NM 2 selon l'état de phosphorylation de la chaîne légère régulatrice. (b) – assemblage de la forme active de la myosine sous formes de mini-filaments qui pourront générer un phénomène de contraction

composées de 3 paires de peptides : 2 chaines lourdes, 2 chaines légères régulatrices et 2 chaines légères essentielles (Figure 8). Elles possèdent 2 têtes, une queue et un cou. Les têtes sont formées par les extrémités N-terminales des deux chaines lourdes. C'est cette partie qui se fixera au filament et sera capable de générer un mouvement couplé à l'hydrolyse de l'ATP. Les parties C-terminales des chaines

lourdes s'enroulent l'une autour de l'autre pour former la queue. Cette zone permet l'assemblage des myosines en mini-filament pour générer un glissement de plusieurs filaments d'actine les uns par rapport aux autres. La partie intermédiaire entre tête et queue constitue le cou. C'est à cet endroit que vont venir se fixer les 4 chaines légères. La chaine régulatrice contrôle l'activité de la myosine. Sous sa forme phosphorylée, elle permet le déroulement de la queue et l'activité motrice ATPasique de la myosine. Sous sa forme non-phosphorylée, elle entraine un repliement de l'ensemble de la structure et empêche la génération de forces. (Figure 8)

L'alpha-actinine est une protéine de pontage de la famille des spectrines. Dans les cellules non-musculaires, elle s'assemble sous la forme d'un homo-dimère allongé possédant un site de fixation à l'actine à chaque extrémité. Les isoformes 1 et 4 sont présentes dans les cellules non-musculaires et se localisent préférentiellement au niveau des adhésions et des fibres de stress. (Sjöblom, Cellular and Molecular Life Sciences, 2008). Elles sont capables de s'associer à de nombreuses protéines (Otey, Cell Motility and the Cytoskeleton, 2004) et sont impliquées dans la transmission des forces au niveau des adhésions. (Roca-Cusachs, PNAS, 2013).

La formation de fibres de stress peut s'effectuer par plusieurs mécanismes. Le premier passe par la réorganisation du lamellipode. C'est en particulier le cas dans des cellules en migration. Un réseau

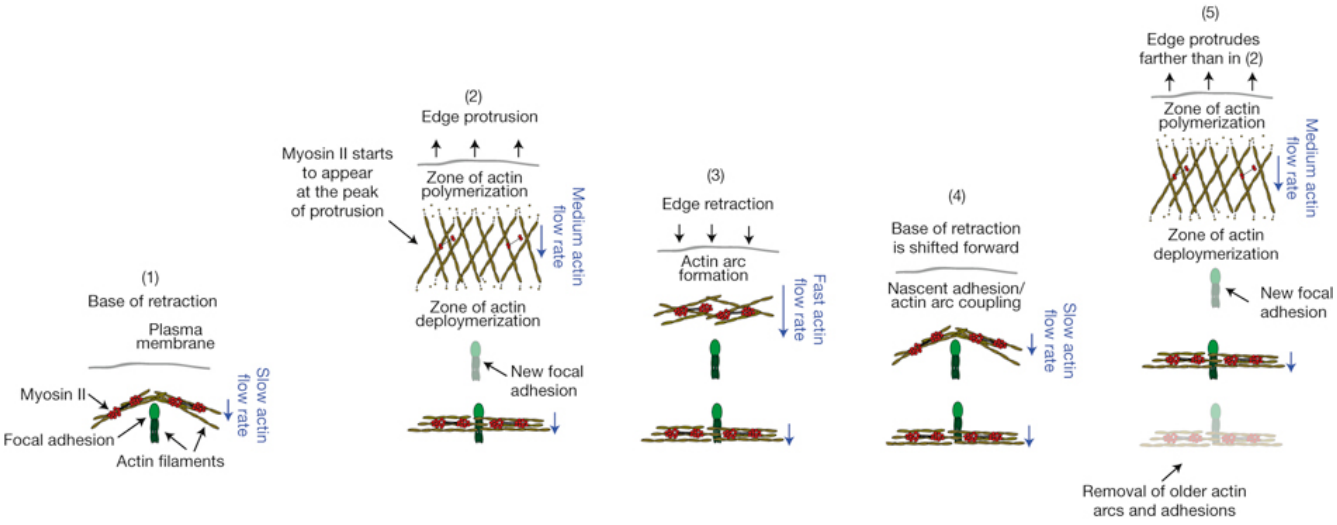

Figure 9 : Schéma expliquant la formation des arcs transverses par les contractions périodiques du lamellipode.

(Burnette, Nature Cell Biology, 2011)

dendritique est rapidement généré à l'avant de la cellule. Celui-ci s'enrichit progressivement en myosine avant de s'effondrer sur lui-même sous l'effet de la myosine, et probablement également de l'ADF/cofiline. En s'effondrant, la structure va permettre le réarrangement des filaments qui la composaient en un arc transverse de filaments antiparallèles (Burnette, Nature Cell Biology, 2011). Cet arc pourra ensuite contacter des fagots parallèles d'actine formés au niveau des adhésions par les

formines (fibres dorsales). L'attachement de ces structures permettra la formation d'une fibre de stress ancrée à ses deux extrémités à des adhésions.

La formation de fibres de stress par assemblage de 2 fibres dorsales a également été décrite. Bien que possible, ce mécanisme ne semble pas être le mécanisme privilégié de formations des fibres de stress car la formation de grandes fibres dorsales est assez rare. Il a d'ailleurs été décrit uniquement dans des cellules où était inhibé le complexe Arp2/3 (Hotulainen, Journal of Cell Biology, 2006), il s'agirait donc plutôt d'un mécanisme de remplacement.

L'activation brusque de la myosine dans des cellules métaboliquement peu actives va également permettre la formation rapide de fibres de stress, sans polymérisation de nouveaux filaments (Nobes, Cell, 1995). La myosine est sans doute capable de réarranger un réseau d'actine diffus (cortex d'actine ?) en fagots antiparallèles lorsqu'elle est massivement activée. Ces fagots pourront ensuite contacter des fibres dorsales et former une fibre de stress.

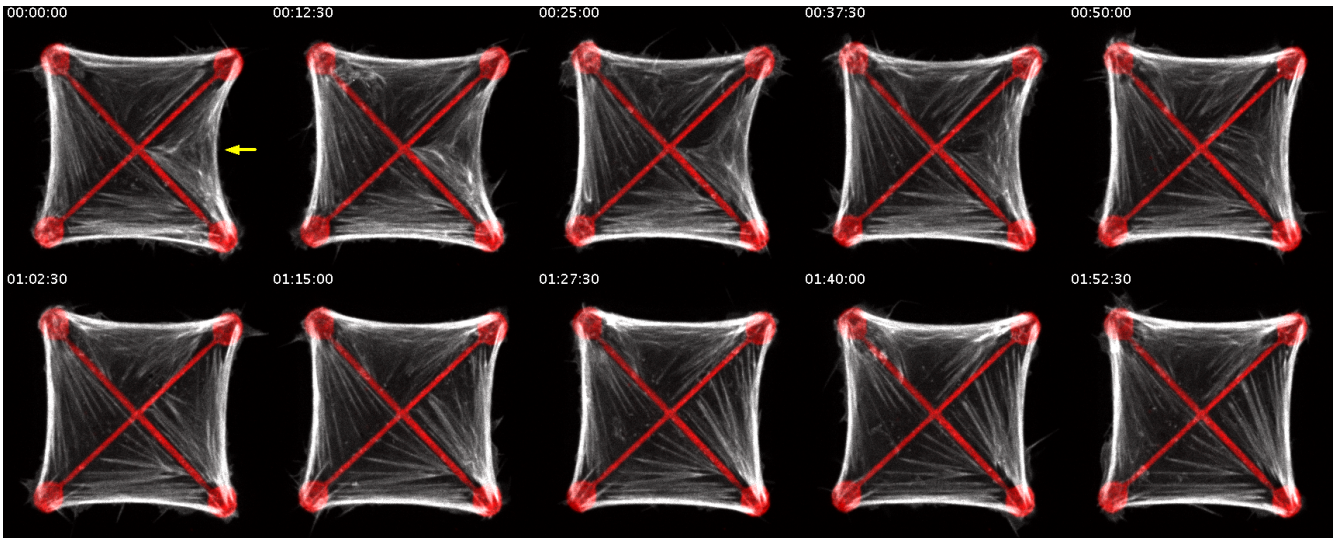

Figure 10 : Formation de fibres de stress à partir d'un réseau diffus d'actine

En blanc le cytosquelette d'actine visualisé par Lifeact-GFP, en rouge le micropattern sur lequel il se trouve. La flèche jaune indique le quart de cellule dans lequel on observe une réorganisation active du cytosquelette qui va conduire à la formation de fibres de stress par coalescence/réorganisation d'un réseau d'actine préexistant.

Les filopodes peuvent également être incorporés dans les fibres de stress. En effet, au moment de l'effondrement du lamellipode, les filopodes peuvent basculer et se retrouver incorporés à un arc transverse puis à une fibre de stress. (Nemethova, Journal of Cell Biology, 2004)

Le turnover de l'actine au sein des fibres de stress varie selon le type de fibres de stress (voir paragraphe suivant) mais la demi-vie des structures est de l'ordre de quelques minutes. Le turnover de la myosine est de l'ordre de la minute et celui de l'alpha-actinine se compte lui en dizaines de secondes. (Hotulainen, Journal of Cell Biology, 2006). Ces mesures sont des moyennes et ces

paramètres sont potentiellement sensibles au niveau de forces au sein de ces structures, certaines protéines sont en effet capables de se relocaliser en fonction du niveau de la force appliquée à la fibre (Colombelli, Journal of Cell Science, 2009).

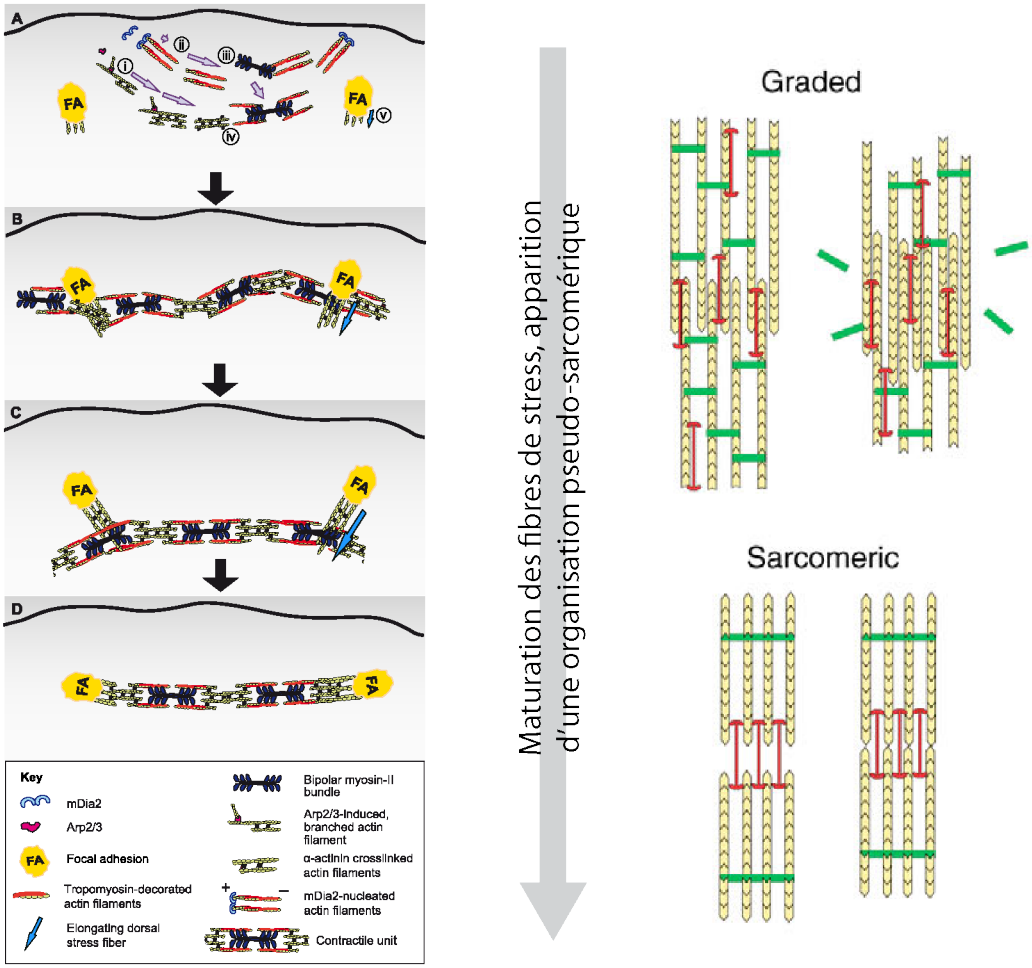

Figure 11 : Formation des fibres de stress à partir des arcs transverses et organisation progressive de l'organisation de l'actine au sein de la fibre

Pellegrin J. Cell Science, 2007 et Tojkander, J. Cell. Science, 2012

Les fibres de stress sont des structures contractiles. Les mécanismes de production de forces au sein de ces structures sont encore mal connus, en partie du fait de leur hétérogénéité structurelle. En effet, une organisation pseudo-sarcomérique de la myosine et de l'alpha-actinine a pu être décrite dans certains types cellulaires (Peterson, Molecular Biology of the Cell, 2004) mais n'est en rien systématique (Cramer, JCB, 1997), (Mseka, CMC, 2009). Des expérimentations in silico et in vitro permettent d'expliquer l'apparition spontanée de cette organisation (Friedrich, Plos Computational Biology, 2012 ; Thoresen, Biophys. J., 2013) cependant celle-ci prend du temps. Il est possible que les fibres de stress activement renouvelées n'atteignent jamais cet état d'équilibre.

Quelle que soit l'organisation, la contractilité au sein de ces structures provient du glissement

des filaments les uns par rapport aux autres par la myosine et du pontage des filaments entre eux. Les différents modèles expliquant la force générée au sein des fibres de stress sont l'objet d'une partie ultérieure de l'introduction.

Un pool d'actine renouvelé, le rôle du désassemblage

Les différents modes d'assemblage de l'actine ont été décrits, cependant, pour que la description soit complète, il est nécessaire d'expliquer comment le stock d'actine monomérique est renouvelé au sein de la cellule. Les différents modules décrits vont pouvoir être détruits par certaines protéines. Il s'agit principalement de l'ADF-cofiline et de la myosine.

Des études récentes (Murrell, PNAS, 2012 ; Vogel, eLife, 2013) suggèrent que les filaments de myosine, en courbant un filament d'actine entre leurs deux extrémités, sont capable de le fragmenter. L'ADF-cofiline précédemment décrite est également capable de fragmenter des filaments existants et jouerait également un rôle dans le détachement des branches d'actine au niveau du complexe Arp2/3.

Ces deux mécanismes vont permettre de libérer des filaments d'actine très courts. Ces derniers pourront ensuite être dépolymérisés pour renouveler le pool d'actine monomérique ou être réutilisés tel quel selon le mécanisme d' « annealing ».

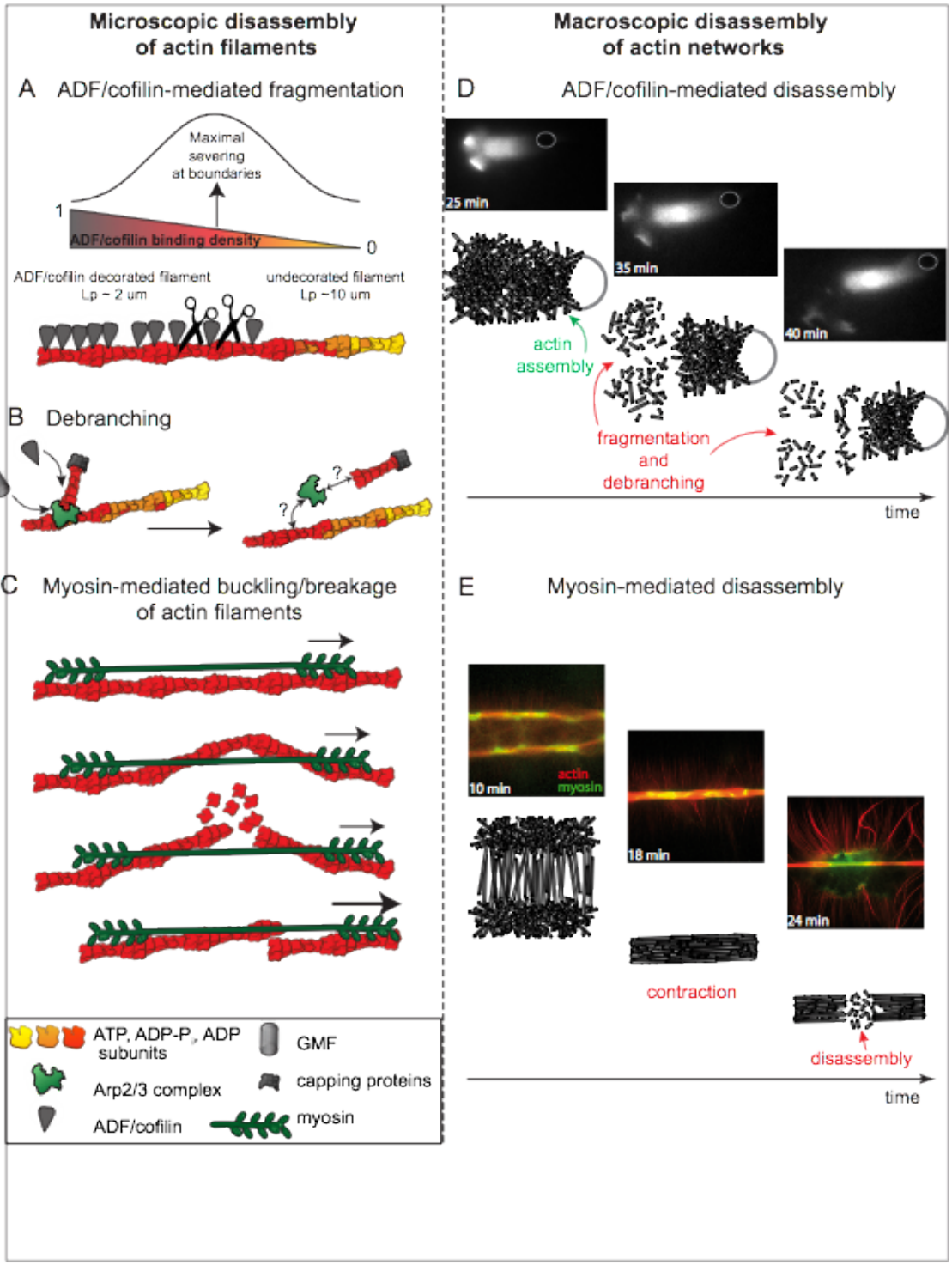

Figure 12 : Mécanismes de désassemblage des modules d'actine.

Blanchoin, Physiological Reviews , 2013

3. COMPORTEMENT MECANIQUE DES FIBRES DE STRESS ET MODELISATION

Le comportement mécanique des fibres de stress a été particulièrement étudié. Leurs formes définies en font des objets plus facilement manipulables qu'un réseau branché ou le cortex d'actine. Plusieurs approches ont été mises en œuvre. L'une des approches de choix a été la coupure de ces fibres au sein de la cellule en utilisant un laser pulsé (Kumar, Biophys. Journal, 2006). Il est ainsi possible, en observant la rétraction des fibres, d'avoir une idée de leur comportement mécanique. Ces expériences ont permis de mettre en évidence les propriétés viscoélastiques de ces fibres, au cours de

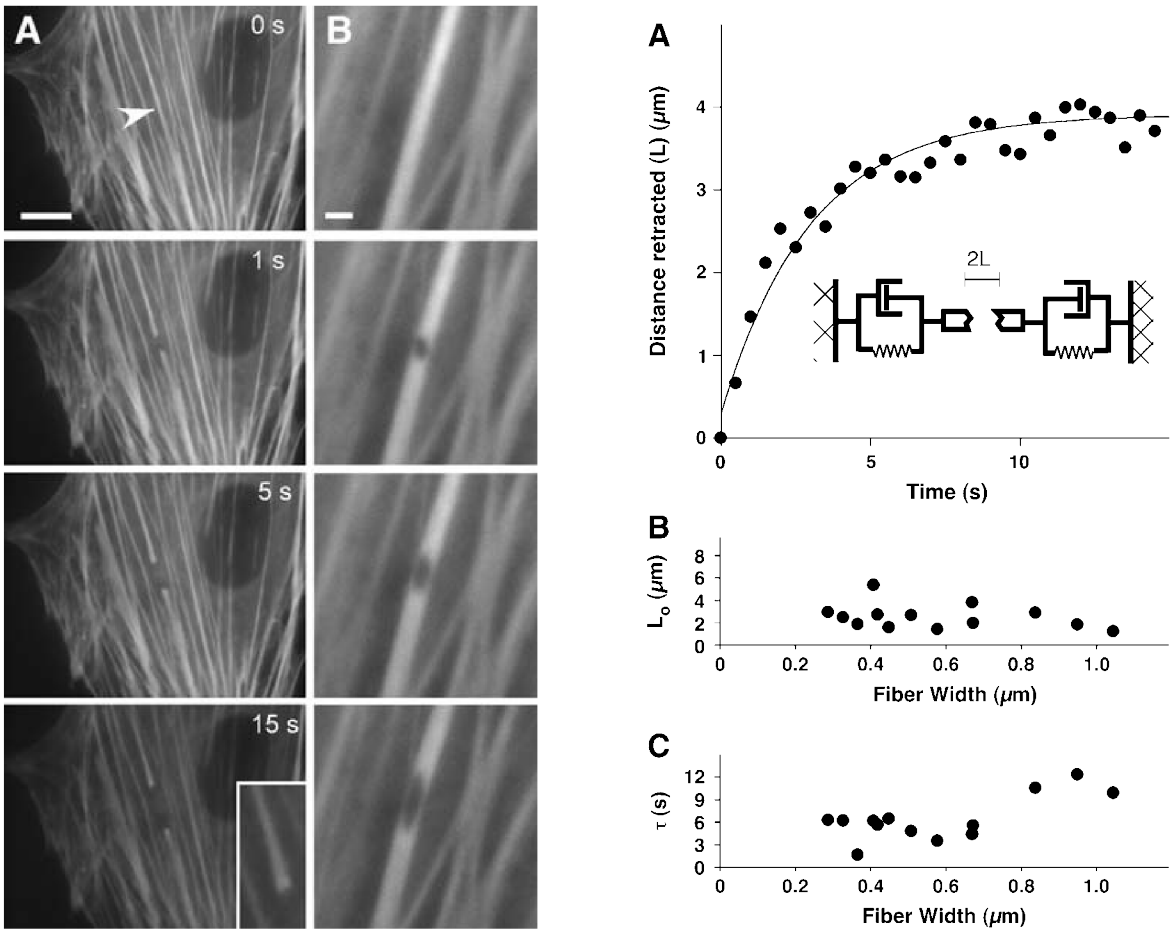

Figure 13 : Retraction viscoélastique des fibres de stress après ablation laser

Kumar, Biophys. J., 2006

Gauche – retraction d'une fibre de stress après coupure. En se retractant, l'extrémité de la fibre s'élargit. **Milieu** – un impact est fait au centre de la fibre, sans la couper complètement. Le trou s'élargi progressivement, ce qui montre l'adaptation de la fibre en réponse à sa perte de résistance à la traction. La fibre se rompt parfois spontanément après 10-20s. **Droite haut** – distance de rétraction d'une des berges de la coupure. **Droite milieu et bas** – il n'y pas de corrélation entre la largeur de la fibre et sa rétraction finale ou la constante de temps de cette rétraction.

leur rétraction. (Figure 13)

Leur aspect contractile a par ailleurs pu être mis en évidence sur des fibres intactes. Des cellules ont été débarrassées de la membrane qui les surmontait et les fibres ont été mises en présence d'ATP pour permettre à la myosine d'entrer en action. (Deguchi, J. Cell. Biochem., 2011). Dans ces conditions, certaines fibres se contractent et d'autres ondulent. Les auteurs en déduisent que les fibres de stress ne se contractent pas toutes de la même façon au sein de la cellule. Les fibres se contractant le plus vont ainsi déplacer la membrane cellulaire et déformer les fibres moins contractiles attachées à proximité. (figure 14)

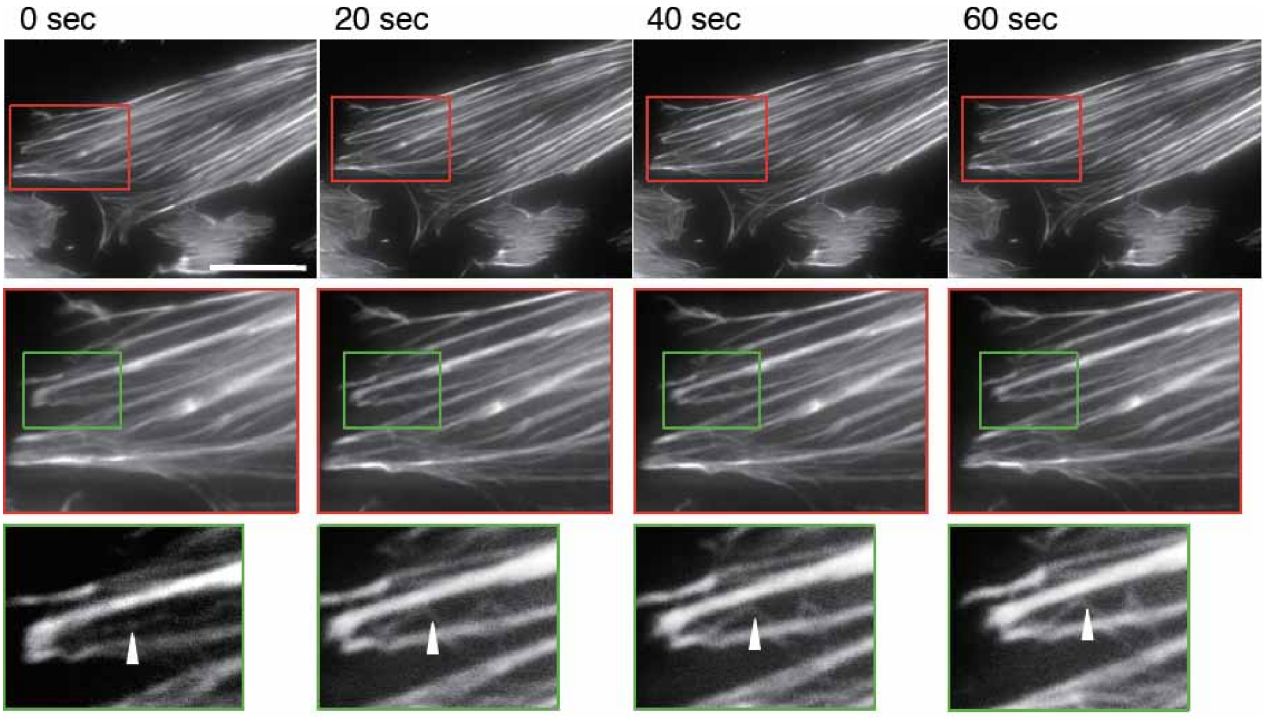

Figure 14 : Contraction et compression simultanées de fibres de stress adjacentes.

Deguchi, J. Cell. Biochem., 2012

La partie supérieure de la membrane des cellules est retirée par un choc hypotonique. Les cellules sont ensuite mises en présence d'un tampon de contraction contenant de l'ATP et du calcium. La flèche montre une petite fibre qui ondule sous l'effet du déplacement imposé par l'imposante fibre voisine

In vivo, des fagots d'actomyosine antiparallèles ont pu être reconstitués (Thoresen, Biophys. J., 2011 et 2013). Ces expériences ont permis de montrer qu'une contraction était possible avec un système minimal et que la force contractile générée au sein de ces structures dépendait du ratio myosine/actine.

De nombreux modèles ont pu être imaginés pour rendre compte de ces observations. Je ne pourrais malheureusement pas être exhaustif dans cette partie devant le nombre impressionnant de

modèles disponibles. Deux m'ont semblé particulièrement pertinents.

Modélisation sarcomérique des fibres de stress

Lorsque la rétraction viscoélastique des fibres de stress par ablation laser a été décrite pour la première fois, un modèle phénoménologique a été imaginé (figure 13). Celui-ci décrit les deux fragments de la fibre comme deux éléments mécaniques comprenant chacun un ressort et un piston en parallèle. Ce modèle initial a ensuite pu être raffiné en ajoutant un moteur à cet assemblage permettant de rendre compte de la force générée par les myosines (corps de Kelvin-Voigt). Pour rendre compte de la structure sarcomérique de la fibre, chaque fragment de fibre a ainsi été considéré comme une succession de ces unités contractiles, branchées en série.

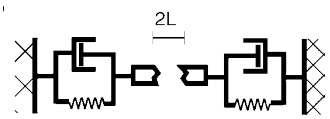

$$u(x) = \frac{F}{k}\left(1 - e^{-\frac{t}{\tau}}\right)$$

$$\tau = \frac{k}{\eta}$$

Kumar, Biophys. J., 2006

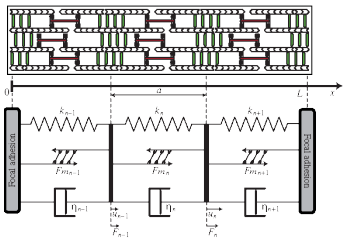

$$u(t) = -\frac{F_{\text{stall}}}{k}\left(1 - e^{-t/\tau}\right)$$

$$\tau = \eta_e / k$$

$$\eta_e = \eta + F_{\text{stall}}/v_0$$

Besser, New J. Phys., 2007

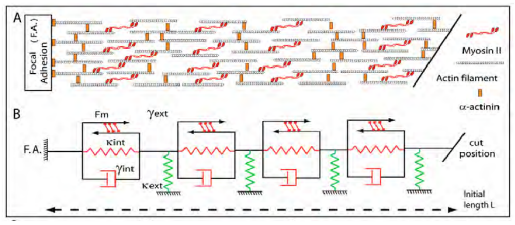

$$a^2 \Delta \dot{u}(x,t) + \tau\, a^2 \Delta \ddot{u}(x,t) - \kappa\, u(x,t) - \tau_e\, \dot{u}(x,t) = 0 \,. \qquad \text{(A5)}$$

Table A1. Model parameter interpretations and values obtained from fits to the data

Parameter	Abbreviation for	Interpretation	Actin-FRAP Mean ± s.d.	α-actinin Mean ± s.d.	P-value (t-test)
κ	k_{ext}/k_{int}	Crosslink ratio	0.035±0.034	0.078±0.059	0.0030014
δ	F_{stall}/k_{int}	Contraction length	0.66±0.36 μm	0.59±0.33 μm	0.35
τ	$(\eta_{int}+F_{stall}/v_0)/k_{int}$	Equilibration time	29±27 seconds	15±11 seconds	0.0029
τ_e	η_{ext}/k_{int}	Equilibration time	0.134±0.23 seconds	0.134±0.27 seconds	0.72

Colombelli, J. Cell. Science, 2009

Figure 15 : Différents modèles mécaniques expliquant la rétraction des fibres de stress.

Ce cadre théorique permet d'extraire des informations mécaniques à partir de la courbe représentant la distance entre les deux extrémités des fragments de la fibre au cours du temps. En effet, cette distance doit suivre une exponentielle dont les paramètres correspondent à des grandeurs physiques caractérisant la fibre. Les paramètres de cette équation sont sa constante de temps et son plateau. Sa constante de temps est liée à la viscosité de la fibre et à son élasticité alors que le plateau dépendra de la force contractile des myosines et de l'élasticité de la fibre (Besser, New J. Phys., 2007).

Ce cadre de lecture a permis de montrer que la localisation des fibres au sein de la cellule avait une importance sur les forces qu'elles généraient : les fibres périphériques se rétractent plus avec un constante de temps plus longue que les fibres centrales ce qui suggère qu'elles exercent plus de forces et qu'elles sont plus rigides. (Tanner, Biophys. J., 2010)

Une autre étude a permis de mettre en évidence le rôle de points d'ancrages mécaniques avec le

substrat tout le long de la fibre. (Colombelli, J. Cell Science, 2009) Cependant, ce modèle suggère que la force relâchée après une coupure se localiserait sur les berges de la coupure et non pas aux extrémités de la fibre, au niveau des adhésions. Les expériences sur substrat déformable couplant la mesure de force et l'ablation laser n'ont pas permis de mettre en évidence un tel phénomène. (Kumar, Biophys. J., 2006).

Modélisation des fibres de stress comme un réseau interconnecté.

Les fibres de stress peuvent également être modélisées comme un réseau interconnecté d'actine, de crosslinkers et de myosines, sans qu'une organisation particulière soit présupposée (Yoshinaga, Phys. Biol, 2012).

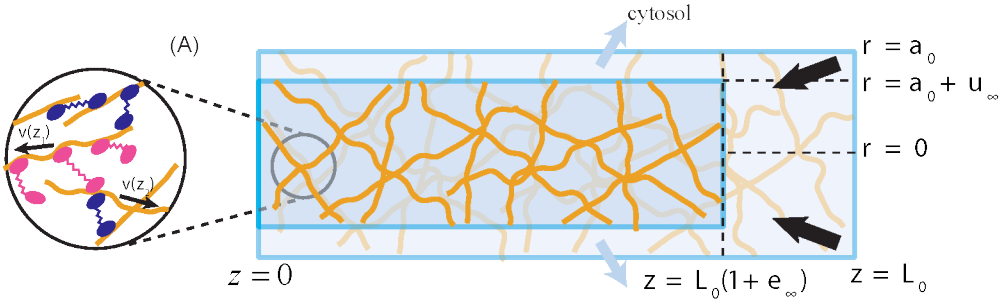

Figure 16 : Contraction d'un fagot d'actomyosine pontée

Yoshinaga, Phys. Biol., 2012

Schéma de la contraction du fagot. Le cytosol présent dans le réseau est expulsé au moment de la contraction. L'extrémité gauche est fixée à l'origine z = 0. Le fagot contracte longitudinalement de L0 à L0 (1+e∞) et radialement de a0 à a0 + u∞. Les molécules de pontage contribuant à la viscosité (resp. élasticité) sont affichées en rouge (resp. bleu). Les turnovers de ces deux composants contribuent à la friction entre les protéines.

Selon ce modèle, le temps caractéristique de contraction varie comme la longueur des filaments d'actineet le temps caractéristique d'attachement des crosslinkers au filament d'actine. Il est inversement proportionnel à la longueur des crosslinkers. Ce modèle prédit également que la contraction des fibres de stress devrait avoir lieu à la fois dans le sens longitudinal mais aussi radial. Cette prédiction n'est cependant pas en accord avec l'expérience : l'extrémité libre des deux fragments de fibres de stress a tendance à s'élargir au moment de la rétraction (Figure 13)

Ces modèles permettent de mieux comprendre les propriétés mécaniques des fibres de stress mais ne rendent pas compte de tout le détail du mécanisme de production de forces. Pour permettre une meilleure compréhension du fonctionnement des fibres de stress, des modèles prenant en compte le caractère inhomogène de la fibre de stress (polarité variable du fait de leur mode de formation avec des

filaments parallèles aux extrémités et antiparallèles au centre de la fibre) et expliquant la localisation et le niveau des forces relâchées après coupures, sont nécessaires. Le modèle de Besser, New J. Phys. est à ce sujet remarquable car il intègre une activation différente des myosines le long de la fibre du fait de la stimulation de la contractilité à partir des adhésions et comprend un rétrocontrôle de la force sur la signalisation au niveau de l'adhésion.

Je vais maintenant décrire plus précisément les adhésions cellulaires. Ces structures sont primordiales dans la régulation de la production de forces et jouent un rôle prépondérant dans l'organisation de l'architecture cellulaire.

4. LES ADHESIONS : AGENTS DOUBLES DANS LA MECHANOTRANSDUCTION

Les adhésions assurent le lien mécanique entre la cellule et son environnement et permettent ainsi la cohésion de nos tissus et la transmission d'informations mécaniques sur des longueurs importantes. La formation des adhésions est un processus progressif qui met en jeux de nombreuses

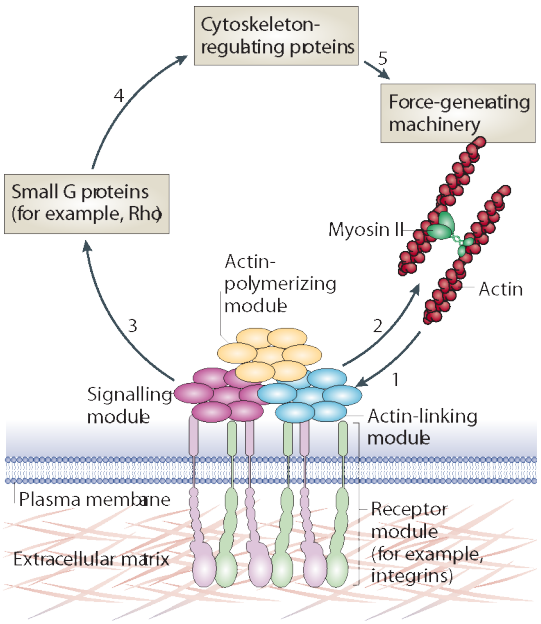

Figure 17 : Interaction entre le cytosquelette d'actine et les adhésions focales.

Geiger, Nature Reviews, 2009

Schéma illustrant l'interaction entre le cytosquelette et les adhésions focales. Une boucle de rétrocontrôle est à l'œuvre dans ce processus. Les adhésions vont pouvoir déclencher une signalisation intracellulaire en réponse aux propriétés physico-chimiques de l'environnement. Cette signalisation va permettre la régulation de composants clés du cytosquelette, notamment des protéines qui s'associent au cytosquelette pour le réguler (moteurs moléculaires, protéine de pontage, protéines de coiffe, …). Le cytosquelette agit lui-même en retour directement au niveau des adhésions, notamment en produisant des forces mécaniques. Ces forces vont pouvoir moduler à leur tour les adhésions. La boucle est bouclée !

protéines. Je vais maintenant décrire les étapes de formation d'une adhésion mature en expliquant le rôle des forces dans ce mécanisme et le lien qu'il peut y avoir entre la taille d'une adhésion et la force qu'elle transmet. Les adhésions ne sont pas seulement un lien entre la cellule et son environnement. Elles jouent également un rôle très important dans le contrôle des voies de régulation biochimiques de la contractilité, cet aspect sera évoqué dans un second temps

A. AGREGATION DES INTEGRINES

Les intégrines forment une famille de protéines transmembranaires. Elles permettent le lien entre l'extérieur de la cellule (les protéines de matrice extracellulaire) et le cytosquelette d'actine via un certain nombre de protéines qui s'associent à leur extrémité intracellulaire. Pour s'activer, les

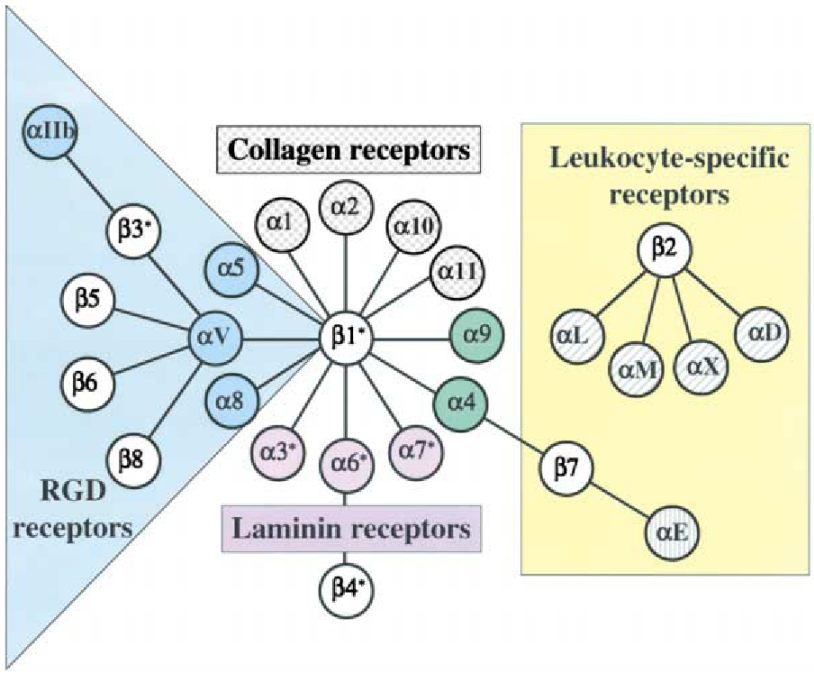

Figure 18 : La famille des intégrines

Hynes, Cell, 2002

La figure représente les sous-unités connues des intégrines. Chaque lien représente une association possible entre sous-unité alpha et béta pour former un dimère fonctionnel. Dans notre système expérimental, la fibronectine est la principale protéine de matrice utilisée. Celle-ci interagit avec les dimères reconnaissant les groupes RGD, représentés dans la partie bleue de la figure.

intégrines s'assemblent sous forment d'hétérodimères composés d'une sous-unité alpha et d'une sous-unité béta. Chaque sous-unité traverse la membrane une seule fois. La majeure partie (>1600 acides

aminés) de la sous-unité se localise dans l'espace extracellulaire alors que la partie cytoplasmique n'est composée que de 2 petits domaines (20-50 acides aminés). 18 sous-unités alpha et 8 sous-unités beta différentes ont à ce jour été identifiées. Elles permettent la formation de 24 hétérodimères fonctionnels différents. La combinaison des sous-unités va permettre de déterminer la spécificité de l'intégrine pour la protéine d'adhésion reconnue. (figure 18)

Pour permettre d'initier la formation d'une adhésion, un seul dimère n'est pas suffisant. Un contrôle environnemental précis du nombre d'adhésions capables de se fixer et de leur espacement a permis de montrer que 4 intégrines espacées les unes des autres de 60 nm ou moins étaient suffisantes pour permettre l'étalement cellulaire (Schvartzman, Nano Letters, 2011), ce qui suggère que la formation d'adhésions est possible. Une densité suffisante de protéines d'adhésions est donc nécessaire pour initier la formation d'une adhésion. Par ailleurs, l'agrégation de plusieurs intégrines n'est pas un processus spontané. Les adhésions se forment préférentiellement à l'arrière du lamellipode. Il est probable que le flux rétrograde d'actine entraine avec lui des intégrines et facilite ainsi leur agrégation. Le rôle de Rac, une protéine stimulant la formation du lamellipode, dans la formation des complexes focaux (Nobes, Cell, 1995) est un argument qui va dans ce sens.

B. DU COMPLEXE FOCAL AU CONTACT FOCAL, UNE SITUATION SOUS-TENSION

Peu après l'agrégation des récepteurs et leur attachement à la matrice, de nombreuses protéines vont être recrutées du côté intracellulaire des intégrines pour former un complexe focal (ou adhésion naissante). La taline, la vinculine et la paxilline en sont les 3 composants les plus étudiés. Ces molécules vont permettre la stabilisation transitoire de l'édifice et une interaction avec d'autres protéines. Le complexe va ensuite pouvoir disparaître ou maturer en un contact focal. La taline joue un grand rôle dans ce processus. Sa structure suggère en effet un changement de conformation sensible à la force d'étirement à laquelle elle soumise. Ce changement de conformation lui permettrait d'interagir plus efficacement avec la vinculine et de recruter massivement cette protéine au niveau de l'adhésion (Hytönen, Plos Comput. Biol., 2008). La vinculine est capable de fixer l'actine et la taline. Elle n'est pas indispensable à la transmission de forces mais joue un rôle important dans le couplage entre la taille de la cellule et le niveau de forces produites (Dumbauld, PNAS, 2013). La paxilline permet le recrutement d'autres partenaires, dont la vinculine et la kinase des adhésions focales (FAK).

Si cette maturation est enclenchée, de nombreuses protéines vont être recrutées (FAK, VASP, alpha-actinine, tensine, zyxine, …). Ces protéines sont regroupées sous le vocable d'adhésome (figure 19). Elles vont permettre de déclencher une signalisation intracellulaire qui aboutira notamment à l'activation de Rho et de ses 2 effecteurs mDia1 et ROCK (Watanabe, Nat. Cell. Biol., 1999). Le

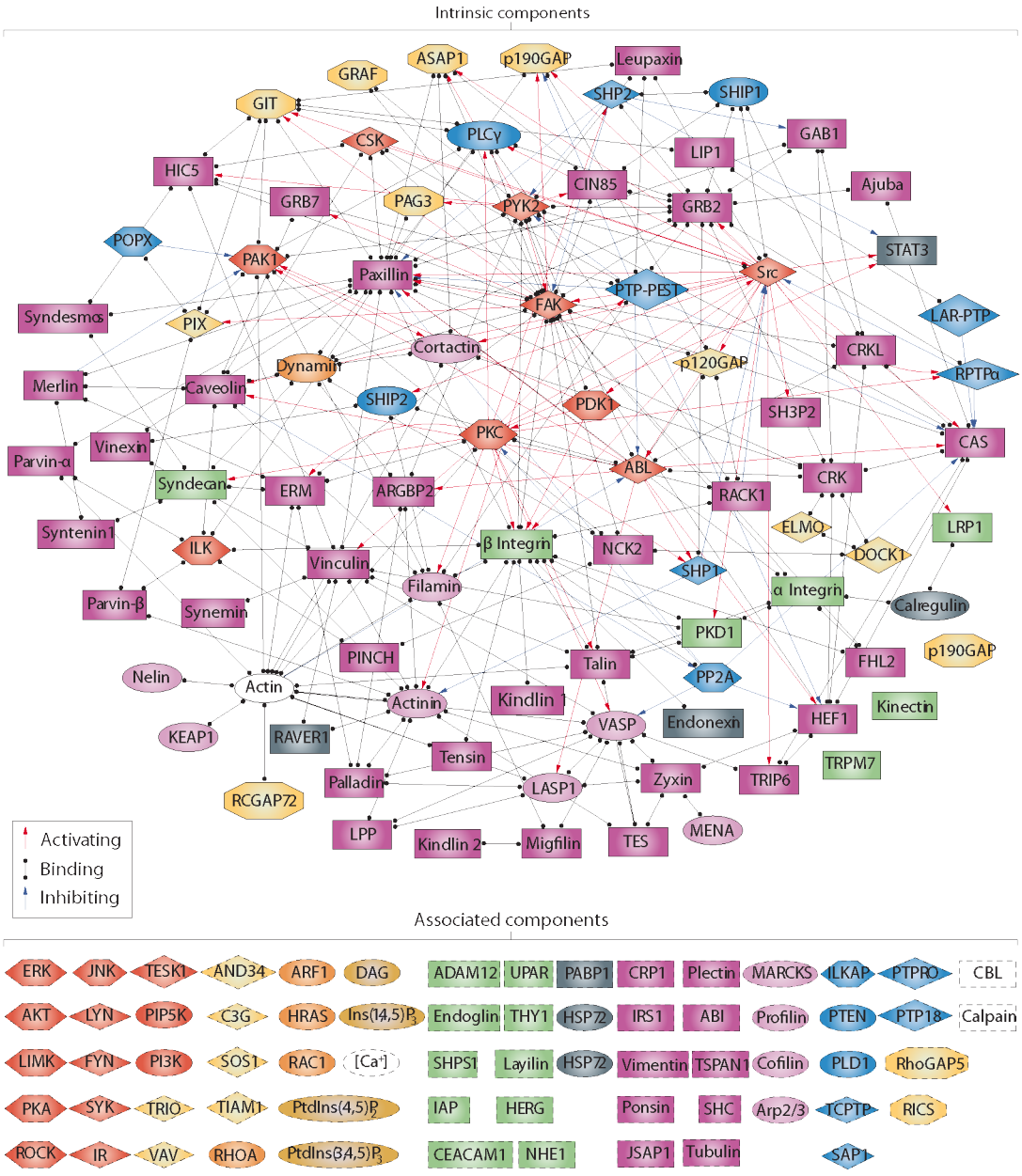

Figure 19 : Le réseau de l'adhésome des intégrines : complexité, fiabilité et sensibilité

Geiger, Nature Reviews, 2009

Les adhésions forment des complexes multi-protéiques qui lient la matrice extracellulaire au cytosquelette d'actine. L'analyse moléculaire de ces structures indique que plus de 160 composants différents participent à cette architecture. La plupart de ces composants sont des constituants intrinsèques des sites d'adhésions (cadres entourés d'une ligne noire). L'observation des interactions qui existent entre les différents constituants de l'adhésome révèle une extraordinaire connectivité. Le réseau complet contient 700 liens, dont la plupart sont des attachements et le reste des interactions de modifications ; dans lesquelles un composant affecte l'activité d'un autre. Les activités biologiques de l'adhésome sont diverses et comprennent des régulateurs de l'actine qui affectent l'organisation du cytosquelette, de nombreuses protéines

adaptatrices qui lient l'actine aux intégrines, directement ou indirectement, et une grande variété de molécules de signalisation comme des kinases, des phosphates, des protéines G et leurs régulateurs. La topologie du réseau montre l'importance du motif à trois nœuds dans lequel un enzyme et son substrat sont recrutés sur le même troisième partenaire. Il semble probable que l'association étroite entre les éléments de structures et de signalisation au sein des adhésions soit un élément clé de ce système de détection.

contact focal aura alors une architecture comprenant des feuillets de protéines et témoignant de son historique d'assemblage (Kanchanawong, Nature, 2010) (figure 20).

Les conditions requises pour permettre la maturation d'un complexe focal en contact focal sont encore aujourd'hui l'objet de débats importants avec des observations qui peuvent sembler déroutantes. Initialement, les forces ont été mises au centre du mécanisme. En effet, l'application d'une force permet la maturation d'un complexe focal en contact focal (Galbraith, JCB, 2002). La taille des adhésions (observée à l'aide de la vinculine) a même pu être corrélée aux forces auxquelles elles sont soumises (Balaban, Nat. Cell Biol., 2001) et la contractilité cellulaire a pu être liée à la surface d'adhésion disponible (Goffin, J. Cell. Biol., 2006). Cette observation a depuis été grandement nuancée. D'autres expériences ont montré que la force augmente transitoirement au moment de la maturation de l'adhésion avant de décroitre rapidement (Beningo, J. Cell Biol., 2001). Cependant cette étude utilise la zyxine comme marqueur des adhésions. Cette protéine est absente des complexes focaux et présente à un étage relativement élevé au sein de l'adhésion contrairement à la vinculine ce qui rend la comparaison avec les autres études difficile. Il se peut que les auteurs n'observent que la phase postérieure à la maturation et que dans ce régime la force ne soit plus proportionnelle à la taille des adhésions. Cette hypothèse a été vérifiée par une étude récente (Stricker, Biophys. J., 2011) dans laquelle les forces générées et la taille des adhésions ont été suivies au cours du temps. On retrouve bien une relation linéaire entre taille des adhésions et forces pendant le processus de maturation. Au delà, aucune corrélation n'est possible entre la taille de l'adhésion et la force générée. (figure 21)

Bien que la maturation des adhésions s'accompagne de cette force importante, d'autres mécanismes sont à l'œuvre au même moment, dont la formation de fibres de stress connectées à ces adhésions. Une telle force est-elle véritablement requise pour la maturation ou est-elle un phénomène secondaire dans ce mécanisme ? Un certain niveau de forces semble nécessaire mais des résultats récents suggèrent que, plus que la force, la formation d'un lien entre l'adhésion et une structure d'actine est le paramètre clé. En effet, l'inhibition de la contractilité cellulaire n'altère pas la maturation des adhésions tant que la vitesse du flux retrograde n'est pas affectée (Stricker, Plos One, 2013) et la maturation des adhésions n'est pas possible sans la formation concomitante d'une fibre dorsale (Oakes, J. Cell Biol., 2012). L'étude du rôle de Rho dans la régulation des adhésions a donné quelques indices qui vont dans le même sens. Rho agit sur le cytosquelette via 2 effecteurs principaux, ROCK et mDia1.

ROCK est une kinase capable de phosphoryler la MLCPhosphatase pour l'inactiver. Cette inactivation favorise la contractilité cellulaire en permettant une augmentation de la MLC sous sa forme phosphorylée. mDia1 est une formine présente au site de l'adhésion. Elle permet la formation des

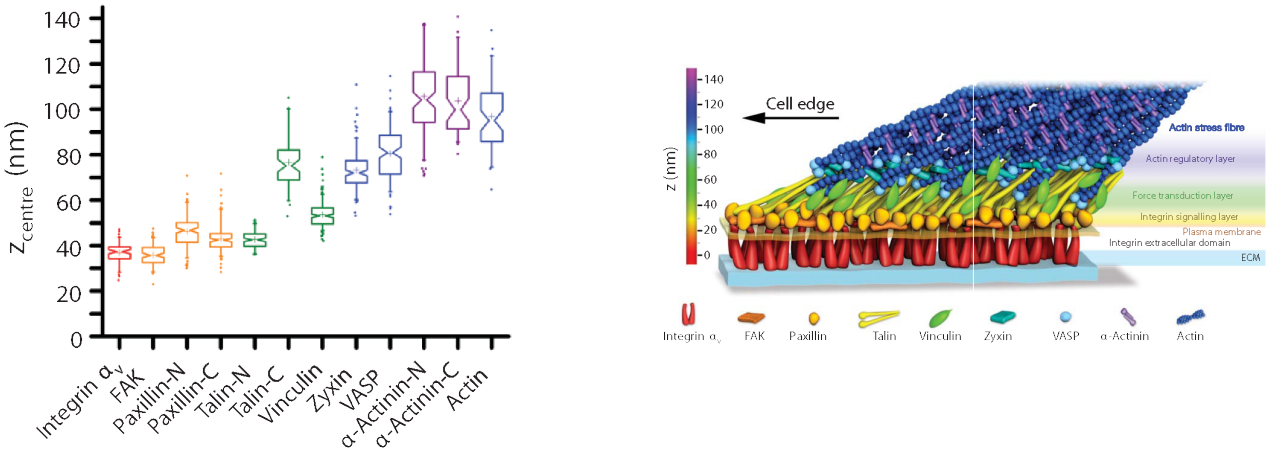

Figure 20 : Organisation nanoscopique des protéines au sein des contacts focaux

Kanchanawong, Nature, 2010

Gauche – position verticale des extrémités des différentes protéines au sein de l'adhésion – Droite, schéma représentatif de l'organisation au sein de l'adhésion. L'orientation de la protéine est prise en compte (N-ter vs C-ter)

fibres dorsales à partir des contacts focaux. Au sein des cellules, seule l'inactivation de mDia1 empêche la maturation des adhésions en réponse à une force extérieure (Riveline, J. Cell. Biol, 2001) ce qui va une fois de plus dans le sens d'un rôle structurel conjugué à un niveau de forces minimum.

Toutes ces études se sont centrées sur le rôle de la force dans la maturation des adhésions mais peu d'entre elles se sont intéressées au rôle de la composition de l'adhésion en intégrines. Ce paramètre pourrait effectivement jouer un rôle important en faisant varier les protéines recrutées au niveau de l'adhésion. Cela pourrait avoir de grandes conséquences sur l'organisation du cytosquelette. La super-résolution a cependant fourni un mécanisme pour la séparation des intégrines au sein de l'adhésion (Rossier, Nat. Cell Biol., 2012). Au sein des adhésions, certaines intégrines sont relativement immobiles (β3) alors que d'autres suivent le flux retrograde (β1). Ces observations permettent d'imaginer la formation de deux zones au sein de l'adhésion. Une région antérieure enrichie en

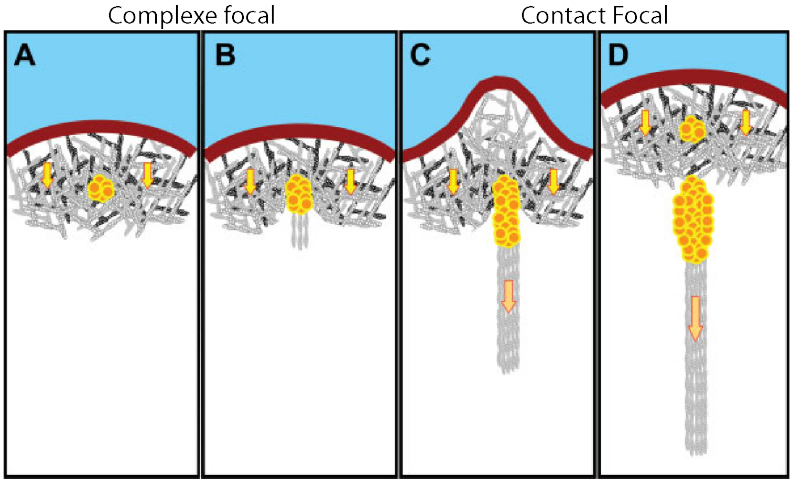

Wolfenson, Cell Motil. Cytoskeleton, 2009

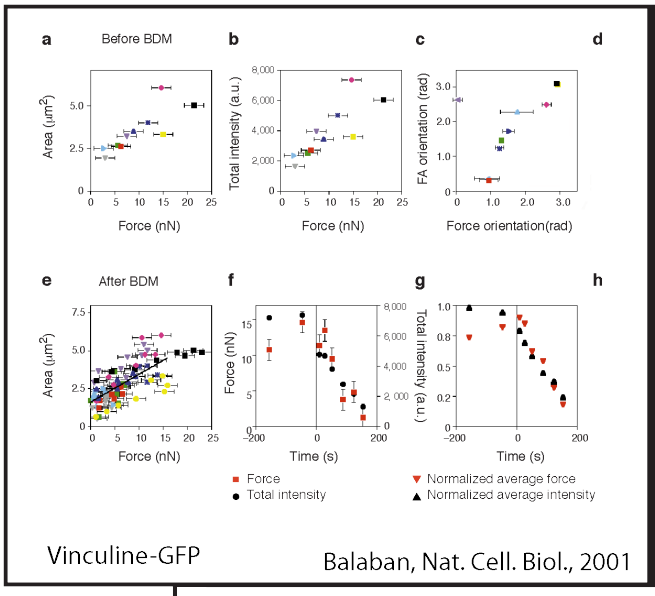

Vinculine-GFP

Balaban, Nat. Cell. Biol., 2001

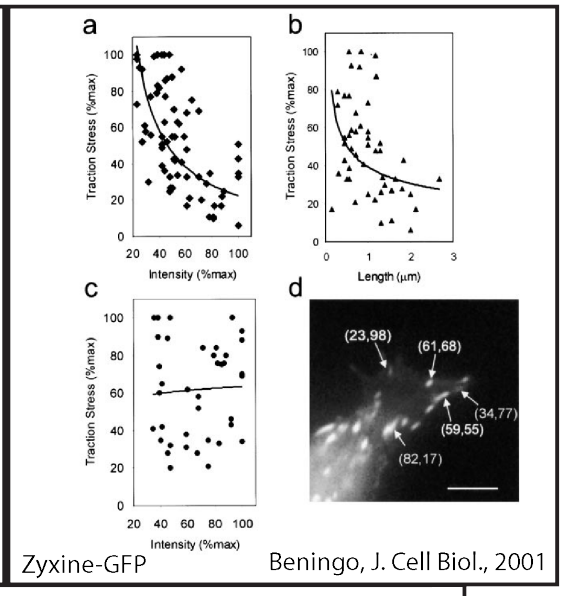

Zyxine-GFP

Beningo, J. Cell Biol., 2001

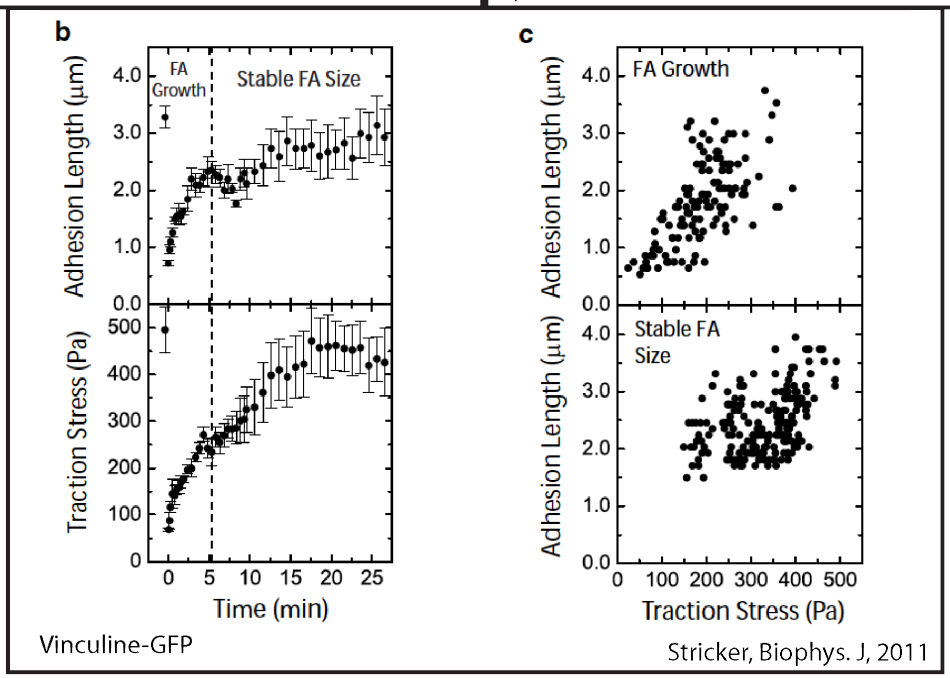

Vinculine-GFP

Stricker, Biophys. J, 2011

Figure 21 : Lien entre taille force et taille des adhésions, une question de maturation

Haut- schéma décrivant les étapes successives de formation et de maturation de l'adhésion depuis un complexe focal vers un contact focal mature. – Milieu gauche – Proportionnalité entre la force générée par les adhésions et leur surface ou intensité de fluorescence pour un composant intrinsèque de l'adhésion : la vinculine. – Milieu droite – Relation inverse entre la longueur des adhésions, leur intensité de fluorescence et la force générée pour les adhésions localisées au front avant de la cellule (a et b) ou à l'arrière de la cellule (c) la protéine ici utilisée pour marquer les adhésions est la zyxine. Cette protéine est sensible à la force et sa présence au sein des adhésions n'est pas systématique. Il se peut que la contradiction entre les résultats vienne de cette différence expérimentale – Bas – Etude de la relation entre force et taille des adhésions au cours du temps. La relation de proportionnalité n'est valable qu'au cours de la croissance de l'adhésion, au delà, la taille n'est plus corrélée à la force au sein de l'adhésion qui peut varier du simple au double (200-400 Pa)

intégrines β3 et une région postérieure enrichie en β1. Cette hétérogénéité pourrait permettre de recruter différentes protéines en fonction des intégrines sous-jacentes. C'est à cet aspect que je vais m'intéresser dans le chapitre III.

Je vais maintenant passer en revue la façon dont les mécanismes d'assemblage de l'actine, de production de forces, d'assemblage des adhésions sont sensibles aux contraintes de l'environnement en essayant de mettre en évidence les lois sous-jacentes à ces observations.

5. AUTO-ORGANISATION DIRIGEE DU CYTOSQUELETTE (ARTICLE)

Review

Special Issue – Synthetic Cell Biology

Directed cytoskeleton self-organization

Timothée Vignaud, Laurent Blanchoin, and Manuel Théry

Laboratoire de Physiologie Cellulaire et Végétale, Institut de Recherche en Technologies et Sciences pour le Vivant, CNRS/UJF/INRA/CEA, 17 Rue des Martyrs, 38054, Grenoble, France

The cytoskeleton architecture supports many cellular functions. Cytoskeleton networks form complex intracellular structures that vary during the cell cycle and between different cell types according to their physiological role. These structures do not emerge spontaneously. They result from the interplay between intrinsic self-organization properties and the conditions imposed by spatial boundaries. Along these boundaries, cytoskeleton filaments are anchored, repulsed, aligned, or reoriented. Such local effects can propagate alterations throughout the network and guide cytoskeleton assembly over relatively large distances. The experimental manipulation of spatial boundaries using microfabrication methods has revealed the underlying physical processes directing cytoskeleton self-organization. Here we review, step-by-step, from molecules to tissues, how the rules that govern assembly have been identified. We describe how complementary approaches, all based on controlling geometric conditions, from *in vitro* reconstruction to *in vivo* observation, shed new light on these fundamental organizing principles.

Setting boundaries

The reproducible shape and spatial organization of organs imply the existence of deterministic rules directing the assembly of complex biological structures. Organ shape depends on cell architecture, which is supported by cytoskeleton networks. The formation of defined and geometrically controlled intracellular structures relies on the self-organization properties of the cytoskeleton. The contribution of self-organization in cell biology is vast and now well documented [1]. Cytoskeleton self-organization is a process in which the consumption (physicists would say dissipation) of energy brings the cytoskeleton away from its thermodynamic equilibrium (i.e., a disordered mixture of poorly dynamic filaments) toward defined and reproducible steady states. This differs from the process of self-assembly, in which components assemble spontaneously – without an external energy source – to form a structure corresponding to the thermodynamic equilibrium. Depending on the rules regulating the interaction of cytoskeleton components, complex structures may self-organize in a robust manner. The purpose of much of the research described in this review has been to identify and formulate these rules to understand how physical principles direct biological morphogenesis.

Corresponding author: Théry, M. (manuel.thery@cea.fr).
Keywords: actin; microtubule; architecture; polarity; microfabrication; micropatterning.

Cytoskeleton self-organization is partially regulated by the action of proteins modulating the biochemical rules of filament growth and interactions. The combination of simple biochemical rules can lead to the formation of complex structures [2]. Robust patterns can emerge from oriented displacements of cytoskeleton filaments by molecular motors in the absence of any external guidance [3–5]. However, these autonomous self-organization processes are extremely sensitive to the presence of spatial boundary conditions (SBCs). An SBC is an external geometrical cue, within or at the periphery of the network, that can locally affect the self-organization of the network. For tissues, an SBC can be a frontier with an external fluid or a contact with bone, muscle, or other organ. For a cell, an SBC can be a neighboring cell or extracellular matrix (ECM). For intracellular cytoskeleton networks, an SBC can be a cell adhesion for the actin network, a centrosome for the microtubule (MT) network, or a frontier such as the plasma membrane or an intracellular organelle.

How an SBC can direct an autonomous self-organization process is the subject of this review. We describe recent advances in the understanding of the role of SBCs in the self-organization of actin networks and MT arrays, how these processes are integrated in the internal organization of a cell, and how this in turn affects tissue architecture. In the formation of cytoskeleton networks, an SBC can bias monomer diffusion and thereby the assembly process ([6] and references therein). Here, we focus on the role of geometrical constraints on the growth, orientation, anchorage, and production of mechanical forces during cytoskeleton assembly.

Actin network self-organization

Actin is an asymmetric protein that can self-assemble to form polarized actin filaments [7]. This spontaneous process can be accelerated and temporally regulated by the energy liberated from the release of a phosphate group from the nucleotide triphosphate bound to actin [8]. Actin filaments can interact to form actin networks. Actin networks can self-organize into several types of structures in cells: bundles comprising aligned long filaments and meshworks comprising branched and intermingled short filaments. Bundles and meshworks form such complex intricate networks in cells [9] that it is difficult to identify the principles of their self-organization.

Biochemists have developed alternative methods to analyze self-organization in controlled conditions *in vitro* by mixing, in defined proportions, the individual components (either purified from tissues or from recombinant

0962-8924/$ – see front matter http://dx.doi.org/10.1016/j.tcb.2012.08.012 Trends in Cell Biology, December 2012, Vol. 22, No. 12

bacteria or yeasts). The kinetic parameters of actin polymerization measured *in vitro* and how these parameters vary in response to the presence of actin-associated proteins has provided key information about the regulation of actin assembly dynamics [10]. However, the rules guiding the spatial organization of the network can be identified only by using controlled geometric boundary conditions.

Symmetry break

Mechanical constraints in an actin network can induce a symmetry break (i.e., the sudden occurrence of a singular axis in isotropic conditions in which all directions were previously equivalent). This propensity for symmetry breaking in actin networks was elegantly revealed using a spherical glass bead coated with actin nucleation factors as a simple SBC [11,12]. Actin nucleation is induced from the bead, and the presence of capping proteins, which block filament elongation from their fast growing end, ensures that the actin filaments are short and form a dense branched meshwork. As the actin filaments grow at the bead surface, material accumulates and the stress increases in the network up to a critical value inducing its rupture [13]. The rupture creates an asymmetry in the pressure applied on the bead such that the bead is displaced (Figure 1a). Repetition of this sequence of events induces saltatory propulsion of the bead [14,15].

In this experimental system, the SBC can easily be manipulated by changing its dimensional parameters. For example, the larger the bead, the shallower the curvature of the bead surface, leading to an increase in the critical value of network thickness before rupture [16,17] and the periodicity of the saltatory propulsion (Figure 1b). An asymmetric SBC can be created using ellipsoidal beads. The difference in surface curvature of the bead biases the location of network rupture, which occurs preferentially in line with or orthogonal to the long axis of the bead [18] (Figure 1c). Higher aspect ratios, obtained by actin nucleation on small glass rods, further increase the spatial bias and branched network growth is restricted to being orthogonal to the long axis of the rod [15]. As the rod length increases, several independent networks can form, revealing the existence of a critical length for subnetwork interconnections (Figure 1d). Interestingly, symmetry break and asymmetric force production are not restricted to branched meshworks of actin, but can also be induced by the bundling and alignment of individual filaments polymerizing against the bead surface [19].

Filament alignment

Several self-organization processes can induce actin filament alignment in response to an SBC. Filaments can become aligned by steric interactions. When two long filaments come close to each other, they prevent the insertion of a short filament between them. Long filaments will be further forced to align by the steric interactions of short filaments around them. Steric interactions between long filament bundles will then promote their orientation in line with the long axis of the volume in which they are confined [20] (Figure 1e). Steric interaction of filaments freely moving on a layer of molecular motors can also result in their alignment along each other [4] and along the SBC [21]. Filaments can become aligned by membrane tension. Two filaments pushing orthogonally to a deformable membrane will coalesce and align to reduce the elastic energy of the membrane [22]. Preassembled filaments can become aligned by defining the anchorage positions with regular arrays of beads or micropillars and adding filamin to crosslink filaments [23,24].

Filaments can become aligned in parallel or antiparallel configurations by controlling the orientation of their growth. Surface micropatterning can be used to manipulate precisely the geometrical boundary conditions of filament growth and orientation [25]. Selective adsorption of actin nucleation-promoting factors on micropatterned regions induces localized formation of a branched meshwork. Only non-branched filaments grow out of the micropattern, with their barbed ends reproducibly oriented outward. Steric interactions force growing filaments to align parallel to each other, orthogonal to the nucleation region (Figure 1g). Distant from the nucleation region, two filaments growing toward each other in nearly opposite directions tend to form antiparallel bundles; whereas two filaments growing toward each other but at an oblique angle tend to form parallel bundles (Figure 1g). However, these tendencies can be biased because adjacent filaments sterically affect each other. The reorientation of filaments during bundle formation guides adjacent filaments also to align with the bundle (Figure 1g). Bundle formation is thus a combination of local probabilistic events, governed by filament flexibility, and the propagation of the alignment configuration to adjacent filaments by steric interactions [25].

In egg extracts, biochemical conditions are less well defined but closer to intracellular conditions. Encapsulation of egg extracts in membrane vesicles revealed that filaments nucleated at the periphery move inward and align to form a central ring. Interestingly, the ring can form only when nucleation is restricted to the vesicle periphery and not distributed evenly throughout the entire volume. A scaling law appears to regulate the ring size in proportion to the vesicle diameter [26] (Figure 1f).

Network contraction

Myosins are oriented motors moving toward a defined extremity of actin filaments. Thus, they have specific actions depending on actin network architecture. They walk along parallel filaments, whereas they slide along antiparallel filaments in opposite directions relative to each other and thus contract the network [27] (Figure 1i). Myosins can also induce the contraction of branched meshworks, because these networks also contain antiparallel filaments. However, the rate of contraction is reduced due to the resistance associated with branches and network anchoring to nucleation regions [27]. It has been shown, based on the use of actomyosin bundles connecting beads, that the contraction rate is proportional to bundle length [28]. In more complex structures comprising various types of network, the contraction rate is determined by the local proportion of parallel and antiparallel bundles and branched meshwork [27]. Variations of these proportions in a given architecture will induce anisotropic contraction, although myosins are present throughout the network (Figure 1i). Therefore, an SBC

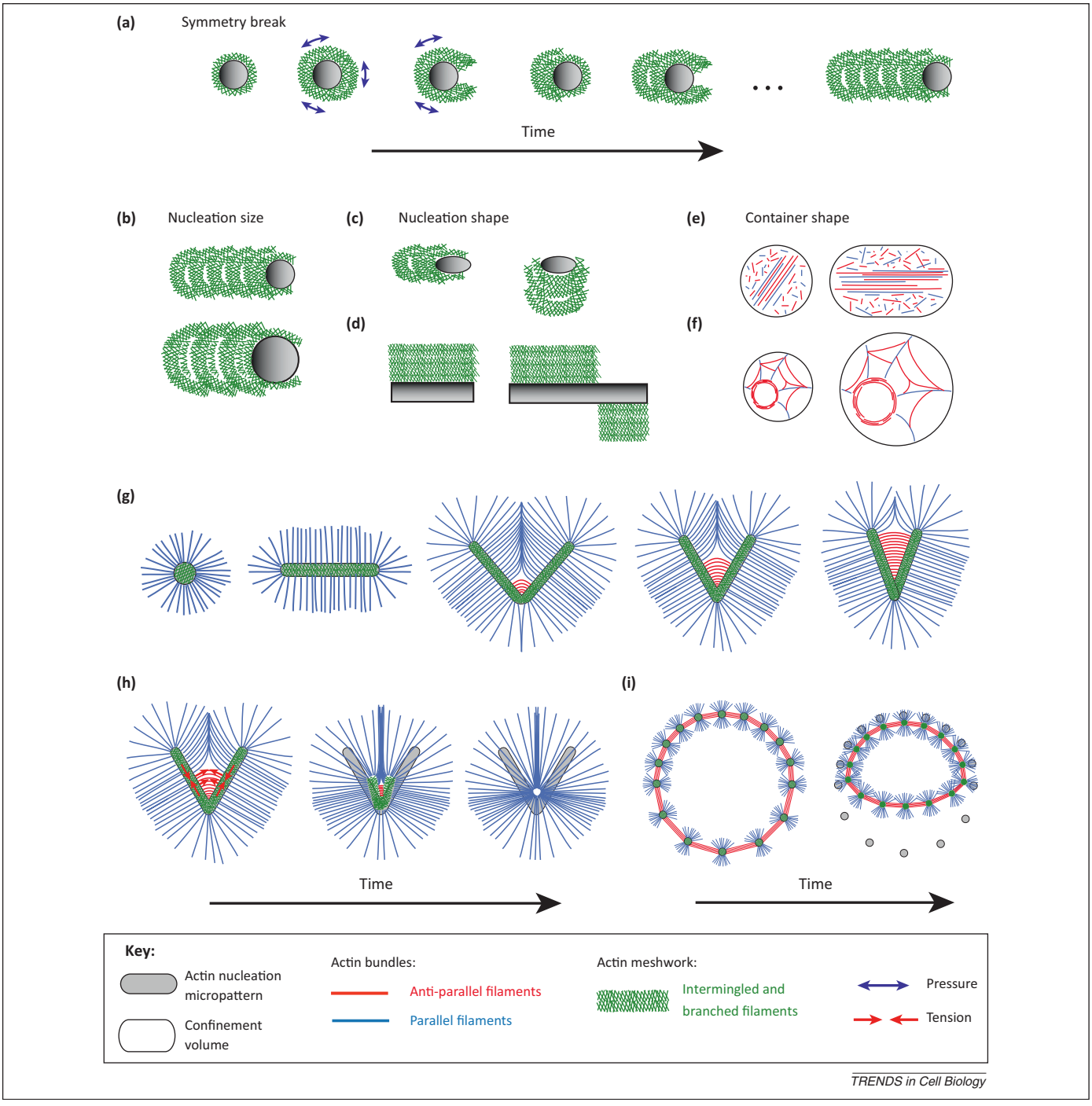

Figure 1. Actin network self-organization. **(a)** Actin meshwork polymerization around beads leads to symmetry breaking, meshwork rupture, and bead propulsion. **(b)** Bead size regulates the period and size of meshwork rupture. **(c)** Bead asymmetry orients meshwork growth. **(d)** Bar length affects network coherence. **(e)** Long filaments self-align to form bundles, which become oriented along the long axis of the container. **(f)** Inward flow of filaments nucleated at the vesicle periphery leads to the formation of a ring, the size of which is in proportion with the vesicle diameter. **(g)** Filament nucleation and growth of micropatterned branched meshworks. The filament interaction angle modulates the probability of association in either parallel (blue filaments) or antiparallel (red filaments) configurations. **(h)** Myosins induce the specific contraction and disassembly of antiparallel bundles and branched meshworks while leaving parallel bundles unaffected. **(i)** Asymmetric distribution of the ratio between branched and antiparallel networks leads to asymmetric contraction.

can define the type of network architecture, which in turn can define its pattern of contraction.

MT network self-organization

Similar to the formation of actin filaments from the self-assembly of actin monomers, tubulin forms asymmetric dimers that can self-assemble into MTs. However, the release of tubulin-bound nucleotide triphosphate is required to accelerate the process [29]. Compared with actin filaments, MTs are much more rigid and almost straight in the dimensions of a single cell. MTs can sustain higher compression forces than actin filaments. They can form bundles, but they cannot form branched networks. MTs are not as numerous as actin filaments in the cell cytoskeleton. MT growth is characterized by long growth phases alternated with short periods of rapid shortening.

The 'plus-end' of the MT is much more dynamic than the 'minus-end', which can be attached to a MT-organizing center (MTOC). In most animal cells, the MT network forms as an aster in which MTs radiate from the MTOC. As cells divide, the MTOC is duplicated and the network forms a bipolar spindle.

Centering

The most straightforward way to investigate MT aster positioning in response to an SBC has been to purify MTOCs from cells and place them in microfabricated chambers of defined dimensions [30]. Hence, the boundaries of the chamber can serve as an external SBC. As MT plus-ends grow and push against the edges of a square chamber, MTs are subjected to compression forces that push the aster toward the geometrical center of the chamber [30] (Figure 2a). When fluctuations cause the MTOC to become off-center in a given direction, MT curvature and pressure increases in that direction and pushes the MTOC back toward the center. Thus, an isotropic array of MTs pushing on peripheral barriers is sufficient to maintain the aster at the center of the volume in which it is confined. However, MTs sliding along the periphery could affect the stability of this centering mechanism by reorienting MTs. In such conditions, both pushing and pulling forces, by minus-end-directed motors attached to the periphery, are necessary to ensure efficient stabilization of the MT aster at the geometrical center of the SBC [31] (Figure 2a).

By contrast, asters with opposite polarities (i.e., with MT plus-ends at the center of the aster) cannot adopt the same steady state. As long as MTs contacting the periphery are short enough to release their elastic energy by straightening, they gently push the aster toward the center. As they get longer, the compression forces in bent MTs increase. The clustering of dynamic plus-ends by kinesins at the aster center is not strong enough to resist these forces and so the aster fragments. The MT network then switches to highly robust vortex-like structures [32] (Figure 2b).

Symmetry break

When an aster is trapped in a water droplet encapsulated in oil, MTs cannot attach to the periphery. The spherical water–oil interface has minimal tangential resistance and is an effective SBC along which MT can slide easily. In these conditions, symmetry breaks in the aster configuration can occur [33] (Figure 2c). In a relatively large spherical volume, few MTs reach the boundaries and the aster is stabilized close to the geometrical center. As the size of the spherical volume is reduced, MTs tend to be longer than the container radius. To minimize their curvature and relax their elastic energy, MTs slip along the edges and align with the SBC [33,34]. This produces an asymmetric redistribution of MTs that pushes the MTOC to the periphery of the droplet [33] (Figure 2c). Interestingly, when the rigidity of the SBC is reduced, clustered MTs push and deform it to the extent that a tubular protrusion can be formed [33,35,36].

Alignment and spindle formation

The formation of bipolar mitotic spindles also depends on geometrical boundary conditions defined by DNA and cell shape. Two mechanisms contribute to mitotic spindle assembly around DNA: the focusing of the minus-ends of MTs that are associated with large DNA clusters to form spindle poles, and the antiparallel alignment of the plus-ends of MTs that are anchored at the two MTOCs such that the aster MTs overlap [37].

Multimeric minus-end-directed motors, such as dyneins, induce the formation of spindle poles. DNA provides guidance cues for initial MT alignment and thus biases bipolar spindle formation [38,39]. MTs tend to align parallel to the surface of a DNA-coated bead. The intrinsic molecular machinery supporting spindle pole focusing and mitotic spindle spatial organization is robust and initially appeared insensitive to configuration of the DNA complex [40]. However, extensive manipulations of the amount of DNA and its spatial distribution using microcontact printing revealed the DNA directing role in spindle assembly [41]. The increase in size of DNA aggregates induces spindle lengthening (Figure 2d). Above a critical size, large DNA aggregates can induce the formation of multiple poles [41] (Figure 2d). Moderately asymmetric distribution of DNA is sufficient to orient spindle formation [40,41] (Figure 2e). Long bars coated with DNA result in the formation of multiple repeats of spindles along the length of the bar and thus revealed the existence of an intrinsic spindle width (Figure 2f). This intrinsic spindle width seems to be defined by the balance between motors forcing the focusing MT ends and the elastic reaction force due to MT bending. In a certain range of parameters defined by the ratio between the DNA aggregate width and MT length, the symmetry is broken and all MTs collapse on one side of the DNA, resulting in an asymmetric configuration of spindles with respect to the long axis of the bar [41] (Figure 2f). Below this critical range, antiparallel MTs from opposite poles (with the bar in between) interact to stabilize the formation of symmetric bipolar spindles; above this range, the two spindle configurations on opposing sides of the DNA bar are independent and both form independent monopolar spindles.

Cellular self-organization

In cells, the organizing principles described above appear applicable but more difficult to reveal and investigate. Both actin and MT networks are regulated by hundreds of different types of binding protein. In addition, the assembly of actin filaments and MTs are affected by each other through physical and biochemical interactions. Cytoskeleton network assembly is regulated at the scale of a cell and is no longer solely dependent on local biochemical and geometrical conditions. The implication of biochemical signals forces the system to break its symmetry and define an axis of polarity. Although actin or MT network assembly is more complex in the cellular context than *in vitro*, some self-organizing principles have been identified.

In simple conditions as near to cellular conditions as can be achieved in experiments *in vitro*, similar self-organized structures can be observed. Cytoskeleton networks in cells from lymphatic lines or in other cells or cell fragments on non-adhesive substrates are subjected to no other geometrical constraints than the flexible plasma membrane. In the absence of MT networks, the actin network contracts and breaks symmetry after a local rupture occurs in the

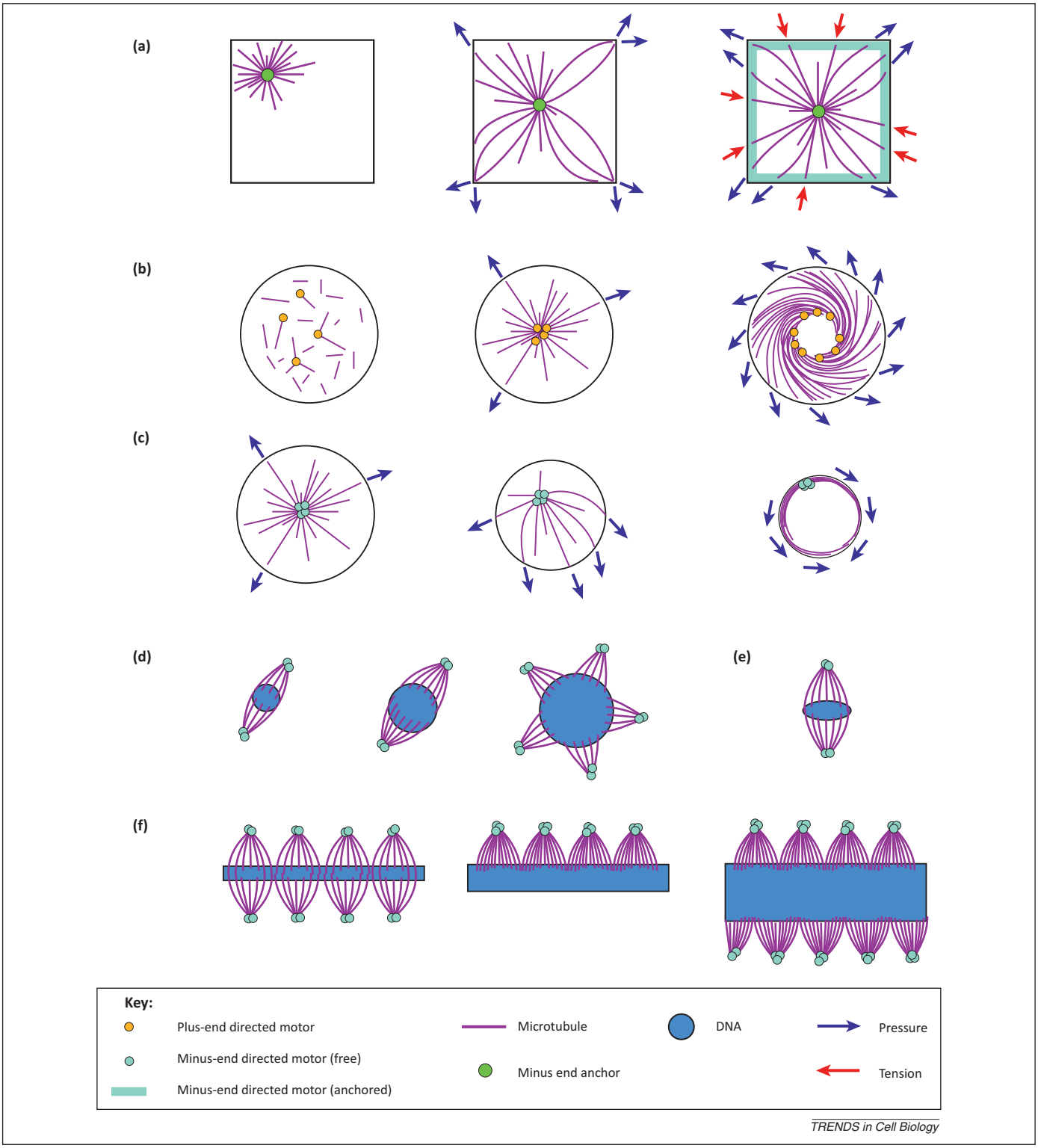

Figure 2. Microtubule (MT) network self-organization. **(a)** Aster off-centering with short MTs in a large container (left). Aster centering by MT sliding and pushing on the container corners (middle). Highly efficient aster centering by pushing and pulling forces (right). **(b)** MT length-dependent aster formation and centering. Short MT 'plus-end' coalescence by motors (left). Aster centering by a few MT 'minus-ends' reaching and pushing on container edges (middle). Aster fragmentation and vortex formation by pushing forces exerted by long MTs on container edges (right). **(c)** MT length-dependent aster off-centering. Aster centering by few MT plus-ends reaching and pushing on container edges (left). Symmetry break and aster off-centering by a few, sliding MTs pushing on container edges (middle). Cortical alignment of MTs and peripheral localization of MT-organizing center (MTOC) due to numerous MTs sliding and pushing on container edges (right). **(d)** DNA cluster size regulates spindle size and pole formation. **(e)** DNA cluster asymmetry regulates spindle orientation. **(f)** DNA cluster width regulates spindle symmetry.

network. With the symmetry breaking, an over-contracted region propagates in the network [42–44]. The process of rupture is similar to what happens in branched meshworks around beads [12], except the occurrence of the rupture results from the contractile force generated by myosins rather than by the pushing force associated with actin polymerization. In the absence of actin networks, MTs pushing on a deformable membrane coalesce, align, and

break symmetry by forming a long tubular protrusion [42,43], reminiscent of their behavior in vesicles [33,35,36]. However, in cellular conditions, actin and MT networks interact and the SBCs are more complex that a freely fluctuating plasma membrane. The ECM and cell neighbors can represent adhesive SBCs. Hence, the precise control and manipulation of cell adhesions, which are cellular structures that interact with the cell's structural microenvironment, reveal how these SBCs could direct intrinsic cytoskeleton self-organizing properties.

Directed shape

Cells spreading on a defined regular array of adhesion spots revealed that the size and spacing between spots was a critical regulator of cell shape. Cells need a minimum spot size to assemble focal adhesions and cannot extend over a maximal distance between these spots [45–48]. Cell shape appears to result from the competition between the force from adhesion-induced spreading and a reaction force from the cell's elasticity and other internal contraction forces [49]. However, some cells, such as fibroblasts, have an intrinsic mechanism to regulate the length of their long axis regardless of their width, which seems to implicate tight crosstalk between actin and the MT network [50,51].

Although cell shape elongation, cytoskeletal alignment, and internal cell polarity orientation are usually correlated, cell shape does not determine actin and MT organization. Modifying the actin network by fluid flow while maintaining constant shape reorients the MT network [52]. Similarly, modifying the MT network independently of cell shape reorients the actin network [53]. Rather, there is an intricate coupling between actin and MT networks that affects their respective spatial organizations and the axis of cell polarity.

Directed actin network architecture

The cellular actin network is organized by a balance between the assembly of a contractile network of aligned filaments and the polymerization of a non-contractile branched meshwork. This balance appears to be finely regulated by the degree of cell adhesion [54].

The branched meshwork assembles at the cell periphery. It is preferentially developed along convex rather than concave cell edges [55]; thus, it promotes the formation of larger membrane deformations at a cell apex [56] (Figure 3a), the size of which increases as the angle of the apex is reduced [57].

Contractile bundles of antiparallel filaments are present throughout the cytoplasm. Peripheral bundles and more interior bundles have distinct dynamics and contraction properties. Components of peripheral bundles move toward the bundle center, whereas components of interior bundles remain static with respect to the bundle organization [58] (Figure 3b). This probably reveals key differences in the polarity of filaments and thus specific contraction properties of these two types of bundle. As cell spreading or the cell aspect ratio increases, cell contraction increases [59–61]. The cell aspect ratio increase induces the alignment of contractile bundles, which form structures such as stress fibers or myofibrils (Figure 3c). Aligned stress fibers and the associated anisotropic contraction along the cell's basal surface are coupled to the assembly of similar structures and force distribution along the cell's apical surface [62,63]. Aligned myofibrils tend to organize their banding patterns in register [64].

Asymmetric SBCs, defined in cell culture by micropatterned adhesion sites, can lead to the development of asymmetric actin networks. Bundles accumulate preferentially along concave rather than convex cell edges [65]. As the cell spreads over an adhesive region, conspicuous contractile bundles are formed that connect this region to other adhesive regions separated by non-adhesive regions [47,66,61], revealing the development of larger traction forces [67] (Figure 3d). A relatively larger distance between adhesion sites leads to a reduced edge curvature and thicker bundles and so probably reflects a larger force between these sites [66,68] (Figure 3e).

Directed MT network

The MT network adapts its dynamics to the various configurations of the actin network. MTs bend and grow along actin contractile bundles, but stop growing when they reach a branched actin meshwork [69]. Interestingly, although an asymmetric actin network will lead to asymmetric organization of MTs, the MTOC remains at its central location (Figure 3f). Centrosome positioning appears to depend on generation of forces by dyneins on MTs [70,71], but also on the forces generated by the less characterized connections with the actomyosin network [71,72]. Centrosome central positioning is even more remarkable given that a large part of the cytoplasm is occupied by the nucleus, on which MTs can also push and pull. The robust mechanism by which the centrosome becomes positioned at the geometrical center of the contour that describes the cell shape, where the actin network is asymmetric and the nucleus occupies a large part of the cytoplasmic volume, remains to be elucidated.

The positioning of the nucleus in a cell in culture is off-center and distal from the cell's adhesion to the ECM and the actin branched meshwork, but is proximal to the contractile bundles [69]. Therefore, the internal polarity, as revealed by the nucleus–centrosome vector, is oriented with respect to ECM and actin network asymmetries [55,69]. Biochemical disruption of the actomyosin network, the MT network or the nucleus–cytoskeleton connections can perturb polarity orientation with respect to cell–ECM SBCs [71,73,75].

The centrosome and nucleus are often described as being in the cell spreading plane in culture, but they can be positioned on an axis orthogonal to this. Moreover, their relative positions can be switched on this axis, depending on the degree of confinement imposed by the available spreading area. Indeed, the centrosome is positioned toward the apical curved surface, above the nucleus, in confined cells and below the nucleus in cells that have spread extensively [76] (Figure 3g).

Directed migration

The asymmetric cytoskeleton organization in response to an asymmetric SBC can affect the direction of a motile cell. The relationship between external asymmetry and oriented motility is not straightforward, because it seems to

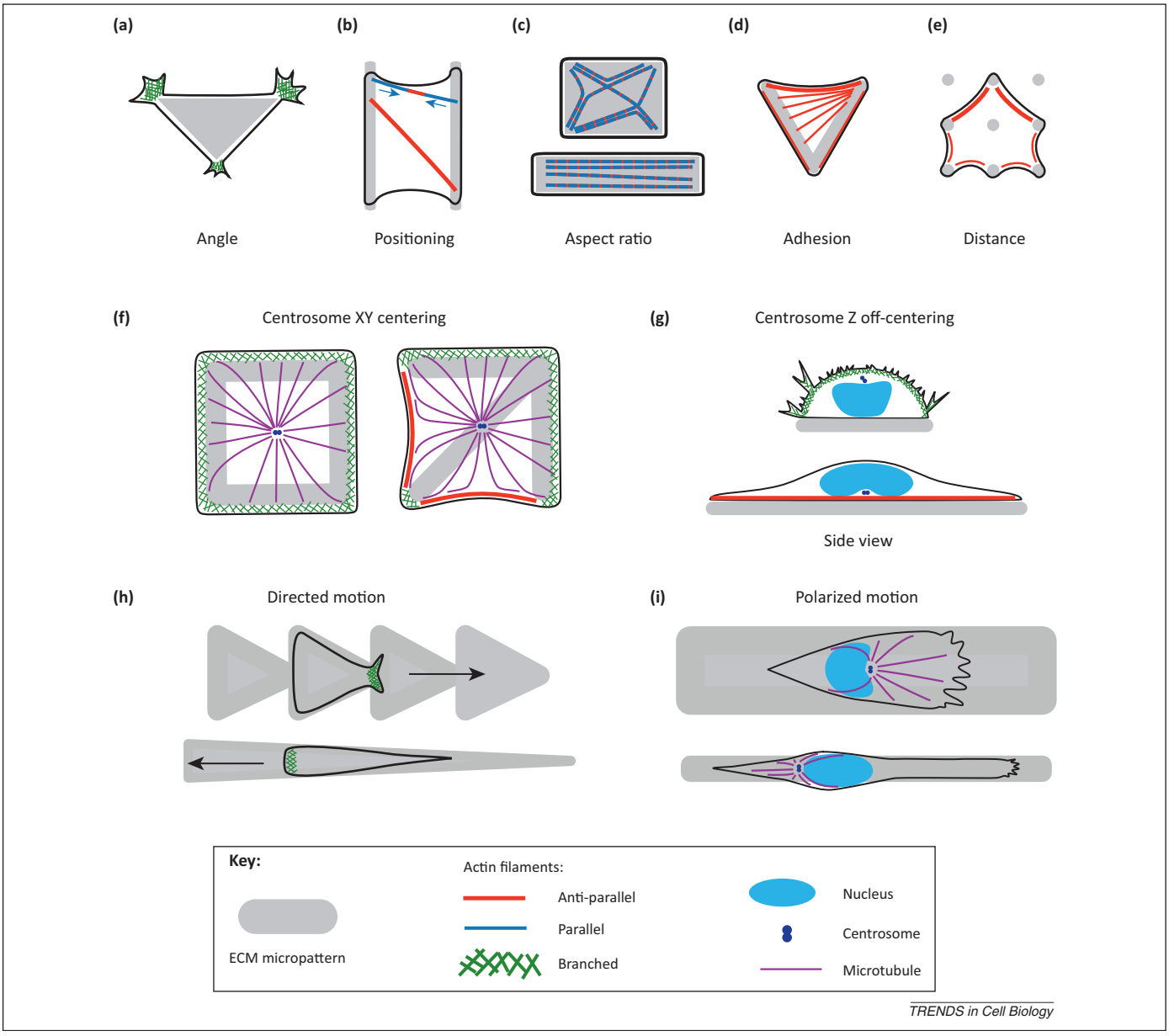

Figure 3. Cellular self-organization. **(a)** Branched meshwork polymerization in acute-angled regions of the cell periphery. **(b)** Inward treadmilling (arrows) in peripheral actin bundles and absence of treadmilling of internal bundles may reveal differences in filament polarities. **(c)** Alignment of myofibrils in response to cell shape elongation. **(d)** Formation of conspicuous actin bundles along non-adhesive edges and thin actin bundles along adhesive edges. **(e)** Longer peripheral bundles are also thicker. **(f)** Microtubules (MTs) adapt their growth to local actin structures. The centrosome maintains its central position in symmetric (left) and asymmetric environments (right). **(g)** Centrosome positioned above the nucleus, close to branched actin meshwork, in spatially confined cells (top). Centrosome positioned below the nucleus, close to actin bundles, in spread cells (bottom). **(h)** Cells move toward confined spaces above a certain threshold (top) and toward open spaces below that threshold (bottom). **(i)** Spread cells move with the centrosome toward the front (top), whereas confined cells move with the centrosome toward the back (bottom).

depend on cell type and the degree of asymmetry. A linear track of repeated micropatterns in the shape of isosceles triangles can lead cells to move toward the acute angle apices of these triangles [77,78]. By contrast, an elongated isosceles triangle with a very acute angle (several degrees only) can lead cells away from the acute angle apex [79] (Figure 3h).

Without an external bias such as those created by asymmetric SBC, the direction of motility is defined by intrinsic cell polarization mechanisms and can be observed in motile cells on adhesive micropatterns in the shape of bars. However, bar width affects actin network organization. Variations in actin network assembly in response to bar width are cell type-specific because keratocytes need large transversal spreading to move relatively fast [80], whereas fibroblast speed is greater when the bar width is narrower [81]. Interestingly, the orientation of internal cell polarity, revealed by the position of the centrosome with respect to the nucleus, also depends on the width of the adhesive micropattern. A cell migrates on a wide bar with the centrosome nearer the leading edge, whereas on a narrow bar, the centrosome is nearer the trailing edge [82] (Figure 3i). How this centrosome positioning is related to the different types of actin organization remains to be investigated.

The speed of migrating cells and their persistence in moving in a given direction are both affected in cells whose internal polarity orientation process is defective [75]. The systematic connection between the actin network machinery powering cell migration and the degree of stability of

spatial organization of the internal cell polarity was further supported by the observation in around a hundred different cell types of a correlation between cell speed and the persistence of the cell in maintaining their direction of migration [83].

Directed cell division

The adaptation of MT network architecture in relation to the actin network architecture and to cell shape is manifest during cell division. The tensions in astral MTs, radiating from the spindle pole toward the cell cortex, exert a torque on the spindle and direct its orientation. The tension in these astral MTs is regulated by the presence of cortical cues associated with the actin network, which orient the cell division axis with respect to cell adhesion cues and the architecture of the actin network [84–87]. Tension can also be exerted throughout the cytoplasm and therefore be proportional to astral MT length; differences in astral MT length can differ with respect to cell shape elongation and these variations can direct the orientation of the division axis accordingly [88,89].

Tissue self-organization

At the level of tissue organization, the complexity of the system increases with greater numbers of components. Nevertheless, precise manipulation of the geometries of SBCs has proven useful in identifying consistent self-organization rules.

Directed cell positioning

Self-organization of cells in a given space depends on the balance of mechanical forces between the cells and the surrounding matrix. Two cells in contact constitute a minimal multicellular structure where cells can form cell–matrix adhesions (CMAs) and cell–cell adhesions (CCAs). When confined on a homogeneous micropattern (i.e., when the cell basal surface is in contact with a continuous layer of ECM), endothelial cells forming CCAs move regularly around each other in the plane of the culture dish, whereas fibroblasts, which cannot form CCAs, do not [90]. Therefore, the formation of CCAs appears to modulate the capacity of the two cells to reach a mechanical balance. The two adhesive systems – CCA and CMA – within a cell can mutually affect their respective localizations [91]. Two cells of a given epithelial cell type confined on micropatterned ECM within a defined area can move or adopt a stationary position in response to subtle changes in ECM geometry [92] (Figure 4a). Indeed, the production of tensional forces on the CCA depends on the spatial organization of the ECM. Intercellular force is higher when the CCA is close to the ECM. This directs the CCA away from the ECM and stabilizes the cell position in this configuration, which corresponds to global minimization of the overall contractile energy [92] (Figure 4a). Conversely, the formation of a CCA prevents the formation of proximal CMAs [74,93]. The mutual exclusions of the two adhesion systems lead to their spatial segregation [91] and directs cell positioning.

Directed collective motion

The collective motion of a large multicellular group depends on the production of intercellular forces, the spatial distribution of which directs the migration of cells with respect to their neighbors. The sudden removal of SBCs, allowing a previously confined group to migrate, revealed that intercellular forces propagate from the migrating front to the group's rear [94] (Figure 4b). Intercellular forces did not appear to pull cells forward but rather to orient the traction force field they develop on the ECM to migrate.

An intriguing recent work revealed that global coherence can emerge in the spatial organization and collective motion of large cell groups [95]. Cells plated as multicellular groups on micropatterned discs do not display any coherent global motion nor specific cell orientation. However, on a torus-shaped micropattern, there is a clear asymmetry in cell orientations such that the long cell axes tilt at similar angles with respect to the torus center (Figure 4c). This appears to be reflected in the direction cells adopt when motile on the torus. The angular direction of cell motility at the peripheral edge of the torus (with positive curvature) tends to be opposite to that at the interior edge of the torus (with negative curvature) (Figure 4c). Therefore, it appears that the symmetry break imposed by the torus arises from this directional property of cell motility at the edges of the torus that is propagated throughout the entire group of cells. Surprisingly, the angular bias of endothelial cell orientation is clockwise, whereas with myoblasts it is counterclockwise. Thus, variations in intracellular parameters presumably can be manifested as specific asymmetries for different cell types. However, no explanation has yet been proposed for this geometrically simple organization resulting from a probably quite complex mechanism. One area where a mechanism may be identified is in the regulation of cell polarity and its relationship to oriented cell motility.

Directed cell polarity

The relationship between the locations of CCAs and CMAs affects nucleus–centrosome axis orientation. The centrosome, with respect to the nucleus, tends to adopt a more distal position from CCAs and a more proximal position to CMAs [73,74,96] (Figure 4d). Thus, the asymmetric locations of both CCAs and CMAs are sufficient to bias the nucleus–centrosome axis [73,74]. CCAs seem to regulate centrosome positioning [73,96], whereas CMAs seem to regulate nucleus off-centering [69,73]. Both actin filaments [96] and MTs [73] have been shown to be involved in the regulation of centrosome positioning away from CCAs. Therefore, the mechanisms by which the cytoskeleton affects centrosome and nucleus positioning remain unclear. In addition, the orientation of cell polarity not only depends on the position of CCAs, but also on the orientation of intercellular force fields [97].

Given that the self-organization of actin filament and MT networks is highly sensitive to SBCs and to the distribution of mechanical constraints, and that both types of network have intrinsic capacities to break symmetry, perhaps biased collective directional motility [95] results from symmetry break in the intracellular actin networks and the consequent asymmetric orientation of internal cell organization [98] (Figure 4e). How these polarized signals propagate to adjacent cells and result in collective oriented motility remains to be elucidated. Particularly, the role of

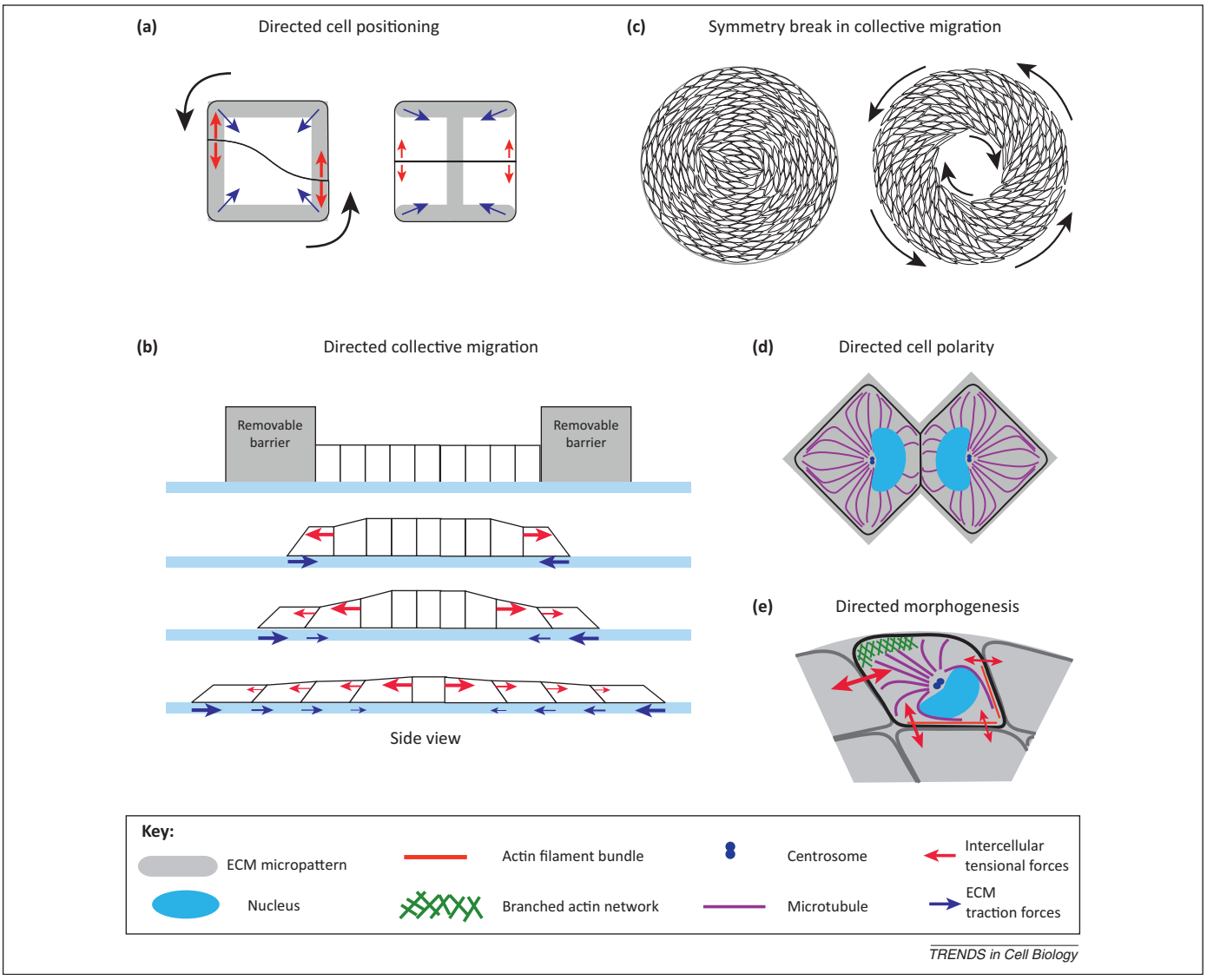

Figure 4. Tissue self-organization. **(a)** Two cells move regularly around each other (black arrows) when extracellular matrix (ECM) is present all along the periphery (left), whereas they stop moving when the extremities of their ECM contact plane reach a region without ECM (right). The presence and absence of ECM regulate intra- and intercellular forces in opposite ways. **(b)** Intercellular forces propagate from the front to the center of a migrating cell group. **(c)** A large multicellular group on a disk of ECM displays no geometrical bias (left), whereas on a torus, symmetry is broken and cells bias their orientation and move (black arrows) in a coherent fashion (right). **(d)** Two adherent cells orient their internal polarity away from their contact plane. **(e)** Speculation on coherent tissue polarity establishment. Symmetry break first occurs in the actin network, followed by microtubule (MT) rerouting and internal polarity reorientation. The asymmetric distribution of internal forces associated with these changes is counterbalanced by asymmetric intercellular forces, which further affect polarity in adjacent cells and propagate asymmetric orientation cues.

internal mechanics and intercellular force transmission could be the key elements supporting intracellular integration of spatial signals and the establishment of coherent cell polarities in dynamic multicellular structures.

Concluding remarks

SBCs play a major role in directing intrinsic cytoskeleton self-organization properties, from the architecture of macromolecular structures to the distribution of cells in tissues. Investigations at each scale – on isolated cytoskeleton components, more complex cell extracts, or entire cells – provide complementary information. All contribute to the establishment of a working framework, which should ultimately allow us to formulate the exact rules of cytoskeleton self-organization during morphogenesis. However, our understanding of the self-organization of minimal molecular systems *in vitro* is not sufficient to account for genuine cellular architectures and dynamics. Additional efforts need to be initiated to connect *in vitro* and *in vivo* self-organized cytoskeleton networks and fully to benefit from the former in understanding the latter.

There is currently a gap between the few self-organized structures that have been characterized *in vitro* and the myriad different structures observed in cells. Efforts should be made to reconstitute all of these structures *in vitro*. This will become possible by: (i) using more complex protein mixtures *in vitro* to recapitulate their effects on cytoskeleton networks observed in cells; (ii) identifying ways to engineer controlled SBCs mimicking actual biological membrane; and (iii) modulating biochemical signaling.

The regulation of network disassembly is as important as the regulation of assembly in network dynamics. There is a critical need to further understand how this network

disassembly is modulated by SBCs. Progress in this direction should allow the reconstitution of dynamic steady states in which manipulation of SBCs and network assembly–disassembly could lead to conditions in which the network persistently self-renews, with its overall structure remaining unaffected. Technological developments are also required to modulate SBCs in real time [47], especially for analyzing dynamic systems and cytoskeleton adaptation to external changes.

However, the considerable efforts made to understand the regulation of the self-organization properties of actin filament or MT networks will not be sufficient to understand their self-organization in a cellular context, because the two networks are not independent of each other. Instead, the two networks are physically and biochemically coupled. It is necessary to design new, controlled *in vitro* biochemical assays in which the two networks can interact and regulate each other. Such assays should offer the possibility to manipulate the geometry of network interactions as well as the spatial distribution of crosslinking proteins and regulating enzymes such as Rho-GTPases. Physical SBCs need to be completed by biochemical SBCs comprising surface-grafted, but also soluble and diffusible, cues.

Notably, understanding of the basic laws governing cytoskeleton assembly can not only provide insights into cell and tissue morphogenesis, but may also have technological applications in the development of microdevices requiring complex and dynamic architectures. A structure whose precise architecture is regulated by deterministic assembly rules, that can grow and self-repair because it self-renews, has advantages over a fixed structure that would have to be repaired or replaced by a prefabricated static component. This new sort of manufacturing would be a useful way to prepare novel biomaterials and should find promising applications in microelectronics and robotics.

Acknowledgments

We apologize to authors whose work on cytoskeleton self-organization was instructive and influential but not cited here because the purpose was to focus on the specific role of SBCs. We thank all members of the Physics of the Cytoskeleton and Morphogenesis Laboratory for their experimental work and discussions. This work was supported by grants from the Human Frontier Science Programs (RGP0004/2011 to L.B. and RGY0088/2012 to M.T.) and Institut National du Cancer (PLBIO 2011-141 to M.T.).

References

1 Karsenti, E. (2008) Self-organization in cell biology: a brief history. *Nat. Rev. Mol. Cell Biol.* 9, 255–262
2 Huber, F. and Käs, J. (2011) Self-regulative organization of the cytoskeleton. *Cytoskeleton (Hoboken)* 68, 259–265
3 Surrey, T. *et al.* (2001) Physical properties determining self-organization of motors and microtubules. *Science* 292, 1167–1171
4 Schaller, V. *et al.* (2010) Polar patterns of driven filaments. *Nature* 467, 73–77
5 Sumino, Y. *et al.* (2012) Large-scale vortex lattice emerging from collectively moving microtubules. *Nature* 483, 448–452
6 Cortès, S. *et al.* (2006) Microtubule self-organisation by reaction-diffusion processes in miniature cell-sized containers and phospholipid vesicles. *Biophys. Chem.* 120, 168–177
7 Pollard, T.D. and Cooper, J.A. (1986) Actin and actin-binding proteins. A critical evaluation of mechanisms and functions. *Annu. Rev. Biochem.* 55, 987–1035
8 De La Cruz, E.M. *et al.* (2000) Polymerization and structure of nucleotide-free actin filaments. *J. Mol. Biol.* 295, 517–526
9 Xu, K. *et al.* (2012) Dual-objective STORM reveals three-dimensional filament organization in the actin cytoskeleton. *Nat. Methods* 9, 185–188
10 Pollard, T.D. (2007) Regulation of actin filament assembly by Arp2/3 complex and formins. *Annu. Rev. Biophys. Biomol. Struct.* 36, 451–477
11 Yarar, D. *et al.* (1999) The Wiskott-Aldrich syndrome protein directs actin-based motility by stimulating actin nucleation with the Arp2/3 complex. *Curr. Biol.* 9, 555–558
12 Oudenaarden, A.V. and Theriot, J.A. (1999) Cooperative symmetry-breaking by actin polymerization in a model for cell motility. *Nat. Cell Biol.* 1, 493–499
13 van der Gucht, J. *et al.* (2005) Stress release drives symmetry breaking for actin-based movement. *Proc. Natl. Acad. Sci. U.S.A.* 102, 7847–7852
14 Bernheim-Groswasser, A. *et al.* (2005) Mechanism of actin-based motility: a dynamic state diagram. *Biophys. J.* 89, 1411–1419
15 Achard, V. *et al.* (2010) A "primer"-based mechanism underlies branched actin filament network formation and motility. *Curr. Biol.* 20, 423–428
16 Noireaux, V. *et al.* (2000) Growing an actin gel on spherical surfaces. *Biophys. J.* 78, 1643–1654
17 Bernheim-Groswasser, A. *et al.* (2002) The dynamics of actin-based motility depend on surface parameters. *Nature* 417, 308–311
18 Lacayo, C.I. *et al.* (2012) Choosing orientation: influence of cargo geometry and ActA polarization on actin comet tails. *Mol. Biol. Cell* 23, 614–629
19 Michelot, A. *et al.* (2007) Actin-filament stochastic dynamics mediated by ADF/cofilin. *Curr. Biol.* 17, 825–833
20 Soares e Silva, M. *et al.* (2011) Self-organized patterns of actin filaments in cell-sized confinement. *Soft Matter* 7, 10631
21 Månsson, A. *et al.* (2012) Self-organization of motor-propelled cytoskeletal filaments at topographically defined borders. *J. Biomed. Biotechnol.* 2012, 647265
22 Liu, A.P. *et al.* (2008) Membrane-induced bundling of actin filaments. *Nat. Phys.* 4, 789–793
23 Roos, W.H. *et al.* (2003) Freely suspended actin cortex models on arrays of microfabricated pillars. *Chemphyschem* 4, 872–877
24 Uhrig, K. *et al.* (2009) Optical force sensor array in a microfluidic device based on holographic optical tweezers. *Lab Chip* 9, 661–668
25 Reymann, A-C. *et al.* (2010) Nucleation geometry governs ordered actin networks structures. *Nat. Mater.* 9, 827–832
26 Pinot, M. *et al.* (2012) Confinement induces actin flow in a meiotic cytoplasm. *Proc. Natl. Acad. Sci. U.S.A.* 109, 11705–11710
27 Reymann, A-C. *et al.* (2012) Actin network architecture can determine myosin motor activity. *Science* 336, 1310–1314
28 Thoresen, T. *et al.* (2011) Reconstitution of contractile actomyosin bundles. *Biophys. J.* 100, 2698–2705
29 Shelanski, M.L. (1973) Chemistry of the filaments and tubules of brain. *J. Histochem. Cytochem.* 21, 529–539
30 Holy, T.E. *et al.* (1997) Assembly and positioning of microtubule asters in microfabricated chambers. *Proc. Natl. Acad. Sci. U.S.A.* 94, 6228–6231
31 Laan, L. *et al.* (2012) Cortical dynein controls microtubule dynamics to generate pulling forces that position microtubule asters. *Cell* 148, 502–514
32 Nedelec, F. *et al.* (1997) Self-organization of microtubules and motors. *Nature* 389, 305–308
33 Pinot, M. *et al.* (2009) Effects of confinement on the self-organization of microtubules and motors. *Curr. Biol.* 19, 954–960
34 Cosentino Lagomarsino, M. *et al.* (2007) Microtubule organization in three-dimensional confined geometries: evaluating the role of elasticity through a combined in vitro and modeling approach. *Biophys. J.* 92, 1046–1057
35 Emsellem, V. *et al.* (1998) Vesicle deformation by microtubules: a phase diagram. *Phys. Rev. E* 58, 4807–4810
36 Fygenson, D. *et al.* (1997) Mechanics of microtubule-based membrane extension. *Phys. Rev. Lett.* 79, 4497–4500
37 Karsenti, E. and Vernos, I. (2001) The mitotic spindle: a self-made machine. *Science* 294, 543–547

38 Heald, R. *et al.* (1996) Self-organization of microtubules into bipolar spindles around artificial chromosomes in *Xenopus* egg extracts. *Nature* 382, 420–425
39 Halpin, D. *et al.* (2011) Mitotic spindle assembly around RCC1-coated beads in *Xenopus* egg extracts. *PLoS Biol.* 9, e1001225
40 Gaetz, J. *et al.* (2006) Examining how the spatial organization of chromatin signals influences metaphase spindle assembly. *Nat. Cell Biol.* 8, 924–932
41 Dinarina, A. *et al.* (2009) Chromatin shapes the mitotic spindle. *Cell* 138, 502–513
42 Bornens, M. *et al.* (1989) The cortical microfilament system of lymphoblasts displays a periodic oscillatory activity in the absence of microtubules: implications for cell polarity. *J. Cell Biol.* 109, 1071–1083
43 Bailly, E. *et al.* (1991) The cortical actomyosin system of cytochalasin D-treated lymphoblasts. *Exp. Cell Res.* 196, 287–293
44 Paluch, E. *et al.* (2005) Cortical actomyosin breakage triggers shape oscillations in cells and cell fragments. *Biophys. J.* 89, 724–733
45 Cavalcanti-Adam, E.A. *et al.* (2007) Cell spreading and focal adhesion dynamics are regulated by spacing of integrin ligands. *Biophys. J.* 92, 2964–2974
46 Schvartzman, M. *et al.* (2011) Nanolithographic control of the spatial organization of cellular adhesion receptors at the single-molecule level. *Nano Lett.* 11, 1306–1312
47 Vignaud, T. *et al.* (2012) Reprogramming cell shape with laser nano-patterning. *J. Cell Sci.* 125, 2134–2140
48 Lehnert, D. *et al.* (2004) Cell behaviour on micropatterned substrata: limits of extracellular matrix geometry for spreading and adhesion. *J. Cell Sci.* 117, 41–52
49 Vianay, B. *et al.* (2010) Single cells spreading on a protein lattice adopt an energy minimizing shape. *Phys. Rev. Lett.* 105, 3–6
50 Levina, E.M. *et al.* (2001) Cytoskeletal control of fibroblast length: experiments with linear strips of substrate. *J. Cell Sci.* 114, 4335–4341
51 Picone, R. *et al.* (2010) A polarised population of dynamic microtubules mediates homeostatic length control in animal cells. *PLoS Biol.* 8, e1000542
52 Vartanian, K.B. *et al.* (2008) Endothelial cell cytoskeletal alignment independent of fluid shear stress on micropatterned surfaces. *Biochem. Biophys. Res. Commun.* 371, 787–792
53 Terenna, C.R. *et al.* (2008) Physical mechanisms redirecting cell polarity and cell shape in fission yeast. *Curr. Biol.* 18, 1748–1753
54 Bergert, M. *et al.* (2012) Cell mechanics control rapid transitions between blebs and lamellipodia during migration. *Proc. Natl. Acad. Sci. U.S.A.* 666, 1–7
55 James, J. *et al.* (2008) Subcellular curvature at the perimeter of micropatterned cells influences lamellipodial distribution and cell polarity. *Cell Motil. Cytoskeleton* 65, 841–852
56 Parker, K.K. *et al.* (2002) Directional control of lamellipodia extension by constraining cell shape and orienting cell tractional forces. *FASEB J.* 16, 1195–1204
57 Brock, A. *et al.* (2003) Geometric determinants of directional cell motility revealed using microcontact printing. *Langmuir* 19, 1611–1617
58 Rossier, O.M. *et al.* (2010) Force generated by actomyosin contraction builds bridges between adhesive contacts. *EMBO J.* 29, 1055–1068
59 Tan, J.L. *et al.* (2003) Cells lying on a bed of microneedles: an approach to isolate mechanical force. *Proc. Natl. Acad. Sci. U.S.A.* 100, 1484–1489
60 Rape, A.D. *et al.* (2011) The regulation of traction force in relation to cell shape and focal adhesions. *Biomaterials* 32, 2043–2051
61 Kilian, K. *et al.* (2010) Geometric cues for directing the differentiation of mesenchymal stem cells. *Proc. Natl. Acad. Sci. U.S.A.* 107, 4872–4877
62 Hu, S. *et al.* (2004) Mechanical anisotropy of adherent cells probed by a 3D magnetic twisting device. *Am. J. Physiol. Cell Physiol.* 287, C1884–C1191
63 Khatau, S.B. *et al.* (2009) A perinuclear actin cap regulates nuclear shape. *Proc. Natl. Acad. Sci. U.S.A.* 106, 19017–19022
64 Bray, M-A. *et al.* (2008) Sarcomere alignment is regulated by myocyte shape. *Cell Motil. Cytoskeleton* 651, 641–651
65 Xu, J. *et al.* (2011) Effects of micropatterned curvature on the motility and mechanical properties of airway smooth muscle cells. *Biochem. Biophys. Res. Commun.* 415, 591–596
66 Théry, M. *et al.* (2006) Cell distribution of stress fibres in response to the geometry of the adhesive environment. *Cell Motil. Cytoskeleton* 63, 341–355
67 Tseng, Q. *et al.* (2011) A new micropatterning method of soft substrates reveals that different tumorigenic signals can promote or reduce cell contraction levels. *Lab Chip* 11, 2231–2240
68 Bischofs, I.B. *et al.* (2008) Filamentous network mechanics and active contractility determine cell and tissue shape. *Biophys. J.* 95, 3488–3496
69 Théry, M. *et al.* (2006) Anisotropy of cell adhesive microenvironment governs cell internal organization and orientation of polarity. *Proc. Natl. Acad. Sci. U.S.A.* 103, 19771–19776
70 Wu, J. *et al.* (2011) Effects of dynein on microtubule mechanics and centrosome positioning. *Mol. Biol. Cell* 22, 4834–4841
71 Hale, C.M. *et al.* (2011) SMRT analysis of MTOC and nuclear positioning reveals the role of EB1 and LIC1 in single-cell polarization. *J. Cell Sci.* 124, 4267–4285
72 Zhu, J. *et al.* (2010) finding the cell center by a balance of dynein and myosin pulling and microtubule pushing: a computational study. *Mol. Biol. Cell* 21, 4418–4427
73 Dupin, I. *et al.* (2009) Classical cadherins control nucleus and centrosome position and cell polarity. *J. Cell Biol.* 185, 779–786
74 Camand, E. *et al.* (2012) N-cadherin expression level modulates integrin-mediated polarity and strongly impacts on the speed and directionality of glial cell migration. *J. Cell Sci.* 125, 844–857
75 Lombardi, M.L. *et al.* (2011) The interaction between nesprins and sun proteins at the nuclear envelope is critical for force transmission between the nucleus and cytoskeleton. *J. Biol. Chem.* 286, 26743–26753
76 Pitaval, A. *et al.* (2010) Cell shape and contractility regulate ciliogenesis in cell cycle-arrested cells. *J. Cell Biol.* 191, 303–312
77 Mahmud, G. *et al.* (2009) Directing cell motions on micropatterned ratchets. *Nat. Phys.* 5, 606–612
78 Kushiro, K. *et al.* (2012) Modular design of micropattern geometry achieves combinatorial enhancements in cell motility. *Langmuir* 28, 4357–4362
79 Yoon, S-H. *et al.* (2011) A biological breadboard platform for cell adhesion and detachment studies. *Lab Chip* 11, 3555–3562
80 Csucs, G. *et al.* (2007) Locomotion of fish epidermal keratocytes on spatially selective adhesion patterns. *Cell Motil. Cytoskeleton* 64, 856–867
81 Doyle, A.D. *et al.* (2009) One-dimensional topography underlies three-dimensional fibrillar cell migration. *J. Cell Biol.* 184, 481–490
82 Pouthas, F. *et al.* (2008) In migrating cells, the Golgi complex and the position of the centrosome depend on geometrical constraints of the substratum. *J. Cell Sci.* 121, 2406–2414
83 Maiuri, P. *et al.* (2012) The world first cell race. *Curr. Biol.* 22, R673–R675
84 Théry, M. *et al.* (2007) Experimental and theoretical study of mitotic spindle orientation. *Nature* 447, 493–496
85 Fink, J. *et al.* (2011) External forces control mitotic spindle positioning. *Nat. Cell Biol.* 13, 771–778
86 Samora, C.P. *et al.* (2011) MAP4 and CLASP1 operate as a safety mechanism to maintain a stable spindle position in mitosis. *Nat. Cell Biol.* 13, 1040–1050
87 Kiyomitsu, T. and Cheeseman, I.M. (2012) Chromosome- and spindle-pole-derived signals generate an intrinsic code for spindle position and orientation. *Nat. Cell Biol.* 14, 311–317
88 Minc, N. *et al.* (2011) Influence of cell geometry on division-plane positioning. *Cell* 144, 414–426
89 Minc, N. and Piel, M. (2012) Predicting division plane position and orientation. *Trends Cell Biol.* 22, 193–200
90 Huang, S. *et al.* (2005) Symmetry-breaking in mammalian cell cohort migration during tissue pattern formation: role of random-walk persistence. *Cell Motil. Cytoskeleton* 61, 201–213
91 Burute, M. and Thery, M. (2012) Spatial segregation of cell–cell and cell–matrix adhesions. *Curr. Opin. Cell Biol.* 24, 628–636
92 Tseng, Q. *et al.* (2012) Spatial organization of the extracellular matrix regulates cell-cell junction positioning. *Proc. Natl. Acad. Sci. U.S.A.* 109, 1506–1511

93 McCain, M.L. *et al.* (2012) Cooperative coupling of cell-matrix and cell-cell adhesions in cardiac muscle. *Proc. Natl. Acad. Sci. U.S.A.* 109, 9881–9886

94 Serra-Picamal, X. *et al.* (2012) Mechanical waves during tissue expansion. *Nat. Phys.* 8, 628–634

95 Wan, L.Q. *et al.* (2011) Micropatterned mammalian cells exhibit phenotype-specific left-right asymmetry. *Proc. Natl. Acad. Sci. U.S.A.* 108, 12295–12300

96 Desai, R.A. *et al.* (2009) Cell polarity triggered by cell-cell adhesion via E-cadherin. *J. Cell Sci.* 122, 905–911

97 Reffay, M. *et al.* (2011) Orientation and polarity in collectively migrating cell structures: statics and dynamics. *Biophys. J.* 100, 2566–2575

98 Mullins, R.D. (2010) Cytoskeletal mechanisms for breaking cellular symmetry. *Cold Spring Harb. Perspect. Biol.* 2, a003392

II. Mesures de Forces : Mode d'Emploi

La mesure des forces générées par la cellule est un challenge technologique auquel de nombreuses solutions ont été proposées au cours des deux dernières décennies. J'ai pour ma part utilisé la microscopie à traction de forces (TFM). Je vais dans un premier temps décrire les paramètres clés auxquels la cellule est capable de répondre en modifiant les forces qu'elle génère. Ces paramètres doivent être contrôlés précisément au cours d'une expérience de mesure de forces pour ne pas obtenir des variations involontaires liées à une maitrise insuffisante des conditions expérimentales. Je décrirai dans un deuxième temps très brièvement les techniques de mesures de forces existantes, leur champ d'application et je justifierai le choix de notre méthode de travail. Enfin, je décrirai le mode de préparation des supports utilisés dans mes expériences et le traitement des données récoltées permettant d'obtenir une estimation de la force générée par la cellule.

1. PARAMETRES CLES DE L'ENVIRONNEMENT

A. RIGIDITE

La rigidité joue un rôle prépondérant dans la régulation des fonctions cellulaires. Cette grandeur permet de quantifier la force générée par le substrat en réponse à une déformation. Chacun de nos organes est caractérisé par une rigidité (Butcher, Nature Reviews, 2009– figure 22).

Les cellules souches peuvent être orientées vers une voie de différentiation ou une autre en fonction de la rigidité du substrat sur lequel elles sont placées (Engler, Cell, 2006). De façon intéressante, si on place les cellules sur des substrats de rigidité croissante, la force augmente jusqu'à saturation (Yip, Biophys. J., 2013), cette augmentation de force s'accompagne d'une réarrangement du cytosquelette avec l'apparition d'importantes fibres de stress (Prager-Khoutorsky, Nat. Cell Biol., 2011). Même sur des temps très courts, la cellule est capable d'adapter les forces qu'elle génère en réponse à une modification de la rigidité de son environnement (Mitrossilis, PNAS, 2010). Ce mécanisme de renforcement des forces joue d'ailleurs certainement un rôle dans la transformation tumorale. En effet, l'un des phénomènes aboutissant à la formation de tumeurs est la fibrose. Ce phénomène se caractérise par une rigidification du tissu en réponse à un stress chronique des cellules qui le compose (infection virale, alcoolisme chronique, tabagisme, …). Cette rigidification permettra aux cellules saines de participer au développement de la tumeur en stimulant leur prolifération (Mason, Springer, 2012) et la perte de leurs liens cellule-cellule (de Rooij, J. Cell Biol, 2005).

Cette sensibilité à la rigidité passe par les adhésions, les protéines sensibles aux forces qui les composent, et les voies de signalisations qu'elles régulent. La rigidité n'est cependant pas le seul

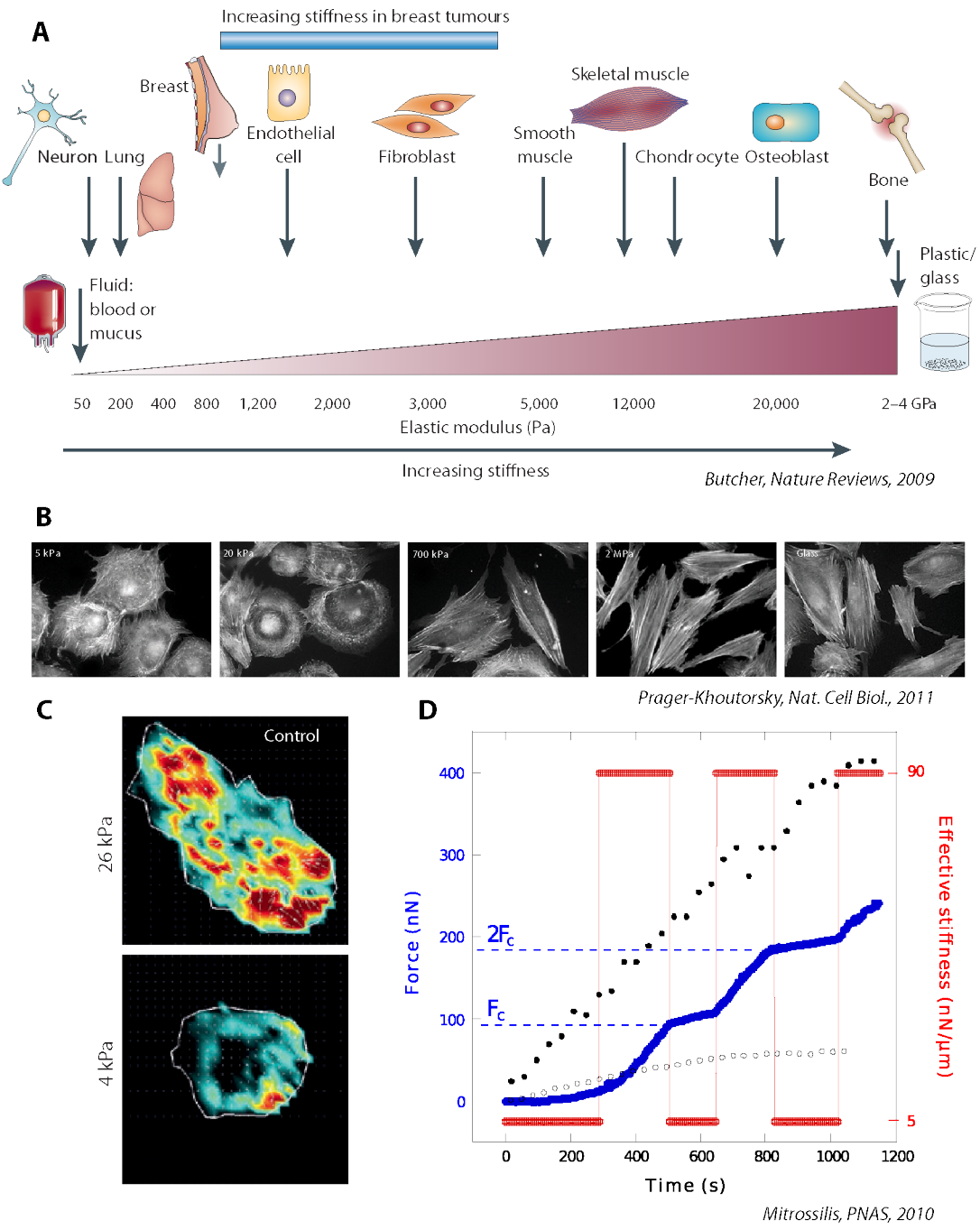

Figure 22 : Adaptation cellulaire à la rigidité

A – Les différentes rigidités des tissus de notre organisme et les types cellulaires qui les composent – B – Réorganisation du cytosquelette en réponse à une rigidité croissante du substrat – C – L'augmentation de la rigidité s'accompagne d'une augmentation de la force générée par la cellule. – D - L'adaptation à la rigidité affecte également les propriétés cinétiques de mise en place de la force. La cellule est capable d'adapter instantanément son taux d'augmentation de forces en réponse à la rigidité à laquelle elle fait face.

mécanisme qui peut modifier les forces. Les intégrines sont capables de se lier à différentes protéines de matrice extracellulaire. La nature de ces protéines et leur disposition spatiale joue également un rôle dans la régulation des forces générées par la cellule.

B. MOLECULES D'ADHESION ET ORGANISATION

La nature des protéines d'adhésions joue un rôle important dans le mécanisme de production de forces. Certaines cellules ne possèdent pas les récepteurs pour telle ou telle protéine. Avant de mesurer les forces dans une condition, il convient de s'assurer que les cellules sont capables d'adhérer au substrat sur lequel elles seront placées. D'autre part, différentes molécules de matrice peuvent engager différentes intégrines qui agiront différemment sur le niveau des forces produites par les cellules. Par ailleurs, l'organisation spatiale de ces molécules d'adhésions va pouvoir conditionner l'organisation du cytosquelette et le niveau de forces (voir I-5). La dimensionnalité de l'environnement (1D/2D/3D/canaux) doit également être prise en compte car des changements radicaux du comportement cellulaire ont pu être observés en réponse à ces facteurs (Doyle, J. Cell, Biol, 2009, Lämmerman, Nature, 2008)

C. MOUVEMENTS DE FLUIDES

Les mouvements de fluides sont souvent négligés au sein des systèmes expérimentaux , sans doute à tort. En effet, les cellules sont capables de sentir les mouvements de fluide et de s'y adapter, cette adaptation a particulièrement été étudiée dans le cas de l'endothélium qui recouvre la face interne de nos vaisseaux (Malek, J. Cell. Science, 1996). Le flux induit un allongement des cellules et une réorganisation du cytosquelette. Il convient de s'assurer dans son système expérimental qu'aucun flux n'est généré durant l'expérimentation. Une attention particulière doit être apportée aux systèmes de maintien en température des microscopes qui peuvent aisément générés des flux convectifs.

Après ces quelques mises en garde, je vais maintenant présenter les différentes approches permettant de mesurer les forces à l'échelle de la cellule unique. Ces approches seront regroupées en deux groupes selon qu'elles permettent ou non le contrôle au cours du temps de la force appliquée à la cellule.

2. MESURER LES FORCES A L'ECHELLE DE LA CELLULE UNIQUE : DIFFERENTES APPROCHES

MESURE PASSIVE DE FORCE	Résolution	Remarques	Ref
elastomères 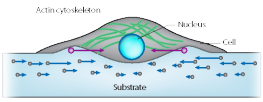	- variable selon la rigidité - limitée par la précision de localisation des billes - mesure dépendante du traite ment des données à posteriori 100 -1000 Pa 10 nN	+ Forces sur la cellule entière + Rapide + Facile + Peu-couteux + compatible avec l'imagerie en fluorescence - détachement de la cellule - mesure indirecte	Sabass, Biophys. J., 2008
micropiliers 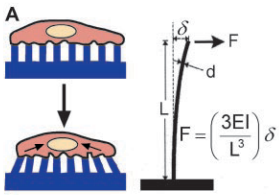	10 nN	+ Mesure directe de la force par le déplacement + Peu-couteux + Facile + Rapide - difficilement compatible avec de la microscopie haute résolution - contraintes sur l'organisation du cytosquelette	Tan, PNAS, 2003
ablation laser 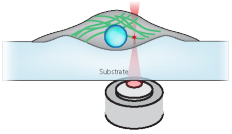	comparaison entre plusieurs conditions approche semi-quantitative	+ mesure de la force liée à un structure isolée + accès à des propriétés mécaniques intracellulaires - couteux - possible dommages cellulaires	Kumar, Biophys. J., 2006
senseurs protéiques (FRET) 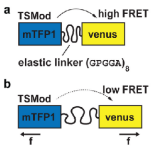	1 pN	+ mesure de l'étirement de protéines - travail de biologie moléculaire en amont	Grashoff, Nature, 2010

MESURE DE FORCES ET STIMULATION			
Hybride PDMS/Acrylamide 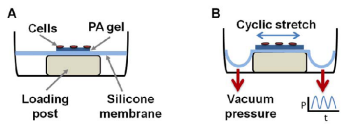	idem elastomères avec la possibilité de générer une force homogène centrifuge		Quinlan, Plos One, 2011
Pinces optiques 	10 pN	+ controle de la force appliquée + accès à des réponses sur des temps courts + mesures de forces très faibles + controle de la rigidité du piège optique - force maximale limitée - mesure de forces en un point unique de la cellule - long à mettre en oeuvre - isolation du dispositif expérimental - couteux	Moffitt, Annu. Rev. Biochem., 2008
AFM/microplateaux flexible 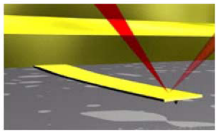 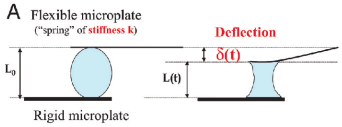	10 pN 1 nN	+ controle de la force appliquée + mesures de forces très faibles + rigidité adaptable en temps réel - mesure d'une force globale pour l'intégralité de la cellule - cout - difficulté à mettre l'échantillon en place	Jalili, Mechatronics, 2004 Mitrossilis, PNAS, 2009

Figure 23 : Présentation des différentes méthodes de mesures des forces à l'échelle de la cellule unique

Les élastomères – microscopie à traction de forces (TFM)

Du fait de leurs propriétés élastiques, les élastomères offrent un excellent moyen de mesurer les forces générées par la cellule. En effet, toute déformation de leur surface suppose que la cellule est capable d'exercer la force responsable de cette déformation. De la déformation peut être déduite la force selon le principe de l'élasticité. Deux élastomères ont principalement été utilisés. Il s'agit du PDMS et du polyacrylamide. Ils offrent un contrôle facile de leur rigidité au moment de leur polymérisation. Pour permettre de visualiser les déformations du gel, plusieurs solutions ont été imaginées. Le but est toujours le même : il s'agit de placer des rapporteurs de déplacements au sein de l'élastomère, le plus proche possible de la surface pour permettre de mesurer les déformations du support. L'utilisation de billes fluorescentes est la stratégie la plus répandue. Deux images sont acquises, l'une avec la cellule sur le support, l'autre après détachement de la cellule. Les forces cellulaires sont responsables du déplacement des billes entre les deux situations. Un traitement théorique de ces deux images va permettre d'estimer les forces, connaissant le module d'Young du gel et son coefficient de poisson. Cette technique permet de réaliser de nombreuses mesures en parallèle et donne accès à la distribution des forces sur l'ensemble de la cellule. Elle est facilement associable à de la microscopie haute résolution.

Les micro-piliers

Le système ressemble à un tapis de fakir cellulaire. Il s'agit d'un champ de piliers de PDMS sur lequel la cellule va venir adhérer. La déflection du sommet du pilier sera proportionnelle à la force tangentielle exercée. Cette relation dépendra de la longueur du pilier et de son élasticité.

Cette technique est extrêmement puissante car elle permet de remonter aux forces sans calculs fastidieux. Par ailleurs, l'organisation initiale des piliers étant connue, il n'est pas nécessaire de détacher les cellules pour connaître les forces.

Cependant, la résolution spatiale est limitée par la densité en piliers. D'autre part les contraintes imposées par les piliers sur l'organisation du cytosquelette (la cellule ne peut pas former d'adhésions à d'autres endroits que sur les piliers) pourraient mener à des résultats contradictoires par rapport à d'autres méthodes. Enfin, la hauteur des piliers rend l'imagerie haute résolution difficile, du fait de la faible distance de travail des objectifs correspondants.

L'ablation laser

L'ablation laser donne accès à l'estimation des forces générées par des composants intracellulaires dans leur situation normale. Un laser pulsé focalisé va permettre de venir détruire des structures intracellulaires. La réponse immédiate de la structure à la rupture de son intégrité va permettre d'estimer ses propriétés mécaniques. Cependant ces estimations reposent sur un cadre théorique et la mesure n'est pas directe. Elle permet cependant de comparer des comportements entre cellules (Tanner, Biophys. J., 2010) et d'obtenir des paramètres clés pour les modèles mécaniques du cytosquelette.

Les molécules étirables

Il s'agit de protéines modifiées pour contenir une portion aux propriétés élastiques connues. Les extrémités de cette portion seront couplées à des protéines fluorescentes. L'état d'étirement va pouvoir être estimé à l'aide du phénomène de FRET (Förster Resonance Energy Transfer). Ce phénomène permet un transfert d'énergie entre les deux fluorophores. L'excitation d'un fluorophore permettra ainsi l'émission de l'autre fluorophore. Ce transfert est d'autant plus efficace que les deux fluorophores sont proches. Ainsi, si peu de forces sont appliquées, la portion insérée dans la protéine est repliée et le transfert optimal. Si en revanche la protéine est mise sous tension, la portion élastique va se déplier progressivement, éloignant ainsi les deux fluorophores et diminuant ainsi l'efficacité de transfert.

Cette technique a permis de décrire le rôle de la tension au sein des adhésions dans leur régulation (Grashoff, Nature, 2010). Elle donne accès à la mesure de la tension au sein de chaque adhésion de façon rapide et fiable. Cependant le principal inconvénient de cette technique est la difficulté à produire les protéines rapporteuses car chaque nouvelle protéine nécessite une série de contrôles pour s'assurer que sa fonction n'est pas altérée au sein de la cellule.

Les techniques présentées jusqu'à présent permettent la mesure de forces générées par la cellule mais ne permettent pas de stimuler la cellule avec des forces contrôlées et de mesurer en retour leur réponse. D'autres méthodes permettent de relever ce challenge. Elles sont l'objet de la section suivante.

B. METHODES D'APPLICATION ET DE MESURE DE FORCES CONCOMITANTES

Combinaison PDMS, gel d'acrylamide

Cette solution combine des expériences d'étirement cellulaire réalisées initialement sur PDMS à la mesure de force sur acrylamide. Pour cela, 2 couches sont superposées. La couche inférieure est faite de PDMS plus rigide que la couche supérieure, composée d'acrylamide contenant des billes

fluorescentes. La couche inférieure va être utilisée pour étirer le substrat. L'étirement sera transmis par l'acrylamide aux cellules. Les cellules pourront en retour déformer l'acrylamide. De la même façon que précédemment les forces pourront être estimées après retrait des cellules. Ce système est ingénieux mais demande de faire face au challenge présenté par la modification de l'emplacement des billes par l'étirement du PDMS, même en absence de cellules.

Pince optique

Les pinces optiques reposent sur l'utilisation d'un laser focalisé couplé à un objet diélectrique transparent (typiquement une bille de polystyrène). La focalisation du laser génère un gradient de forces optiques : la réfraction de la lumière au sein de la bille va l'entrainer vers les zones d'intensité maximale (le point de focalisation du laser) et le champ électrique généré par le laser va polariser la bille et l'attirer vers le centre du faisceau. Si la bille s'éloigne du point de focalisation du faisceau, elle va subir une force de rappel proportionnelle à son éloignement. Le piège optique se comporte donc comme un ressort dont la rigidité dépend de l'intensité du faisceau.

Ce système permet d'appliquer une force à la cellule en attachant la bille à la surface de la cellule puis en éloignant le faisceau laser, pour mettre le « ressort » sous tension. Il permet également de mesurer des forces en laissant le faisceau laser fixe et en observant de quelle distance la cellule éloigne la bille du centre du faisceau. Le maintien d'une distance constante entre la bille et le centre du faisceau par un système de rétrocontrôle permet d'exercer une force constante sur l'objet.

Microscope à force atomique/Micro-languettes flexibles

Le microscope à force atomique (AFM) et le système de micro-languettes flexibles reposent sur des principes similaires. Un objet longiligne va être utilisé pour appliquer des forces sur la cellule mais également mesurer les forces qu'elles génèrent. De la même façon que pour les piliers précédemment, la déformation de ces objets par une force tangentielle va être proportionnelle à la force appliquée. De la même façon que pour les pinces optiques, un rétrocontrôle va permettre d'obtenir une force constante si on déplace l'échantillon pour permettre d'obtenir une déflexion constante. Une déformation constante de la cellule pourra également être obtenue si on maintient la position de l'extrémité de la cellule sans se préoccuper de la déflexion de la sonde. Ces 2 procédures donnent accès à des modalités nouvelles de stimulations permettant d'étudier la réponse de la cellule à des modifications rapides et complexes de son environnement. Cependant, comme les techniques précédentes de stimulation, elles souffrent de l'impossibilité de réaliser plusieurs mesures en parallèle.

3. CHOIX DE NOTRE METHODE DE TRAVAIL POUR L'ETUDE DES FIBRES DE STRESS

J'avais besoin besoin pour mon étude de pouvoir mesurer la force générée au sein des fibres de stress dans différentes conditions. Mon choix s'est orienté vers l'utilisation de substrat d'acrylamide « micro-patterné ». Cette technique permet d'appliquer la TFM mais à des cellules dont l'organisation intracellulaire est contrainte par une organisation spatiale contrôlée des protéines de matrice à la surface de l'acrylamide. On peut ainsi obtenir la même organisation de façon robuste et répétitive ce qui rend la reproduction des expériences beaucoup plus aisée. On s'affranchit en même temps des variations de forces dues à une modification de la surface de la cellule ou au processus de migration (protrusion – contraction – retraction)

Pour avoir accès à la force dans une fibre unique, j'ai pris le parti de venir détruire cette structure par nano-ablation. La conjonction de la TFM, du micro-patterning et de la nano-ablation me permet ainsi de mesurer la force générée par une structure, en parallèle sur de nombreuses cellules et dans un grand nombre de conditions différentes.

Je vais maintenant décrire le processus de fabrication du substrat d'acrylamide micro-patterné. Un protocole avait déjà été développé au sein de notre équipe (Tseng, Lab On Chip, 2011) mais j'ai eu l'occasion de le repenser au cours de ma thèse pour permettre d'en améliorer certains aspects, notamment l'homogénéité de la rigidité et la conservation de la fluorescence des billes situées immédiatement sous le micro-pattern.

4. POLYACRYLAMIDE HYDROGEL MICROPATTERNING (ARTICLE – ACCEPTED)

Polyacrylamide hydrogel micropatterning

Timothée Vignaud[1-4], Hajer Ennomani[1-4], Manuel Théry[1-4]

1 CNRS, Laboratoire de Physiologie Cellulaire & Végétale, UMR 5168, F-38054 Grenoble, France

2 Univ. Grenoble Alpes, LPCV, F-38054 Grenoble, France

3 CEA, DSV, iRTSV, LPCV, F-38054 Grenoble, France

4 INRA, LPCV, USC1359, F-38054 Grenoble, France

Table of Contents

I. Introduction and Rationale

Since the introduction of cell culture experiments in Petri dishes, several technical improvements have been developed to better reproduce in vitro the actual physiological metazoan cell micro-environment. Microenvironment geometry and architecture can be mimicked and modulated using surface micropatterning. It consists of the creation of extracellular matrix (ECM) protein islands of controlled size and shape, called micropatterns, surrounded by antifouling polymers preventing non-specific protein and cell adhesion. Surface micropatterning has already revealed the implication of cell adhesive micro-environment geometry in the regulation of many critical physiological processes (cell shape, cell architecture, internal cell organization, cell migration, cell division, cell differentiation, tissue architecture…)(Théry, 2010; Vignaud et al., 2012a)

Microenvironment rigidity has also been shown to be a key parameter in the regulation of several key physiological processes, including pathological ones (cell polarity, cell growth, cell differentiation, tumoral transformation, …) (Engler et al., 2006; Prager-Khoutorsky et al., 2011; de Rooij et al., 2005; Klein et al., 2009; Pitaval et al., 2010).

As both the spatial organization of the ECM protein and the substrate stiffness have implications for cell physiology it is relevant to combine both in order to faithfully reproduce and control cell microenvironment. Polyacrylamide (PAA) hydrogels have several interesting physic-chemical properties that are useful for protein and cell micropatterning. They are optically transparent,

low cost and chemically simple compounds that can be used in almost any lab. They have been used for decades for molecular biology, notably for the manufacturing of western blots, due to the possibility to modulate their mesh size by changing the ratio of monomers to crosslinkers before polymerization. Interestingly, this mesh size is also related to the stiffness of the gel and this technique has been successfully adapted for the production of cell culture substrates of defined mechanical properties ((Pelham and Wang, 1997)). Importantly for mechanical measurements, the stiffness of the gel does not depend on the applied strain ((Storm et al., 2005)). In addition, PAA has constitutive antifouling properties preventing non-specific protein and cell adsorption. Alternatively acrylamide groups can be used as a substrate to make covalent link with proteins of interest. Therefore many recent efforts have been devoted to the development of experimental methods to micropattern proteins on PAA hydrogels ((Wang et al., 2002; Zhang et al., 2013; Damljanovic et al., 2005; Versaevel et al., 2012; Tseng et al., 2011; Rape et al., 2011; Tang et al., 2012; Polio et al., 2012; Yu et al., 2012; Grevesse et al., 2013)). However, these methods still have intrinsic limitations. Most of them involve a microcontact printing step to physically pattern the proteins onto the PAA. This step is time consuming, poorly reproducible in terms of amount of transferred proteins and has a limited spatial resolution (typically few micrometers). We circumvent these limitations by using a direct (one step) activation of the PAA with deep UV through a photomask in contact with the gel ((Tseng et al., 2011)) and improve the spatial resolution of the micropatterns. In addition, most methods require chemical crosslinkers such as sulfo-SANPAH or NHS-EDC, to bind the proteins of interest to the PAA. However, these reagents are poorly stable in the presence of water and the efficiency of the crosslinking is variable. Recently, Wang and colleagues used PAA polymerization itself to directly bind the protein of interest and transfer pre-patterned proteins onto the PAA ((Rape et al., 2011)). Here we propose two rapid, accurate, reliable and easy-to-use methods that combines all these improvements. They are based on production of micropatterns on hard substrate using deep-UV photo-patterning followed by protein transfer on PAA hydrogel. Thereby we associated the advantages of deep-UV patterning (micrometer to sub-micrometer resolution, production of highly reproducible micropatterns) to the efficacy and reproducibility of protein covalent linking with acrylamide polymerization. The “glass method” is based on the transfer from a micropatterned glass coverslip while the “mask method” produces micropatterns directly on the quartz photomask before transfer on PAA, thus bringing the resolution of the technique to sub-micrometer level.

II. Safety recommendations

• Many of the reagents used during the processes described below are potentially dangerous. Acrylamide, acetone, isopropanol, silane, TEMED, are very volatile compounds that should be handled under a chemical hood with adapted personal security protection (lab coat, gloves, protective glasses) and should be discarded specifically as they usually have particular destruction circuits.

• The UV lamp will produce some ozone gas by the reaction of UV with the dioxygen from the air. As a consequence, the UV lamp should also be placed in a chemical hood.

III. Preparation of reagents common to both techniques

A. Materials

• Glass coverslip no 1 (Knittek glass, Germany)

• Ethanol

• Silane solution (3-(Trimethoxysilyl)propyl methacrylate, M6514, Sigma, USA)

• pLL-PEG as powder (PLL20K-G35-PEG2K, JenKem Technology, USA)

• HEPES (HN 77.5, Carl Roth, Germany)

• Parafilm

• Ice

• Acrylamide solution (01697, Fluka Analytical, USA)

• N,N',methylenebisacrylamide solution (66675, Fluka Analytical, USA)

• TEMED (N,N,N',N'-Tetramethylethylenediamine, T9281, Sigma, USA)

• Ammonium persulfate (APS) (A3678, Sigma, USA)

• Water milliQ

• Filter 0.222 μm pore size (SLGP033RS, Millex, IRL)

• Acetic acid

B. Equipment

• pH meter

• Plasma cleaner

• Beaker

• Oven

• Your favorite metallic tweezers to handle glass coverslip

• Upright fluorescence microscope

C. Methods

1. Coverslip silanization

- This glass treatment is necessary to ensure a good attachment between the PAA gel and the underlying coverslip.
- As silane solutions are very toxic, as many steps as possible of this process should be performed under a chemical hood with appropriate user protection, at least the silane solution should not leave the hood outside of a hermetically closed container.
- Start the oven at 120°C and let it warm up.
- Warm up the pump of the plasma cleaner for few minutes (according to manufacturer's instruction)
- In a 500 mL beaker, prepare a solution of ethanol containing 2% (v/v) 3-(trimethoxysilyl)propyl methacrylate and 1% (v/v) acetic acid (silanization solution)
- Put the glass coverslips in your plasma cleaner either horizontally or in a specific holder that will allow both sides of coverslips to be in contact with the ionized gaz during the plasma treatment.
- Start pumping out the air in the reactor and wait for the pressure to stabilize (2 min)
- Open the oxygen inlet, set the gaz flow to 5 mL/min (sscm) and wait 2 min for the pressure to stabilize (if you can control the pressure on your device, set it to 1 Torr = 133 Pa)
- Run the plasma for 3 min at 100 W
- Close the gas inlet, stop pumping and ventilate the reactor (a filter should be placed on the air inlet to avoid dust intake into the reactor)
- If the coverslips were horizontal in the reactor, flip them and repeat the plasma process (vacuum-oxygen-plasma)
- Soak the coverslips in the silanization solution one by one for 10 min altogether in the solution, shake occasionally
- Discard solution
- Rinse once with ethanol in the same beaker and then remove them from the ethanol one by one with a tweezers (while others staying in the ethanol) and rinse once again in another beaker of ethanol (keep holding the coverslip with the tweezers) and finally blow off the ethanol carefully using pistol airflow and place them on the oven plate
- Cure for 1 hour at 120°C

• Blow off dust with pistol airflow and store at room temperature. This treatment is quite stable over few weeks so you can do many coverslips at the same time to avoid always repeating this fastidious time consuming process.

2. pLL-PEG solution preparation

• This solution will be used for the passivation of coverslips before UV insolation and protein coating to avoid unspecific adsorption of protein outside of the insolated area.

• pLL-PEG is usually received as powder and should be stored under protective atmosphere (Argon) if possible, at -20°C. The final concentration we want to achieve is 0.1 mg/mL. Since the powder is usually made of grains that weigh a few mg each, we first produce 1 mg/mL solution that is aliquoted and stored at -20°C. The final solution will be diluted from stock.

• Prepare HEPES 10 mM from powder and milliQ water.

• Equilibrate the pH of the HEPES solution to 7.4 using NaOH

• Weigh the pLL-PEG and add corresponding HEPES volume to reach a final concentration of 1mg/mL. Then filter the solution using a syringe and a filter of 0.22 μm mesh size. Aliquot the solution and store a -20°C

• When needed, thaw an aliquot and dilute it 10 times in HEPES solution to achieve at 0.1 mg/mL pLL-PEG concentration. The pLL-PEG solution should be then stored at 4°C and used within few days

3. Preparation of acrylamide solution and polymerization reagent

• Again, as acrylamide is carcinogenic, handle it with care under chemical hood and using proper user protection

• Gel stiffness from a given acrylamide/bis-acrylamide ratio was reproducible in our hands but the stiffness measured using AFM for a given acry/bis-acrylamide ratio was very different from those reported by others, so we highly recommend to verify the actual stiffness of the gel in your own experimental conditions. As a starting point, one can use the table from ((Tse and Engler, 2001)) which covers a wide range of stiffnesses.

• Mix acrylamide and bis-acrylamide solution in water to obtain the desired concentration

• This solution can be stored for few weeks at 4°C

• TEMED solution was used as received without further preparation

• APS solution was prepared from powder in water milliQ at a concentration of 10% w/w and immediately frozen in small 10 uL aliquots and stored at -20°C

• Since APS is not very stable, one aliquot was used for each experiment and the remaining solution was systematically discarded

IV. Acrylamide patterning from UV glass patterning ("glass method")

A. Materials

• Extracellular matrix protein solution (i.e. Fibronectin solution (FF1141, Sigma, USA) and fibrinogen (FNG) Alexa Fluor 647 conjugate solution (F35200, Invitrogen, USA)

• Photomask (Toppan, France). Be careful to use a photomask compatible with deep-UV exposure. (see (Azioune et al., 2010) for more information)

• Silanized glass coverslip (see section II.C.1.)

• Glass coverslips

• pLL-PEG solution (0.1 mg/mL in HEPES 10 mM, see section II.C.2)

• Sodium bicarbonate solution 100 mM pH 8.3 (0865 AMRESCO, USA)

• Tryspin/EDTA

• Cell culture medium

• Dulbecco's Phosphate Buffered Saline (DPBS) (14190, Gibco, France)

• Cell culture dish

B. Equipment

• Deep UV lamp (UVO Cleaner Model NO.342A-220, Jelight Company, USA)

• Oxygen Plasma oven

• Vacuum mask holder (custom, SMGOP, France) (see supplementary information for a picture of the mask holder)

• Vacuum bell

C. Methods

1. pLL-PEG glass coating

• Remove dust from the glass coverslips

• Warm up the pump of the plasma cleaner for few minutes (according to manufacturer's instruction)

• Put the glass coverslips in your plasma cleaner either horizontally or in a specific holder that will allow both sides of coverslips to be in contact with the ionized gas during the plasma treatment.

• Start pumping out the air in the reactor and wait for the pressure to stabilize (2 min)

• Open the oxygen inlet, set the gas flow to 5 mL/min (sscm) and wait for the pressure to stabilize (2 min)

• Run the plasma for 15 seconds at 30 W

• Close the gas inlet, stop pumping and ventilate the reactor (a filter should be placed on the air inlet to avoid dust intake into the reactor)

• Meanwhile put a drop of pLL-PEG solution (25uL/cm2) on parafilm

• Take the coverslip with tweezers and flip it on the droplet in order to have the plasma activated side of the coverslip facing the pLL-PEG solution and let incubate for 30 min

• Afterwards, gently lift up the coverslip from the side using tweezers and put it vertically. Let the pLL-PEG run off by gravity. If needed, pipette the solution and put it back on the coverslip to help it run off the coverslip. Usually, one drop remains at the corner of the coverslip. You can remove it by gentle airflow from the other side of the coverslip in the direction of the corner.

• Store the coverslips at 4°C with nothing in contact with the treated side of the coverslip and use within 2 days

2. Deep UV insolation

• At this step, we will burn the passivized surface at specific positions by shining UV light through the chrome photomask. This will then allow us to adsorb protein at these specific positions.

• Heat up the UV lamp. This is very important. Power measurements of the lamp have shown that the steady state power is reached after 2 to 5 min (see supplementary information figure 1 for curve of the power in function of time) depending on the age of the lamp. We usually let it run for 5 min and then immediately put the sample inside the lamp and start the insolation process. The power measured at steady state was 6 mW/cm2 at a distance of one centimeter from the lamp and a wavelength of 190 nm (you should take care to control the power frequently).

• Clean the photomask. First rinse it with milliQ water, then remove the liquid carefully using nitrogen gas flow, repeat the procedure with acetone and then isopropanol.

• Remove dust from the pLL-PEG coated glass coverslips, then put them on the vacuum mask holder, treated sides facing up. You should put at least 3 coverslips to have the mask horizontal. Then put carefully the mask on top, with the chrome side facing the coverslips. Plug the mask holder to house vacuum. The mask holder has a grid etched on it that corresponds to the grid we design on the photomask to easily find the shapes we want to produce. Then, put metallic pillars on 2 sides of the grip. Put the border of the mask in contact with these pillars in order to have a proper positioning of the coverslips in front of the desired matrix of shape on the mask.

• Put the entire set up in the warmed up UV lamp with the mask a few millimeters from the UV source. Expose for 5 min

• Unplug the mask holder from the vacuum. Then carefully flip the photomask. If the contact between the mask and the coverslip was sufficient (no dust, no leaking of air from the side of the mask holder), the coverslips should stay stuck to the photomask

• Detach the coverslips from the mask using a flexible tube connected to vacuum. Then store them activated side facing up at 4°C and use within few days.

3. Protein coating and transfer on acrylamide gel

• The protein coating and the transfer on acrylamide gel should be performed in succession because otherwise the transfer is not as efficient. Here we will attach the ECM protein at the UV activated sites on the glass coverslips and then transfer this protein on acrylamide gel by polymerization in contact.

• Prepare protein coating solution: we use a solution of 20 μg/mL of fibronectin diluted in sodium bicarbonate 100 mM. A small amount of fluorescently labeled protein could be added in order to see the micropatterns by fluorescence microscopy (typically 2μg/mL of FNG-Alexa 647). Store the solution on ice.

• Rinse once the insolated side of the pLL-PEG coated coverslip with sodium bicarbonate and let the solution run of by putting the coverslip vertically. If some solution remains on the other side, it is not a problem.

• Put a droplet of protein solution on parafilm (25uL/cm2) and then put the pLL-PEG-UV-insolated side of the coverslip on the droplet. Protect from light and let it incubate for 30 min

• In the meantime, aliquot the desired amount of acrylamide solution and allow it to degas in a vacuum bell

• At the end of the incubation, put the glass vertically and let it dry. Then rinse 3 times with PBS

• If you have used fluorescently labeled protein, check the quality of the procedure with fluorescence microscopy

4. Transfer on acrylamide gel

• Here we will polymerize the acrylamide gel sandwiched between the patterned coverslip and the silanized coverslip. During detachment, the gel will stay attached to the silanized coverslip and the protein from the patterned coverslip will be transferred to the free surface of the acrylamide gel, resulting in a micropatterned acrylamide surface.

• If possible, one should use a silanized coverslip and patterned coverslips of two different sizes because it will then be much easier to detach them from each other.

• Put the larger of the 2 coverslips on a parafilm with the side of interest facing up. If both are of the same size, put a small drop of water on the parafilm and cover it with the patterned coverslip with the side of interest facing up. The small drop of water will prevent the acrylamide solution from sliding under the patterned coverslip.

• Collect the acrylamide solution from the vacuum bell and keep the container closed.

• Optional: If you want to add some fluorescent beads to your gel for force measurements, they should be added at this stage of the process in the acrylamide solution and the solution should be sonicated for 5 min to destroy any bead aggregates that could have formed during storage.

• Prepare TEMED, APS and other coverslips. You will add TEMED and APS solution the acrylamide with the following proportions 1 µL of TEMED and 1 µL of APS 10% for 165 µL of acrylamide solution. You should proceed as fast as possible in the next steps.

• Add TEMED to the acrylamide solution, mix briefly but vigorously

• Add APS solution to the acrylamide solution, mix briefly but vigorously

• Put a drop of 7 µL/cm2 of the acrylamide polymerization mix on each glass coverslip previously placed on parafilm

• Slowly place the other coverslip of interest on top while taking care to avoid bubbles.

• Put a cap (to prevent evaporation) and let the gel polymerize for 30 minutes. Keep the rest of the acrylamide in a closed container as a control of gel polymerization.

• Once the polymerization is finished (you should check it by detaching the remaining acrylamide from the tube, it should have the shape of the container and be elastic if your try to pinch it with a pipette tip), immerse the sandwiched coverslips in PBS and let the gel hydrate for 5 minutes.

• Detach the patterned glass coverslip form the acrylamide gel using a scalpel, make sure that the gel is fully immersed during the entire detachment process, otherwise you will end up with collapsed micropatterns.

• Rinse the acrylamide gel attached to silanized coverslip (acrylamide coverslips) in PBS several times

• Control quality with fluorescence microscopy if possible

• Store at 4°C and use as soon as possible.

5. Cell seeding

• Warm up your cell culture reagents as usual

• Using ethanol sterilized tweezers, transfer the acrylamide coverslip in sterile tissue culture petri dish filled with sterile PBS (gel facing up)

• Rinse once with PBS and cover with warmed medium

• In the meantime resuspend your cell in warmed medium

• Remove the medium from the petri dish and center the coverslip in the middle of the dish. This way, if convection movements of fluid tend to aggregate cell in the middle of the dish, it will be over the acrylamide gel.

• Gently cover the gel with the cell suspension (a deposition of 100 000 cells/cm2 has shown optimal cell attachment for RPE1, this should be adapted to your favorite cell line).

• Put the petri dish in the incubator

• Check the cell attachment regularly (every 30 min). When a substantial number of cells have started spreading on micropatterns, renew the medium to remove unattached cells and replace in the incubator for further spreading.

• Have a nice experiment!

V. Acrylamide patterning from patterning on quartz photomask ("mask method")

• Here the procedure relies on the same principles except that the first patterned surface is produced directly on the chrome photomask. This allows higher resolution and thus will produce much more defined structures due to the absence of diffraction issues during insolation. We will activate the chromium side of the mask, coat it with pLL-PEG to prevent unspecific protein adsorption, burn the coating by shining UV through the shapes of the photomask, coat the insolated zones with ECM protein and finally transfer these motifs by acrylamide polymerization in contact.

A. Materials

• Extracellular matrix protein solution (i.e. Fibronectin solution (FF1141, Sigma, USA) and fibrinogen (FNG) Alexa Fluor 647 conjugate solution (F35200, Invitrogen, USA)

• Photomask (Toppan, France). Be careful to use a photomask compatible with deep-UV exposure. (see (Azioune et al., 2010) for more information)

• Silanized glass coverslip (see section II.C.1.)

• Glass coverslips

• PLL-PEG solution (0.1 mg/mL in HEPES 10 mM, see section II.C.2)

• Sodium bicarbonate solution 100 mM pH 8.3 (0865 AMRESCO, USA)

- Tryspin/EDTA
- Cell culture medium
- Dulbecco's Phosphate Buffered Saline (DPBS) (14190, Gibco, France)
- Cell culture dish

B. Equipment

- Deep UV lamp (UVO Cleaner Model NO.342A-220, Jelight Company, USA)
- Oxygen Plasma oven big enough for the photomask to fit in, you can also consider cutting the mask into pieces that you can handle separately, since you don't need to use the vacuum mask holder in this case.
- Vacuum bell

C. Method

1. pLL-PEG quartz mask coating

- Remove dust from the glass coverslips and clean the photomask. First wash it with soap, then rinse it with water milliQ, then remove the liquid carefully using nitrogen gas flow.
- Put the mask (chromium side facing the air) and the coverslips in the plasma.
- Start pumping out the air in the reactor and wait for the pressure to stabilize (2 min)
- Open the oxygen inlet, set the gas flow to 5 mL/min (sscm) and wait 2 min for the pressure to stabilize (if you can control the pressure on your device, set it to 1 Torr = 133 Pa)
- Run the plasma at 100W for 3 min. This time is higher than for glass because the photomask is reused several times while glass coverslips are usually already quite clean. Exposition to successive coatings of protein makes it necessary to use a long plasma treatment to clean the mask properly.
- Close the gas inlet, stop pumping and ventilate the reactor (a filter should be placed on the air inlet to avoid dust intake into the reactor)
- Put one drop of pLL-PEG solution (25µL/cm2) on the region of interest on the mask
- Cover the drop by flipping the activated glass coverslip on it and let it incubate for 30 min.

• At the end of the incubation, lift the coverslips carefully without scratching the coating on the photomask. Put the photomask vertically and let it dry. The solution should run off by itself. If it is not the case, you can collect again the solution that has fallen down and but it back on the region of interest. This should help the drying process. As the coverslips have been coated at the same time, we will keep them for the incubation with the ECM protein; they will provide a fully passivized surface that will be used to sandwich the ECM droplet on the activated mask after UV insolation. You should rinse them once with water and let them dry. Be careful to remember which size has been coated with pLL-PEG and to prevent any damage on this side.

2. Deep UV insolation and protein coating

• At this step, we will burn the passivized surface at specific positions by shining UV light through the chrome photomask from the unpassivized side. The UV light will burn the passivized treatment directly on the mask and this will then allow us to adsorb protein at these specific positions.

• Heat up the UV lamp. This is very important. Power measurements of the lamp have shown that the steady state power is reached after 2 to 5 min depending on the age of the lamp. We usually let it run for 5 min and then immediately put the sample inside the lamp and start the insolation process. The power measured at steady state was 6 mW/cm2 at a distance of one centimeter from the lamp and a wavelength of 190 nm (you should take care to control the power frequently).

• Flip the mask to have the coated side away from the UV source. You can use small holders on the squares of the mask to prevent scratching of the coating. Expose to UV for 5 min.

• Prepare protein coating solution: we use a solution of 20 μg/mL of fibronectin diluted in sodium bicarbonate 100 mM. A small amount of fluorescently labeled protein could be added in order to see the micropatterns by fluorescence microscopy. Store the solution on ice.

• Remove the mask from the UV lamp and set it on a horizontal surface, passivized side now facing up.

• Put a droplet of protein solution (25μL/cm2) on the region of interest and then put the pLL-PEG coated coverslips (saved at step V.C.1) on the top, passivized side facing the droplet. Protect from light and let it incubate for 30 min

• In the meantime, aliquot the desired amount of acrylamide solution and put it to degas in a vacuum bell

• At the end of the incubation, remove the glass coverslips and discard them. Put the mask vertically and pour some bicarbonate solution on it to rinse. Let the solution dry by itself.

3. Transfer on acrylamide gel

• Here we will polymerize the acrylamide gel sandwiched between the patterned photomask and the silanized coverslips. During detachment, the gel will stay attached to the silanized coverslip and the protein from the patterned mask will be transferred of the free surface of the acrylamide gel, resulting in a micropatterned acrylamide surface.

• Set the photomask horizontally with the pattern side facing up. Make sure that you have waited long enough for the solution to dry

• Collect the acrylamide solution from the vacuum bell and keep the container closed

• Optional: If you want to add some fluorescent beads in your gel for force measurements, they should be added at this stage of the process in the acrylamide solution and the solution should be sonicated for 5 min to destroy any bead aggregates that could have formed during the storage.

• Prepare TEMED and APS and silanized coverslips. You will add TEMED and APS solution to the acrylamide with the following proportions 1 µL of TEMED and 1 µL of APS 10% for 165 µL of acrylamide solution. You should proceed as fast as possible in the next steps.

• Add TEMED to the acrylamide solution, briefly but vigorously mix

• Add APS solution to the acrylamide solution, briefly but vigorously mix

• Put a drop of 7 µL/cm2 of the acrylamide polymerization mix on the mask each patterned area of interest.

• Slowly place the silanized coverslip on top while taking care to avoid bubbles.

• Put a cap (to prevent evaporation) and let the gel polymerize for 30 minutes. Keep the rest of acrylamide in a closed container as a control of gel polymerization.

• Once the polymerization is finished (you should check it by detaching the remaining acrylamide from the tube, it should have the shape of the container and be elastic if your try to pinch it with the a pipette tip), cover the coverslips with PBS and let the gel hydrate for 5 min

• Detach the acrylamide gel by carefully lifting the silanized coverslip using a razor blade. Due to the silanization process, the gel will stay attached to the coverslip. Make sure that the gel is fully immersed during the entire detachment process otherwise you will end up with collapsed micropatterns.

• Rinse the acrylamide gel attached to silanized coverslip (acrylamide coverslips) in PBS several times

• Control quality with fluorescence microscope if possible

• Store at 4°C and use as soon as possible.

4. Cell seeding

• For the cell seeding, proceed as described in section IV.C.5.

VI. Discussion

A. Storage

• The best results were obtained when the gels were used immediately after production. If one wants to use a lot of gels on the same day, the "glass method" can be interrupted at the step of protein coating on the template. You can then produce many templates and store them in buffer for few days before transfer. The template should not be stored dry because it impairs the efficiency of the transfer process (Figure 3 A.). If the storage of the gel is really necessary, one should store it wet in buffer as dry storage irreversibly deforms the micropatterns and detaches part of the protein coating (Figure 3 B.).

B. Chemical modifications of protein for stronger protein adhesion to the PAA gel

• Here we have described a protocol of protein transfer on acrylamide gel that doesn't require any specific chemistry for the crosslinking of the ECM protein to the gel. Observations of the fluorescence on the template micropatterned substrate (Figure 2 A. and B.) clearly show that the proteins were efficiently transferred on the acrylamide gel and cells were stably confined for a few days but not weeks. The technique was efficiently used on PAA gels of stiffnesses from 0.5 to 30 kPa (Figure 2 C.) and used to perform traction forces experiments ((Schiller et al., 2013)).

• Interestingly, if a polystyrene coated coverslip was used for the template production, the transfer was then inefficient. The polystyrene coating has been shown to increase micropatterns stability for cell lines producing strong forces. In that case, the strength of the bond between acrylamide and the ECM protein is likely to be stronger than between ECM and glass, but weaker than between ECM and polystyrene (see (Tang et al., 2012) for a detailed description of the detachment process and critical parameters). This strength is sufficient for the cell lines we have been using (RPE1, MCF10A, Mouse fibroblasts) but it could be insufficient for other cell lines or for very long cell confinement. The passivation of the PAA could be improved by BSA incubation after micropattern production, and the stability of the micropatterns can be increased via chemical crosslinking strategies. Some groups have already put effort in this direction. (Damljanovic et al., 2005) used a reducing agent, hydrazine hydrate, to modify nonreactive amide groups in polyacrylamide to highly reactive hydrazide groups that can form covalent bonds with aldehyde or ketone groups in oxidized proteins. ECM protein were oxidized using sodium periodate.(Polio et al., 2012) dissolved NHS-ester in neutralized acrylamide solution before polymerization. NHS-groups then react with amino groups on the proteins to form covalent bonds. The rest of the gel was then passivized by BSA incubation. (Grevesse et al., 2013) replaced NHS-esters by N-hydroxyethylacrylamide monomers resulting in the presence of hydroxyl groups in the acrylamide gel that could form Hydrogen bonds with proteins. One should play around with these solutions if an improvement of the stability of the protein attachment to the acrylamide gel is required.

C. Resolution considerations

• Even though both methods seem very similar, the maximal resolution that each can achieve is not the same. The "mask method" allows for a very faithful reproduction of the shape on the mask because the UV light is burning the surface directly in front of the shapes on the photomask (Figure 1 II. and Figure 3. C.) whereas there is a small distance between the passivized coverslip and the photomask at the step of UV insolation in the "glass method". Due to diffraction of the UV light, the burned area on the coverslip will be larger and smoother than the original shape on the mask. The linescans on fluorescently labeled micropatterns suggest that sub-micrometer resolution is achieved using patterning on the photomask.

• On the other hand, if your micropatterns can suffer a little enlargement then patterning on glass will allow you to produce many coverslips much more quickly. You can treat many coverslips with pLL-PEG at the same time, then insolate them sequentially and proceed through the other steps in parallel, while the full process has to be repeated sequentially when using the mask as the template surface.

• The “glass method” might also be more suitable for sending coverslips to collaborators. Since the patterns on acrylamide should be used as soon as possible, one should consider sending UV activated glass coverslips (produced at step IV.C.2) that are more stable over time. The rest of the process (protein coating and transfer on acrylamide) doesn’t require any expensive equipment and can be performed in any lab. You could even consider buying commercially available activated glass coverslips from micropatterning companies and just proceed through the protein coating and the transfer on acrylamide, with minimal equipment requirements.

D. Comparison to other techniques

• The idea of producing micropatterns on acrylamide is not new. Several solutions have already been proposed to do this (Figure 4 and Table 1), most of them are adaptations of existing techniques for micropatterning on hard substrates.

• PDMS stencils (Figure 4.A.) allows treatment at specific regions of the gel while keeping other regions unexposed. Once the gel is protected, the usual techniques of protein PAA functionalization can be used ((Wang et al., 2002)). Due to the elastic nature of the stencil, micropatterns may vary in their shapes due to deformation. Very small features are difficult to produce using this technique. If sulfo-SANPAH and UV insolation are performed through the stencil, a local modification of the stiffness of the acrylamide is likely to be created, at the sites of micropatterns

• Microcontact printing (μCP) (Figure 4.B.) can also be performed on activated PAA ((Damljanovic et al., 2005; Versaevel et al., 2012)). A stamp covered with ECM protein is brought in contact with the activated PAA. This technique is difficult to perform on very soft gel and suffers from variability in protein transfer. Also deformation in the array of the micropatterns can occur if the PDMS is deformed at the step of stamping.

• Deep-UV patterning (Figure 4.C.) was successfully adapted to PAA patterning (()). The gel is polymerized in contact with the photomask and then activated at specific loci using deep UV exposure. Incubation with chemical crosslinkers and ECM proteins leads to the production of micropatterned PAA gel. This technique creates patterns of very defined shape and organization due to the direct polymerization of the gel on the mask. This allows the development of force measurement techniques based only on the deformation of the micropattern with no need for TFM expertise and cell detachment ((Tseng et al., 2011)). However, the use of sensitive chemical crosslinkers such as EDC introduces some variability in the protein attachment and deep-UV exposure of the gel locally modifies the stiffness of the gel.

• Transfer from micropatterned hard substrate (Figure 4.D.) relies on polymerization of the acrylamide gel in contact with a previously patterned substrate ((Rape et al., 2011; Polio et al., 2012; Tang et al., 2012)). Crosslinkers in the solution allow for the transfer of ECM protein from the initial substrate to the surface of the acrylamide gel. This procedure is very attractive for laboratories that are already using micropatterns on hard substrate because only the transfer step has to be added to their standard protocol. However, the attachment between the initial hard substrate and the ECM protein has to be weak enough to allow for the transfer of the protein to the acrylamide gel. The resolution of the micropatterns is quite good in this case. However it is less accurate than deep-UV patterning due to the limitations of the technique used for the production of the template micropatterned substrate (μCP, stencil, …).

• Transfer from patterned polyvinyl alcohol film (PVA) (Figure 4.E.) ((Yu et al., 2012)) has been developed to solve the issues of μCP such as gel deformation due to mechanical contact and pattern deformation due to sticky interaction between the stamp and the PAA gel. Again, patterns are first produced on PVA film, then the PVA is put into contact with the activated soft substrate and dissolved in PBS. Thus, no deformation of the gel is induced by stamp detachment and the patterning is more accurate. However, the elastic properties of the layer could introduce some deformations in the micropatterns as for the stencil method. This technique is very promising for the patterning of curved surface such as implants or surgical tools since the initial PVA layer is flexible.

• The method described here is combining many advantages that are found isolated in the other methods: no need for a chemical crosslinkers, easy stamp production, no modification of acrylamide substrate due to crosslinkers or UV insolation, compatible with very soft gel (>1kPa). Then one will have to choose between higher spatial resolution (“mask method”) and higher throughput or multiple protein patterning (“glass method”).

E. Future challenges and development

• The process described here allows the robust and precise production of micropatterns on acrylamide gel of various stiffness. Multiple patterning can also be performed easily by the "glass method" technique with sequential insolation and protein coating on the glass template.

• Sub-micrometer multiple patterning could be achieved using sequential laser patterning ((Doyle et al., 2009; Nakanishi et al., 2007; Kim et al., 2010)) on glass or PVA and then transfer on acrylamide gel but the "mask method" is not suitable for this purpose. This will then provide heterogeneous cell environment for cell culture experiments that is more likely to reproduce complex *in vivo* cellular environment. It allows for the study of complex processes such as asymmetric stem cell division or tissue self-organization.

• Traction force measurement based on dots micropatterns has been proposed as an alternative to fluorescent beads embedded in the acrylamide gel. ((Polio et al., 2012)). This creates a platform for force measurement that is then quite similar to micropatterned PDMS microposts ((Han et al., 2012) and Sniadecki *et al.* 2013 in this issue) including the aspects of force computation from displacements. The technique described here is perfectly suited for this purpose.

• Transfer on acrylamide from heterogeneous patterns produced on 3D substrate represents the next step in the improvement of these techniques i.e. for tissue engineering. It could provide the control of both topography and spatial localization of ECM protein. As the transfer is done using polymerization in contact with the template, the reproduction of topographical features is completely feasible ((Charest et al., 2011)). If one is able to produce micropatterns on topographical features, using laserpatterning on PDMS or polystyrene microstructures for instance, the transfer in acrylamide is then just one step ahead.

• Real time modification of the micropattern is something very challenging. This is already possible on hard substrates ((Nakanishi et al., 2007; Vignaud et al., 2012b) (Mandal et al., 2012)) but as not yet been done on acrylamide. It could be another very useful tool for cell behavior studies and tissue engineering.

• Finally, micropatterning has recently also been used for in vitro experiments ((Reymann et al., 2010)Reymann *et al.* 2013 in this issue). Patterning the nucleation of cytoskeleton proteins makes it possible to precisely study the role of boundary conditions in cytoskeleton organization with a minimal reconstituted system. Using patterning on polyacrylamide in the same way could allow for the study of the forces produced by these minimal mechanical architectures.

VII. Summary

• This chapter describes the production of micropatterns of ECM proteins on a 2D flat polyacrylamide gel. The technique is divided into two parts. First, micropatterns are produced on glass or directly on a photomask using deep UV. Then the micropatterns are transferred on acrylamide gel by polymerization of the gel directly on the template coverslip.

• This procedure is easy to perform and doesn't require any expensive equipment. It can be performed in no more than 2 hours once you get your hands on it. It combines the advantages of other existing techniques: good spatial resolution, suitable for very soft gel, no need for the use of chemical crosslinkers for attachment of the proteins to the acrylamide, no modification of the mechanical properties of the gel by the process and suitable for multiple protein patterning.

• We also discuss the storage issues of such substrates and provide a brief review of other existing techniques for micropatterning on polyacrylamide.

VIII. Acknowledgments

• We would like to thank Mithila Burute for useful discussions on the micropatterning process and manuscript editing, Ben Fogelson and Aldo Leal-Egana for careful reading of the manuscript.

IX. References

Azioune, A., N. Carpi, Q. Tseng, M. Théry, and M. Piel. 2010. Protein micropatterns: A direct printing protocol using deep UVs. *Methods Cell Biol.* 97:133–146. doi:10.1016/S0091-679X(10)97008-8.

Charest, J.M., J.P. Califano, S.P. Carey, and C.A. Reinhart-King. 2011. Fabrication of Substrates with Defined Mechanical Properties and Topographical Features for the Study of Cell Migration. *Macromol. Biosci.* 12:12–20. doi:10.1002/mabi.201100264.

Damljanovic, V., B. Christoffer Lagerholm, and K. Jacobson. 2005. Bulk and micropatterned conjugation of extracellular matrix proteins to characterized polyacrylamide substrates for cell mechanotransduction assays. *Biotech.* 39:847–851. doi:10.2144/000112026.

de Rooij, J., A. Kerstens, G. Danuser, M.A. Schwartz, and C.M. Waterman-Storer. 2005. Integrin-dependent actomyosin contraction regulates epithelial cell scattering. *J. Cell Biol.* 171:153–164. doi:10.1083/jcb.200506152.

Doyle, A.D., F.W. Wang, K. Matsumoto, and K.M. Yamada. 2009. One-dimensional topography underlies three-dimensional fibrillar cell migration. *J. Cell Biol.* 184:481–490. doi:10.1073/pnas.0604460103.

Engler, A.J., S. Sen, H.L. Sweeney, and D.E. Discher. 2006. Matrix elasticity directs stem cell lineage specification. *Cell*. 126:677–689. doi:10.1016/j.cell.2006.06.044.

Grevesse, T., M. Versaevel, G. Circelli, S. Desprez, and S. Gabriele. 2013. A simple route to functionalize polyacrylamide hydrogels for the independent tuning of mechanotransduction cues. *Lab Chip*. 13:777–780. doi:10.1039/c2lc41168g.

Han, S.J., K.S. Bielawski, L.H. Ting, M.L. Rodriguez, and N.J. Sniadecki. 2012. Decoupling substrate stiffness, spread area, and micropost density: a close spatial relationship between traction forces and focal adhesions. *Biophys. J.* 103:640–648. doi:10.1016/j.bpj.2012.07.023.

Kim, M., J.-C. Choi, H.-R. Jung, J.S. Katz, M.-G. Kim, and J. Doh. 2010. Addressable micropatterning of multiple proteins and cells by microscope projection photolithography based on a protein friendly photoresist. *Langmuir*. 26:12112–12118. doi:10.1021/la1014253.

Klein, E.A., L. Yin, D. Kothapalli, P. Castagnino, F.J. Byfield, T. Xu, I. Levental, E. Hawthorne, P.A. Janmey, and R.K. Assoian. 2009. Cell-cycle control by physiological matrix elasticity and in vivo tissue stiffening. *Curr. Biol.* 19:1511–1518. doi:10.1016/j.cub.2009.07.069.

Mandal, K., M. Balland, and L. Bureau. 2012. Thermoresponsive micropatterned substrates for single cell studies. *PLoS ONE*. 7:e37548. doi:10.1371/journal.pone.0037548.g001.

Nakanishi, J., Y. Kikuchi, S. Inoue, K. Yamaguchi, T. Takarada, and M. Maeda. 2007. Spatiotemporal Control of Migration of Single Cells on a Photoactivatable Cell Microarray. *J. Am. Chem. Soc.* 129:6694–6695. doi:10.1021/ja070294p.

Pelham, R.J., and Y.L. Wang. 1997. Cell locomotion and focal adhesions are regulated by substrate flexibility. *Proc. Natl. Acad. Sci. U.S.A.* 94:13661–13665.

Pitaval, A., Q. Tseng, M. Bornens, and M. Thery. 2010. Cell shape and contractility regulate ciliogenesis in cell cycle-arrested cells. *J. Cell Biol.* 191:303–312. doi:10.1083/jcb.201004003.dv.

Polio, S.R., K.E. Rothenberg, D. Stamenović, and M.L. Smith. 2012. A micropatterning and image processing approach to simplify measurement of cellular traction forces. *Acta Biomaterialia*. 8:82–88. doi:10.1016/j.actbio.2011.08.013.

Prager-Khoutorsky, M., A. Lichtenstein, R. Krishnan, K. Rajendran, A. Mayo, Z. Kam, B. Geiger, and A.D. Bershadsky. 2011. Fibroblast polarization is a matrix-rigidity-dependent process controlled by focal adhesion mechanosensing. *Nat. Cell Biol.* 13:1–10. doi:10.1038/ncb2370.

Rape, A.D., W.-H. Guo, and Y.-L. Wang. 2011. The regulation of traction force in relation to cell shape and focal adhesions. *Biomaterials*. 32:2043–2051. doi:10.1016/j.biomaterials.2010.11.044.

Reymann, A.-C., J.-L. Martiel, T. Cambier, L. Blanchoin, R. Boujemaa-Paterski, and M. Théry. 2010. Nucleation geometry governs ordered actin networks structures. *Nature Materials*. 9:827–832. doi:10.1038/nmat2855.

Schiller, H.B., M.-R. Hermann, J. Polleux, T. Vignaud, S. Zanivan, C.C. Friedel, Z. Sun, A. Raducanu, K.-E. Gottschalk, M. Théry, M. Mann, and R. Fässler. 2013. β1- and αv-class integrins cooperate to regulate myosin II during rigidity sensing of fibronectin-based microenvironments. *Nat. Cell Biol.*

15:625–636. doi:10.1038/ncb2747.

Storm, C., J.J. Pastore, F.C. MacKintosh, T.C. Lubensky, and P.A. Janmey. 2005. Nonlinear elasticity in biological gels. *Nature*. 435:191–194. doi:10.1038/nature03521.

Tang, X., M. Yakut Ali, and M.T.A. Saif. 2012. A novel technique for micro-patterning proteins and cells on polyacrylamide gels. *Soft Matter*. 8:7197. doi:10.1039/c2sm25533b.

Théry, M. 2010. Micropatterning as a tool to decipher cell morphogenesis and functions. *J. Cell. Sci.* 123:4201–4213. doi:10.1242/jcs.075150.

Tse, J.R., and A.J. Engler. 2001. Preparation of Hydrogel Substrates with Tunable Mechanical Properties. John Wiley & Sons, Inc., Hoboken, NJ, USA.

Tseng, Q., I. Wang, E. Duchemin-Pelletier, A. Azioune, N. Carpi, J. Gao, O. Filhol, M. Piel, M. Théry, and M. Balland. 2011. A new micropatterning method of soft substrates reveals that different tumorigenic signals can promote or reduce cell contraction levels. *Lab Chip*. 11:2231–2240. doi:10.1039/c0lc00641f.

Versaevel, M., T. Grevesse, and S. Gabriele. 2012. Spatial coordination between cell and nuclear shape within micropatterned endothelial cells. *Nat Commun*. 3:671. doi:10.1038/ncomms1668.

Vignaud, T., L. Blanchoin, and M. Théry. 2012a. Directed cytoskeleton self-organization. *Trends Cell Biol.* 22:671–682. doi:10.1016/j.tcb.2012.08.012.

Vignaud, T., R. Galland, Q. Tseng, L. Blanchoin, J. Colombelli, and M. Théry. 2012b. Reprogramming cell shape with laser nano-patterning. *J. Cell. Sci.* 125:2134–2140. doi:10.1242/jcs.104901.

Wang, N., E. Ostuni, G.M. Whitesides, and D.E. Ingber. 2002. Micropatterning tractional forces in living cells. *Cell Motil. Cytoskeleton*. 52:97–106. doi:10.1002/cm.10037.

WO Patent App PCT/EP2012/052,050. WO Patent App PCT/EP2012/052,050.

Yu, H., S. Xiong, C.Y. Tay, W.S. Leong, and L.P. Tan. 2012. A novel and simple microcontact printing technique for tacky, soft substrates and/or complex surfaces in soft tissue engineering. *Acta Biomaterialia*. 8:1267–1272. doi:10.1016/j.actbio.2011.09.006.

Zhang, J., W.-H. Guo, A. Rape, and Y.-L. Wang. 2013. Micropatterning cell adhesion on polyacrylamide hydrogels. *Methods Mol. Biol.* 1066:147–156. doi:10.1007/978-1-62703-604-7_13.

Figure Legends

Figure 1

Description of the procedure

Two variants of the same technique are described. One is using the transfer from micropatterns produced on glass while the other from micropatterns directly produced on the quartz photomask. This latter procedure allow for production of micropattern with sub-micrometer spatial resolution.

I. Transfer from a micropatterned glass coverslip (referred to as the "glass method")

This process consists in glass activation by plasma (a), coating with the repellent compound poly-L-lysine-PEG (pLL-PEG) (b), surface activation of the surface through a chrome photomask using deep UV (c), ECM protein adsorption on the UV-activated sites (d) leading to the production of a glass micropatterned coverslip as previously described (Azioune *et al.* (2010)). Then, a drop of PAA solution mix is sandwiched between the patterned coverslip and a silanized glass coverslip (e). After 30 min polymerization, the patterned coverslip is detached from the acrylamide gel while ECM protein remains on the gel (f). Note that due to the diffraction of the UV light at step (c), the shape of the final micropatterns is larger than the original on the photomask.

II. Transfer from micropatterns produced directly on the quartz photomask (referred to as the "mask method")

This process is the same as previously except that the initial micropatterns are now produced directly on the quartz photomask. First, the mask and a glass coverslip are activated together with plasma (a), then a pLL-PEG drop is sandwiched between the chrome side of the mask and the glass coverslip (b). After 30 minutes incubation, the glass coverslip is removed and saved for step (d) as it is now a passivated surface. The photomask is exposed to deep UV from the quartz side (c), activating the pLL-PEG at defined loci with minimum loss of resolution due to diffraction. Then again, a drop of ECM protein is sandwiched between the mask and the passivated glass coverslip and incubated for 30 minutes (d). Transfer on acrylamide is then performed as in I. (e-f).

Figure 2

Both techniques provide robust protein transfer over a wide range of PAA stiffnesses

A. Both techniques are presented in parallel. (Left) Micropatterns labelled with FN-Cy3 before transfer on acrylamide, (Middle- left) remaining fluorescence on the initial micropatterned surface after transfer on acrylamide, (Middle - right) micropatterns on acrylamide gel after detachment from the initially patterned surface. (Right) Phase contrast images of RPE1 cells 4 hours after cell seeding.

B. Linescan of ECM protein fluorescence taken along several micropatterns, showing reproducible spacing between micropatterns and robust fluorescence intensity.

C. Fluorescence pictures of micropatterns labelled with FN-Cy3 produced using both techniques on PAA gel of 0.5 (left), 1 (middle) and 30 kPa (right).

All scale bars correspond to 100 µm

Figure 3

Conservation advice and micro-pattern resolution

A. Fluorescent images of FN-Cy3 micropatterns on acrylamide gel. The template micropatterned glass coverslip was stored for 0 min (left), 7 hours in PBS (middle) or 7 hours dry (right) before acrylamide transfer.

B. Fluorescent images of FN-Cy3 micropatterns on PAA after storage of the gel for 5 days in PBS (left), 5 days dryed (middle), 5 days dryed and after 30 min rehydration in PBS (right).

C. Assessment of the spatial resolution of both techniques. Theoretical shape of the micropatterns (up left), FN-Cy3 picture of a typical micropattern produced with the "glass method" (up middle) or the "mask method" (up right). Average of 20 linescans across the central line joining the head of the dumbbell shape of the micropatterns (down, red curve for the "glass method", blue curve for the "mask method", gray area for theoretical shape of the micropattern). The widths at half fluorescence maximum (doted lines) show that the "mask method" is very precise in reproducing the theoretical shape while the "glass method" suffers from enlargement of the micropatterns shape due to UV diffraction.

All scale bars correspond to 20 µm.

Figure 4

Existing techniques of micropatterning of polyacrylamide, see part VI. D. for the description of each of them.

Table 1

Comparison of pros and cons of existing techniques

Fig 1

Experimental procedure

I. Transfer from a micropatterned glass coverslip (referred to as the «glass method»)

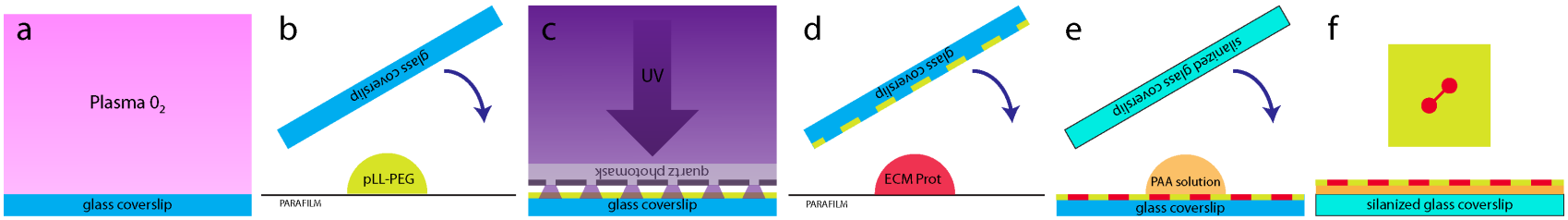

Plasma activation | PLL-PEG coating | deep UV insolation | Protein coating | Transfer on acrylamide gel

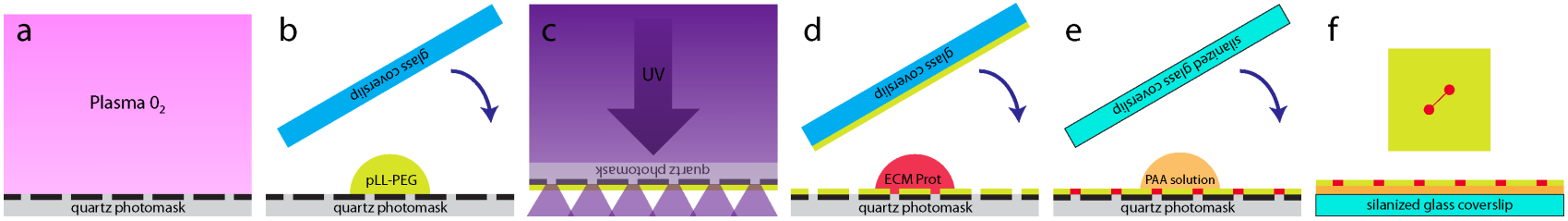

II. Transfer from micropatterns produced directly on the quartz photomask (referred to as the «mask method»)

Fig 2

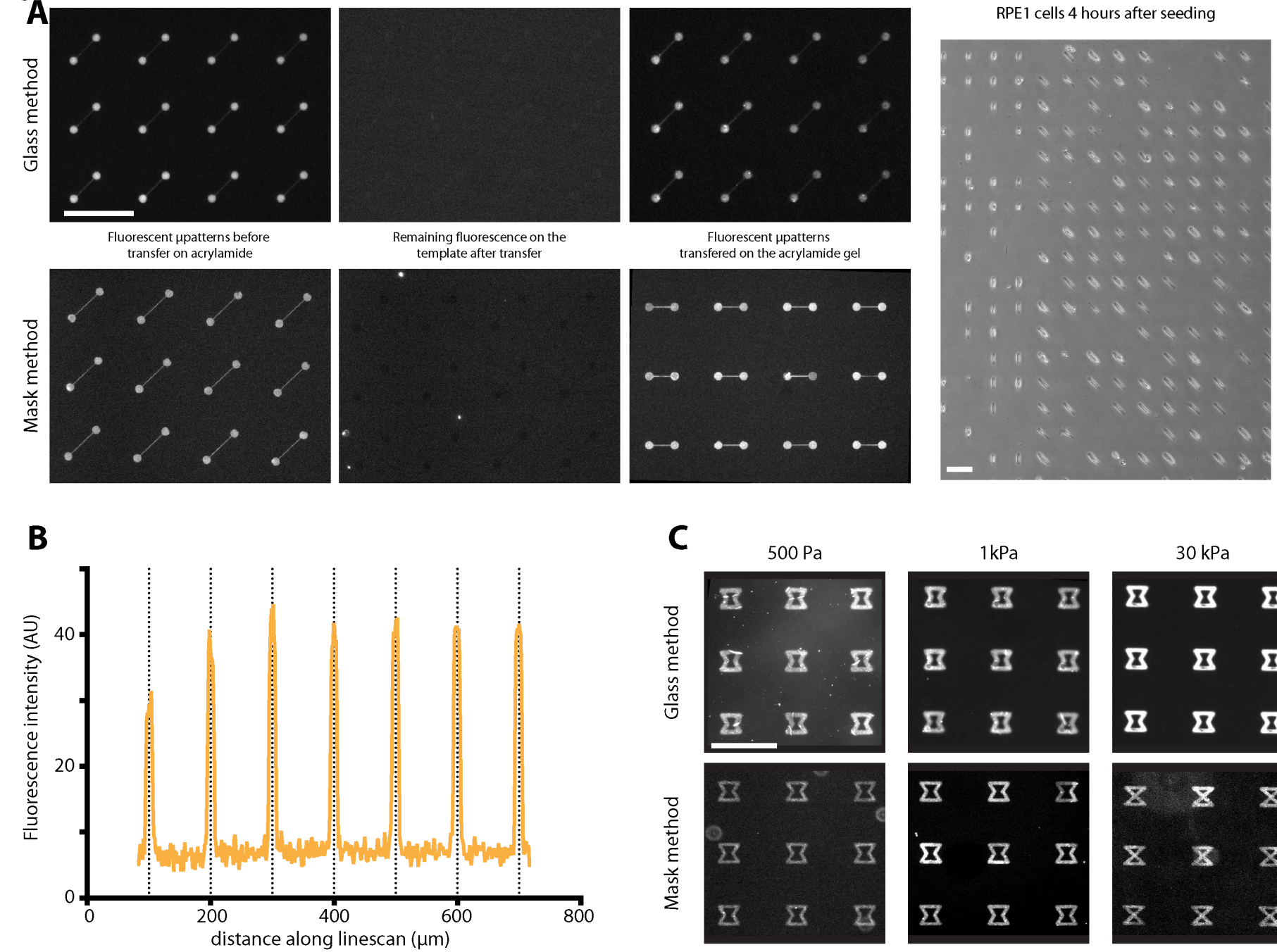
A
Glass method
Mask method
Fluorescent µpatterns before transfer on acrylamide
Remaining fluorescence on the template after transfer
Fluorescent µpatterns transfered on the acrylamide gel
RPE1 cells 4 hours after seeding
B
Fluorescence intensity (AU)
0
20
40
0
200
400
600
800
distance along linescan (µm)
C
500 Pa
1kPa
30 kPa
Glass method
Mask method

Fig 3

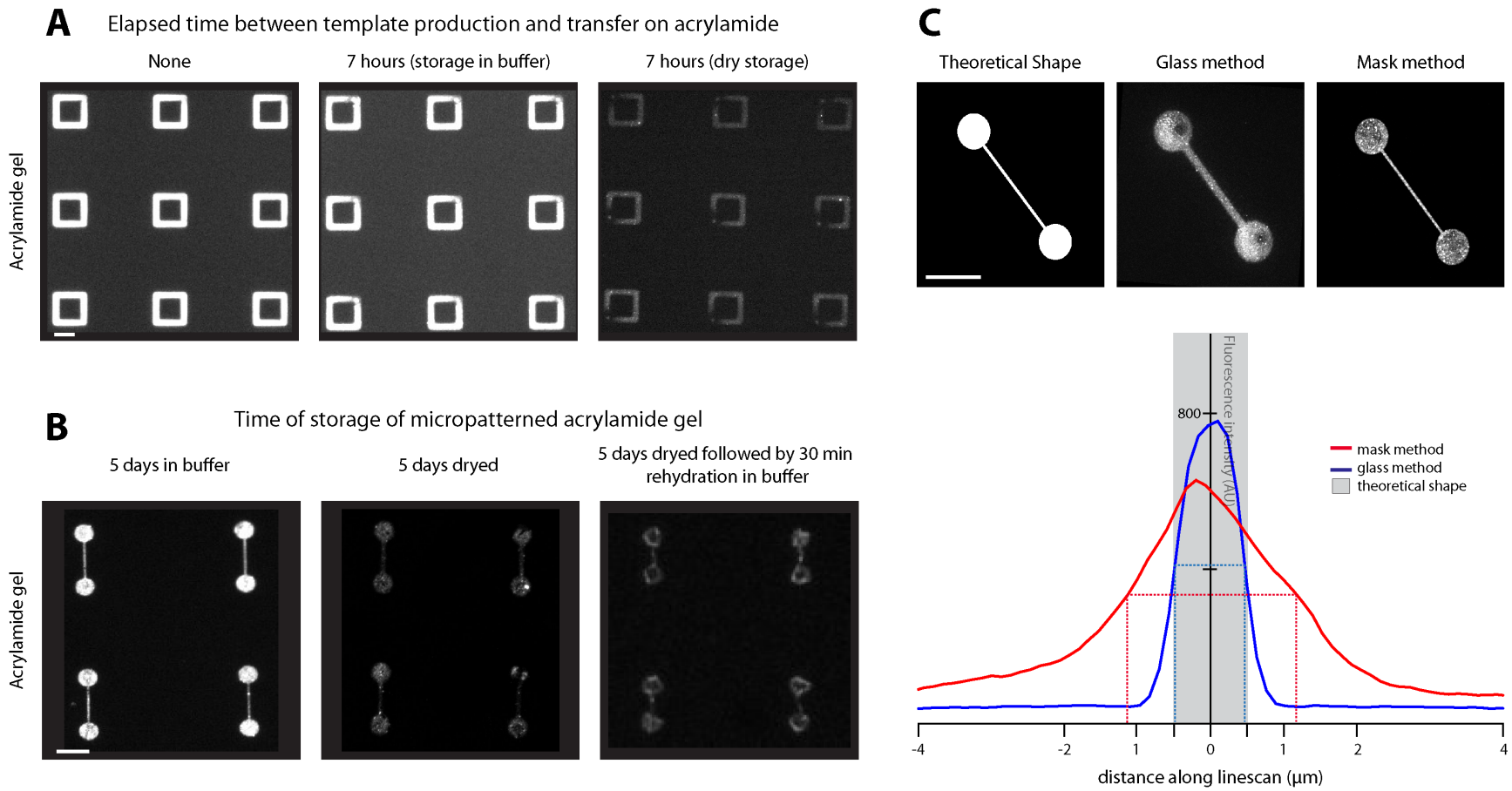
A
Elapsed time between template production and transfer on acrylamide
None
7 hours (storage in buffer)
7 hours (dry storage)
Acrylamide gel
B
Time of storage of micropatterned acrylamide gel
5 days in buffer
5 days dryed
5 days dryed followed by 30 min rehydration in buffer
Acrylamide gel
C
Theoretical Shape
Glass method
Mask method
800
Fluorescence intensity (AU)
mask method
glass method
theoretical shape
-4
-2
1
0
1
2
4
distance along linescan (µm)

Fig 4

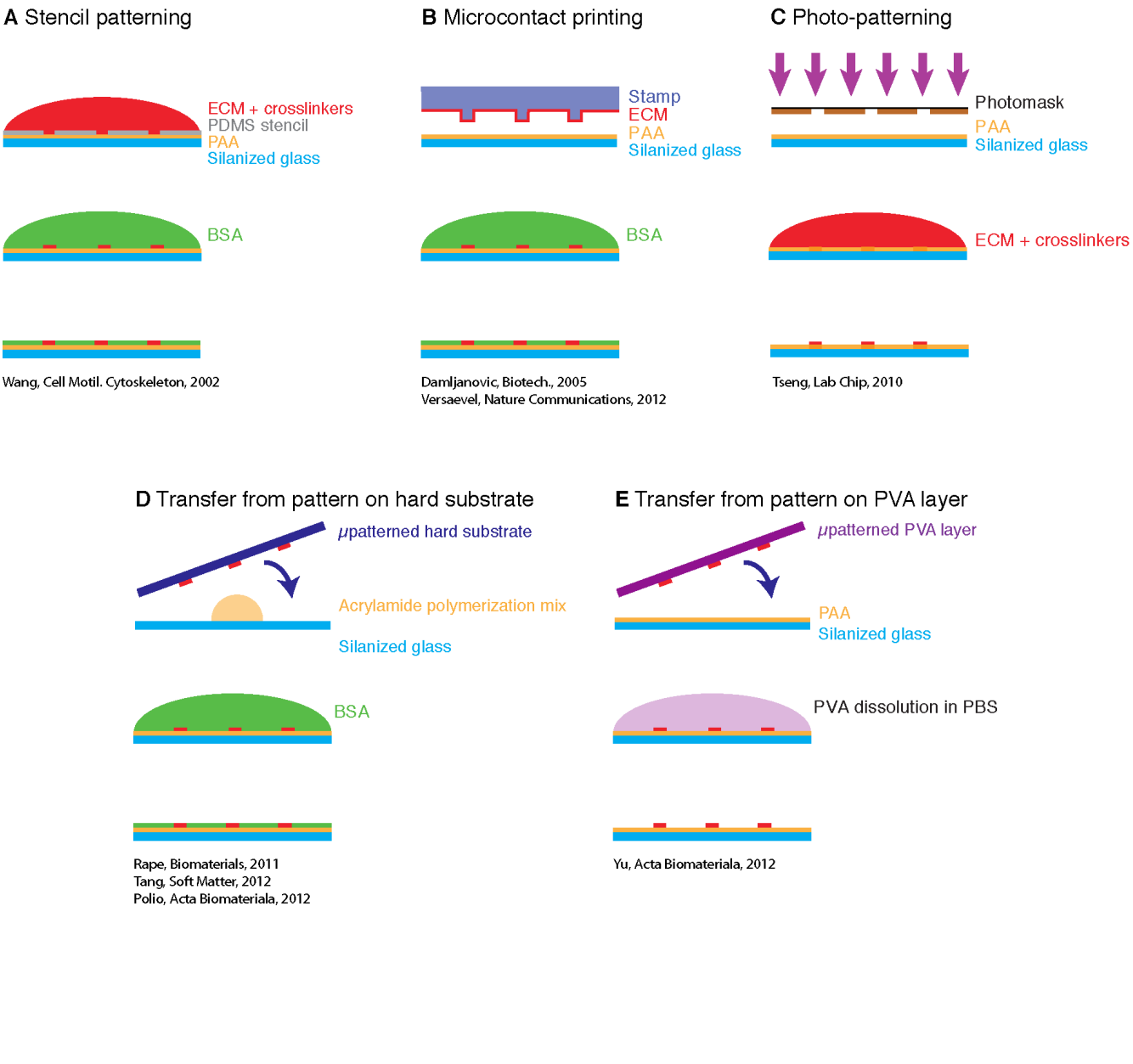
A Stencil patterning
ECM + crosslinkers
PDMS stencil
PAA
Silanized glass
BSA
Wang, Cell Motil. Cytoskeleton, 2002
B Microcontact printing
Stamp
ECM
PAA
Silanized glass
BSA
Damljanovic, Biotech., 2005
Versaevel, Nature Communications, 2012
C Photo-patterning
Photomask
PAA
Silanized glass
ECM + crosslinkers
Tseng, Lab Chip, 2010
D Transfer from pattern on hard substrate
μpatterned hard substrate
Acrylamide polymerization mix
Silanized glass
BSA
Rape, Biomaterials, 2011
Tang, Soft Matter, 2012
Polio, Acta Biomateriala, 2012
E Transfer from pattern on PVA layer
μpatterned PVA layer
PAA
Silanized glass
PVA dissolution in PBS
Yu, Acta Biomateriala, 2012

Table 1 - Pros and cons of existing techniques for acrylamide patterning

	Spatial Resolution	robust pattern shape (no elastic deformation)	Suitable for soft (<1kPa) substrate	crosslinker free procedure	unchanged μpattern stiffness	Sequential patterning
Stencil patterning	1-10 μm	-	+	-	+/-	+
Microcontact printing	1-10 μm	-	-	-	+	+
Photo-patterning	>1 μm	+	+	-	-	-
Transfer from pattern on hard substrate	1-10 μm	-	+	+/-	+	+/-
Transfer from pattern on PVA layer	1-10 μm	-	+	-	+	+
Mask Method	>1μm	+	+	+	+	-
Glass Method	1-2 μm	+	+	+	+	+

5. ASPECTS THEORIQUES DE LA MICROSCOPIE A TRACTION DE FORCES

Le principe de la microscopie à traction de forces a été décrit un peu plus haut. Je vais ici décrire ses bases théoriques. Une mise en pratique pas à pas est disponible en annexe.

La reconstruction des forces à partir de la paire d'images des billes intégrées à l'acrylamide se fait en deux étapes. La première étape va consister à déterminer le champ de déplacements des billes au sein de l'image. La deuxième étape déterminera les forces à partir de ce champ de déplacements. A chaque étape, plusieurs solutions ont été développées par différents groupes. Je ne décrirai pour ma part que la PIV (Particle Image Velocimetry) pour la détermination des déplacements et la FTTC (Fourier Transform Traction Cytometry) pour le calcul des forces correspondantes.

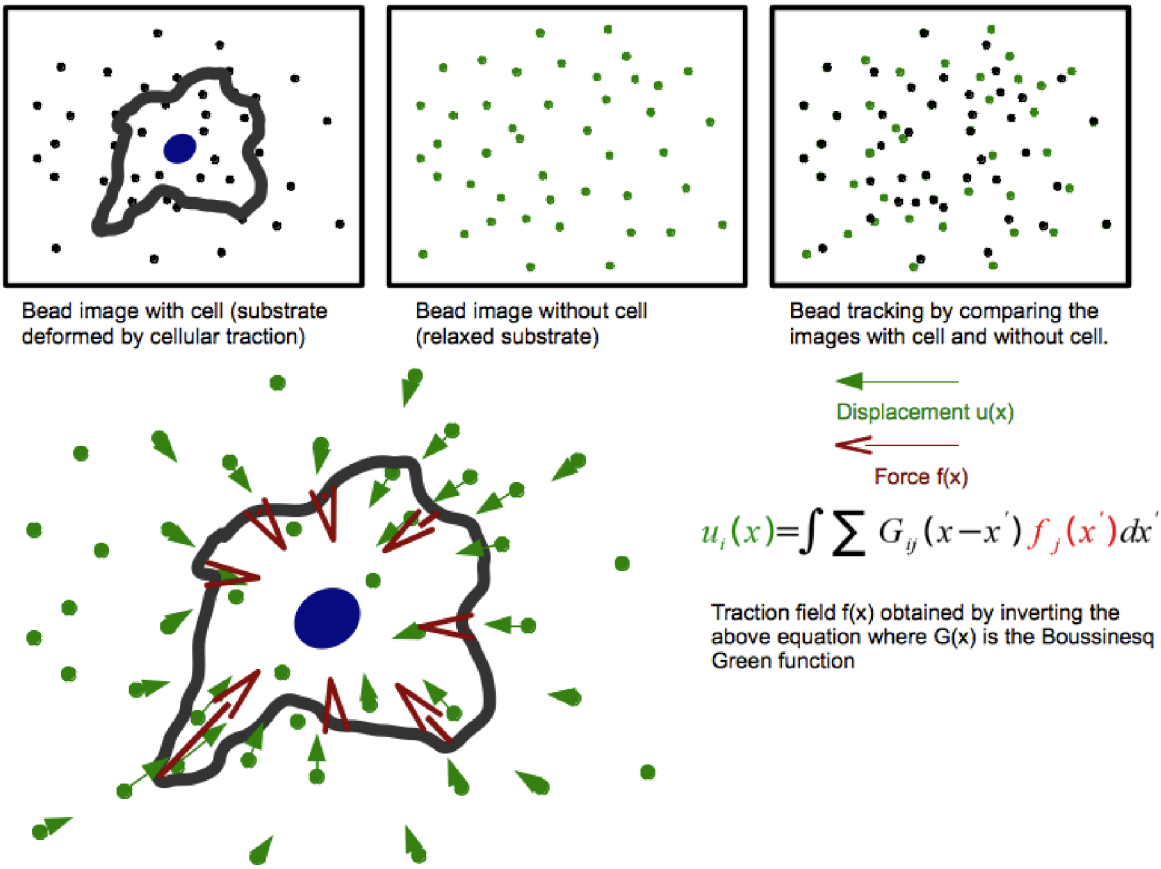

Figure 24 : Principe général de la microscopie à traction de forces

Mesure de déplacements des billes

Dans la PIV, les billes ne vont pas être suivies individuellement. La paire d'image est divisée en sous régions, appelées fenêtres d'interrogations, et le champ de déplacement est calculé par corrélation croisée entre les fenêtres se correspondant sur les deux images. La limite de cette procédure est le cas de grands déplacements. Si les billes ont trop été déplacées d'une image par rapport à l'autre, elles vont

sortir de la fenêtre d'interrogation et le déplacement ne pourra pas être établi précisément. Une solution à ce problème est l'utilisation itérative de la PIV avec des fenêtres d'interrogation de tailles décroissantes. Les premiers déplacements mesurés permettront de guider les mesures suivantes pour ne pas manquer de grands déplacements. L'utilisation d'une fenêtre de recherche plus grande que la fenêtre d'interrogation permet également de résoudre ce problème. Le logiciel tente ainsi de superposer la fenêtre d'interrogation de l'image 1 sur l'image 2 le mieux possible au sein de la fenêtre de recherche.

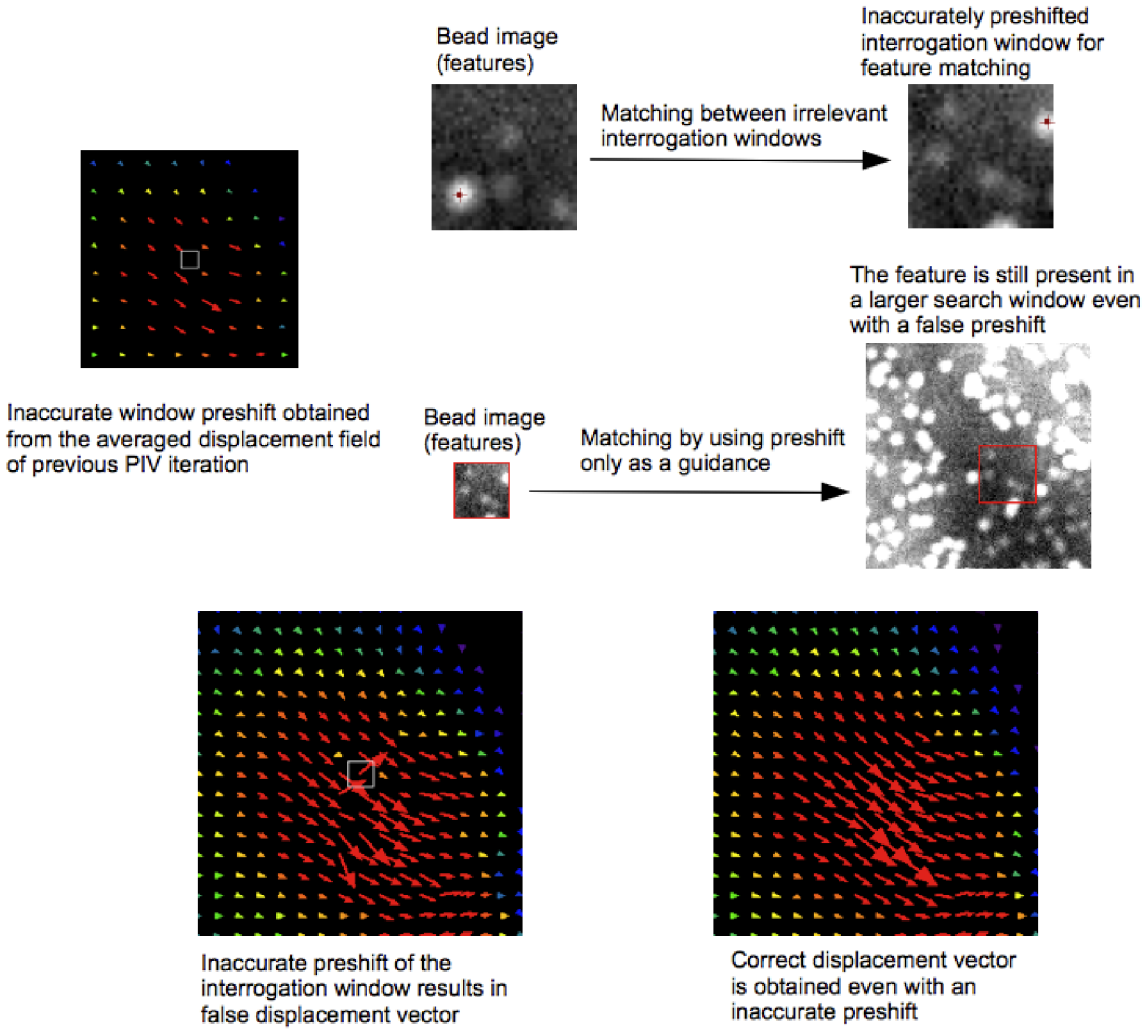

Figure 25 : Amélioration de la PIV itérative par l'utilisation d'une fenêtre de recherche

Quand la fenêtre d'interrogation devient petite, des problèmes de fausses corrélations peuvent apparaître car peu de billes sont présentes au sein de la fenêtre. Ces faux positifs vont ajouter du bruit à la mesure. Il peut être tentant de remplacer la mesure aberrante par une moyenne des mesures avoisinantes mais cela constitue une perte d'information. Dans la technique utilisée ici, le pic choisi ne l'est pas seulement sur la base de sa valeur de corrélation mais également sur sa cohérence avec le déplacement calculé à l'itération précédente (avec une fenêtre plus large). Cela permet de compenser le

bruit sans pertes d'informations

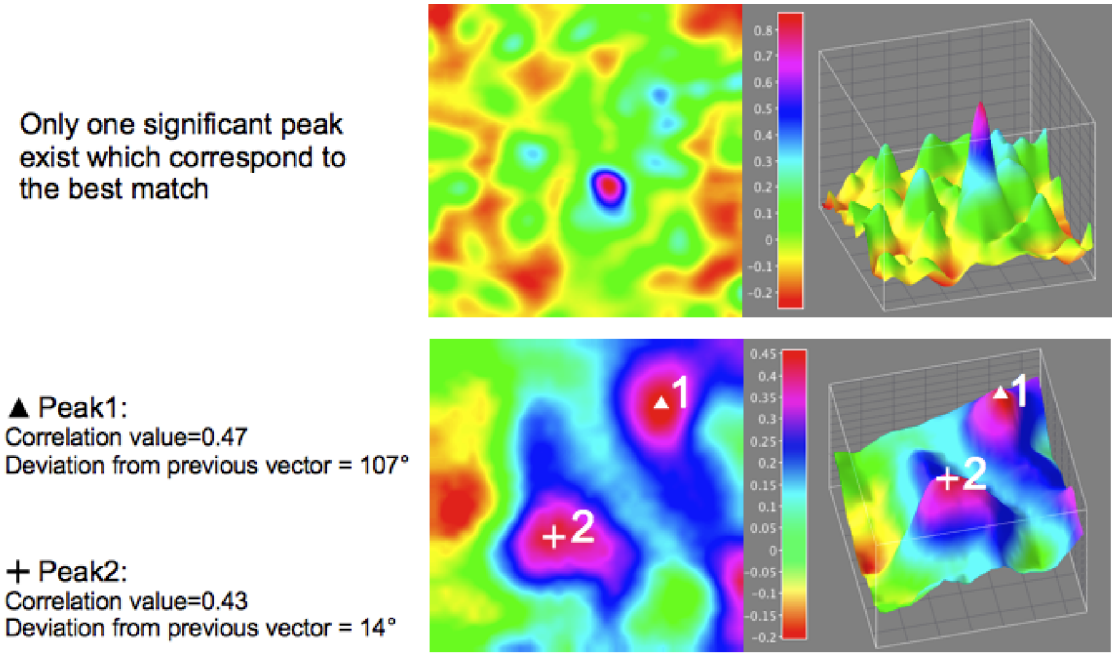

Figure 26 : Isolation du meilleur pic de corrélation sur la base de la valeur de la corrélation et du déplacement mesuré à l'itération précédente

Ces améliorations de la technique de détection ont été apportées par un précédent étudiant de l'équipe (Qingzong Tseng). Ils permettent d'obtenir des champs de déplacement moins bruités qu'avec des méthodes de PIV conventionnelles.

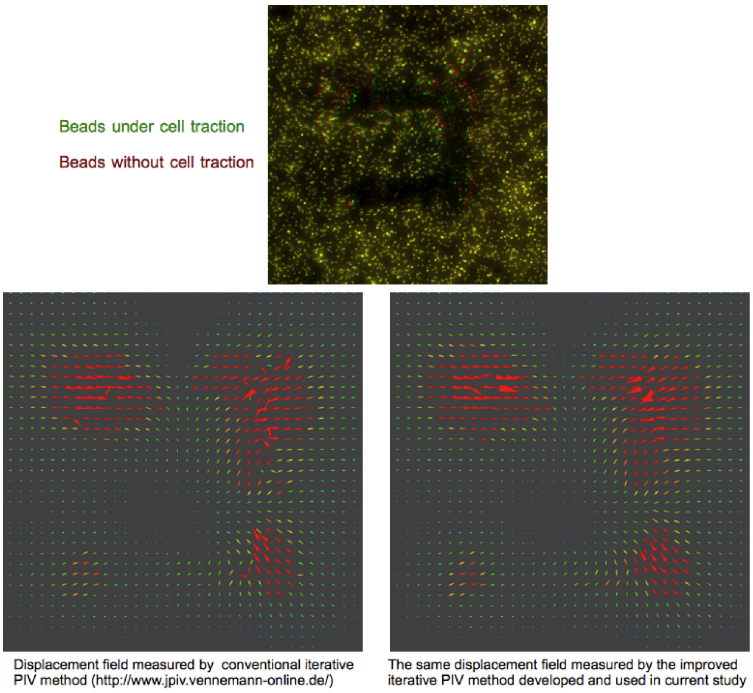

Figure 27 : Comparaison du champ de déplacement obtenu par une technique de PIV classique par rapport à la méthode de PIV améliorée

Reconstruction des forces de traction

En considérant que les déplacements sont essentiellement parallèles à la surface du gel et qu'ils sont très petits devant l'épaisseur du gel, celui-ci peut-être considéré comme un demi-espace semi infini. Les déplacements $u(x_1, x_2)$ à la surface de ce demi-espace sont décrits comme la convolution entre les forces ponctuelles $f(x_1', x_2')$et le tenseur élastique de la fonction de Green $G_{ij}(x_1 - x_1', x_2 - x_2')$, dans lequel les indices i,j prennent des valeurs de 1 à 2 en négligeant la force et le déplacement orthogonaux à la surface du gel (Equation 1). L'expression explicite de ce tenseur est la solution de Boussinesq (Landau, 2006). En conséquence, la solution du champ de force passe par la déconvolution du champ de déplacements par la fonction de Green.

$$u_i(x) = \int \sum_j G_{ij}(x - x') f_j(x') dx' \qquad (1)$$

Dans l'espace de Fourier, la convolution devient une simple multiplication et l'équation 1 peut-être réinterprétée pour donner l'équation 2, dans laquelle l'indice k représente le mode dans le domaine de fréquences

$$\tilde{u}_{ik} = \left\{\sum_j \tilde{G}_{ij} \tilde{f}_j\right\}_k \qquad (2)$$

$\tilde{f}$ est le champ de forces dans l'espace de Fourier, $\tilde{u}$ est le champ de déplacement dans l'espace de Fourier et $\tilde{G}$ est la fonction de Green dans l'espace de Fourier, exprimée de la façon suivante :

$$\tilde{G}_k = \frac{2(1+\mathcal{V})}{Ek^3} \begin{pmatrix} (1+\mathcal{V})k^3 + \mathcal{V}k_y^2 & -\mathcal{V}k_x k_y \\ -\mathcal{V}k_x k_y & (1-\mathcal{V})k^3 + \mathcal{V}k_x^2 \end{pmatrix} \qquad (3)$$

E est le module d'Young élastique du gel, $\mathcal{V}$ le coefficient de poisson, et k le vecteur d'onde correspondant dans l'espace de Fourier.

Le champ de traction peut à présent être calculé dans l'espace de Fourier, $\tilde{G}_{ij}^{-1}$ témoigne de l'inversion du tenseur de Green.

$$\tilde{f}_{ik} = \left\{\sum_j \tilde{G}_{ij}^{-1} \tilde{u}_j\right\}_k \qquad (4)$$

En accord avec Sabass et al., un schéma de régularisation peut être mis en place selon l'équation suivante pour permettre une reconstruction des forces efficace et fiable (équation 5)

$$\tilde{f}_{ik} = \left\{\sum_{l,j} \left[\sum_m \tilde{G}_{ml} \tilde{G}_{mi} + \lambda^2 I\right]^{-1} \tilde{G}_{jl}^{-1} \tilde{u}_j\right\}_k \qquad (5)$$

Comme nous pouvons le voir dans les équations ci-dessus, la difficulté principale du calcul des forces est le manque d'information sur leur localisation. A moins de considérer que les adhésions sont le point d'application des forces (Balaban, Nat. Cell Biol., 2001), d'autres stratégies sont requises. En l'absence de ces hypothèses fortes, le champ de force est estimé à partir d'un maillage régulier des forces (FTTC). L'ensemble de ces procédures est librement téléchargeable sous la forme de plugins ImageJ disponibles à l'adresse suivante : https://sites.google.com/site/qingzongtseng/tfm

III. Contacts focaux : l'union fait la force

1. REPROGRAMMATION DE LA FORME DE LA CELLULE PAR NANO-PATTERNING LASER (ARTICLE)

A. INTRODUCTION

L'article de revue (I-5) nous a permis de mettre en évidence le rôle primordial du contrôle de l'environnement adhésif, notamment la forme d'un micropattern, dans l'organisation de la cellule. Néanmoins, ces méthodes sont limitées par la forme définitive du micropattern. Au sein de nos tissus au contraire, l'environnement est en perpétuel renouvellement. Il serait donc extrêmement utile de pouvoir modifier ce micropattern en temps réel et ainsi observer de façon répétée une transition d'un état « A » vers un état « B » et d'observer les mécanismes nécessaires à cette transition. Différents groupes ont déjà proposés des solutions innovantes à ce sujet. L'objet de mon travail a été la mise en œuvre d'une telle technique en utilisant un laser UV pulsé.

B. ARTICLE

Reprogramming cell shape with laser nano-patterning

Timothée Vignaud[1], Rémi Galland[1], Qingzong Tseng[1], Laurent Blanchoin[1], Julien Colombelli[2,*] and Manuel Théry[1,*]

[1]Laboratoire de Physiologie Cellulaire et Végétale, Institut de Recherche en Technologies et Sciences pour le Vivant, CNRS/UJF/INRA/CEA, 17 rue des Martyrs, 38054 Grenoble, France
[2]Advanced Digital Microscopy, Institute for Research in Biomedicine, Baldiri Reixac 10, E-08028 Barcelona, Spain
*Author for correspondence (julien.colombelli@irbbarcelona.org; manuel.thery@cea.fr)

Accepted 10 January 2012
Journal of Cell Science 125, 2134–2140

doi: 10.1242/jcs.104901

Summary

Cell shape in vitro can be directed by geometrically defined micropatterned adhesion substrates. However conventional methods are limited by the fixed micropattern design, which cannot recapitulate the dynamic changes of the cell microenvironment. Here, we manipulate the shape of living cells in real time by using a tightly focused pulsed laser to introduce additional geometrically defined adhesion sites. The sub-micrometer resolution of the laser patterning allowed us to identify the critical distances between cell adhesion sites required for cell shape extension and contraction. This easy-to-handle method allows the precise control of specific actin-based structures that regulate cell architecture. Actin filament bundles or branched meshworks were induced, displaced or removed in response to specific dynamic modifications of the cell adhesion pattern. Isotropic branched actin meshworks could be forced to assemble new stress fibers locally and polarised in response to specific geometrical cues.

Key words: Actin cytoskeleton, Cell adhesion, Cell architecture, Live patterning, Micropattern

Introduction

The control of cell shape in vitro by the use of different designs of micropatterned substrates has been a useful tool to investigate the fundamental rules of morphogenesis (Théry, 2010). This method has revealed that in addition to shape, cell behavior is also sensitive to the spatial distribution of its extracellular adhesions. The cell adhesion pattern has notably been shown to regulate cell architecture (Brock et al., 2003; Parker et al., 2002; Rossier et al., 2010; Théry et al., 2006a), polarity (Desai et al., 2009; James et al., 2008; Lombardi et al., 2011; Pitaval et al., 2010), migration (Doyle et al., 2009; Pouthas et al., 2008), division (Fink et al., 2011; Samora et al., 2011; Théry et al., 2007) and differentiation (Dupont et al., 2011; Kilian et al., 2010; McBeath et al., 2004).

The dynamics of cellular responses to changes in the microenvironment is a fundamental property of living systems that ensures the functional and mechanical coherence of tissues during development or renewal (Lu et al., 2011). However, the manipulation of changes in the microenvironment in vitro is limited in conventional surface micropatterning methods because the design of the micropattern is fixed at the point of fabrication. Hence, cellular responses to the geometry of these micropatterns can only be observed at steady state; whereas cellular responses in real time to changes in the microenvironment cannot be measured. This has been a major limitation to the experimental investigation of the dynamic processes that support cell and tissue morphogenesis.

Several approaches have been used to overcome this limitation and alter the adhesive environment surrounding the micropatterns on which living cells are attached (Nakanishi et al., 2008). Electric potential has been used to detach cell-repellent coatings, either by detaching micropatterned electroactive groups (Raghavan et al., 2010) or by desorbing coatings on electrodes (Gabi et al., 2010; Kaji et al., 2006), thereby allowing constrained multicellular groups of cells on large micropatterns to specifically invade the activated regions. The minimum size of these regions was about 10 μm (Gabi et al., 2010). Alternatively, cell-repellent moieties have been chemically linked to the silane coating by photo-cleavable groups so that they are released in response to UV light. Similarly, loss of the cell-repellent coating could promote the local attachment of cells in suspension (Kikuchi et al., 2008b), trigger cell migration (Nakanishi et al., 2007) or promote the invasion of new areas by multicellular groups (Kikuchi et al., 2008a). With this method, substrate exposure to UV through a photomask placed in the optical plane of a microscope allowed the addition of new adhesive regions whose size could be as small as 5 μm (Nakanishi et al., 2007).

Here, we have developed a simple method to ablate the cell-repellent properties of the polyethylene glycol (PEG) coating in the vicinity of a live single cell already attached to a micropatterned substrate. The method uses a commercially available polymer to coat the cell culture substrate (poly-L-lysine–PEG) and a pulsed UV laser to introduce additional adhesive regions. The manipulation of the adherent properties in the microenvironment of a single cell with sub-micrometer resolution enables the precise control of intracellular architecture remodeling in real time.

Results and Discussion

Laser patterning

Oxidation of a PEG layer on polystyrene (PS)-coated glass is an efficient and versatile micropatterning method to accurately define geometries that can stereotypically direct cell adhesion and cell shape. Oxidation of PEG can be achieved by deep UV

(wavelength below 200 nm) exposure through a chromium mask (Azioune et al., 2010; Azioune et al., 2009). Deep UV creates ozone that oxidizes the surface and allows protein adsorption (Mitchell et al., 2004). To create new micropatterned regions in the presence of living cells, we used a Q-switched laser producing 300 picoseconds pulses at 355 nm and a high numerical aperture objective (Fig. 1A). The accumulation of pulses of energy in a highly confined volume induced the formation of localized plasma responsible for local oxidation and further destruction of irradiated materials (Colombelli et al., 2004; Colombelli et al., 2007; Pfleging et al., 2009; Vogel et al., 2005). We modulated the number and repetition rate of laser pulses as well as the laser power to control the size of individual spots. Laser patterning was conducted in the presence of Alexa-Fluor-546-labeled fibrinogen to detect protein adsorption on exposed regions (Fig. 1A). Surface modifications were also characterized by atomic force microscopy (AFM). Hexagonal arrays of spots separated by 160 nm were made using high or low laser power. The high-power beam did not allow homogeneous fibrinogen adsorption and resulted in a honeycomb-like topography within the glass slide, as seen by AFM, with holes corresponding to laser spots (Fig. 1B). The low-power beam resulted in superficial (4 nm) removal of the poly-L-lysine–PEG and PS layers, and efficient protein adsorption (Fig. 1C). Therefore, these conditions were further adopted for live-cell patterning in the rest of the study. However, the roughness of the PS layer induced a noisy AFM signal, preventing the measurement of single laser spot width. Therefore, we decide to measure single spot size with the intermediate power beam and a smaller polystyrene surface to induce detectable surface modifications without affecting the glass coverslip. In these conditions, the size of a single spot was 300 nm in diameter (Fig. 1D). However, it should be noted that the intermediate power used in this procedure led to an overestimation of the spatial resolution. In the regular, low-power conditions used for live-cell patterning, the spot size was probably smaller.

Critical geometrical determinants

Initial cell adhesion and early spreading, when cells just contacted the substrate, depend on the micro- and nano-scale organization of adhesive ligands (Geiger et al., 2009). Integrins are transmembrane proteins connecting the ECM and the intracellular actin network. The engagement of actin filaments between individual integrins contributes to the clustering of integrins and the stimulation of membrane deformation and cell spreading. The distance between individual integrins needs to be smaller than 70 nm to allow actin filaments to connect their intracellular domains (Arnold et al., 2004). Integrin clusters must contain at least four integrin molecules within 60 nm to allow cell attachment (Schvartzman et al., 2011). The critical distance between these clusters that allows cell spreading depends on cluster size. It can be 25 μm on 9 μm^2 adhesion spots, but is reduced to 5 μm on 0.1 μm^2 spots (Lehnert et al., 2004). This suggests that, after the spreading phase, the subsequent cell

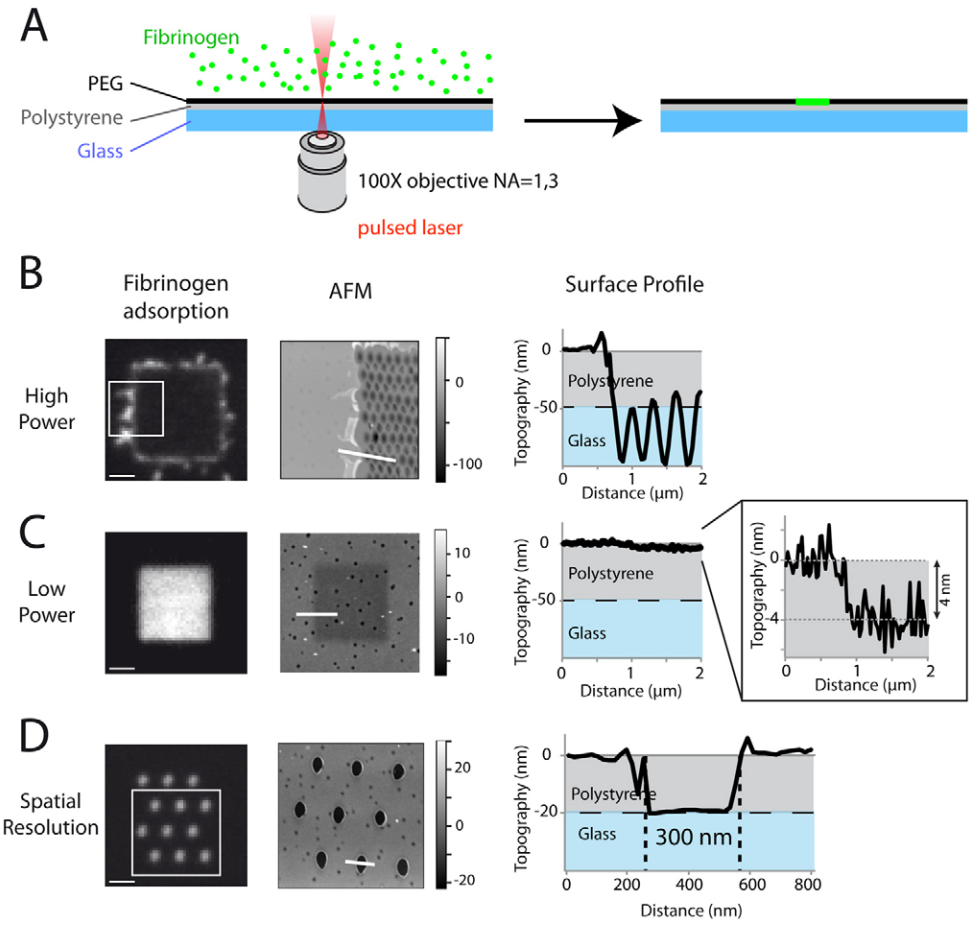

Fig. 1. Laser patterning. (**A**) Schematic representation of laser patterning. UV pulses locally remove the PEG coating and allow protein adsorption. (**B**,**C**) Arrays of spots separated by 160 nm were made using high (B) or low (C) laser beam power. (B) Fluorescence image of fibrinogen adsorption (left). High-power beam did not allow homogeneous fibrinogen adsorption and resulted in a honeycomb-like topography as seen by AFM imaging of the region within the white square depicted on the fluorescence image (middle), with holes corresponding to laser spots. The surface profile along the white line depicted in the AFM image was plotted (right). The polystyrene layer was removed and the glass coverslip was drilled. (C) Low-power beam allows fibrinogen adsorption (left) and samples exhibit little surface modification (middle). A 4 nm step was measured between non-exposed and exposed surfaces (right). (**D**) Intermediate-power beam on thin polystyrene layer allowed fibrinogen adsorption (left) and resulted in holes reaching the glass surface (middle). The size of a single spot was 300 nm in diameter (right). Scale bars: 2 μm.

extension and contraction onto the new adhesion sites could also depend on nano- and micro-scale organization of those adhesive sites.

The 300 nm width of single spots (Fig. 1D) allowed us to investigate the nano- and micro-scale dependency of the cell extension and contraction phase. RPE1 cells were first plated on micropatterns made with classical deep-UV exposure through a photomask) Azioune et al., 2010; Azioune et al., 2009). They were allowed to spread and contract until their shape adopted the convex envelope of the micropattern (Rossier et al., 2010; Théry et al., 2006a). Then, using galvanometric mirrors, the laser beam was scanned on the substrate to draw the regions to be oxidized (Fig. 2A). This scanning method was a versatile and modular way to design any kind of geometry anywhere around cells. Similar results could also be obtained by moving the sample rather than the laser beam. Local PEG oxidation allowed cells to form new adhesions and to extend on the irradiated regions. The distance between individual adhesion spots could be varied up to the formation of a contiguous adhesive line (Fig. 2A). Hence, this allowed us to identify the critical geometrical parameters

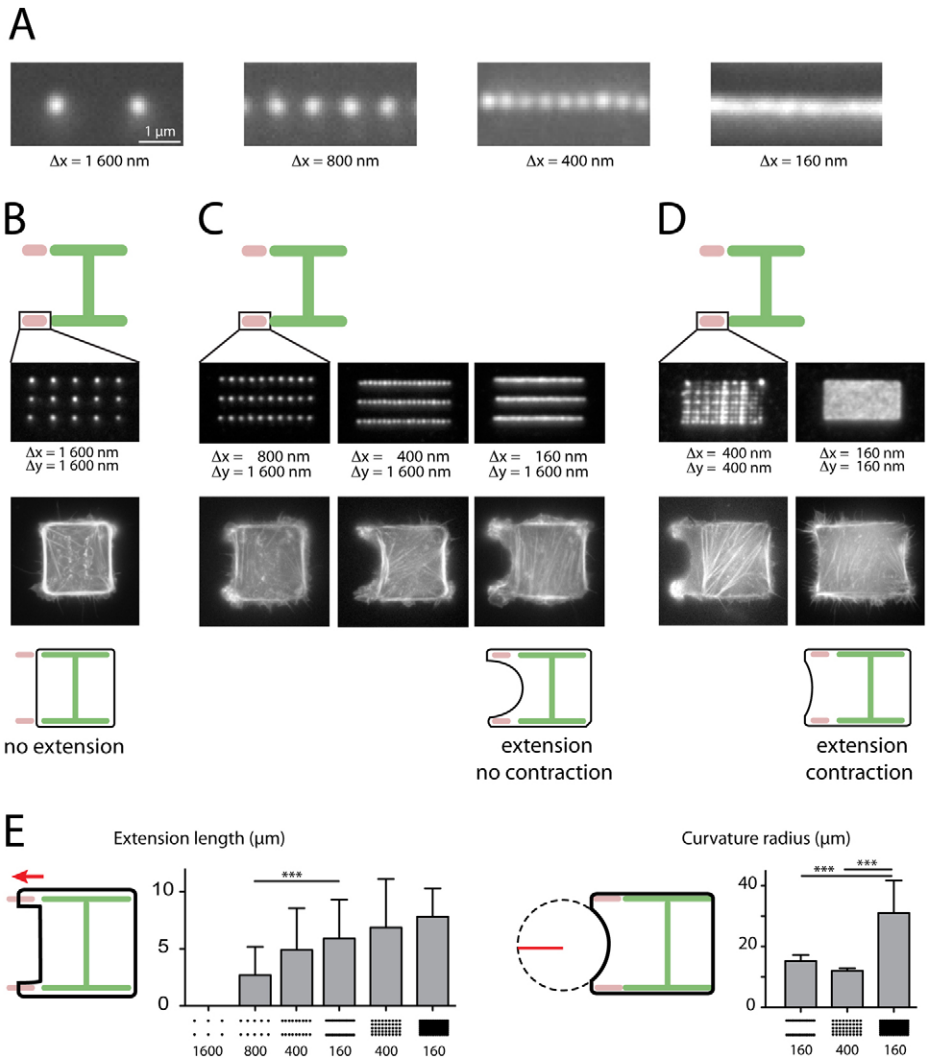

Fig. 2. Nano- and microscale characteristics for cell extension and contraction. (**A**) Each spot corresponds to exposure of PEG-coated polystyrene to 12 pulses for 20 mseconds in the presence of fibrinogen–Alexa-Fluor-546. Fibrinogen was immediately bound to the exposed regions. Drawing regions of interest in imaging software controlled displacements of galvanometric mirrors and laser positioning. Spot density along lines could be precisely controlled. (**B**–**D**) Cells were plated on H-shaped micropatterns (green) and reprogrammed using laser patterning (red). The horizontal and vertical spacing between spots were varied from 1600 to 160 nm. New patterned regions are shown in the presence of fibrinogen–Alexa-Fluor-546 for clarity (top images), but no fibrinogen was used during the experiments with cells. Images show the cells 3 hours after laser patterning. (B) Square arrays of dots with 1600 nm spacing did not allow cell extension on the newly patterned regions. (C) Newly patterned lines with a variety of spot spacing. Spots separated by 1600 nm promoted cell extension, but not cell contraction. (D) Square arrays of spots spaced at 400 nm allowed cell extension, but not cell contraction, whereas 160 nm spacing allowed both. (**E**) Mean measurement of cell extension length (n=18–20) on 10 µm laser-patterned regions corresponding to the above conditions. The number on the x-axis indicates the spot spacing (left). Mean measurement of free membrane curvature on horizontal lines with 160 nm spacing between the spots and on square arrays of spots separated by 400 nm or 160 nm (right). Measurements were performed only in cells forming full extensions on the two new patterned regions. The large curvature radius revealed a cell contraction between the new adhesive regions made of square arrays of spots separated by 160 nm. Error bars represent s.d.; statistical tests correspond to one-way ANOVA analyses. ***P<0.001.

allowing cell extension and contraction. Cells were attached to H-shaped micropatterns and adopted a square shape of about 900 μm^2. To test the requirements for the induction of a cell extension and the assembly of a new filament bundle, the two adhesive bars were extended at one side of the H with two new adhesive regions, made of parallel lines of adhesion spots. Cells did not extend on lines made of spots separated by 1600 nm (Fig. 2B). Only a few cells could initiate extension on lines made of spots separated by 800 nm. More cells extended onto these lines when the inter-spot distance was reduced to less than 400 nm (Fig. 2C,E). However, the cell extensions could not generate a substantial contraction between the new adhesive regions, as revealed by the low values of the cell edge curvature radius (Théry et al., 2006a) (Fig. 2C,E). Lines perpendicular to the longitudinal orientation of the H bar induced the same phenotypes (supplementary material Fig. S1). Interestingly, although cells could easily extend on dense square arrays of spots in which the inter-spot distance was 400 nm, they could only generate a substantial contraction between the new adhesive regions when this distance was reduced to 160 nm, i.e. when the region was almost continuously adhesive (Fig. 2D,E). These results show that RPE1 cells require the adhesion spots to be separated by less than 400 nm to stabilize the new cell extension and a continuous adhesive region to generate a substantial contraction force. Previous reports showed that mouse melanoma cells can spread on similar arrays of 300-nm-wide adhesion spots if their spacing is smaller than 5 μm (Lehnert et al., 2004). This suggests that the critical distance for extension and contraction in spread cells is one order of magnitude smaller than the critical distance for attachment and spreading.

Cell-shape reprogramming

Cell shape could be reprogrammed by adding the dense adhesive regions described above. For example, it was possible to remove the PEG from a region defined by a horizontal bar next to an apex of a triangularly-shaped cell constrained on a V shape (Fig. 3A). After this ablation, the cell also adhered to this region and adopted a square shape (Fig. 3B). Actin network reorganization during this cellular transformation was followed by monitoring Lifeact–GFP (Riedl et al., 2008). As the cell spread on the new bar, it formed many new actin cables, which connected the original and the new micropatterns. This showed that cells not only spread on to the laser-designed regions but also developed new internal cables during cell shape deformation from triangle to square (Fig. 3B). The tension in these cables was probably required to support cell shape changes (Rossier et al., 2010; Théry et al., 2006a). We further investigated cell shape changes by adding two bars, above and below the original V-shaped micropattern, and monitored cell shape extension in real time (Fig. 3C and supplementary material Movie 1). As the cell shape changed, some peripheral actin cables disappeared (arrowhead in Fig. 3C) whereas others were assembled (arrows in Fig. 3C). This suggested that cell shape reprogramming is supported by complex remodeling of intracellular structures.

Control of actin network remodelling

Cell shape is supported by various structural elements made of actin filaments. They can be classified into branched meshworks and filament bundles (Michelot and Drubin, 2011). Both are highly dynamic and remodeled during cell shape changes (Rafelski and Theriot, 2004). We further tested whether laser-based patterning could be used to guide not only cell shape changes but also precise intracellular remodeling of these structural elements. Assembly of each structural element is dependent on local adhesion geometry (Brock et al., 2003; Parker et al., 2002; Théry et al., 2006a). When cultured on an H-shaped micropattern, cells adopt a square shape. For a given cell, branched meshworks were established along the adhesive bars and actin bundles across the gaps. Each type of actin-based structure could be induced, displaced or removed during square cell shape transformation into a rectangle by adding new adhesive regions of defined geometries. Extending the length of the juxtaposed bars on one side promoted the displacement of the actin bundle so that it remained situated between the tips of the two bars (Fig. 4A). Connecting the tips of two bars with a contiguous adhesive region favored actin bundle disassembly and the formation of a branched meshwork (Fig. 4B). Adding two small bars perpendicular to one of the H bars induced formation of an additional peripheral actin bundle (Fig. 4C). These results showed that in addition to controlling the global

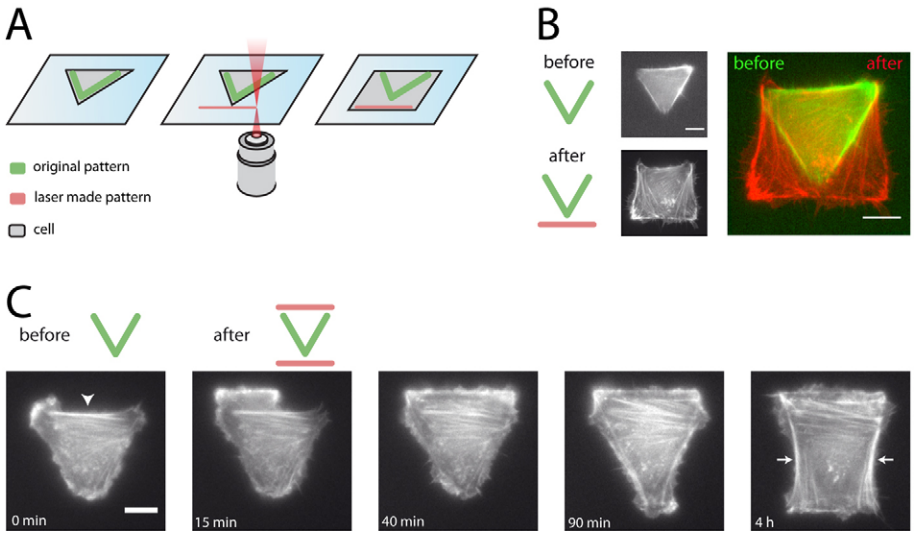

Fig. 3. Cell shape reprogramming. (**A**) Cells shape is first constrained on a classical micropattern (green). A pulsed laser is used to create new adhesive regions (red) to reprogram cell shape. (**B**) A RPE1 cell expressing Lifeact–GFP is first constrained to have a triangular shape on a V shaped micropattern (top, green in the overlay) and then reprogrammed to become square (bottom, red in the overlay) by drawing a bar below the V shape with the laser. Scale bars: 10 μm. (**C**) Monitoring of cell shape changes. A triangular cell is first constrained on a V-shaped micropattern (green in the scheme) and reprogrammed to become rectangular by adding two horizontal bars above and below the original micropattern (red in the scheme). Cell shape changes were monitored by video-microscopy and observing Lifeact–GFP. Some actin filament bundles disappear (arrowhead) whereas others were assembled (arrows). Scale bar: 10 μm.

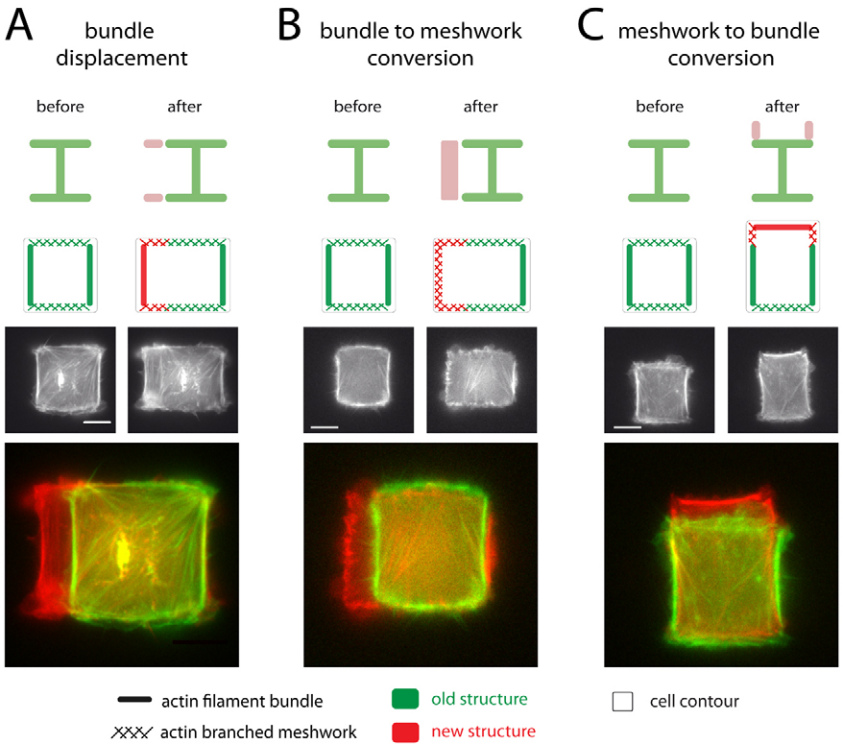

Fig. 4. Cell architecture manipulation. Cells were plated on H-shaped micropatterns (green in the upper schemes). Cell actin architecture was mainly composed of branched meshworks (thin crosses in the lower schemes) and filament bundles (thick bars). It was remodelled with laser patterning. Pre-existing structures are drawn in green in the lower schemes and shown in green in the images overlay, new ones are in red. Actin network architecture is revealed by the expression of Lifeact–GFP. Left images show the cell before and right images show the cell 2–4 hours after laser patterning. (**A**) Extending the two H bars (red in the upper schemes) in the same longitudinal direction as the original ones induced the disassembly of the pre-existing bundle and assembly of a new one connecting the tips of the new bars. (**B**) Connecting the tips of two H bars with a new perpendicular bar induced the disassembly of the pre-existing bundle and the formation of a branched meshwork on the new bar. (**C**) Adding two bars perpendicular and each at the tip of one of the H bars turned the branched meshwork along the original bar into a filament bundle in between the new bars. Scale bars: 10 µm.

cell shape, the geometry and position of new adhesive regions can be used to finely control intracellular architecture remodeling.

In polarized cells, such as migrating cells or epithelial cells, the actin network is polarized into a branched meshwork on one cell side and contractile stress fibers on the other. The precise subcellular location of stress fibers and acto-myosin contractile activity are crucial to the determination of actin network polarity (Cramer, 2010) and internal cell polarity (Théry et al., 2006b). Live patterning could be used to precisely control and orient this actin network polarization step. A bar was added next to cells plated on discoidal micropatterns (Fig. 5A). Initially, actin networks did not display any significant polarized architecture. After live patterning, cells rapidly extended on the new bar and initiated the formation of contractile stress fibers along the edges connecting the disc and the tip of the bar (Fig. 5B and

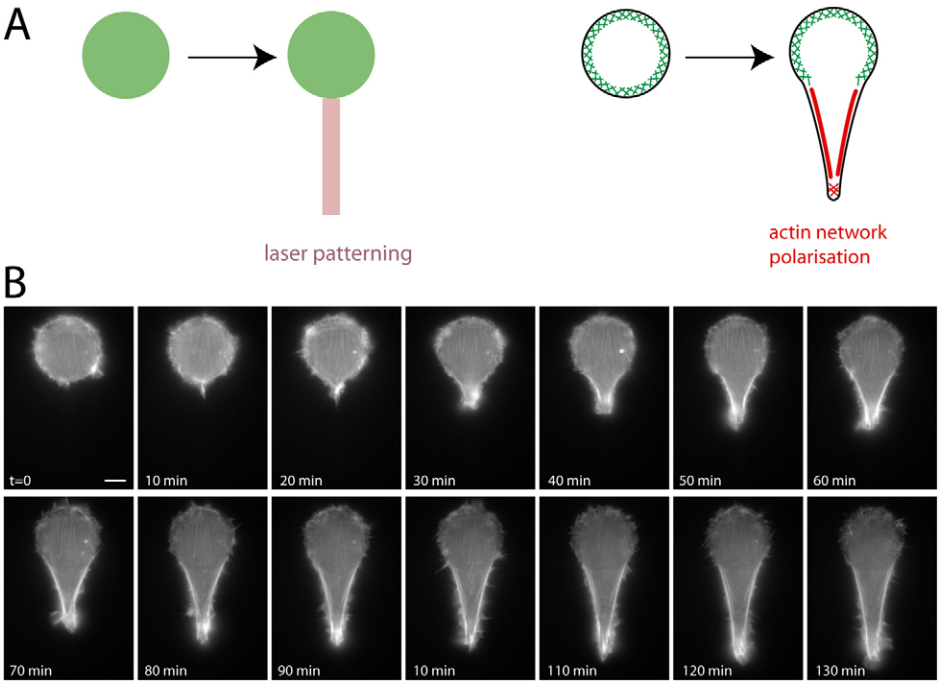

Fig. 5. Actin network polarisation. (**A**) Cells were plated on discoidal micropatterns (green). Cell actin architecture was initially mainly composed of an isotropic branched meshwork all along cell periphery (green crosses). A bar perpendicular to disc border was added with laser patterning (red). Cells rapidly formed stress fibers connecting the disc and the bar tip (red bars). Pre-existing structures are drawn in green and new ones are in red. (**B**) During this transformation, actin network architecture remodeling was monitored with Lifeact–GFP. Stress fibers were clearly visible after 30 minutes. They then get thicker and longer as the cells extended along the bar. Scale bar: 10 µm.

supplementary material Movie 2). Upon completion of this extension and contraction phase, cells ended up with a highly asymmetrical shape and polarized actin network.

Discussion

The laser-patterning method we developed will find a broad range of applications in addition to its role in the study of living cells. The non-specific action of this method represents a versatile way to design micropatterns on various surfaces. It does not require specific photo-activatable substrates or photo-sensitive ligands, it simply ablates the protein-repellent coating. Therefore, it could be applied to any PEG-coated surfaces. In addition, it is a contact-less patterning method, which therefore offers the possibility of designing micropatterns on three-dimensional substrates or in close microfluidic devices. Finally, rounds of laser patterning and protein adsorption can be repeated at will to allow multi-protein patterning of substrates.

Here, we have demonstrated that this new and simple method for surface nano-patterning in live cell culture offers a precise control in real time of cell shape modifications and of intracellular architecture. This method should pave the way for further investigations of dynamic cellular responses to nano- and micro-scale changes in the microenvironment. It also opens new possibilities to adapt 'on the fly' the design of new geometrical constraints to the observed cell behavior. Therefore, it will enable the fabrication of micropatterned regions during the growth of multi-cellular colonies. This will enable new insights into tissue engineering.

Materials and Methods

Deep-UV patterning

Glass coverslip micro-patterning has been described elsewhere (Azioune et al., 2010). Briefly, coverslips were first spin-coated for 30 seconds at 3000 r.p.m. with adhesion promoter Ti-Prime (MicroChemicals), baked for 2 minutes at 120℃ and then spin-coated with 1% polystyrene solution (Sigma) in toluene (Sigma) at 1000 r.p.m. for 30 seconds. Polystyrene-coated coverslips were oxidized through oxygen plasma (FEMTO, Diener Electronics) for 10 seconds at 30 W before incubating with 0.1 mg/ml poly-L-lysine (PLL)–PEG (Cytoo) in 10 mM HEPES, pH 7.4, for 15 minutes. After drying, coverslips were exposed to 165 nm UV (UVO cleaner, Jelight) through a photomask (Toppan) for 2 minutes. After UV activation, coverslips were incubated with a 20 µg/ml of fibronectin (Sigma) and 10 µg/ml Alexa Fluor 546 fibrinogen conjugate (Invitrogen) in phosphate-buffered saline (PBS) solution for 30 minutes. Coverslips were mounted in magnetic chambers (Cytoo) and washed three times with sterile PBS before plating cells.

Lifeact molecular cloning, lentiviral expression and cell transduction

LifeAct–mGFP plasmids were kindly provided by Wedlich-Soldner (Riedl et al., 2008). The lifeact–mGFP fragment was amplified by PCR using primers flanked with specific restriction enzyme sites (namely *Eco*RI and *Not*I). This fragment was subsequently cut and ligated with the pLVX lentiviral vector (Dupont et al., 2011) (Clontech), which was also cut with corresponding restriction enzyme. The virus carrying lifeact–mGFP was generated using the lenti-X packaging system (Dupont et al., 2011) (Clontech). hTERT-RPE1 cells (infinity telomerase-immortalised retinal pigment epithelial human cell line) were subsequently infected with the virus followed by antibiotic selection, according to the manufacturer's instructions (Clontech).

Cell culture

hTERT-RPE1 cells were cultured in DMEM F-12 (Gibco) supplemented with 10% fetal bovine serum (A15-551, PAA), 50 units/ml penicillin and 50 µg/ml streptomycin (Gibco). Cells were cultured in a 5% CO_2 incubator at 37℃. Cells were trypsinized, centrifuged, resuspended in fresh medium and allowed to spread on micropattern for 4 hours before the beginning of the experiment.

Laser patterning

Laser patterning was performed using of a Laser illuminator iLasPulse (Roper Scientific) set-up on an inverted microscope (TE2000-E, Nikon). iLasPulse is a dual-axis galvanometer-based optical scanner that focuses the laser beam on the sample (diffraction limited spot size) on the whole field of view of the camera. It includes a telescope to adjust laser focalization with image focalization and a polarizer to control beam power. The laser used is a passively Q-switched laser (STV-E, TeemPhotonics), which produces 300 picosecond pulses at 355 nm (energy/pulse, 1.2 µJ; peak power 4 kW; variable repetition rate, 0.01–2 kHz; average power, ≤2.4 mW). Laser displacement, exposure time and repetition rate were controlled using Metamorph software (Universal Imaging Corporation). The objective used was a 100× CFI S Fluor oil objective (MRH02900, Nikon). The area to pattern was filled with different density of spot. Each spot was exposed for 20 mseconds at a repetition rate of 600 Hz. The polarizer was set to have an energy per pulse of 300 nJ.

To visualize the patterned zone, a polystyrene- and PLL–PEG-treated coverslip without cells was mounted in a magnetic chamber. This chamber was filled with a 20 µg/ml fibronectin (Sigma) and 10 µg/ml fluorescent fibrinogen conjugate (Invitrogen) PBS solution. Laser patterning was then conducted as described above and protein adsorption was allowed for 30 minutes. Coverslips were rinsed with PBS and fluorescent images were then taken using a 100× UplanSApo oil objective (Olympus) using an Olympus BX61 microscope and a CoolSNAP HQ2 camera (Photometrics).

Image acquisition

Magnetic chambers containing the coverslips and filled with cell culture medium were placed on the microscope (TE2000-E, Nikon, France) in a stage incubator system at 37℃ and 5% CO_2 (Chamlide WP, Live Cell Instruments). Epifluorescence images of cells were acquired through a 100× CFI Plan Fluor oil objective or 60× CFI Apo TIRF oil objective (MRH02900 and MBH76162, respectively, Nikon) and a QUANTEM:512SC cooled EMCCD camera (Photometrics). The whole system was controlled by Metamorph software (Universal Imaging Corporation).

Cell extension and membrane curvature measurements

Extension and curvature measurements were performed using ImageJ software. For extension measurements, the distance between the border of the initial pattern and the border of the cell extended on the new pattern was measured. Two measures were performed for each cell (one for each extension zone). For curvature measurements, a circle was manually drawn along the unattached edge of the cell joining the two new adherent zone and the radius of the circle was measured automatically. Only cells that had extended on both bars were measured. All the measurement series were compared using a one-way ANOVA comparison test. Means were considered as significantly different when the P value was below 0.05.

Atomic force microscopy

Laser-made micropatterns were observed and quantified by atomic force microscopy (AFM) to see the topographical effect induced by the procedure. AFM was performed on a 5500 LS AFM stage (Agilent) or a DI 3100 AFM stage (Veeco). Coverslips were attached to a glass slide and mounted in the AFM. Ambient tapping mode imaging was performed using a NSC19 cantilever (Mikromasch). Scan parameters were optimized to minimize the difference between the set point and the amplitude of the free cantilever while maintaining a stable image.

To estimate the size of a single spot, a polystyrene- and PLL-PEG-treated coverslip without cells was mounted in a magnetic chamber. Because the single spot margins could not be clearly seen in AFM owing to the small size of the topographical step (8 nm) compared with the polystyrene surface roughness (see Fig. 1), the laser beam intensity was increased to make small holes in the polystyrene layer. Therefore the width of 300 nm is an overestimation of the actual spot we used in the experiments in the presence of cells.

Acknowledgements

We thank David Peyrade and Patrice Baldeck for technical help during preliminary experiments and Simon Le Denmat for AFM analyses.

Funding

This work was supported by grants from Agence National pour la Recherche [grant numbers ANR-PCV08-322457 and ANR-08-JC-0103 to M.T.]; two PhD fellowships from the IRTELIS program of the CEA to T.V. and Q.T.; and a postdoctoral fellowship from the Chimtronique program of the CEA to R.G.

Supplementary material available online at
http://jcs.biologists.org/lookup/suppl/doi:10.1242/jcs.104901/-/DC1

References

Arnold, M., Cavalcanti-Adam, E. A., Glass, R., Blümmel, J., Eck, W., Kantlehner, M., Kessler, H. and Spatz, J. P. (2004). Activation of integrin function by nanopatterned adhesive interfaces. *ChemPhysChem* **5**, 383-388.

Azioune, A., Storch, M., Bornens, M., Théry, M. and Piel, M. (2009). Simple and rapid process for single cell micro-patterning. *Lab Chip* **9**, 1640-1642.

Azioune, A., Carpi, N., Tseng, Q., Théry, M. and Piel, M. (2010). Protein micropatterns: A direct printing protocol using deep UVs. *Methods Cell Biol.* **97**, 133-146.

Brock, A., Chang, E., Ho, C. C., LeDuc, P., Jiang, X., Whitesides, G. M. and Ingber, D. E. (2003). Geometric determinants of directional cell motility revealed using microcontact printing. *Langmuir* **19**, 1611-1617.

Colombelli, J., Grill, S. W. and Stelzer, E. H. K. (2004). Ultraviolet diffraction limited nanosurgery of live biological tissues. *Rev. Sci. Instrum.* **75**, 472-478.

Colombelli, J., Reynaud, E. G. and Stelzer, E. H. (2007). Investigating relaxation processes in cells and developing organisms: from cell ablation to cytoskeleton nanosurgery. *Methods Cell Biol.* **82**, 267-291.

Cramer, L. P. (2010). Forming the cell rear first: breaking cell symmetry to trigger directed cell migration. *Nat. Cell Biol.* **12**, 628-632.

Desai, R. A., Gao, L., Raghavan, S., Liu, W. F. and Chen, C. S. (2009). Cell polarity triggered by cell-cell adhesion via E-cadherin. *J. Cell Sci.* **122**, 905-911.

Doyle, A. D., Wang, F. W., Matsumoto, K. and Yamada, K. M. (2009). One-dimensional topography underlies three-dimensional fibrillar cell migration. *J. Cell Biol.* **184**, 481-490.

Dupont, S., Morsut, L., Aragona, M., Enzo, E., Giulitti, S., Cordenonsi, M., Zanconato, F., Le Digabel, J., Forcato, M., Bicciato, S. et al. (2011). Role of YAP/TAZ in mechanotransduction. *Nature* **474**, 179-183.

Fink, J., Carpi, N., Betz, T., Bétard, A., Chebah, M., Azioune, A., Bornens, M., Sykes, C., Fetler, L., Cuvelier, D. et al. (2011). External forces control mitotic spindle positioning. *Nat. Cell Biol.* **13**, 771-778.

Gabi, M., Larmagnac, A., Schulte, P. and Vörös, J. (2010). Electrically controlling cell adhesion, growth and migration. *Colloids Surf. B Biointerfaces* **79**, 365-371.

Geiger, B., Spatz, J. P. and Bershadsky, A. D. (2009). Environmental sensing through focal adhesions. *Nat. Rev. Mol. Cell Biol.* **10**, 21-33.

James, J., Goluch, E. D., Hu, H., Liu, C. and Mrksich, M. (2008). Subcellular curvature at the perimeter of micropatterned cells influences lamellipodial distribution and cell polarity. *Cell Motil. Cytoskeleton* **65**, 841-852.

Kaji, H., Kawashima, T. and Nishizawa, M. (2006). Patterning cellular motility using an electrochemical technique and a geometrically confined environment. *Langmuir* **22**, 10784-10787.

Kikuchi, Y., Nakanishi, J., Nakayama, H., Shimizu, T., Yoshino, Y., Yamaguchi, K., Yoshida, Y. and Horiike, Y. (2008a). Grafting poly(ethylene glycol) to a glass surface via a photocleavable linker for light-induced cell micropatterning and cell proliferation control. *Chem. Lett.* **37**, 1062-1063.

Kikuchi, Y., Nakanishi, J., Shimizu, T., Nakayama, H., Inoue, S., Yamaguchi, K., Iwai, H., Yoshida, Y., Horiike, Y., Takarada, T. et al. (2008b). Arraying heterotypic single cells on photoactivatable cell-culturing substrates. *Langmuir* **24**, 13084-13095.

Kilian, K. A., Bugarija, B., Lahn, B. T. and Mrksich, M. (2010). Geometric cues for directing the differentiation of mesenchymal stem cells. *Proc. Natl. Acad. Sci. USA* **107**, 4872-4877.

Lehnert, D., Wehrle-Haller, B., David, C., Weiland, U., Ballestrem, C., Imhof, B. A. and Bastmeyer, M. (2004). Cell behaviour on micropatterned substrata: limits of extracellular matrix geometry for spreading and adhesion. *J. Cell Sci.* **117**, 41-52.

Lombardi, M. L., Jaalouk, D. E., Shanahan, C. M., Burke, B., Roux, K. J. and Lammerding, J. (2011). The interaction between nesprins and sun proteins at the nuclear envelope is critical for force transmission between the nucleus and cytoskeleton. *J. Biol. Chem.* **286**, 26743-26753.

Lu, P., Takai, K., Weaver, V. M. and Werb, Z. (2011). Extracellular matrix degradation and remodeling in development and disease. *Cold Spring Harb. Perspect. Biol.* **3**, a005058.

McBeath, R., Pirone, D. M., Nelson, C. M., Bhadriraju, K. and Chen, C. S. (2004). Cell shape, cytoskeletal tension, and RhoA regulate stem cell lineage commitment. *Dev. Cell* **6**, 483-495.

Michelot, A. and Drubin, D. G. (2011). Building distinct actin filament networks in a common cytoplasm. *Curr. Biol.* **21**, R560-R569.

Mitchell, S. A., Poulsson, A. H., Davidson, M. R., Emmison, N., Shard, A. G. and Bradley, R. H. (2004). Cellular attachment and spatial control of cells using micro-patterned ultra-violet/ozone treatment in serum enriched media. *Biomaterials* **25**, 4079-4086.

Nakanishi, J., Kikuchi, Y., Inoue, S., Yamaguchi, K., Takarada, T. and Maeda, M. (2007). Spatiotemporal control of migration of single cells on a photoactivatable cell microarray. *J. Am. Chem. Soc.* **129**, 6694-6695.

Nakanishi, J., Takarada, T., Yamaguchi, K. and Maeda, M. (2008). Recent advances in cell micropatterning techniques for bioanalytical and biomedical sciences. *Anal. Sci.* **24**, 67-72.

Parker, K. K., Brock, A. L., Brangwynne, C., Mannix, R. J., Wang, N., Ostuni, E., Geisse, N. A., Adams, J. C., Whitesides, G. M. and Ingber, D. E. (2002). Directional control of lamellipodia extension by constraining cell shape and orienting cell tractional forces. *FASEB J.* **16**, 1195-1204.

Pfleging, W., Torge, M., Bruns, M., Trouillet, V., Welle, A. and Wilson, S. (2009). Laser- and UV-assisted modification of polystyrene surfaces for control of protein adsorption and cell adhesion. *Appl. Surf. Sci.* **255**, 5453-5457.

Pitaval, A., Tseng, Q., Bornens, M. and Théry, M. (2010). Cell shape and contractility regulate ciliogenesis in cell cycle-arrested cells. *J. Cell Biol.* **191**, 303-312.

Pouthas, F., Girard, P., Lecaudey, V., Ly, T. B., Gilmour, D., Boulin, C., Pepperkok, R. and Reynaud, E. G. (2008). In migrating cells, the Golgi complex and the position of the centrosome depend on geometrical constraints of the substratum. *J. Cell Sci.* **121**, 2406-2414.

Rafelski, S. M. and Theriot, J. A. (2004). Crawling toward a unified model of cell mobility: spatial and temporal regulation of actin dynamics. *Annu. Rev. Biochem.* **73**, 209-239.

Raghavan, S., Desai, R. A., Kwon, Y., Mrksich, M. and Chen, C. S. (2010). Micropatterned dynamically adhesive substrates for cell migration. *Langmuir* **26**, 17733-17738.

Riedl, J., Crevenna, A. H., Kessenbrock, K., Yu, J. H., Neukirchen, D., Bista, M., Bradke, F., Jenne, D., Holak, T. A., Werb, Z. et al. (2008). Lifeact: a versatile marker to visualize F-actin. *Nat. Methods* **5**, 605-607.

Rossier, O. M., Gauthier, N., Biais, N., Vonnegut, W., Fardin, M. A., Avigan, P., Heller, E. R., Mathur, A., Ghassemi, S., Koeckert, M. S. et al. (2010). Force generated by actomyosin contraction builds bridges between adhesive contacts. *EMBO J.* **29**, 1055-1068.

Samora, C. P., Mogessie, B., Conway, L., Ross, J. L., Straube, A. and McAinsh, A. D. (2011). MAP4 and CLASP1 operate as a safety mechanism to maintain a stable spindle position in mitosis. *Nat. Cell Biol.* **13**, 1040-1050.

Schvartzman, M., Palma, M., Sable, J., Abramson, J., Hu, X., Sheetz, M. P. and Wind, S. J. (2011). Nanolithographic control of the spatial organization of cellular adhesion receptors at the single-molecule level. *Nano Lett.* **11**, 1306-1312.

Théry, M. (2010). Micropatterning as a tool to decipher cell morphogenesis and functions. *J. Cell Sci.* **123**, 4201-4213.

Théry, M., Jiménez-Dalmaroni, A., Racine, V., Bornens, M. and Jülicher, F. (2007). Experimental and theoretical study of mitotic spindle orientation. *Nature* **447**, 493-496.

Théry, M., Pépin, A., Dressaire, E., Chen, Y. and Bornens, M. (2006a). Cell distribution of stress fibres in response to the geometry of the adhesive environment. *Cell Motil. Cytoskeleton* **63**, 341-355.

Théry, M., Racine, V., Piel, M., Pépin, A., Dimitrov, A., Chen, Y., Sibarita, J. B. and Bornens, M. (2006b). Anisotropy of cell adhesive microenvironment governs cell internal organization and orientation of polarity. *Proc. Natl. Acad. Sci. USA* **103**, 19771-19776.

Théry, M., Jiménez-Dalmaroni, A., Racine, V., Bornens, M. and Jülicher, F. (2007). Experimental and theoretical study of mitotic spindle orientation. *Nature* **447**, 493-496.

Vogel, A., Noack, J., Huttman, G. and Paltauf, G. (2005). Mechanisms of femtosecond laser nanosurgery of cells and tissues. *Appl. Phys. B* **81**, 1015-1047.

A

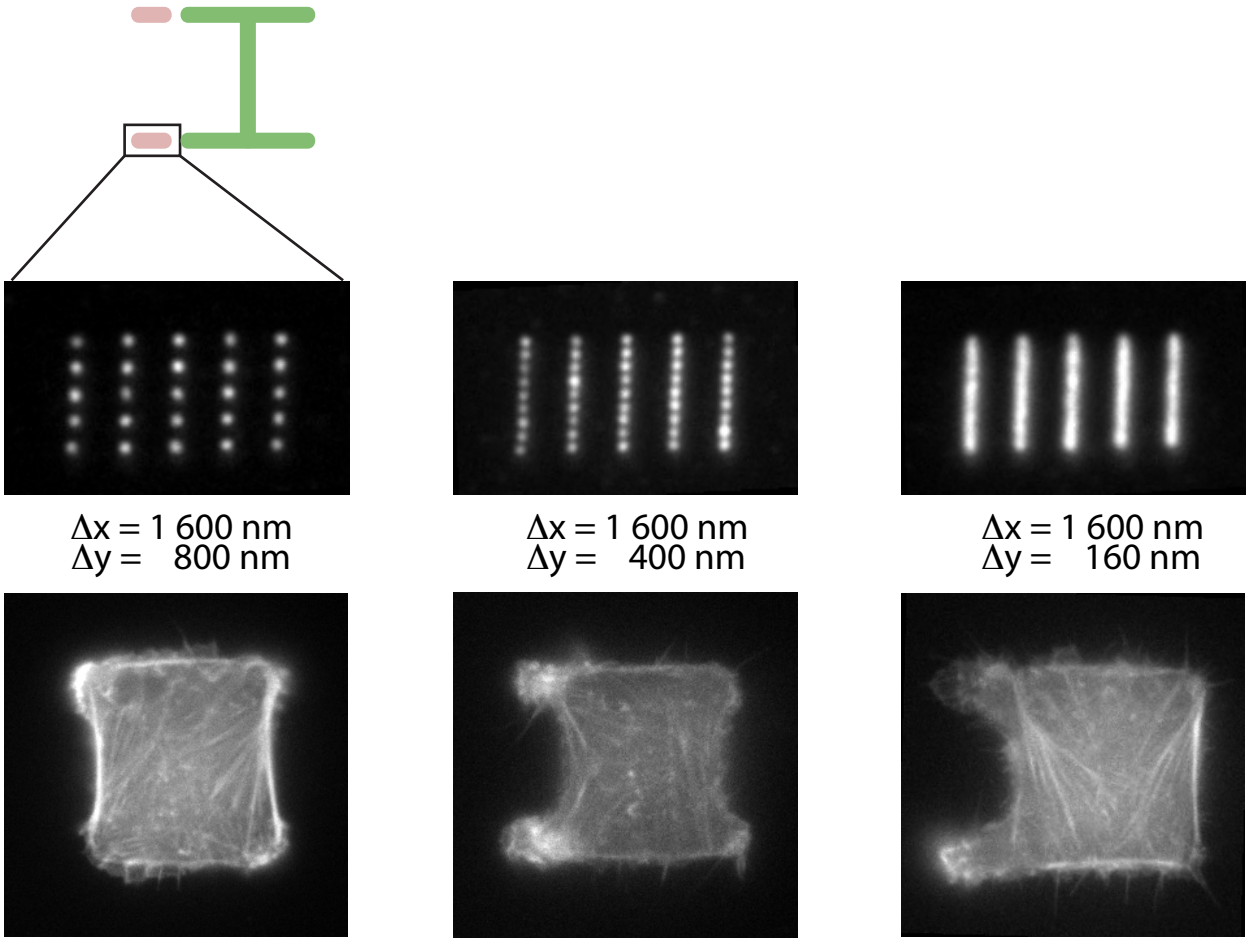
Δx = 1 600 nm
Δy = 800 nm
Δx = 1 600 nm
Δy = 400 nm
Δx = 1 600 nm
Δy = 160 nm

B

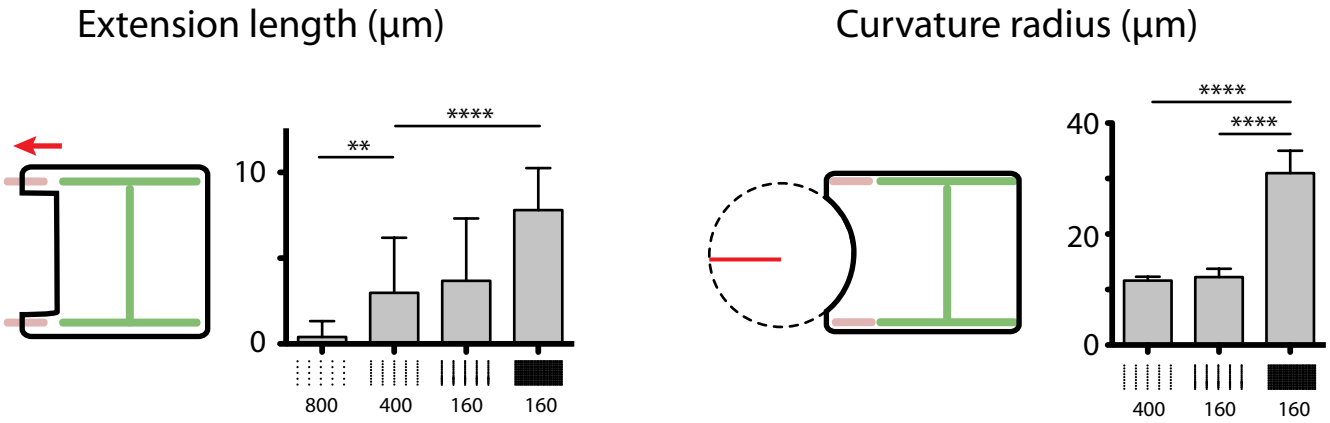
Extension length (µm)
Curvature radius (µm)
**
****
10
0
800
400
160
160
****
****
40
20
0
400
160
160

Les applications potentielles de la technique développée vont bien au delà de celles mises en œuvre dans ce travail. Le tissu engineering, le patterning séquentiel de plusieurs protéines, des changements de polarité contrôlés, le patterning en 3 dimensions, la création de réseaux de neurones dont les connexions sont contrôlées, sont quelques unes des voies prometteuses qui pourraient être empruntées (figure 28)

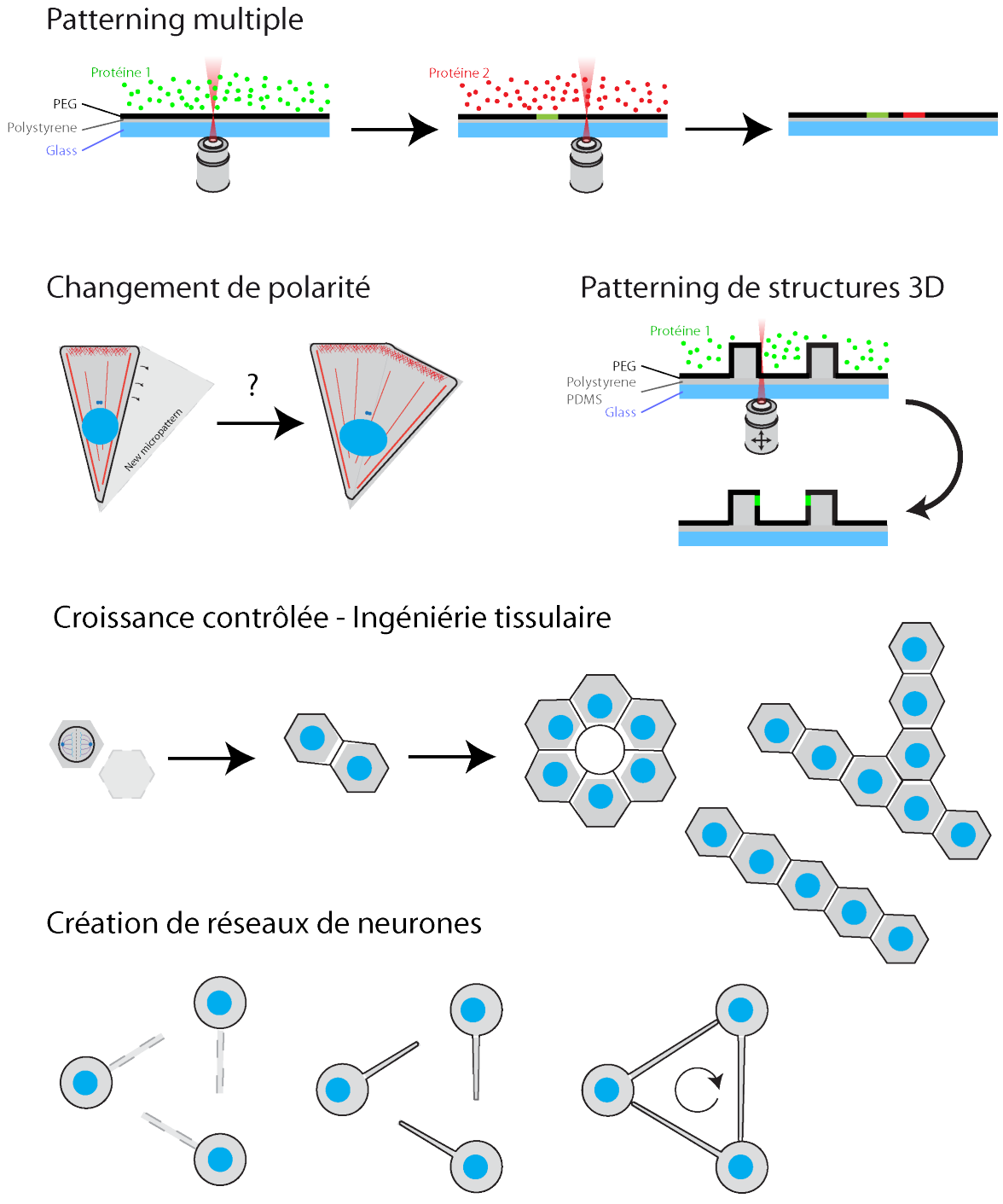

Figure 28 : Exemple d'utilisation possible de la technique développée

D'autre part la caractérisation des paramètres géométriques permettant l'extension cellulaire permet de mettre en avant des phénomènes importants. Même si les conditions nécessaires à la formation des adhésions ont déjà été décrites (voir intro), elles ne l'ont jamais été dans des conditions où la cellule est déjà étalée et tente de s'étendre sur une zone supplémentaire. La nécessité d'une surface d'adhérence jointive pour permettre la contraction de la cellule fait écho à la maturation des adhésions par leur taille. Il est probable que dans ces conditions, seuls des complexes focaux puissent être formés et que ces derniers ne soient pas capables de s'associer à des fibres de stress d'actine qui permettraient la contraction du bord de la cellule.

Par ailleurs, ces observations mettent en avant la régulation locale de la contractilité cellulaire là où d'autres études s'étaient intéressées à l'effet global de la taille des adhésions sur la contractilité cellulaire (Goffin, J. Cell Biol. 2006). En effet, l'autre bord de la cellule reste en tension pendant toute la durée de l'expérience et ce n'est que localement que la cellule ne parvient pas à établir les structures suffisantes à sa contraction. Ces observations mettent en avant le contrôle local de la contractilité par les adhésions et leur rôle primordial dans la régulation de l'organisation du cytosquelette.

L'étude suivante s'intéresse au rôle de la composition en intégrines des adhésions et va nous permettre de nous intéresser aux variations de l'adhésome en fonction de ce paramètre.

2. LA COOPERATION DE DIFFERENTES INTEGRINES AU SEIN DE L'ADHESION EST NECESSAIRE POUR L'ADAPTATION DE LA CONTRACTILITE CELLULAIRE A SON ENVIRONNEMENT (ARTICLE)

A. INTRODUCTION

Différentes intégrines sont capables de s'attacher à la même protéine de matrice extracellulaire. La façon dont elles vont permettre de déclencher des fonctions spécifiques est encore inconnue aujourd'hui. Le but de cette étude était d'étudier le rôle spécifique de 2 intégrines (αvβ3 et α5β1), fixant la fibronectine dans le processus de mécano-transduction. Pour cela ont été utilisées des cellules auxquelles toutes les autres intégrines avaient été retirées pour éviter toute compensation possible qui aurait obscurci les résultats.

La diversité des méthodes employées peut rendre la compréhension de cet article difficile. Je vais ici introduire le principe des techniques de protéomique utilisées dans l'article pour permettre une lecture plus aisée par la suite.

La spectrométrie de masse permet la quantification précise de protéines en solution. Les protéines sont digérées en fragments à l'aide d'enzymes. Ces fragments sont ensuite vaporisés, ionisés et projetés sur une cible en traversant un champ magnétique. Les particules vont ainsi être déviées en fonction de leur charge et de leur masse. Le spectre généré par ces fragments permet d'identifier les

protéines et de mesurer leur quantité. (Bantscheff, Anal Bioanal Chem, 2012)

Cette technique peut-être précédée de technique de biologie moléculaire pour permettre la sélection de protéines d'intérêt avant la quantification. C'est cette stratégie qui a été utilisé dans notre étude.

Pour l'analyse globale des protéines associées aux adhésions (figure 29) , les cellules ont été tout d'abord cultivées dans différentes conditions. Les interactions entre les adhésions et les protéines associées ont été stabilisées par une étape de pontage chimique non-spécifique des protéines. Les cellules sont ensuite lysées et un cisaillement hydrodynamique est généré pour évacuer toutes les protéines qui ne sont pas fixées au substrat, directement ou indirectement. Cette étape permet d'éliminer toutes les protéines qui n'ont pas été pontées avec les adhésions car elles n'interagissaient pas avec ces dernières. Pour récupérer les protéines qui nous intéressent, les protéines sont ensuite remises en solution avec un traitement réducteur et précipitée à nouveau pour les concentrer. La spectrométrie de masse peut ensuite être mise en œuvre. Cette technique permet la comparaison de la quantité de nombreuses protéines en fonction de conditions variables.

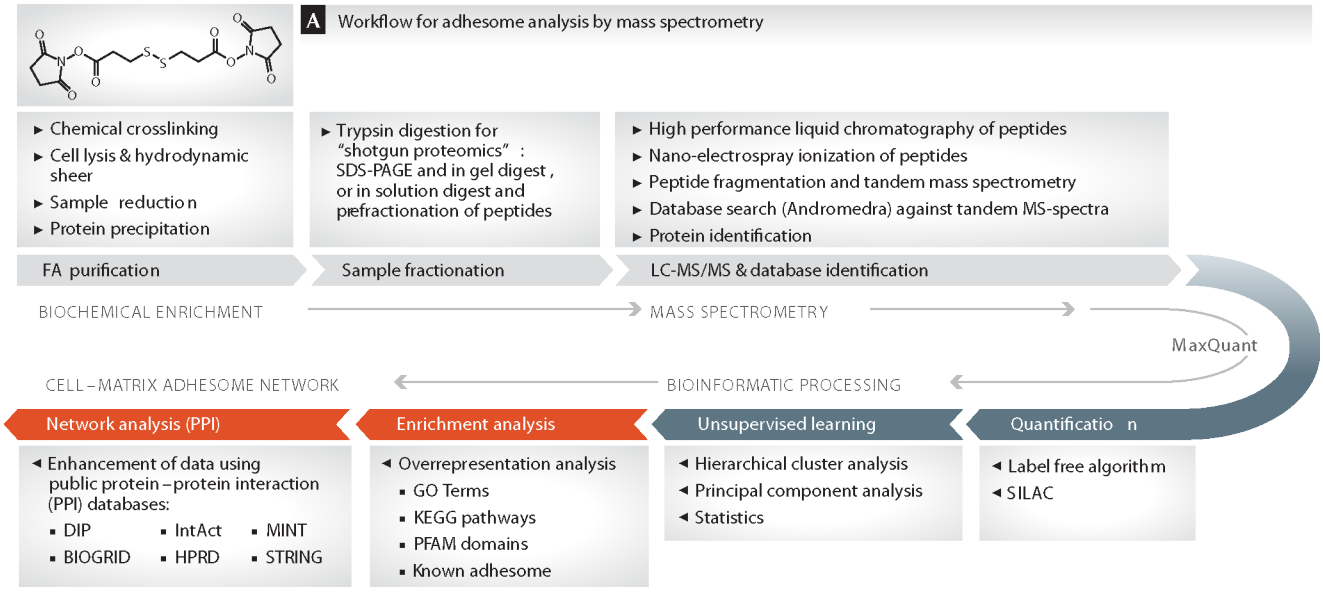

Figure 29 : Détermination de l'adhésome cellulaire par spectrométrie de masse (SM)
Schiller, EMBO Reports, 2013

Pour permettre une quantification plus fine des protéines interagissant avec les deux intégrines au centre de notre étude, les résultats obtenus ont été confirmés par pull-down couplé à la technique de SILAC (Stable isotope labelling by amino acids in cell culture) (figure 30).

Des cellules sont cultivées en présence ou non d'acides aminés marqués par des isotopes lourds. Ces acides aminés vont être incorporés aux protéines nouvellement formées au sein de la cellule. Ils

SILAC Based Pull-down

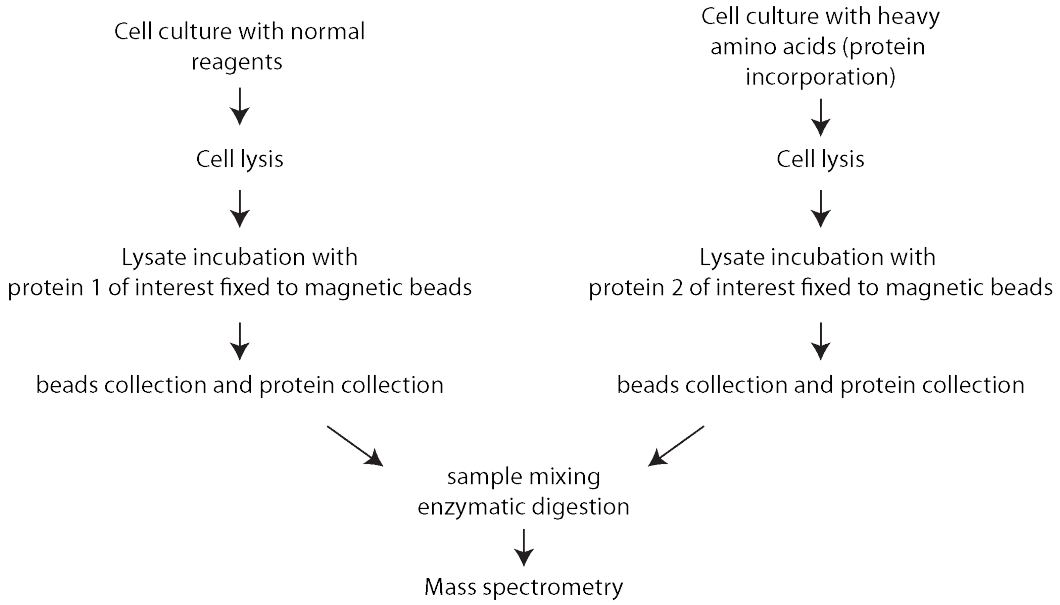

$$\textbf{for protein X, SILAC ratio} = \frac{\textbf{(protein X quantity in heavy form)}}{\textbf{(protein X quantity in light form)}}$$

Forward and reverse cases

	β_1- coated bead	β_3- coated bead
forward	Heavy extract	Light extract
reverse	Light extract	Heavy extract

for protein X identified in MS :

$$\text{SILAC ratio forward} = \frac{\text{Protein count from } \beta_1 \text{ pulldown}}{\text{Protein count from } \beta_3 \text{pulldown}}$$

$$\text{SILAC ratio reverse} = \frac{\text{Protein count from } \beta_3 \text{pulldown}}{\text{Protein count from } \beta_1 \text{pulldown}}$$

$$\text{SILAC ratio forward} \approx \frac{1}{\text{SILAC ratio reverse}}$$

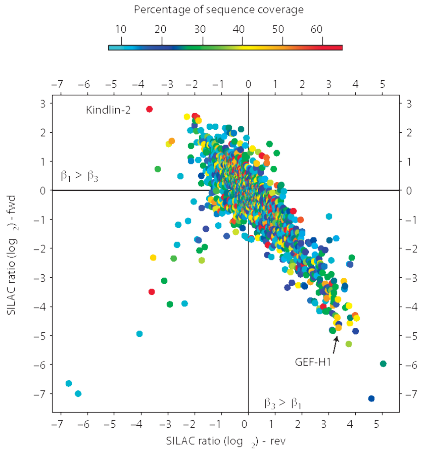

then plot of ratio forward vs reverse should give a linear distribution in log/log coordinates one point correspond to a single protein

Figure 30 : Schéma de fonctionnement du pull-down couplé au SILAC et la SM

alourdiront les fragments analysés par spectrométrie de masse et permettront de les différencier des fragments légers provenant d'un autre échantillon, qui servira de référence. Pour sélectionner les protéines d'intérêt, des extraits cellulaires (lourd et léger) sont incubés en parallèle avec des billes magnétiques auxquelles sont fixées l'une ou l'autre des chaines β qui nous intéressent. Les protéines d'intérêts vont ainsi venir s'associer avec les billes via les intégrines. Les billes sont collectées à l'aide d'un aimant, entrainant avec elles les protéines attachées. Ces protéines sont ensuite regroupées dans un même échantillon, les protéines lourdes ayant été sélectionnées par l'une des intégrines et les protéines légères par l'autre. La spectrométrie de masse va permettre de quantifier la quantité de chaque protéine sous sa forme lourde et légère et d'en faire le ratio. Le ratio calculé est toujours la quantité de protéines lourdes sur la quantité de protéines légères. Il permet de savoir si une protéine est plus abondante dans une condition que dans l'autre.

Pour éliminer les faux positifs, la même procédure est répétée mais en inversant les fractions lourdes et légères au moment de l'incubation avec les billes magnétiques. Le ratio calculé dans le cas « reverse » devrait donc être l'inverse de celui calculé dans le premier cas (« forward »). Cette procédure permet d'éliminer les faux positifs en confirmant le résultat par une deuxième mesure. Les ratios sont généralement représentés sous forme de nuage de points sur un graphe log/log. Chaque protéine est représentée par un point dont l'abscisse est son ratio reverse et l'ordonné son ratio forward. Sa couleur permet de préciser quelle proportion de sa séquence a été identifiée par spectrométrie de masse. Plus celle-ci est importante, plus le résultat est robuste. Du fait de la relation inverse entre ratio forward et reverse, le nuage de points doit laisser deviner une droite dans un système de coordonnées log/log.

Enfin, pour permettre la comparaison des niveaux de phosphorylations entre nos 3 conditions cellulaires (αvβ3, α5β1 et αvβ3/α5β1), la technique de SILAC a été combinée à celle d'isolation des protéines associées aux adhésions. Chaque lignée cellulaire a respectivement été cultivée avec des acides aminés légers, intermédiaires ou lourds. Les extraits protéiques ont ensuite été mélangés, digérés et enrichis pour les fragments phosphorylés avec du dioxyde de Titanium. Les fragments ont ensuite pu être analysés par SM et la quantité de chaque protéine présente sous forme phosphorylée établie pour chacune des conditions grâce aux acides aminés légers, intermédiaires et lourds.

Les réseaux d'interaction représentés en figure supplémentaire repose sur l'analyse des résultats à l'aide de banques contenant les interactions connues entre protéines et leur rôle activateur ou inhibiteur.

B. ARTICLE

nature cell biology

β_1- and α_v-class integrins cooperate to regulate myosin II during rigidity sensing of fibronectin-based microenvironments

Herbert B. Schiller[1,6], Michaela-Rosemarie Hermann[1,6], Julien Polleux[1], Timothée Vignaud[2], Sara Zanivan[3], Caroline C. Friedel[4], Zhiqi Sun[1], Aurelia Raducanu[1], Kay-E. Gottschalk[5], Manuel Théry[2], Matthias Mann[3] and Reinhard Fässler[1,7]

How different integrins that bind to the same type of extracellular matrix protein mediate specific functions is unclear. We report the functional analysis of β_1- and α_v-class integrins expressed in pan-integrin-null fibroblasts seeded on fibronectin. Reconstitution with β_1-class integrins promotes myosin-II-independent formation of small peripheral adhesions and cell protrusions, whereas expression of α_v-class integrins induces the formation of large focal adhesions. Co-expression of both integrin classes leads to full myosin activation and traction-force development on stiff fibronectin-coated substrates, with α_v-class integrins accumulating in adhesion areas exposed to high traction forces. Quantitative proteomics linked α_v-class integrins to a GEF-H1–RhoA pathway coupled to the formin mDia1 but not myosin II, and $\alpha_5\beta_1$ integrins to a RhoA–Rock–myosin II pathway. Our study assigns specific functions to distinct fibronectin-binding integrins, demonstrating that $\alpha_5\beta_1$ integrins accomplish force generation, whereas α_v-class integrins mediate the structural adaptations to forces, which cooperatively enable cells to sense the rigidity of fibronectin-based microenvironments.

Integrins are α/β heterodimers that mediate cell adhesion to the extracellular matrix (ECM) and to receptors on other cells[1], thereby regulating numerous biological processes that are essential for development, postnatal homeostasis and pathology[1–4]. The mammalian genome encodes 18 α and 8 β integrin genes, which form 24 heterodimers. Mammalian cells usually co-express several integrins, which recognize ECM components by binding specific amino-acid stretches such as the Arg-Gly-Asp (RGD) motif[1,5]. RGD motifs are found in many matrix proteins including fibronectin, in which RGD mediates binding to $\alpha_5\beta_1$ and all α_v-class integrins[6]. *In vivo* and *in vitro* studies indicated that $\alpha_5\beta_1$ and α_v-class integrins (for example, $\alpha_v\beta_3$) exert both specific and redundant functions[7–15]; however, how these distinct integrins accomplish their individual functions and whether these cooperate remains unclear. The signalling properties and functions of integrins are executed by specialized adhesive structures with distinct morphology, subcellular localization, lifespan and molecular composition. Nascent adhesions are short-lived adhesive structures in membrane protrusions[16] that promote the activity of Rho–GTPases such as Rac1. Some nascent adhesions develop into large focal adhesions that initiate multiple signalling pathways, which activate effectors including myosin II. Myosin II exerts contractile forces resulting in adhesion reinforcement and recruitment of more proteins to focal adhesions, which induces a further increase in myosin II activity[17]. This feedback signalling to myosin II critically depends on biophysical parameters such as ECM stiffness. The identity of mechanosensor(s) in focal adhesions, whether it is an integrin, a focal adhesion protein or a combination of both, is unknown[18]. Quantitative mass spectrometry (MS) was previously used to determine the protein composition of adhesion structures (adhesomes) of cells seeded on fibronectin, and the dynamic changes on myosin-II-induced adhesion maturation[19,20]. As cells recruit different integrin classes to fibronectin-induced adhesions, these studies did not assign specific proteins and signalling outputs to particular integrins.

Here we developed a cell system to investigate the protein composition and signalling properties of adhesion sites anchored selectively through $\alpha_5\beta_1$ and/or α_v-class integrins. We found marked integrin-class-specific differences in the morphology of focal adhesions, in their requirement for mechanical tension, in the protein composition of their adhesomes and their signalling capacity. Furthermore, we

[1]Department of Molecular Medicine, Max Planck Institute of Biochemistry, 82152 Martinsried, Germany. [2]Laboratoire de Physiologie Cellulaire et Végétale, Institut de Recherche en Technologies et Sciences pour le Vivant, CNRS/UJF/INRA/CEA, 17 Rue des Martyrs, 38054 Grenoble, France. [3]Department of Proteomics and Signal Transduction, Max Planck Institute of Biochemistry, 82152 Martinsried, Germany. [4]Institute for Informatics, Ludwig-Maximilians-Universität München, 80333 Munich, Germany. [5]Institute of Experimental Physics, University of Ulm, 89069 Ulm, Germany. [6]These authors contributed equally to this work.
[7]Correspondence should be addressed to R.F. (e-mail: faessler@biochem.mpg.de)

Received 2 November 2012; accepted 4 April 2013; published online 26 May 2013; DOI: 10.1038/ncb2747

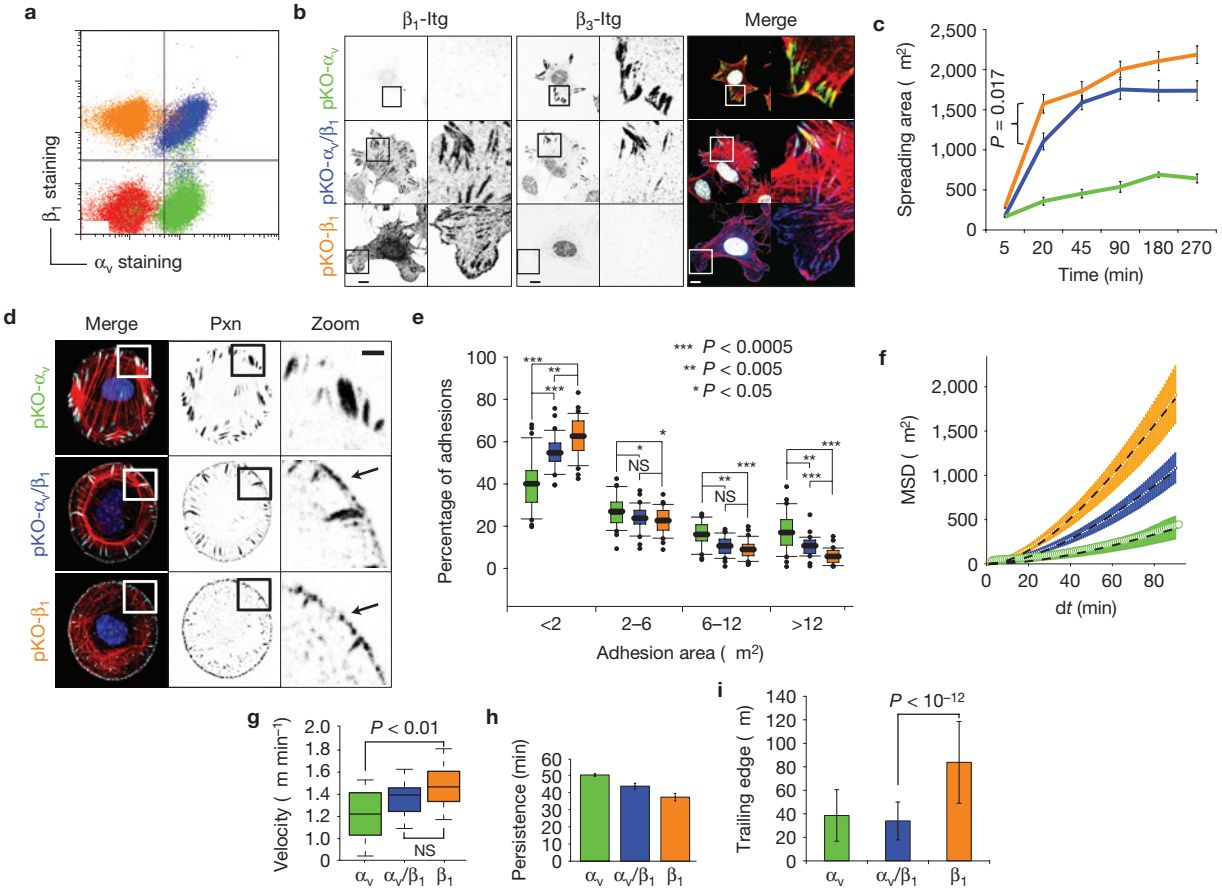

Figure 1 Different morphologies and adhesive functions of pKO-α_v, pKO-β_1 and pKO-α_v/β_1 cells. (**a**) Flow cytometry analysis of β_1 and α_v cell surface levels. (**b**) Immunostaining of indicated cell types plated for 90 min on fibronectin for β_1 and β_3. The merged images show an overlay of integrin (β_1, blue; β_3, green), F-actin (red) and nuclear (DAPI, blue) staining. Scale bars, 10 μm. (**c**) Spreading areas of cells seeded on fibronectin. Error bars represent s.e.m. ($n = 20$ cells per time point; 1 representative of 2 independent experiments is shown). The P value is derived from a t-test. (**d**) Cells were plated on circular fibronectin-coated micropatterns and immunostained for paxillin (Pxn). The merged images show an overlay of paxillin (white), F-actin (red) and nuclear (DAPI, blue) staining. Arrows indicate nascent adhesions (<2 μm^2) in the cell periphery. Scale bar, 10 μm. (**e**) Boxplots show the distribution of adhesion size classes. Significance was calculated using a t-test ($n = 30$ cells; 1 representative of 2 independent experiments is shown; boxplot whisker ends are at 1.5 interquartile range and outliers are shown as dots). (**f-h**) Migration velocity (**g**) and mean persistence time (**h**) was determined with the MSD values of cell nuclei (**f**) by filming migrating cells over a period of 90 min with a 1 min time lapse (pKO-α_v $n = 12$, pKO-β_1 $n = 14$, pKO-α_v/β_1 $n = 12$; data aggregated over 5 independent experiments). The P value for velocities (**g**) was calculated using an unpaired Wilcoxon test and the persistence time bar graph (**g**) shows the fit error as implemented in the MatLab software. NS, not significant. (**i**) Trailing edge lengths of migrating cells are shown with mean lengths from the cell rear to the middle of the nucleus. Error bars represent s.d. and the P values were calculated using a t-test (pKO-α_v $n = 51$, pKO-β_1 $n = 66$, pKO-α_v/β_1 $n = 40$; 1 representative of 2 independent experiments is shown). pKO-α_v, green; pKO-α_v/β_1, blue; pKO-β_1, orange.

identified a functional synergy between $\alpha_5\beta_1$ and α_v-class integrin signalling hubs leading to feedback amplification of myosin II activity required for focal-adhesion-mediated rigidity sensing.

RESULTS

Differential functions of $\alpha_5\beta_1$ and α_v-class integrins in adhesion formation and cell migration

To obtain cells expressing β_1- and/or α_v-class integrins we intercrossed mice carrying conditional null mutations for the α_v and β_1 integrin genes and constitutive null mutations for the β_2 and β_7 integrin genes ($\beta_1^{f/f}$, $\alpha_v^{f/f}$, $\beta_2^{-/-}$, $\beta_7^{-/-}$ mice)[21], isolated kidney fibroblasts and immortalized them with the SV40 large T antigen (parental fibroblasts). Deletion of floxed α_v and β_1 integrin genes by adenoviral *Cre* transduction removed all integrins from the parental fibroblast clones (pan-knockouts, pKO; Supplementary Fig. S1a–c). Next we transduced parental fibroblasts with α_v or β_1 or both complementary DNAs and simultaneously transduced *Cre* to delete the floxed integrin alleles. This produced cells expressing α_v (pKO-α_v), β_1 (pKO-β_1) or α_v and β_1 (pKO-α_v/β_1) integrins, respectively (Fig. 1a). The pKO-α_v, pKO-β_1 and pKO-α_v/β_1 cells were sorted for comparable integrin surface levels to the parental cell clones (Supplementary Fig. S1d,e). Using western blotting, flow cytometry and MS we identified the following fibronectin-binding integrins; $\alpha_5\beta_1$ in pKO-β_1 cells, $\alpha_v\beta_3$ and $\alpha_v\beta_5$ in pKO-α_v cells, and $\alpha_5\beta_1$, $\alpha_v\beta_3$ and $\alpha_v\beta_5$ in pKO-α_v/β_1 cells (Supplementary Fig. S1f,g). Calibration of our flow cytometry analysis estimated the presence of 170,000 $\alpha_5\beta_1$ and 300,000 α_v-class integrins on the surface of each cell, resulting in approximately equimolar surface levels for β_1, β_3 and β_5 integrins.

All three cell lines specifically adhered to fibronectin, whereas adhesion on vitronectin was similar for pKO-α_v and pKO-α_v/β_1 cells

and absent for pKO-β_1 cells (Supplementary Fig. S1h). To compare the size distribution of focal adhesions we seeded cells for 90 min on fibronectin and immunostained for paxillin, integrin β_1 and β_3 (Fig. 1b and Supplementary Fig. S2a,b). The percentage of small nascent adhesions ($<2\,\mu m^2$) was significantly elevated in pKO-β_1 and pKO-α_v/β_1 cells, whereas large focal adhesions of 6–12 μm^2 dominated in pKO-α_v cells (Supplementary Fig. S2a,b). The cell spreading area on fibronectin was significantly lower in pKO-α_v relative to pKO-β_1 and pKO-α_v/β_1 cells and reduced in pKO-α_v/β_1 relative to pKO-β_1 (Fig. 1c and Supplementary Fig. S1i). As cell shape and spreading area can affect cell contractility, focal adhesion size and distribution[22], we seeded cells on circular fibronectin-coated micropatterns surrounded by non-adhesive polyethylene glycol (PEG), and confirmed the different adhesion size distribution in the three cell lines (Fig. 1d,e). pKO-α_v/β_1 cells contained both small nascent adhesions and large focal adhesions (Fig. 1d). pKO-β_1 and pKO-α_v/β_1 cells showed increased protrusive activity when compared with pKO-α_v cells (Supplementary Fig. S2a,c), which correlated with increased migration speed. The mean square displacement (MSD) of cells migrating on fibronectin showed that pKO-β_1 cells migrated significantly faster than pKO-α_v cells, and that pKO-α_v/β_1 cells exhibited an intermediate migration speed (Fig. 1f,g). As previously shown[13,23,24], expression of α_v-class integrins increased migration persistence (Fig. 1h). pKO-β_1 cells exhibited a significant defect in trailing edge detachment (Fig. 1i and Supplementary Fig. S2c and Videos S1–S3). These results identify a role for $\alpha_5\beta_1$ in protrusive activities and nascent adhesion formation, whereas co-expression of α_v-class integrins also promotes the production of large, stable focal adhesions and trailing edge detachment in migrating cells.

Differential functions of $\alpha_5\beta_1$ and α_v-class integrins synergize to regulate cell contractility

Adhesion maturation and trailing edge retraction in migrating fibroblasts requires coordinated control of myosin-II-mediated cell contractility[25]. We measured myosin II activity using fibronectin-coated X- or crossbow-shaped micropatterns, which report subtle changes in myosin II activity and traction forces along non-adhesive edges[26–28]. Parental fibroblasts cultured on X-shaped fibronectin-coated micropatterns showed a dose-dependent decrease of phosphoT18/S19-myosin light chain (pMLC), paxillin fluorescence intensities and cell area following treatment with the myosin II inhibitor blebbistatin (Supplementary Fig. S2d–g). Crossbow patterns polarize cells into a low contractile front and a highly contractile rear[28]. Immunofluorescence analysis revealed that pMLC and paxillin intensities were the highest in pKO-α_v/β_1, lower in pKO-β_1 and the lowest in pKO-α_v cells (Fig. 2a). Myosin II activity was low in the cell front (Fig. 2b) and high in the cell rear (Fig. 2c) and the cooperative effect of the two integrin classes on pMLC and paxillin intensities in pKO-α_v/β_1 was most prominent in the cell rear (Fig. 2a–c). Treatment with the α_v-class-specific small-molecule inhibitor cilengitide reduced contractility of pKO-α_v/β_1 cells to intermediate levels (Fig. 2b,c), confirming that the adhesive function of α_v-class integrins is required for the synergy with $\alpha_5\beta_1$. We corroborated these results with fibronectin-coated X-shapes, revealing phenotypes that resembled the rear of crossbow shapes (Supplementary Fig. S2h–j).

The ability to form large focal adhesions and stress fibres indicative of high contractile forces together with low pMLC levels in pKO-α_v cells was surprising. Traction-force microscopy experiments on polyacrylamide gels of 35 kPa stiffness revealed good correlation of traction forces and pMLC levels, confirming that traction forces on fibronectin-coated crossbow micropatterns are the lowest in pKO-α_v, the highest in pKO-α_v/β_1 and intermediate in pKO-β_1 cells (Fig. 2d). Along the cell front, traction forces were significantly higher in pKO-β_1 cells when compared with pKO-α_v cells and the highest in pKO-α_v/β_1 (Fig. 2e). Similar differences were observed by calculating the total contractile energy of individual cells (Fig. 2f).

α_v-class integrins accumulate in areas of high traction force and mediate rigidity sensing

$\alpha_v\beta_3$ integrins are known to become immobilized in large and static focal adhesions, whereas $\alpha_5\beta_1$ integrins are mobile, separate from the $\alpha_v\beta_3$ integrins and translocate rearward to fibrillar adhesions[10,29]. To investigate whether $\alpha_5\beta_1$ and α_v-class integrins segregate owing to differential dependence on myosin-II-mediated tension at focal adhesions we seeded pKO-α_v/β_1 and parental floxed cells on fibronectin-coated crossbow shapes and immunostained β_1 and β_3 integrins. Indeed, β_3 heavily accumulated in areas that were shown to be exposed to the highest traction forces, whereas β_1 levels remained very low at these sites (Fig. 3a,b). The β_3 integrins in contractile focal adhesions at the cell rear were lost following blebbistatin treatment, whereas small β_1-containing focal adhesions in the cell periphery were still forming (Fig. 3a). To confirm these findings we plated pKO-α_v/β_1 cells on 1-μm-thin fibronectin-coated lines separated by 3-μm-wide non-adhesive PEG lines. This set-up allows distinguishing ligand-bound from unbound integrins, which is impossible on uniformly coated fibronectin surfaces. Whereas the β_1 integrin staining co-localized with fibronectin lines almost throughout the entire cell length, small β_3 clusters overlaid with lines in the cell periphery associated with F-actin bundles. Blebbistatin treatment or inhibition of Rock with Y-27632 disassembled the β_3 integrin clusters on fibronectin lines, whereas β_1 remained unchanged (Fig. 3c). The differential dependence of $\alpha_5\beta_1$ and α_v-class integrins on myosin-II-mediated tension at focal adhesions suggested that tension-dependent stabilization of α_v-class integrins contributes to rigidity sensing. In line with this hypothesis, traction-force measurements of pKO-β_1 and pKO-α_v/β_1 cells plated on micropatterned polyacrylamide gels of 3 different rigidities (1.4, 10 and 35 kPa) revealed that only pKO-α_v/β_1, but not pKO-β_1, cells were able to increase contractile energies concomitantly with the substrate rigidity. Most notably, the traction forces and contractile energies generated by pKO-β_1 and pKO-α_v/β_1 cells were similar on soft, 1.4 kPa substrates, whereas they differed significantly on stiffer substrates (Fig. 3d,e). We therefore conclude that stabilization of $\alpha_v\beta_3$–fibronectin bonds through actomyosin-mediated tension is required to adjust cell contractility to defined substrate stiffnesses.

Adhesome composition and stoichiometry is controlled by the integrin class and myosin II activity

Cells sense their environment through integrins and numerous plaque proteins in focal adhesions[17,30]. The composition and stoichiometry of the adhesome in fibronectin-bound fibroblasts is controlled by myosin II (refs 19,20). We therefore reasoned that specific binding activities of the integrin cytoplasmic tails and also the differential myosin II activities in pKO-α_v, pKO-β_1 and pKO-α_v/β_1

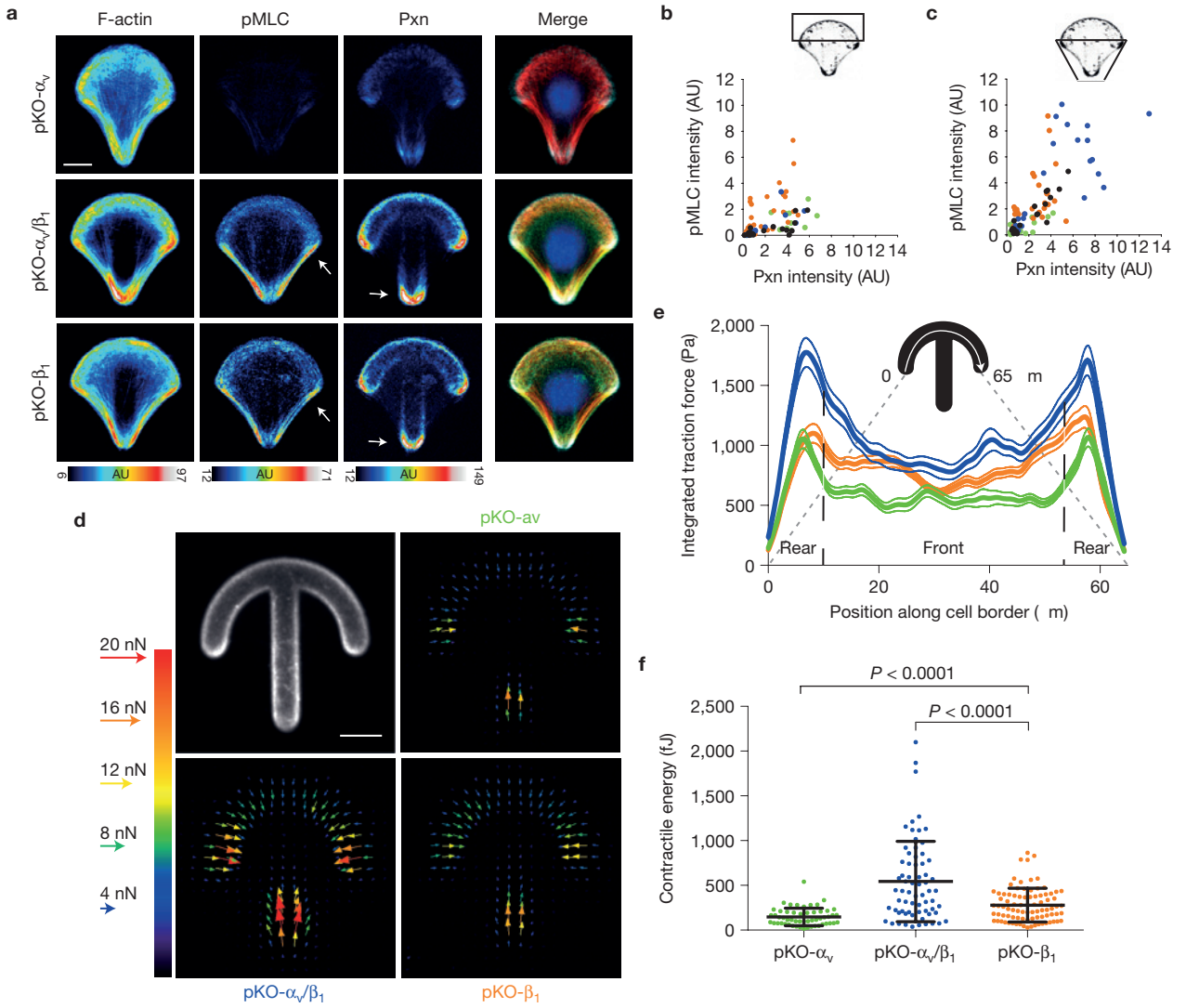

Figure 2 α_v-class integrins cooperate with $\alpha_5\beta_1$ for myosin II reinforcement on stiff fibronectin-coated substrates. (**a**) Averaged confocal images of immunostainings (Merge: F-actin, red; pMLC, green; paxillin, blue; DAPI, blue) of the indicated cell lines plated for 3 h on fibronectin-coated micropatterns (pKO-α_v $n = 55$, pKO-β_1 $n = 36$, pKO-α_v/β_1 $n = 71$; data aggregated over 3 independent experiments). Areas with strong pMLC and paxillin fluorescent signals are marked with arrows. Scale bar, 10 μm. (**b**,**c**) Intensities of pMLC and paxillin (Pxn) fluorescence in the front (**b**) and rear (**c**) regions of individual cells (pKO-α_v $n = 25$, pKO-β_1 $n = 32$, pKO-α_v/β_1 $n = 26$; 1 representative of 3 independent experiments is shown). Optionally, cells were treated with the α_v-class integrin inhibitor cilengitide (1 μM). (**d**) Average traction-force fields of indicated cell types (pKO-α_v $n = 54$, pKO-β_1 $n = 86$, pKO-α_v/β_1 $n = 68$; data aggregated over 3 independent experiments). Arrows indicate force orientation; colour and length represent local force magnitude in nanonewtons. Scale bar, 10 μm. (**e**) Average integrated traction forces along the cell border (pKO-α_v $n = 54$, pKO-β_1 $n = 86$, pKO-α_v/β_1 $n = 58$; data aggregated over 3 independent experiments; thin lines represent s.e.m.). (**f**) Contractile energy of individual cells (pKO-α_v $n = 54$, pKO-β_1 $n = 86$, pKO-α_v/β_1 $n = 68$; data aggregated over 3 independent experiments). Each data point corresponds to the total contractile energy of an individual cell measured by traction-force microscopy. All statistical comparisons were *t*-tests (error bars represent s.e.m.). pKO-α_v (green); pKO-α_v/β_1 (blue); pKO-β_1 (orange); pKOα_v/β_1 + 1 μM cilengitide (black).

cells may contribute to their specific adhesome composition. To test this hypothesis we determined the integrin-class-specific protein composition of focal adhesions. The three cell lines were plated for 45 or 90 min on fibronectin or poly-L-lysine (PLL; permits integrin-independent adhesion) followed by chemical crosslinking and purification of focal adhesions, sample elution and quantitative MS as described previously[19] (Supplementary Fig. S4a and Table S1). Isolated adhesome proteins were quantified using the label-free quantification algorithm of the MaxQuant software[31]. We calculated median MS intensities of 3–4 replicates and performed hierarchical clustering to compare the three cell lines at different time points with and without blebbistatin. This approach allowed identifying protein groups with high correlation of their intensity changes across different substrates, time points and cell lines. We identified a cluster containing 168 proteins significantly enriched for known (previously annotated) focal adhesion proteins. In addition to the 168 proteins, we also considered all previously annotated focal adhesion proteins[32] assigned to other clusters in our analysis. This led to 245 proteins used for further analysis (Supplementary Fig. S4b). Analysis of variance (ANOVA) tests revealed that MS intensities of 62% (152/245) of them were significantly changed

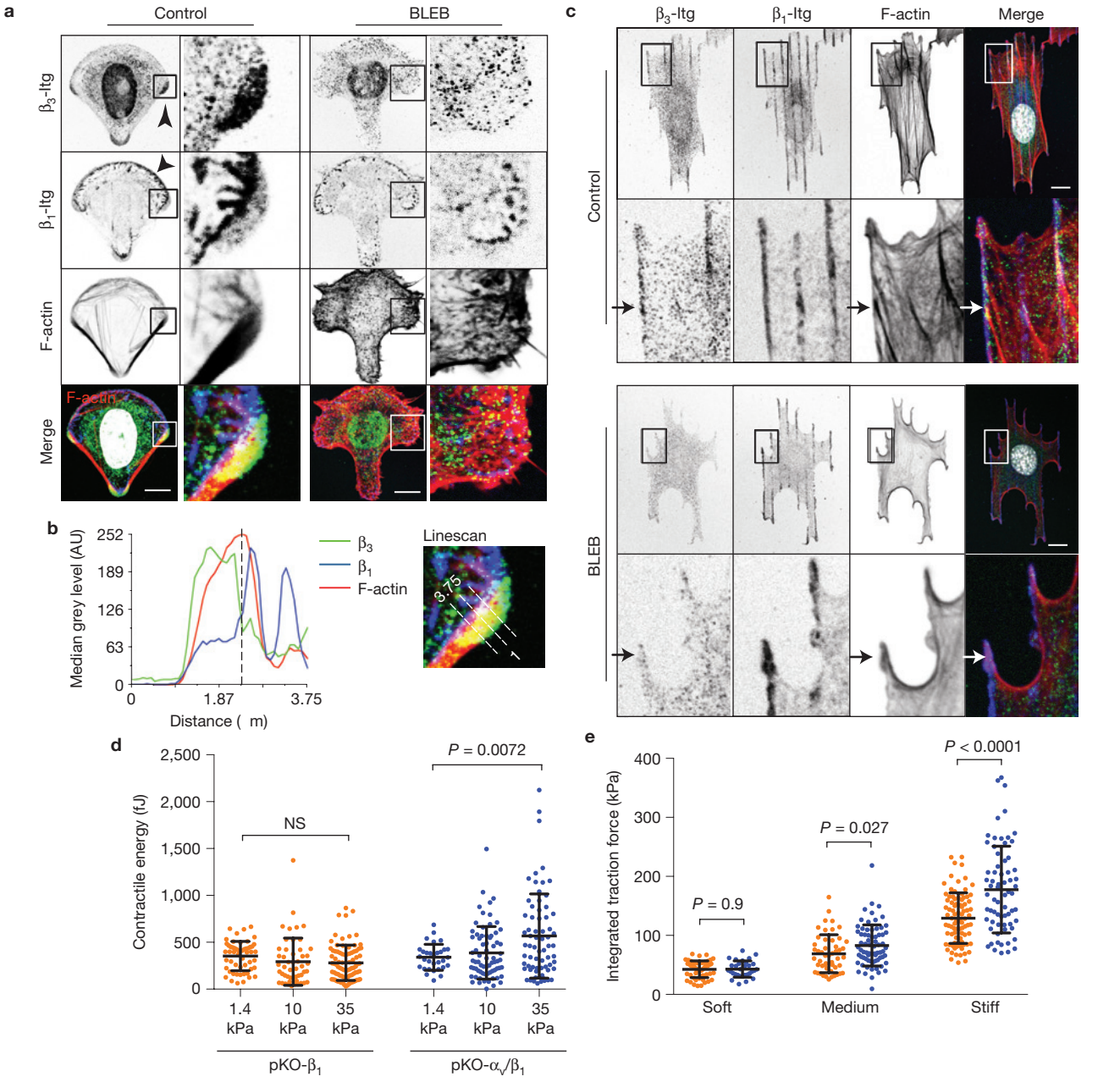

Figure 3 α_v-class integrins accumulate in adhesion areas exposed to high traction force and cooperate with $\alpha_5\beta_1$ for rigidity sensing on fibronectin. (**a**) pKO-α_v/β_1 cells were plated on fibronectin-coated crossbow shapes for 3 h with and without blebbistatin (BLEB) and immunostained for β_1 (blue), β_3 (green) integrins and F-actin (red). Scale bars, 10 μm. DAPI, white (left panel, merge). (**b**) Fluorescence intensity profile of the indicated stainings along the depicted linescan (3.75 μm). (**c**) pKO-α_v/β_1 cells were plated on 1 μm thin fibronectin-coated lines for 90 min with and without blebbistatin and stained for β_1 (blue), β_3 (green) integrin and F-actin (red). Scale bars, 10 μm. DAPI, white (merge). (**d**) Each data point represents the total contractile energy of individual cells measured by traction-force microscopy on gels of indicated rigidities (pKO-β_1: soft $n = 54$, medium $n = 50$, stiff $n = 86$; pKO-α_v/β_1: soft $n = 31$, medium $n = 71$, stiff $n = 68$; data aggregated over 3 independent experiments; all pairwise statistical comparisons from *t*-tests are shown in Supplementary Table S5; NS, not significant). (**e**) Each data point represents the total integrated traction force in kilo Pascal (kPa) of individual cells measured by traction-force microscopy on gels of indicated rigidities (pKO-β_1: soft $n = 54$, medium $n = 50$, stiff $n = 86$; pKO-α_v/β_1: soft $n = 31$, medium $n = 71$, stiff $n = 68$; data aggregated over 3 independent experiments; *P* values of pairwise comparisons were calculated with a *t*-test). pKO-α_v/β_1 (blue); pKO-β_1 (orange).

in at least one of the three cell lines or one of the two time points (Supplementary Table S1).

In line with our previous report[19], blebbistatin induced different intensity reductions in floxed fibroblasts for different classes of adhesome proteins. Following blebbistatin treatment pKO-α_v/β_1 and pKO-β_1 cells were still able to recruit integrin-proximal proteins such as Talin-1, Kindlin-2 and ILK, whereas LIM-domain-containing proteins were reduced to background levels defined by MS intensities from cells seeded on PLL (Fig. 4a). Strikingly, blebbistatin reduced almost all focal adhesion proteins to background levels in pKO-α_v cells, indicating that

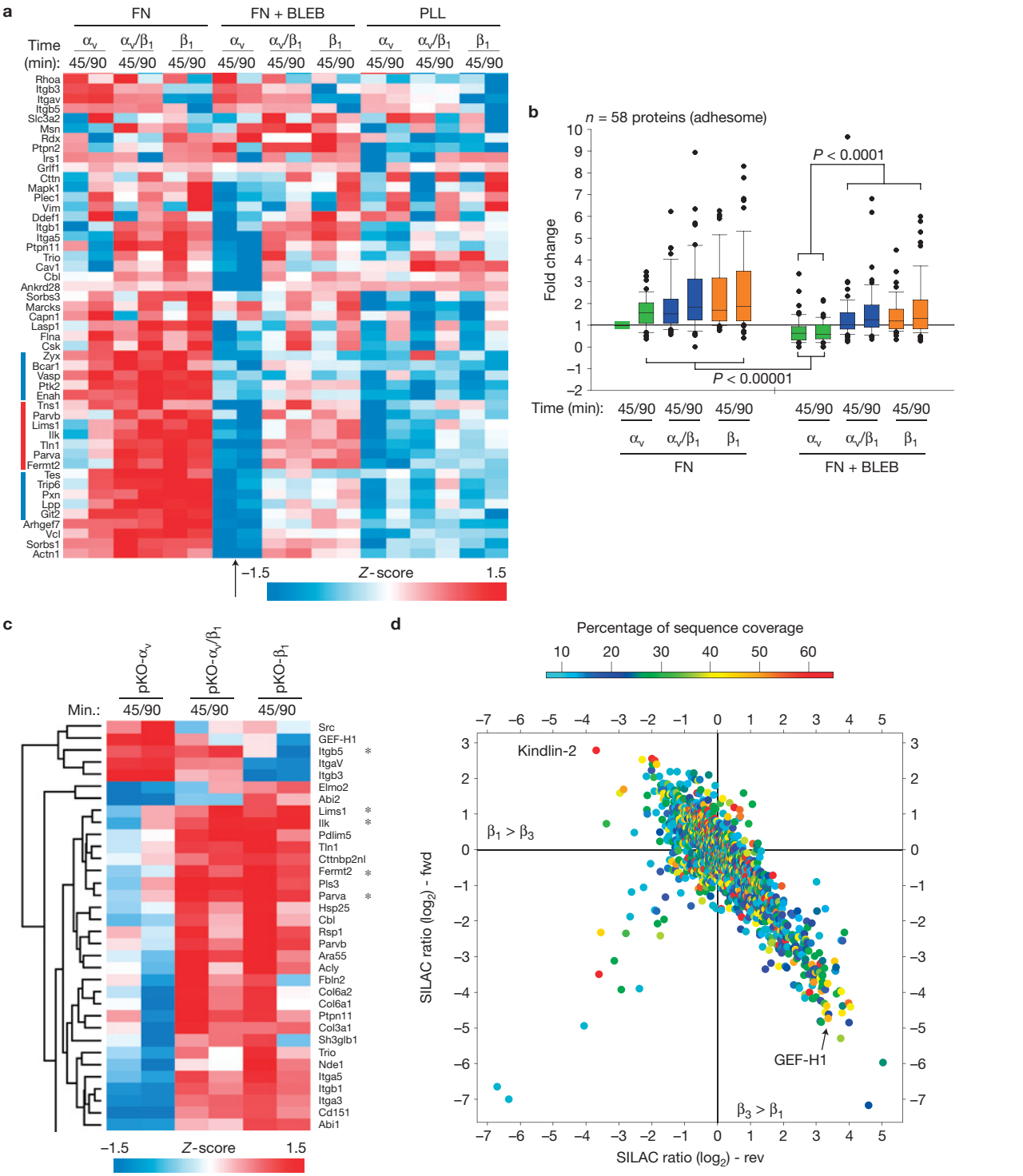

Figure 4 Composition and stoichiometry of the adhesome is determined by the individual integrin and myosin II activity. (**a**) Focal-adhesion-enriched fractions analysed by MS before and after blebbistatin (BLEB) treatment. The *Z*-scores of median MS intensities ($n = 3$–4) are colour coded to show relative protein abundance. A blebbistatin-insensitive cluster is marked with a red bar and blebbistatin-sensitive clusters are marked with blue bars. The arrow highlights the pronounced effect of blebbistatin on pKO-α_v cells. FN, fibronectin. (**b**) Boxplots showing MS intensity differences of 58 known focal adhesion proteins of the indicated cells relative to pKO-α_v cells cultured for 45 min without blebbistatin. A *t*-test revealed significant MS intensity changes after blebbistatin treatment. Boxplot whisker ends are at 1.5 interquartile range and outliers are shown as dots. (**c**) Focal adhesion proteins with similar *Z*-score profiles (colour coded) as $\alpha_5\beta_1$ or α_v-class integrins (selection based on Supplementary Fig. S6) were subjected to hierarchical cluster analysis. Focal-adhesion-enriched fractions were collected 45 and 90 min after plating on fibronectin. (**d**) SILAC ratio plot from label-inverted replicates comparing β_1 with β_3 tail pulldowns. Specific interactors have high SILAC ratios in the forward experiment (fwd) and low SILAC ratios in the label swapped reverse experiment (rev). The colour code shows the percentage of sequence coverage of the proteins identified by MS analysis ($n = 4$; 2 independent experiments). pKO-α_v (green); pKO-α_v/β_1 (blue); pKO-β_1 (orange).

the protein recruitment to focal adhesions in blebbistatin-treated pKO-α_v/β_1 cells was mediated by $\alpha_5\beta_1$ (Fig. 4a). A paired Student's *t*-test for 58 known focal adhesion proteins confirmed a significant reduction of crosslinked focal adhesion proteins in pKO-α_v cells by blebbistatin (Fig. 4b). Furthermore, comparing the 45 and 90 min time points revealed that protein recruitment to focal adhesions was delayed in pKO-α_v cells (Fig. 4a,b). Importantly, blebbistatin did not change the MS intensities of α_v-class integrins, excluding inefficient integrin crosslinking as the cause for the diminished recruitment of focal adhesion proteins, and indicating that short-lived/weak α_v-class integrin–fibronectin interactions occur in the absence of cell contractility and can be crosslinked. These findings together with those depicted in Fig. 3 indicate that $\alpha_5\beta_1$ can cluster and induce adhesome assemblies in the absence of myosin-II-mediated tension, whereas the ability of α_v-class integrins to cluster and recruit adhesome proteins depends on myosin II activation and/or the stress fibre architecture at focal adhesions.

ILK and GEF-H1 are required for myosin II reinforcement on stiff substrates

Consulting published protein–protein interactions within the adhesome[30], we established a putative core interactome of fibronectin-bound $\alpha_5\beta_1$ or α_v-class integrins (Supplementary Fig. S5). Hierarchical cluster analysis of MS intensities of the 125 core proteins of the integrin interactome from all conditions tested (Supplementary Fig. S6) revealed 29 proteins correlating with MS intensities of $\alpha_5\beta_1$ at both time points and 2 proteins correlating with MS intensities of α_v-class integrins (Fig. 4c). In addition to this integrin interactome, we analysed the MS intensities of all actin-binding proteins in the focal-adhesion-enriched fraction and found that WAVE and Arp2/3 complexes, which drive lamellipodia formation, correlated with $\alpha_5\beta_1$, whereas the RhoA effector mDia1 (Diap1), which drives stress-fibre formation, correlated with α_v-class integrins (Supplementary Fig. S7). We performed stable isotope labelling with amino acids in cell culture (SILAC)-based peptide pulldown assays with β_1 and β_3 integrin tail peptides and scrambled control peptides followed by MS (ref. 33) to identify which of the 29 $\alpha_5\beta_1$-enriched and 2 αv-class integrin-enriched adhesome proteins were enriched through differential associations with integrin cytoplasmic tails. Comparison of integrin-tail interactors with scrambled peptide interactors identified common and specific β_1 tail- and β_3 tail-binding proteins (Supplementary Fig. S8). Talin-1 showed equal binding to β_1 and β_3 tails and was therefore used to control the experiments. In line with the adhesome analysis (Fig. 4c) we observed very high β_1-tail-specific enrichment for Kindlin-2 and a lower enrichment for the ILK/PINCH/Parvin (IPP) complex, and a high β_3-tail-specific enrichment of the RhoA guanine nucleotide exchange factor GEF-H1 (Fig. 4d). Thus, the recruitment of Kindlin-2, the IPP complex and GEF-H1 to focal adhesions is controlled by the integrin tail sequence rather than the different focal adhesion architecture in pKO-β_1 and pKO-α_v cells. Ratiometric analysis of fluorescence intensities in focal adhesions confirmed higher Kindlin-2 and ILK levels in pKO-β_1 cells and pKO-α_v/β_1 cells (Fig. 5a–d). To analyse GEF-H1 levels in focal adhesions we first chemically crosslinked and unroofed the cells to remove the large cytoplasmic and microtubule-associated GEF-H1 pool, and then performed immunostainings, which revealed that crosslinked GEF-H1 levels were significantly higher in pKO-α_v and pKO-α_v/β_1 cells than in pKO-β_1 cells (Fig. 5e–g).

To investigate whether the IPP complex and GEF-H1 contribute to myosin II regulation by $\alpha_5\beta_1$ and α_v-class integrins we seeded $ILK^{fl/fl}$ (control) and $ILK^{-/-}$ fibroblasts[34] on fibronectin-coated X-shapes and stained for pMLC. $ILK^{-/-}$ fibroblasts had similarly low pMLC signals as pKO-α_v cells (Fig. 5h,i). Furthermore, inhibition of $\alpha_5\beta_1$ with blocking antibodies or α_v-class integrins with cilengitide in $ILK^{fl/fl}$ cells significantly reduced pMLC levels (Fig. 5h,i), confirming that both fibronectin-binding integrin classes are required to activate myosin II. To examine whether GEF-H1 regulates integrin-mediated activation of myosin II on fibronectin-coated X-shapes we depleted GEF-H1 messenger RNA using short interfering RNA (siRNA; Fig. 5j) and found significantly reduced pMLC levels in GEF-H1-silenced pKO-α_v/β_1 cells, slightly reduced levels in pKO-β_1 cells and unaffected levels in pKO-α_v cells (Fig. 5k,l) indicating that GEF-H1 reinforces myosin II activity in a $\alpha_5\beta_1$-dependent manner.

The IPP complex and GEF-H1 have been implicated in cell contractility regulation by tuning RhoA GTPases[35–37]. Therefore, we investigated whether the activity of RhoA and Rac1 are affected in our cell lines. Seeding the three cell lines for 45 min on fibronectin induced a significantly higher RhoA activity in pKO-α_v cells when compared with pKO-β_1 and pKO-α_v/β_1 cells (Fig. 5m). Rac1 activity was the lowest in pKO-α_v cells, higher in pKO-β_1 and the highest in pKO-α_v/β_1 cells (Fig. 5n). As the high GEF-H1 and RhoA levels in focal adhesions of pKO-α_v cells are not able to promote high pMLC, we conclude that only $\alpha_5\beta_1$ can elicit signals for mediating RhoA-driven myosin II activation.

Integrin-specific signalling pathways cooperate for feedback regulation of myosin II

The coupling of active RhoA to its effector Rock requires unknown signalling events that depend on cell adhesion, cell shape and cytoskeletal tension[22]. To uncover integrin-specific regulators of myosin II upstream and downstream of active RhoA we performed SILAC-based quantitative phosphoproteomics of adhesion signalling on fibronectin. We quantified a total of 3,180 proteins (Supplementary Table S2) and 7,529 phosphorylation sites (Supplementary Table S3) in the three cell lines seeded for 45 min on fibronectin. ANOVA tests of triplicate experiments identified 150 proteins and 1,010 phosphorylation events as significantly regulated in at least one of the three cell lines (Fig. 6a and Supplementary Fig. S9, Tables S2 and S3). Hierarchical cluster analysis of the SILAC ratios of the 1,010 phosphorylation events revealed clusters dominated by $\alpha_5\beta_1$ and clusters dominated by α_v-class integrins. We also observed clusters regulated oppositely by $\alpha_5\beta_1$ and α_v-class integrins, indicating antagonistic regulation, and clusters regulated by both integrin classes, indicating synergistic regulation. Using ratio thresholds for the different pairwise comparisons allowed assignment of 646 of the 1,010 determined phospho-sites into either the antagonistic, dominant or synergistic category (Fig. 6b and Supplementary Table S4).

We searched for phospho-sites that influence myosin II activity in an integrin-dependent manner and found that pKO-β_1 and pKO-$\alpha_v\beta_1$ cells showed increased phosphorylation of the RhoA/Rock targets S693-myosin phosphatase-1 (Mypt1; Fig. 6c–e) and S3-cofilin (Fig. 6c–e). MLC phosphorylation can also be induced by Mlck, whose activity is controlled by Ca^{2+} or Erk2 in focal adhesions[38,39]. We observed synergistic downregulation of S364-Mlck and synergistic

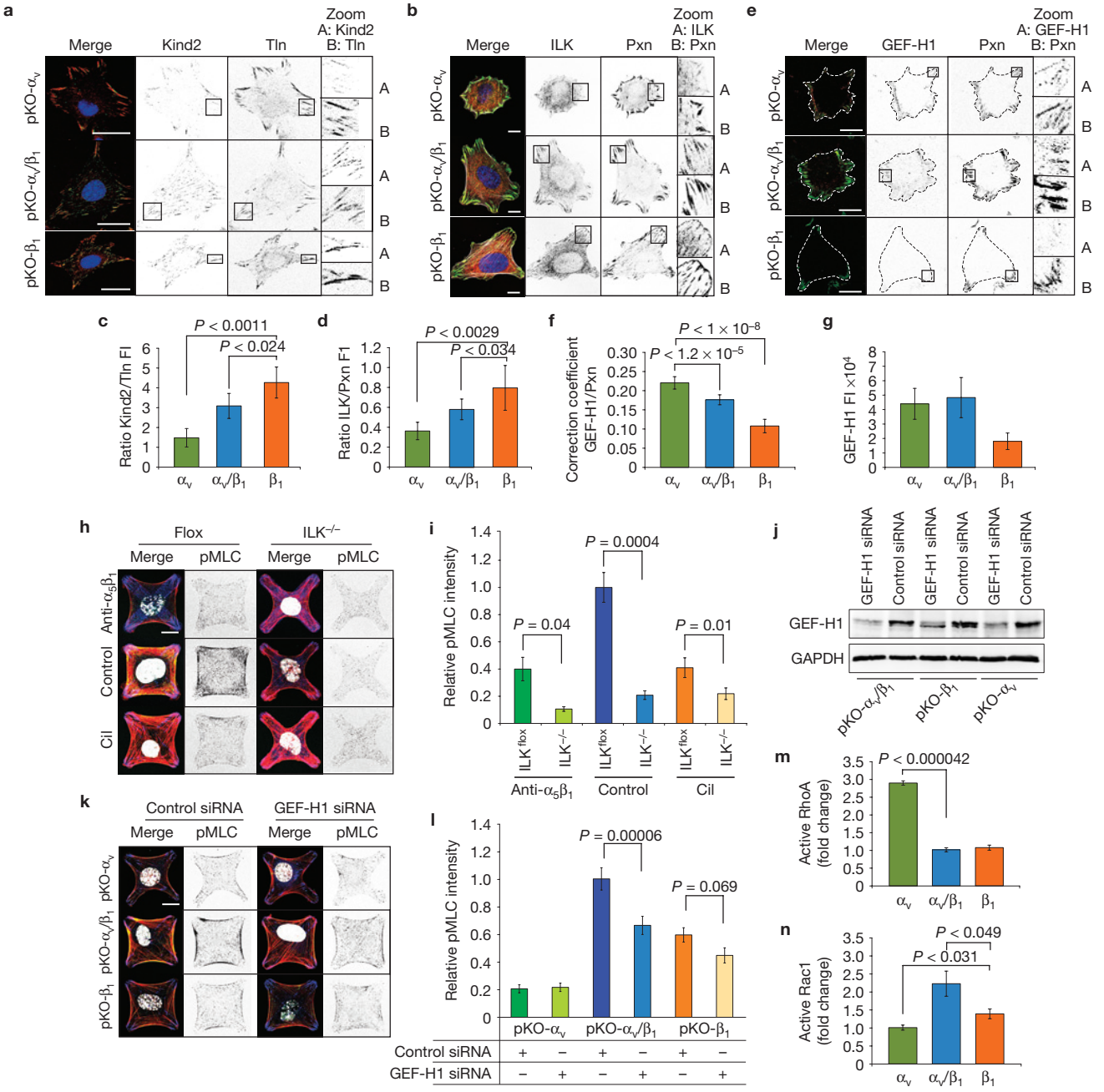

Figure 5 α_v- and β_1-mediated activation of myosin II requires ILK and GEF-H1. (**a**–**f**) Cells were plated on fibronectin-coated glass coverslips for 90 min and immunostained for: Talin-1 (Tln; red) and Kindlin-2 (Kind2; green) (**a**); ILK (red), paxillin (Pxn; green) and F-actin (white) (**b**); or GEF-H1 (red) and paxillin (green) (**e**); scale bars, 10 μm. DAPI, blue (**a**,**b**). Ratios of thresholded fluorescence intensities (FI) were calculated for Kindlin-2 and Talin-1 (pKO-α_v $n = 12$, pKO-β_1 $n = 22$, pKO-α_v/β_1 $n = 22$; results are aggregated over 3 independent experiments) (**c**), and ILK and paxillin (pKO-α_v $n = 33$, pKO-β_1 $n = 40$, pKO-α_v/β_1 $n = 40$; aggregated over 3 independent experiments) (**d**). The correlation coefficient for GEF-H1 and paxillin staining (pKO-α_v $n = 11$, pKO-β_1 $n = 10$, pKO-α_v/β_1 $n = 15$; aggregated over 3 independent experiments) was determined (**f**). (**g**) Total fluorescence intensity of focal-adhesion-retained GEF-H1 after crosslinking and unroofing of cells (pKO-α_v $n = 11$, pKO-β_1 $n = 10$, pKO-α_v/β_1 $n = 15$; aggregated over 3 independent experiments). (**h**) *ILK*$^{-/-}$ and ILK-floxed fibroblasts plated for 3 h on fibronectin-coated X-shapes stained for pMLC, F-actin and paxillin were treated with cilengitide (Cil) to block α_v-class integrins and with monoclonal antibody 2575 to block $\alpha_5\beta_1$. Scale bar, 10 μm. (**i**) Quantification of the relative fluorescence intensities for pMLC to untreated ILK-floxed cells (ILK-flox $n = 26$; ILK-null $n = 17$; ILK-flox +Cil $n = 24$; ILK-null +Cil $n = 12$; ILK-flox +anti-$\alpha_5\beta_1$ $n = 16$, ILK-null anti-$\alpha_5\beta_1$ $n = 10$; data aggregated over 2 independent experiments). (**j**) siRNA-mediated depletion of GEF-H1 confirmed by western blotting. (**k**) Cells were plated on fibronectin-coated X-shapes and stained for pMLC, F-actin and paxillin. Scale bar, 10 μm. (**l**) Quantification of the relative fluorescence intensities for pMLC in siRNA-treated cells (pKO-α_v +control siRNA $n = 24$, pKO-β_1 +control siRNA $n = 48$, pKO-α_v/β_1 +control siRNA $n = 56$, pKO-α_v + GefH1 siRNA $n = 22$, pKO-β_1 + GefH1 siRNA $n = 34$, pKO-α_v/β_1 + GefH1 siRNA $n = 59$; data aggregated over 2 independent experiments). (**m**) Relative RhoA–GTP loading in cells plated for 45 min on fibronectin ($n = 9$; 1 representative of 3 independent experiments is shown). (**n**) Relative Rac1–GTP loading in cells plated for 45 min on fibronectin ($n = 9$; 1 representative out of 3 independent experiments is shown). Error bars represent s.e.m. and *P* values were calculated using a *t*-test. pKO-α_v (green); pKO-α_v/β_1 (blue); pKO-β_1 (orange).

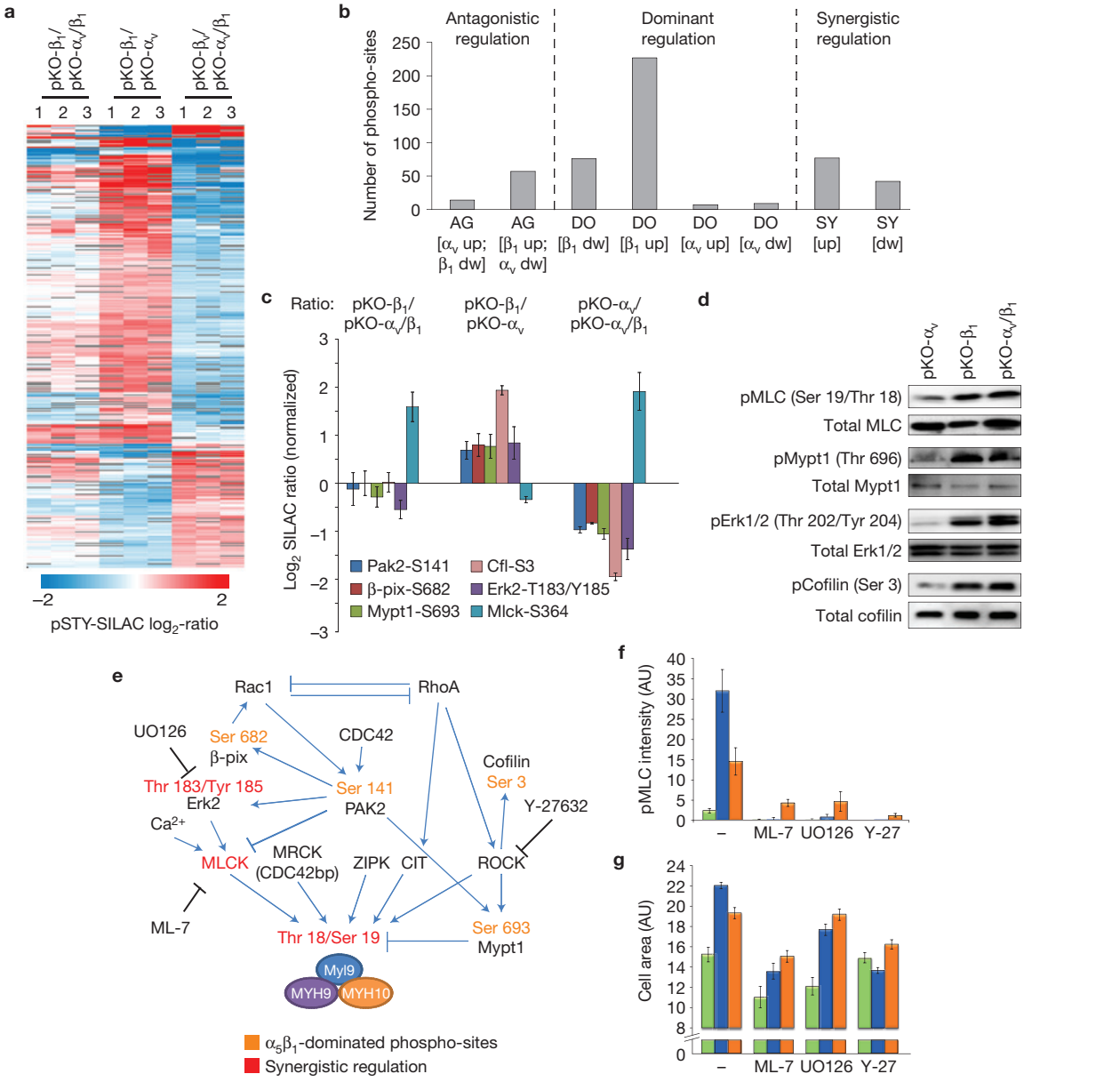

Figure 6 Integrin-specific phosphorylation landscapes on adhesion to fibronectin. (**a**) Hierarchical cluster analysis of SILAC ratios of 1,010 significantly regulated (ANOVA test and Benjamini/Hochberg false discovery rate) phosphorylation events in the indicated cells plated for 45 min on fibronectin from 3 independent replicates. The colour code depicts the normalized $\log_2$ SILAC ratio between cell lines. (**b**) The bar graph shows the number of phosphorylation events grouped into different modes of regulation based on the indicated SILAC ratio threshold criteria. AG, antagonistic; DO, dominant; SY, synergistic. (**c**) SILAC ratios for selected phosphorylation events. The bar graph depicts the median of 3 independent experiments with error bars showing the s.d. (**d**) A selection of differentially regulated phosphorylation events confirmed by western blotting using phospho-site-specific antibodies. (**e**) Signalling network with differentially regulated phosphorylation events shown to be functionally relevant in cell protrusion or contraction. Sites dominated by $\alpha_5\beta_1$ or synergistically upregulated in pKO-α_v/β_1 cells are shown. (**f**,**g**) Mean pMLC fluorescence intensity (**f**) and mean cell area (**g**) on fibronectin-coated X-shapes before and after treatment with ML-7 (25 μM) to inhibit Mlck, UO126 (50 μM) to inhibit ERK and Y-27632 (10 μM) to inhibit Rock. (pKO-α_v: untreated $n = 12$, +ML-7 $n = 10$, +U0126 $n = 15$, +Y-27 $n = 16$; pKO-β_1: untreated $n = 16$, +ML-7 $n = 17$, +U0126 $n = 19$, +Y-27 $n = 21$; pKO-α_v/β_1: untreated $n = 11$, +ML-7 $n = 18$, +U0126 $n = 19$, +Y-27 $n = 30$; 1 representative of 3 independent experiments is shown; all pairwise statistical comparisons using *t*-tests are shown in Supplementary Table S5; error bars represent s.e.m.). pKO-α_v, green; pKO-α_v/β_1, blue; pKO-β_1, orange.

upregulation of pT183/pY185-Erk2 activities in pKO-α_v/β_1 cells (Fig. 6c–e). Western blotting using phospho-site-specific antibodies corroborated these results (Fig. 6d). We uncovered three pathways (Erk2, Rock, Mlck) that were differentially regulated by the two integrin classes following adhesion to fibronectin, and reasoned that inhibition of either one or any combination of these pathways would abrogate synergistic myosin II reinforcement. Indeed, the cooperative activation of myosin II in pKO-α_v/β_1 cells was blocked by inhibiting Erk (UO126), Rock (Y-27632) or Mlck (ML-7; Fig. 6f,g). To confirm the relevance of this finding, we overexpressed constitutively active (ca-) kinase

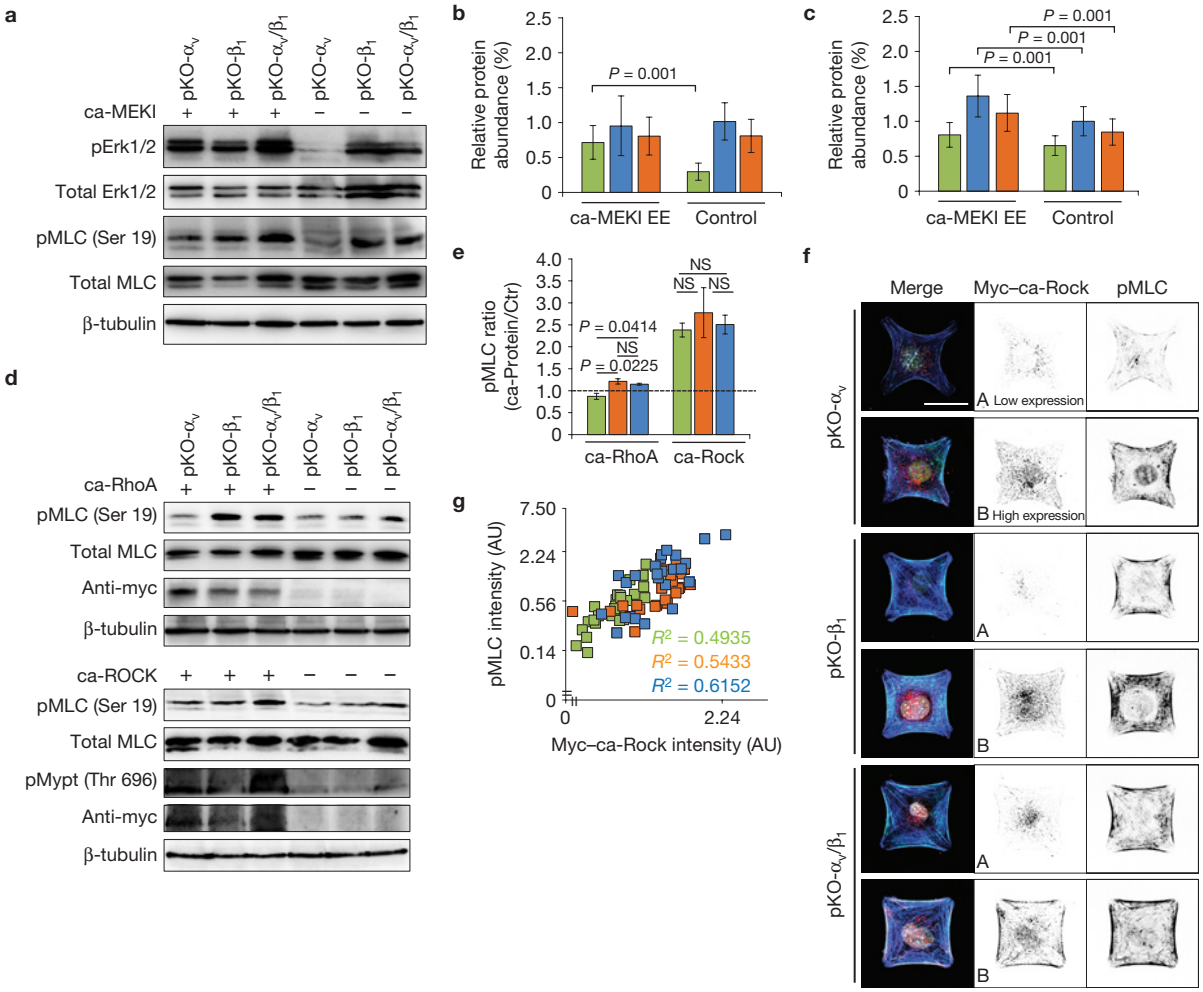

Figure 7 Activation of Rock is $\alpha_5\beta_1$-dependent. (**a**–**c**) Total cell lysates of cells plated for 90 min on fibronectin in the indicated conditions and analysed by western blotting with phospho-specific antibodies. The levels of pErk2 (**b**) and pMLC (**c**) were quantified using densitometry ($n = 3$). (**d**) A representative western blot analysis of cells transfected with myc-tagged ca-RhoA or myc-tagged ca-ROCK constructs and probed with the indicated antibodies. (**e**) Densitometric quantification of western blots ($n = 3$). The bar graphs show ratios of pMLC signals from cells expressing ca-RhoA or ca-Rock over the empty vector control. NS, not significant. (**f**) Confocal image of indicated cells transfected with a myc-tagged ca-ROCK construct, seeded on fibronectin-coated crossbow shapes and immunostained with Myc (red), pMLC (green), F-actin (blue) and DAPI (white). Scale bar, 25 μm. (**g**) Pearson correlation coefficient of fluorescence intensities of pMLC and Myc staining for the three cell lines (pKO-α_v $n = 30$; pKO-β_1 $n = 25$; pKO-α_v/β_1 $n = 25$; 1 representative of 3 independent experiments is shown). All error bars represent s.d. and P values were calculated using a t-test. pKO-α_v (green); pKO-α_v/β_1 (blue); pKO-β_1 (orange). Uncropped images of blots are shown in Supplementary Fig. S10.

constructs and measured their effects on pMLC. Overexpression of ca-MEK1 rescued the low pErk2 levels and significantly increased pMLC in pKO-α_v cells (Fig. 7a–c). The high RhoA and low Rock and pMLC activities in pKO-α_v cells (Figs 5 and 6) suggest that α_v-class integrins are unable to couple active RhoA to Rock, which was tested by overexpressing ca-RhoA or ca-Rock in the three cell lines. Whereas ca-RhoA significantly increased pMLC in pKO-β_1 and pKO-α_v/β_1, pMLC levels remained unchanged in pKO-α_v cells. In sharp contrast, ca-Rock increased pMLC twofold in all three cell lines (Fig. 7d,e), indicating that endogenous Rock in pKO-α_v cells remained inactive even in the presence of high RhoA–GTP. This finding was further confirmed with pMLC staining of cells seeded on fibronectin-coated X shapes (Fig. 7f,g). In conclusion, the Mek1/Erk2 and the RhoA/Rock/pMLC pathways are preferentially induced by $\alpha_5\beta_1$, whereas the high RhoA activity induced in pKO-α_v cells is not coupled to Rock/pMLC.

DISCUSSION

We reconstituted pan-integrin-deficient fibroblasts with β_1- and/or α_v-class integrins and correlated integrin-class-specific cellular phenotypes with integrin-class-specific adhesome composition and signalling events. Fibroblasts exploring fibronectin-based microenvironments engage $\alpha_5\beta_1$ and α_v-class integrins to orchestrate membrane protrusions, cell contractility and cell migration. Our cell line analyses revealed a series of signalling events accomplished by $\alpha_5\beta_1$ integrins, which activate Rac1, induce membrane protrusions, assemble nascent adhesions and generate RhoA/Rock-mediated myosin II activity. In conjunction with these events, mechanosensitive α_v-class integrins accumulate in areas subjected to high tension and reinforce adhesive sites to induce further activation of myosin II and development of large focal adhesions and actomyosin bundles (Fig. 8). Our study uncovers a sequence of tightly integrated biophysical and biochemical events induced by $\alpha_5\beta_1$ and

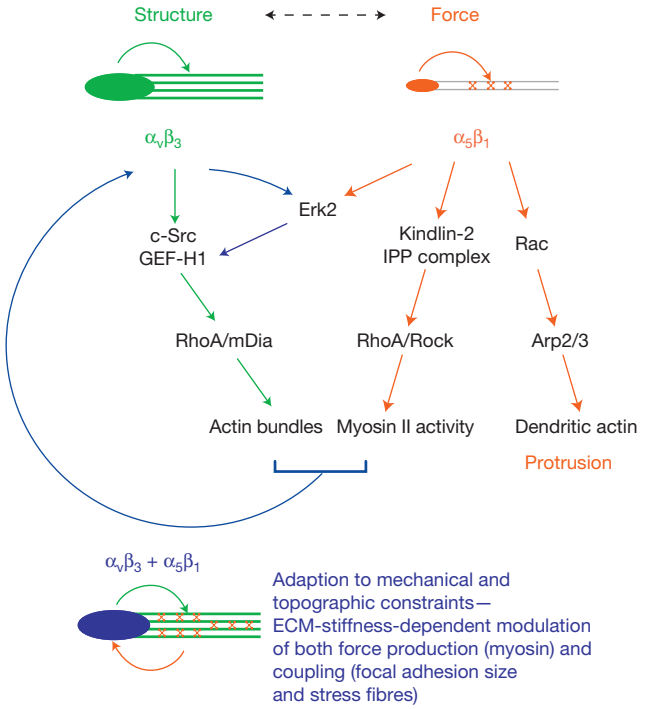

Figure 8 Model of $\alpha_5\beta_1$ and α_v-class integrin cooperation during rigidity sensing. $\alpha_5\beta_1$ integrins adhere to fibronectin, and assemble Kindlin-2- and ILK-rich small peripheral adhesions in a myosin-II-independent manner. The protein assembly in $\alpha_5\beta_1$-containing adhesions activates Rac1, Wave and Arp2/3-driven actin polymerization to induce membrane protrusions, and RhoA/Rock-mediated myosin II activation to induce tension. This tension increases the adhesion lifetime of α_v-class integrins bound to ligand on stiff substrates, which reinforces and stabilizes focal adhesions. α_v-class integrins recruit GEF-H1 to focal adhesions, which reinforces RhoA/myosin II in a $\alpha_5\beta_1$-dependent manner, and increases RhoA activity to promote mDia-mediated stress fibre formation. The combination of α_v-class integrin-mediated structure (focal-adhesion anchoring and stress-fibre formation) with the $\alpha_5\beta_1$-mediated force generation (myosin II activity) constitutes a synergistic system, which is important for adapting cellular contractility and architecture to the rigidity of fibronectin-based microenvironments.

α_v-class integrins that adjust fibroblast contractility to the rigidity of fibronectin-coated substrates. The cooperation of $\alpha_5\beta_1$ and α_v-class integrins to sense the rigidity of fibronectin-based microenvironments predicts that cell migration towards a rigidity gradient, called durotaxis, may also depend on the cooperation of both integrins. These findings have potential ramifications for certain pathologies, such as fibrosis and tumour metastasis where rigidity sensing of fibronectin matrices is crucial in disease progression[40].

To better understand how distinct integrin classes individually and cooperatively probe the biophysical properties of a fibronectin-based microenvironment, we established a cell model system and used proteomics methods to characterize their focal adhesion composition, phospho-signalling and proteome changes. Our comprehensive proteomic data set of adhesion signalling revealed that integrin-class-specific adhesomes and phospho-proteomes are enriched with integrin-specific adapter proteins and signalling intermediates. Several well-known integrin outside-in signalling pathways, including the Rac1/Wave/Arp2,3 and RhoA/Rock pathways, were dominated by $\alpha_5\beta_1$ integrins. Interestingly, the pKO-β_1 cells developed very few stress fibres, indicating that $\alpha_5\beta_1$-induced RhoA activity was preferably used for production of myosin-II-mediated force but not formin-mediated stress-fibre formation. In contrast, the pKO-α_v cells exhibited high RhoA activity, which in turn induced the formation of thick stress fibres, most likely through the activation of mDia, but did not activate Rock/pMLC/myosin II. The coupling of active RhoA to different downstream effectors by distinct integrin classes was unanticipated. The underlying mechanism(s) are unclear, but probably involve specific mark(s) either attached to active RhoA or to the effectors enabling differential interactions with GTP-bound RhoA.

Although forces play an important role in the assembly of focal adhesions, pKO-α_v cells induced the largest focal adhesions among the three cell lines and also exhibited the lowest myosin II activities and traction forces. Focal adhesion size is not the sole predictor of traction forces and the final focal adhesion size can also be determined by an mDia-dependent mechanism[41,42]. Therefore, we propose that the large size of focal adhesions in pKO-α_v cells depends on RhoA/mDia-induced stress fibres rather than on myosin II. However, although the final focal adhesion size in pKO-α_v cells was myosin-II-independent, their formation and/or stability were strictly myosin-II-dependent, evidenced by the pronounced destabilization of α_v-class integrin adhesions with blebbistatin. A role for α_v-class integrins for focal adhesion stabilization has also been obtained from single-protein tracking experiments of β_1 and β_3 integrins, which showed that β_3 integrins are immobilized in large focal adhesions, whereas β_1 integrins are more mobile[29]. The necessity of $\alpha_v\beta_3$ for cell stiffening following force application has also been postulated[43]. Similarly, the recruitment of GEF-H1 to focal adhesions and Erk2 activity was reported as necessary for cell stiffening following force application[35]. Our results link these observations and suggest that force-mediated stabilization of α_v–fibronectin bonds will reinforce focal adhesions, increase local concentrations of GEF-H1 and activate RhoA following $\alpha_5\beta_1$-induced Erk2 activation. Therefore, α_v-class integrins could be capable of forming stronger extracellular catch bonds with fibronectin than $\alpha_5\beta_1$ integrins do[44], resulting in longer bond lifetimes of α_v-class integrins with fibronectin when force is applied. However, as the influence of force on the on and off rates of $\alpha_5\beta_1$ and α_v-class integrins with fibronectin have not been systematically studied, this hypothesis awaits future testing. □

METHODS

Methods and any associated references are available in the online version of the paper.

Note: Supplementary Information is available in the online version of the paper

ACKNOWLEDGEMENTS

We thank J. Cox for software tool development, U. Kuhn and C. Boulegue (MPIB) and A. F. Christ (CNRS/UJF/INRA/CEA) for excellent technical support, and A. Meves, T. Geiger and D. Boettiger for discussions. H.B.S. was a fellow of the European Molecular Biology Organisation (EMBO) and M-R.H. a fellow of the Boehringer Ingelheim fonds. The work was financially supported by the ERC, DFG and the Max Planck Society.

AUTHOR CONTRIBUTIONS

R.F. initiated the project; R.F. and H.B.S. designed the experiments and wrote the paper; H.B.S., M-R.H., T.V., S.Z., J.P., Z.S. and A.R. performed experiments; H.B.S., M-R.H., T.V., S.Z., K-E.G., C.C.F. and R.F. analysed data; J.P., M.T., K-E.G. and M.M. provided important reagents and/or analytical tools; all authors read and approved the manuscript.

COMPETING FINANCIAL INTERESTS
The authors declare no competing financial interests.

Published online at www.nature.com/doifinder/10.1038/ncb2747
Reprints and permissions information is available online at www.nature.com/reprints

1. Hynes, R. O. Integrins: bidirectional, allosteric signaling machines. *Cell* **110,** 673–687 (2002).
2. Desgrosellier, J. S. & Cheresh, D. A. Integrins in cancer: biological implications and therapeutic opportunities. *Nat. Rev. Cancer* **10,** 9–22 (2010).
3. Avraamides, C. J., Garmy-Susini, B. & Varner, J. A. Integrins in angiogenesis and lymphangiogenesis. *Nat. Rev. Cancer* **8,** 604–617 (2008).
4. Liu, H. *et al.* MYC suppresses cancer metastasis by direct transcriptional silencing of α(v) and β(3) integrin subunits. *Nat. Cell Biol.* **14,** 567–574 (2012).
5. Humphries, J. D., Byron, A. & Humphries, M. J. Integrin ligands at a glance. *J. Cell Sci.* **119,** 3901–3903 (2006).
6. Leiss, M., Beckmann, K., Giros, A., Costell, M. & Fassler, R. The role of integrin binding sites in fibronectin matrix assembly *in vivo*. *Curr. Opin. Cell Biol.* **20,** 502–507 (2008).
7. Yang, J. T., Rayburn, H. & Hynes, R. O. Embryonic mesodermal defects in α_5 integrin-deficient mice. *Development* **119,** 1093–1105 (1993).
8. Bader, B. L., Rayburn, H., Crowley, D. & Hynes, R. O. Extensive vasculogenesis, angiogenesis, and organogenesis precede lethality in mice lacking all α_v integrins. *Cell* **95,** 507–519 (1998).
9. Yang, J. T. *et al.* Overlapping and independent functions of fibronectin receptor integrins in early mesodermal development. *Dev. Biol.* **215,** 264–277 (1999).
10. Zamir, E. *et al.* Dynamics and segregation of cell–matrix adhesions in cultured fibroblasts. *Nat. Cell Biol.* **2,** 191–196 (2000).
11. Ballestrem, C., Hinz, B., Imhof, B. A. & Wehrle-Haller, B. Marching at the front and dragging behind: differential $\alpha_v\beta_3$-integrin turnover regulates focal adhesion behavior. *J. Cell Biol.* **155,** 1319–1332 (2001).
12. Danen, E. H., Sonneveld, P., Brakebusch, C., Fassler, R. & Sonnenberg, A. The fibronectin-binding integrins $\alpha_5\beta_1$ and $\alpha_v\beta_3$ differentially modulate RhoA–GTP loading, organization of cell matrix adhesions, and fibronectin fibrillogenesis. *J. Cell Biol.* **159,** 1071–1086 (2002).
13. White, D. P., Caswell, P. T. & Norman, J. C. $\alpha_v\beta_3$ and $\alpha_5\beta_1$ integrin recycling pathways dictate downstream Rho kinase signaling to regulate persistent cell migration. *J. Cell Biol.* **177,** 515–525 (2007).
14. Morgan, M. R., Byron, A., Humphries, M. J. & Bass, M. D. Giving off mixed signals-distinct functions of α(5)β(1) and α(v)β(3) integrins in regulating cell behaviour. *IUBMB Life* **61,** 731–738 (2009).
15. Van der Flier, A. *et al.* Endothelial α_5 and α_v integrins cooperate in remodeling of the vasculature during development. *Development* **137,** 2439–2449 (2010).
16. Choi, C. K. *et al.* Actin and α-actinin orchestrate the assembly and maturation of nascent adhesions in a myosin II motor-independent manner. *Nat. Cell Biol.* **10,** 1039–1050 (2008).
17. Geiger, B., Spatz, J. P. & Bershadsky, A. D. Environmental sensing through focal adhesions. *Nat. Rev. Mol. Cell Biol.* **10,** 21–33 (2009).
18. Bershadsky, A., Kozlov, M. & Geiger, B. Adhesion-mediated mechanosensitivity: a time to experiment, and a time to theorize. *Curr. Opin. Cell Biol.* **18,** 472–481 (2006).
19. Schiller, H. B., Friedel, C. C., Boulegue, C. & Fassler, R. Quantitative proteomics of the integrin adhesome show a myosin II-dependent recruitment of LIM domain proteins. *EMBO Rep.* **12,** 259–266 (2011).
20. Kuo, J. C., Han, X., Hsiao, C. T., Yates Iii, J. R. & Waterman, C. M. Analysis of the myosin II-responsive focal adhesion proteome reveals a role for β-Pix in negative regulation of focal adhesion maturation. *Nat. Cell Biol.* **13,** 383–393 (2011).
21. Lammermann, T. *et al.* Rapid leukocyte migration by integrin-independent flowing and squeezing. *Nature* **453,** 51–55 (2008).
22. Bhadriraju, K. *et al.* Activation of ROCK by RhoA is regulated by cell adhesion, shape, and cytoskeletal tension. *Exp. Cell Res.* **313,** 3616–3623 (2007).
23. Danen, E. H. *et al.* Integrins control motile strategy through a Rho-cofilin pathway. *J. Cell Biol.* **169,** 515–526 (2005).
24. Worth, D. C. *et al.* $\alpha_v\beta_3$ integrin spatially regulates VASP and RIAM to control adhesion dynamics and migration. *J. Cell Biol.* **189,** 369–383 (2010).
25. Huttenlocher, A. & Horwitz, A. R. Integrins in cell migration. *Cold Spr. Harbor Perspec. Biol.* **3,** a005074 (2011).
26. Thery, M. *et al.* Anisotropy of cell adhesive microenvironment governs cell internal organization and orientation of polarity. *Proc. Natl Acad. Sci. USA* **103,** 19771–19776 (2006).
27. Thery, M. Micropatterning as a tool to decipher cell morphogenesis and functions. *J. Cell Sci.* **123,** 4201–4213 (2010).
28. Tseng, Q. *et al.* A new micropatterning method of soft substrates reveals that different tumorigenic signals can promote or reduce cell contraction levels. *Lab on a Chip* **11,** 2231–2240 (2011).
29. Rossier, O. *et al.* Integrins β_1 and β_3 exhibit distinct dynamic nanoscale organizations inside focal adhesions. *Nat. Cell Biol.* **14,** 1057–1067 (2012).
30. Zaidel-Bar, R., Itzkovitz, S., Ma'ayan, A., Iyengar, R. & Geiger, B. Functional atlas of the integrin adhesome. *Nat. Cell Biol.* **9,** 858–867 (2007).
31. Cox, J. & Mann, M. MaxQuant enables high peptide identification rates, individualized p.p.b.-range mass accuracies and proteome-wide protein quantification. *Nat. Biotech.* **26,** 1367–1372 (2008).
32. Zaidel-Bar, R. & Geiger, B. The switchable integrin adhesome. *J. Cell Sci.* **123,** 1385–1388 (2010).
33. Meves, A. *et al.* {β}1 integrin cytoplasmic tyrosines promote skin tumorigenesis independent of their phosphorylation. *Proc. Natl Acad. Sci. USA* **108,** 15213–15218 (2011).
34. Sakai, T. *et al.* Integrin-linked kinase (ILK) is required for polarizing the epiblast, cell adhesion, and controlling actin accumulation. *Genes Dev.* **17,** 926–940 (2003).
35. Guilluy, C. *et al.* The Rho GEFs LARG and GEF-H1 regulate the mechanical response to force on integrins. *Nat. Cell Biol.* **13,** 722–727 (2011).
36. Montanez, E., Wickstrom, S. A., Altstatter, J., Chu, H. & Fassler, R. α-parvin controls vascular mural cell recruitment to vessel wall by regulating RhoA/ROCK signalling. *EMBO J.* **28,** 3132–3144 (2009).
37. Montanez, E. *et al.* Kindlin-2 controls bidirectional signaling of integrins. *Genes Dev.* **22,** 1325–1330 (2008).
38. Holzapfel, G., Wehland, J. & Weber, K. Calcium control of actin-myosin based contraction in triton models of mouse 3T3 fibroblasts is mediated by the myosin light chain kinase (MLCK)-calmodulin complex. *Exp. Cell Res.* **148,** 117–126 (1983).
39. Fincham, V. J., James, M., Frame, M. C. & Winder, S. J. Active ERK/MAP kinase is targeted to newly forming cell–matrix adhesions by integrin engagement and v-Src. *EMBO J.* **19,** 2911–2923 (2000).
40. Butcher, D. T., Alliston, T. & Weaver, V. M. A tense situation: forcing tumour progression. *Nat. Rev. Cancer* **9,** 108–122 (2009).
41. Oakes, P. W., Beckham, Y., Stricker, J. & Gardel, M. L. Tension is required but not sufficient for focal adhesion maturation without a stress fibre template. *J. Cell Biol.* **196,** 363–374 (2012).
42. Stricker, J., Aratyn-Schaus, Y., Oakes, P. W. & Gardel, M. L. Spatiotemporal constraints on the force-dependent growth of focal adhesions. *Biophys. J.* **100,** 2883–2893 (2011).
43. Roca-Cusachs, P., Gauthier, N. C., Del Rio, A. & Sheetz, M. P. Clustering of α(5)β(1) integrins determines adhesion strength whereas α(*v*)β(3) and talin enable mechanotransduction. *Proc. Natl Acad. Sci. USA* **106,** 16245–16250 (2009).
44. Kong, F., Garcia, A. J., Mould, A. P., Humphries, M. J. & Zhu, C. Demonstration of catch bonds between an integrin and its ligand. *J. Cell Biol.* **185,** 1275–1284 (2009).

METHODS

Antibodies. Information about antibodies is provided in Supplementary Table S6.

Isolation, immortalization, viral reconstitution and transfection of cell lines. Mouse pKO fibroblasts and reconstituted pKO-α_v, pKO-β_1 and pKOα_v/β_1 cell lines were generated from fibroblasts (floxed parental) derived from the kidney of 21-day-old male mice carrying floxed α_v and β_1 alleles ($\alpha_v^{flox/flox}$, $\beta_1^{flox/flox}$), and constitutive β_2 and β_7 null alleles ($\beta_2^{-/-}$, $\beta_7^{-/-}$; ref. 21). Individual kidney fibroblast clones were immortalized by retroviral delivery of the SV40 large T. The immortalized floxed fibroblast clones were then retrovirally transduced with mouse α_v and/or β_1 integrin cDNAs and the endogenous floxed β_1 and α_v integrin loci were simultaneously deleted by adenoviral transduction of the *Cre* recombinase. Reconstituted cell lines were FACS sorted to obtain cell populations with comparable integrin surface levels to the parental cell clones. Transduction of ca-RhoA (myc–RhoA pcDNA3.1) and ca-ROCK (myc–ROCKD4 pcDNA3.1) was carried out with Lipofectamine 2000 (Invitrogen through Life Technologies) according to the manufacturer's instructions. The transfection control was an empty pcDNA3.1 vector.

Adhesion and cell migration analysis. Adhesion assays were carried out as previously described[45]. Briefly, cells were plated for 20 min in 96-well plates coated with varying concentrations of ECM ligands. After washing the plates the number of adhered cells that remained on the plate was quantified using attenuance at 595 nm.

To analyse random migration, cell culture dishes were coated with fibronectin (5 μg ml^{-1} in PBS; 2 h at room temperature) and blocked with 1% BSA in PBS. After seeding, video time-lapse microscopy was performed using phase contrast at ×20 magnification. A total of 12 migrating pKO-α_v, 12 migrating pKO-α_v/β_1 and 14 migrating pKO-β_1 cells from 5 independent movies were analysed. One pixel in each cell nucleus was marked manually and served as the cell's coordinate. Each tracked cell j with a track length N_j was recorded by its $x_{j,i}$ and yj,i position for every frame i. A tracking point was made every $D_t = 1$ min. The time difference between the tracking coordinates $x_{j,i}$ and $x_{j,i+n}$ is $t = nD_t$, where n is the frame number. The mean squared displacement (msd) of the cell j at time $t = nD_t$ was calculated by

$$msd_j(t) = \frac{1}{N_j - n}\sum_{i=1}^{N_j-n}\left[\left(x_{j,i+n} - x_{j,i}\right)^2 + \left(y_{j,i+n} - y_{j,i}\right)^2\right]$$

All msd values were calculated for all cells and averaged. The used propagated uncertainty for the $msd(t)$ is the standard deviation of the mean. For an increasing n the number of given tracks contributes to $msd(t)$ decreases as well as the propagated uncertainty caused by the tracking uncertainty increases. Therefore, the $msd(t)$ has been cut at $n = 90$. To determine the persistence time P and the diffusion constant D, Fürths formula

$$msd(t) = 4D\left(t - P\left(1 - \exp\left(-\frac{t}{P}\right)\right)\right)$$

has been fitted through the data. The mean velocity of a cell j has been computed as the average of the distance travelled each time step divided by the time step.

Micropatterning and immunostainings. Micropatterns were generated on PEG-coated glass coverslips with deep-ultraviolet lithography[46]. Glass coverslips were incubated in a 1 mM solution of a linear PEG, CH_3–$(O$–CH_2–$CH_2)_{43}$–NH–CO–NH–CH_2–CH_2–CH_2–$Si(OEt)_3$ in dry toluene for 20 h at 80 °C under a nitrogen atmosphere. The substrates were removed, rinsed intensively with ethyl acetate, methanol and water, and dried with nitrogen. A pegylated glass coverslip and a chromium-coated quartz photomask (ML&C, Jena) were immobilized with vacuum onto a mask holder, which was immediately exposed to deep ultraviolet light using a low-pressure mercury lamp (NIQ 60/35 XL longlife lamp, quartz tube, 60 W from Heraeus Noblelight) at 5 cm distance for 7 min. The patterned substrates were subsequently incubated overnight with 100 μl of fibronectin (20 μg ml^{-1} in PBS) at 4 °C and washed once with PBS.

For immunofluorescence microscopy, cells were seeded on micropatterns in DMEM (GIBCO by Life Technologies) containing 0.5 % FBS at 37 °C, 5% CO_2. After 90 or 180 min the medium was soaked off, and cells were fixed with 3% PFA in PBS for 5 min at room temperature, washed with PBS, blocked with 1% BSA in PBS for 1 h at room temperature and then incubated with antibodies. The fluorescent images were collected with a laser scanning confocal microscope (Leica SP5).

Acrylamide micropatterning. Micropatterns were first produced on glass coverslips as previously described[46]. Briefly, 20 mm square glass coverslips were oxidized through oxygen plasma (FEMTO, Diener Electronics) for 10 s at 30 W before incubating with 0.1 mg ml^{-1} poly-L-lysine (PLL)–PEG (PLL20K-G35-PEG2K, JenKem) in 10 mM HEPES, pH 7.4, for 30 min. After drying, coverslips were exposed to 165 nm ultraviolet (UVO cleaner, Jelight) through a photomask (Toppan) for 5 min. Then, coverslips were incubated with 20 mg ml^{-1} of fibronectin (Sigma) and 2 mg ml^{-1} of rhodamine-labelled fibronectin (Cytoskeleton) in 100 mM sodium bicarbonate solution for 30 min. Acrylamide solution containing acrylamide and bisacrylamide (Sigma) was degassed for 20 min under house vacuum and mixed with passivated fluorescent beads (Invitrogen) by sonication before addition of APS and TEMED. A 25 μl drop of this solution was put directly on the micropatterned glass coverslip. A silanized coverslip was placed over the drop and left polymerizing for 30 min (fluorescent beads passivation and glass silanization were performed as previously described[4]). The sandwich was then put in 100 mM sodium bicarbonate solution and the gel was gently removed from the patterned glass coverslip while staying attached to the other coverslip owing to the silanization treatment. This process transferred the protein micropatterns onto the gel as previously described[47]. Three different solutions of 3%/0.225%, 5%/0.225%, 8%/0.264% acrylamide/bisacrylamide were used. The corresponding Young's modulus of the gels was 1.4, 9.6 and 34.8 kPa respectively as measured using AFM. Coverslips were mounted in magnetic chambers (Cytoo) and washed with sterile PBS before plating cells.

AFM measurements of the Young's modulus of acrylamide gels. We measured gel stiffness through nanoindentation using an atomic force microscope (Bruker Nanoscope) mounted with silica-bead-tipped cantilevers (r(bead) = 2.5 μm, nominal spring constant 0.06 N m^{-1}, Novascan Technologies). Initially, we determined the sensitivity of the photodiode to cantilever deflection by measuring the slope of a force distance curve when pressing the cantilever onto a glass coverslip, and the force constant of the cantilever using the thermal noise method included in the Bruker Nanoscope software. For each acrylamide/bisacrylamide ratio used in the traction-force microscopy measurements we acquired 27 force curves in 3 by 3 grids (2 μm spacing between points) at three different locations on the gels. Before and during indentation experiments gels were kept in PBS. To obtain stiffness values from force curves we used the NanoScope Analysis software. Specifically, we corrected for baseline tilt, and used the linear fitting option for the Hertz model with a Poisson ration of 0.48 on the indentation curve.

Traction-force microscopy and image analysis. Confocal acquisition was performed on an Eclipse TI-E Nikon inverted microscope equipped with a CSUX1-A1 Yokogawa confocal head and an Evolve EMCCD camera (Ropert Scientific, Princeton Instrument). A CFI Plan APO VC oil ×60/1.4 objective (Nikon) was used. The system was driven by the Metamorph software (Universal Imaging).

Traction-force microscopy was performed as previously described[28]. Displacement fields describing the deformation of the polyacrylamide substrate are determined from the analysis of fluorescent bead images before and after removal of the adhering cell with trypsin treatment. Images of fluorescent beads were first aligned to correct experimental drift using the Align slices in stack ImageJ plugin. The displacement field was subsequently calculated by a custom-written particle image velocimetry (PIV) program implemented as an ImageJ (http://rsb.info.nih.gov/ij) plugin. The PIV was performed through an iterative scheme. In all iterations the displacement was calculated by the normalized correlation coefficient algorithm, so that an individual interrogation window was compared with a larger searching window. The next iteration takes into account the displacement field measured previously, so that a false correlation peak due to insufficient image features is avoided. The normalized cross-correlation also allowed us to define an arbitrary threshold to filter out low correlation values due to insufficient beads present in the window. The resulting final grid size for the displacement field was 2.67 × 2.67 μm. The erroneous displacement vectors due to insufficient beads present in the window were filtered out by their low correlation value and replaced by the median value from the neighbouring vectors. With the displacement field obtained from the PIV analysis, the traction-force field was reconstructed by the Fourier transform traction cytometry (FTTC) method with regularized scheme on the same grid (2.67 × 2.67 μm) without further interpolation or remapping. The regularization parameter was set at 1 × 10–11 for all traction-force reconstructions. The Fourier transform traction cytometry code was also written in Java as an ImageJ plugin, so that the whole traction-force microscopy procedure from PIV to force calculation could be performed with ImageJ. The entire package of traction-force microscopy software is available at https://sites.google.com/site/qingzongtseng/tfm. Contractile

DOI: 10.1038/ncb2747

energy was then computed as the integral under the cell of the scalar product of force and displacement vectors using a custom-written code in MatLab. Force profiles along the cell front were generated by integration of the traction maps over the width of the circular part of the pattern. Average pictures were generated after alignment using the Align slices in stack ImageJ plugin. Focal adhesion intensity profiles were generated by integration of the paxillin intensity along the border of the circular part of the micropattern.

Rho–GTPase assays. Cells were serum-starved overnight, detached with trypsin–EDTA and kept in suspension in serum-free medium for 1 h. Cells were then plated on fibronectin-coated dishes (blocked with 1% BSA) in serum-free medium for 45 min. Cell lysis and active Rho–GTPase pulldown was performed using the active Rac1 Pull-Down and Detection Kit or the active Rho Pull-Down and Detection Kit (Cat#16118, 16116, Pierce) according to the manufacturer's instruction. The active GTPase signal was normalized to total protein level of the GTPase. Western blots were quantified with Totallab.

RNA interference. Cells were transiently transfected with a final concentration of 300 nM siRNA (stealth RNAi; Invitrogen) using Lipofectamine 2000 (Invitrogen) according to the manufacturer's protocol, using the targeting sequence sense-5′-CCCGGAACUUUGUCAUCCAUCGUUU-3′ for GEF-H1. As a control we used the scrambled sequence sense-5′-CCCUCAAUGUUCUACCUACGGGUUU-3′.

MS. For proteome and phosphoproteome analysis fibroblasts were cultured in lysine/arginine-free DMEM with 10% FBS (10 KDa dialysed, PAA) and SILAC labelled with light (L-arginine (R0) and L-lysine (K0))], medium (L-arginine-U-$^{13}C_6$ (R6) and L-lysine-$^{2}H_4$(K4)) or heavy (L-arginine-U-$^{13}C_6$ $-^{15}N_4$ (R10) and L-lysine-U-$^{13}C_6$ $-^{15}N_2$ (K8)) amino acids (Cambridge Isotope Laboratories). For phosphoproteome analysis, cells were serum-starved for 6 h and then plated in serum-free medium on fibronectin-coated and BSA-blocked culture dishes for 45 min. Cells were lysed in lysis buffer (100 mM Tris–HCl, at pH 7.5, containing 4% SDS and 100 mM dithiothreitol), boiled 5 min at 95 °C, and sonicated. Lysate was clarified by a 10 min centrifugation at 16,000*g*. Cleared light/medium/heavy proteins were mixed at a 1:1:1 ratio and digested with trypsin using the FASP protocol[48]. For proteome analysis, 40 µg of peptides was separated with strong anion exchange chromatography[49]. For phosphoproteome analysis, 3 mg of peptides was fractionated with strong cation exchange chromatography and enriched for phosphorylated peptides with titanium dioxide (TiO_2) as described previously[50]. Peptides were then analysed on a LTQ-Orbitrap Velos equipped with a nanoelectrospray source (Thermo Fisher Scientific). The full-scan MS spectra were acquired in the Orbitrap with a resolution of 30,000 at m/z 400. The ten most intense ions were fragmented by higher-energy collisional dissociation and the spectra of the fragmented ions were acquired in the Orbitrap analyser with a resolution of 7,500. Peptides were identified and quantified using the MaxQuant software[31] and searched with the Andromeda search engine against the mouse IPI database 3.68 (ref. 51). Phosphorylations were assigned as previously described[50].

The adhesome analysis was performed as previously described[19]. In brief, cells were serum-starved for 4 h and plated for either 45 or 90 min in serum-free medium on fibronectin-coated, BSA-blocked, culture dishes. Optionally, cells were treated with 50 µM blebbistatin for 30 or 75 min. Enrichment for focal-adhesion-associated proteins was achieved by shortly fixing the ventral cell cortex using chemical crosslinkers, followed by removal of non-crosslinked proteins and big organelles by stringent cell lysis and hydrodynamic sheer flow washing. Quantitative mass spectrometric analysis was performed on an LTQ Orbitrap mass spectrometer (Thermo Electron) and analysed using the label-free quantification algorithm[52], which is embedded in the MaxQuant software[31], as previously described[19].

For in-gel digestion, gel bands were cut into 1 mm^3 cubes and washed two times with 50 mM ammonium bicarbonate in 50% ethanol. For protein reduction, gel pieces were incubated with 10 mM dithiothreitol in 50 mM ammonium bicarbonate for 1 h at 56 °C. Alkylation of cysteines was performed with 10 mM iodoacetamide in 50 mM ammonium bicarbonate for 45 min at 25 °C in the dark. Gel pieces were washed two times with 50 mM ammonium bicarbonate in 50% ethanol, dehydrated with 100% ethanol, and dried in a vacuum concentrator. The gel pieces were rehydrated with 12.5 ng μl^{-1} trypsin (sequencing grade, Promega) in 50 mM ammonium bicarbonate and digested overnight at 37 °C. Supernatants were transferred to fresh tubes, and the remaining peptides were extracted by incubating gel pieces two times with 30% acetonitrile in 3% TFA followed by dehydration with 100% acetonitrile. The extracts were combined and desalted using RP-C18 StageTip columns, and the eluted peptides used for mass spectrometric analysis.

For nanoLC–MS/MS, peptide mixtures were separated by on-line nanoLC and analysed by electrospray tandem MS. The experiments were performed on an Agilent 1200 nanoflow system connected to an LTQ Orbitrap mass spectrometer (Thermo Electron) equipped with a nanoelectrospray ion source (Proxeon Biosystems). Binding and chromatographic separation of the peptides took place in a 15-cm fused-silica emitter (75-µm inner diameter from Proxeon Biosystems) in-house packed with reversed-phase ReproSil-Pur C18-AQ 3 µm resin (Dr. Maisch). Peptide mixtures were injected onto the column with a flow of 500 nl min^{-1} and subsequently eluted with a flow of 2500 nl min^{-1} from 2% to 40% acetonitrile in 0.5% acetic acid, in a 100 min gradient. The precursor ion spectra were acquired in the Orbitrap analyser (m/z 300–1,800, $R = 60{,}000$, and ion accumulation to a target value of 1,000,000), and the ten most intense ions were fragmented and recorded in the ion trap. The lock mass option enabled accurate mass measurement in both MS and Orbitrap MS/MS mode as described previously[53]. Target ions already selected for MS/MS were dynamically excluded for 60 s.

For peptide identification and peptide quantification, the data analysis was performed with the MaxQuant software as described previously[31,54], supported by Andromeda as the database search engine for peptide identifications. Peaks in MS scans were determined as three-dimensional hills in the mass-retention time plane. MS/MS peak lists were filtered to contain at most six peaks per 100 Da interval and searched by Andromeda (in-house-developed software) against the Mouse International Protein Index database. The initial mass tolerance in MS mode was set to 7 ppm and MS/MS mass tolerance was 0.5 Da. Cysteine carbamidomethylation was searched as a fixed modification, whereas N-acetyl protein, oxidized methionine, *N*-carbamidomethylated DSP protein and carbamidomethylated DSP lysine were searched as variable modifications. Finally, the label-free quantification algorithm implemented in the MaxQuant software was used as described earlier[52].

SILAC-based peptide pulldowns were carried out with the cytoplasmic tails of β_1 integrin (5′-HDRREFAKFEKEKMNAKWDTGENPIYKSAVTTVVNPKYEGK-3′) and the tails of β_3 integrin (5′-HDRKEFAKFEEERARAKWDTANNPLYKEATS-TFTNITYRGT-3′). The tail peptides were *de novo* synthesized with a desthiobiotin on the amino terminus, coupled to magnetic streptavidin beads (MyOne Streptavidin C1—Invitrogen) and pulldowns from SILAC-labelled cell lysates were performed as described previously[33]. After a mild wash the bound proteins were eluted from the magnet using 16 mM biotin (Sigma-Aldrich). After protein precipitation and in-solution digestion, LC-MS/MS and data analysis was performed as described above. The peptide pulldown experiments were done as reverse SILAC labelling experiments in duplicate (4 biological replicates). We generally considered outliers with high SILAC ratios and high sequence coverage/intensity as more significant than proteins that had only a high SILAC ratio.

Bioinformatics and statistics. ANOVA analysis of the cellular proteome and phosphoproteome was performed using the Perseus bioinformatics toolbox of MaxQuant (J. Cox *et al.*; manuscript in preparation). Multiple testing corrections were performed using the inbuilt permutation method and significant hits were identified at a significance level of 0.01 and 0.05, respectively. ANOVA analysis of the 245 core adhesome proteins was performed using the statistical programming language R (http://www.R-project.org) with the adaptive Benjamini and Hochberg step-up false discovery rate-controlling procedure for multiple testing and a significance level of 0.05. Hierarchical clustering was performed using an average linkage approach and Euclidean distances. Enrichment analysis of clusters for Gene Ontology (GO) terms, KEGG pathways and PFAM and INTERPRO protein domains was performed with the DAVID webserver[55] using the multiple testing correction method by Benjamini and Hochberg and a significance level of 0.05. Protein–protein interactions (PPIs) were compiled from different sources including: PPI databases (DIP (ref. 56; version of December 2009), IntAct (ref. 57) and MINT (ref. 58) (both downloaded on 19 May 2010), BIOGRID (ref. 59; version 3.0.64) and HPRD (ref. 60; Release 9)); the adhesome network database[32]; and the KEGG pathway database[61]. For the adhesome network database, we distinguished between undirected PPIs and directed activating and inhibiting interactions as annotated in the adhesome database and in KEGG. Human and mouse interactions were combined using the orthologue tables of the Mouse Genome Database (MGI) to increase coverage. The high-confidence network of PPIs from public databases contained only interactions reported in at least two separate publications. Networks were visualized using the Cytoscape software. Bar graphs throughout the study were generated in Microsoft Office and depict, unless otherwise indicated, the means and standard errors of the means. Box plots and dot plots were generated using the SigmaPlot software or the MatLab software.

Data deposition. Raw data for the phosphoproteome and proteome analyses of the three cell lines are deposited in the Tranche database (https://proteomecommons.org/tranche/) with the following accession numbers: Schiller_Integrins_Phosphoproteome, on33gw4tEXu5YErn5zrp; Schiller_Integrins_Proteome, EvAbqut9c7fC9OQTyawI.

45. Schiller, H. B., Szekeres, A., Binder, B. R., Stockinger, H. & Leksa, V. Mannose 6-phosphate/insulin-like growth factor 2 receptor limits cell invasion by controlling $\alpha_v\beta_3$ integrin expression and proteolytic processing of urokinase-type plasminogen activator receptor. *Mol. Biol. Cell* **20,** 745–756 (2009).
46. Azioune, A., Carpi, N., Tseng, Q., Thery, M. & Piel, M. Protein micropatterns: a direct printing protocol using deep UVs. *Meth. Cell Biol.* **97,** 133–146 (2010).
47. Rape, A. D., Guo, W. H. & Wang, Y. L. The regulation of traction force in relation to cell shape and focal adhesions. *Biomaterials* **32,** 2043–2051 (2011).
48. Wisniewski, J. R., Zougman, A., Nagaraj, N. & Mann, M. Universal sample preparation method for proteome analysis. *Nat. Methods* **6,** 359–362 (2009).
49. Wisniewski, J. R., Zougman, A. & Mann, M. Combination of FASP and StageTip-based fractionation allows in-depth analysis of the hippocampal membrane proteome. *J. Proteome Res.* **8,** 5674–5678 (2009).
50. Olsen, J. V. *et al*. Global, *in vivo*, and site-specific phosphorylation dynamics in signaling networks. *Cell* **127,** 635–648 (2006).
51. Cox, J. *et al*. Andromeda: a peptide search engine integrated into the MaxQuant environment. *J. Proteome Res.* **10,** 1794–1805 (2011).
52. Luber, C. A. *et al*. Quantitative proteomics reveals subset-specific viral recognition in dendritic cells. *Immunity* **32,** 279–289 (2010).
53. Olsen, J. V. *et al*. Parts per million mass accuracy on an Orbitrap mass spectrometer via lock mass injection into a C-trap. *Mol. Cell Proteomics* **4,** 2010–2021 (2005).
54. Cox, J. *et al*. A practical guide to the MaxQuant computational platform for SILAC-based quantitative proteomics. *Nat. Protocols* **4,** 698–705 (2009).
55. Huang da, W., Sherman, B. T. & Lempicki, R. A. Systematic and integrative analysis of large gene lists using DAVID bioinformatics resources. *Nat. Protocols* **4,** 44–57 (2009).
56. Xenarios, I. *et al*. DIP, the database of interacting proteins: a research tool for studying cellular networks of protein interactions. *Nucleic Acids Res.* **30,** 303–305 (2002).
57. Aranda, B. *et al*. The IntAct molecular interaction database in 2010. *Nucleic Acids Res.* **38,** D525–D531 (2010).
58. Ceol, A. *et al*. MINT, the molecular interaction database: 2009 update. *Nucleic Acids Res.* **38,** D532–D539 (2010).
59. Breitkreutz, B. J. *et al*. The BioGRID Interaction Database: 2008 update. *Nucleic Acids Res.* **36,** D637–D640 (2008).
60. Prasad, T. S., Kandasamy, K. & Pandey, A. Human protein reference database and human proteinpedia as discovery tools for systems biology. *Methods Mol. Biol.* **577,** 67–79 (2009).
61. Kanehisa, M., Goto, S., Sato, Y., Furumichi, M. & Tanabe, M. KEGG for integration and interpretation of large-scale molecular data sets. *Nucleic Acids Res.* **40,** D109–D114 (2012).

DOI: 10.1038/ncb2747

nature cell biology

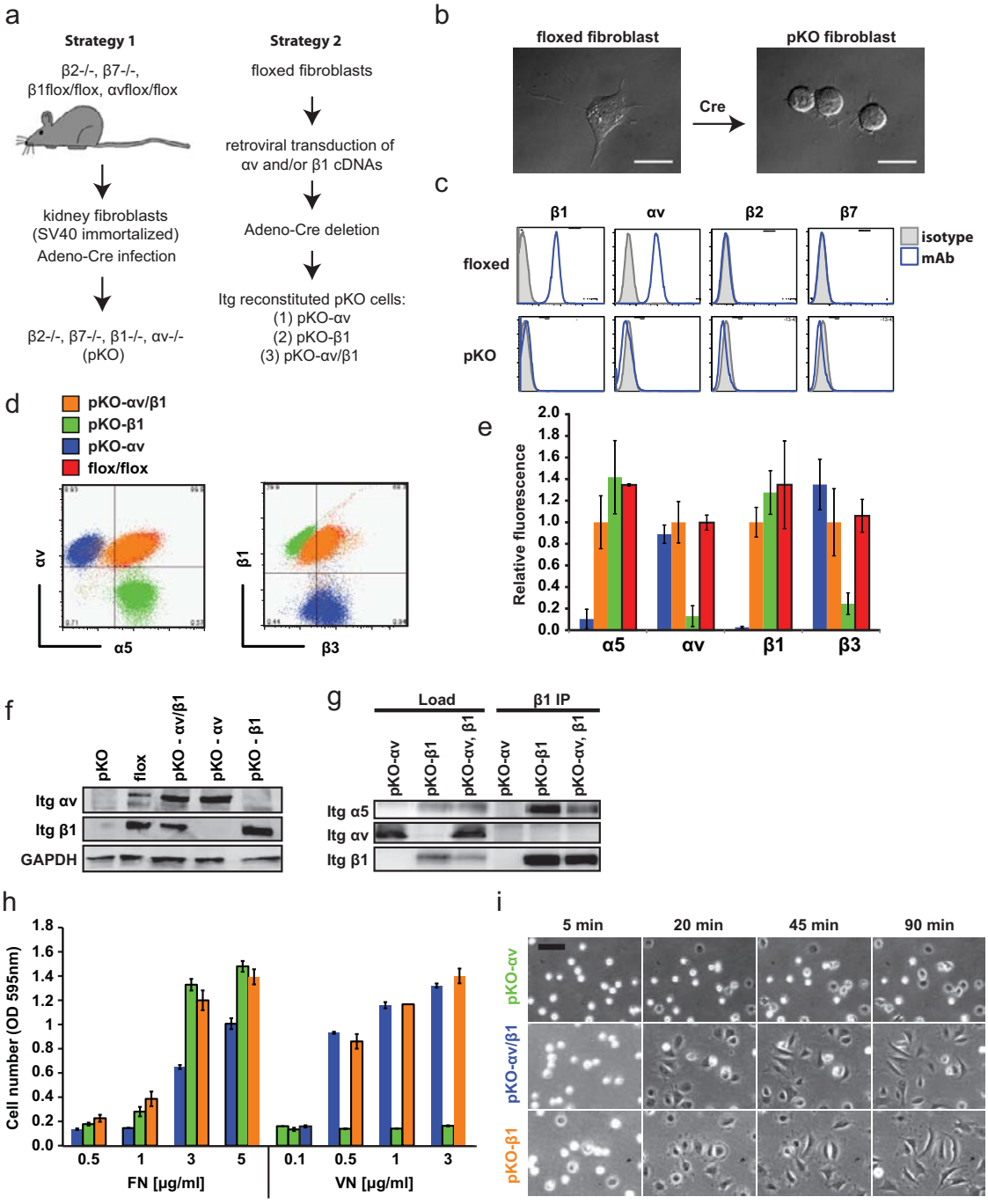

Figure S1 Generation of pKO-αv, pKO-β1 and pKO-αv/β1 cell lines. (**a**) Workflow of the generation of pKO kidney fibroblasts (strategy 1) and integrin reconstituted pKO fibroblasts (strategy 2). (**b**) Phase contrast image of the floxed and pKO cells plated on FN. Scale bar 20 μm. (**c**) Integrin profile of floxed and pKO cells analysed by flow cytometry. (**d**) Cell surface levels of indicated integrins analysed by flow cytometry. (**e**) Relative fluorescence intensities of indicated integrins from three independent stainings analysed by flow cytometry. The means (n=3) and standard deviations are shown. (**f**) Western blots for αv and β1 integrins. GAPDH was used as loading control. (**g**) Cell lysates and immunoprecipitates of β1 integrin were immunoblotted for αv, α5 and β1 integrins. Note that αv does not associate with β1 in pKO-αv/β1 cells. (**h**) Adhesion assay on fibronectin (FN) or vitronectin (VN). Numbers of adherent cells 20 minutes after seeding are shown as relative values of OD=595nm. The bar graph shows the mean and s.e.m. (n=3; one representative out of 2 independent experiments is shown). (i) Cells plated on FN and time-lapse imaged using a phase contrast microscope at 20x magnification. Scale bar 100 μm. pKO-β1 (green); pKO-αv (blue); pKO-αv/β1 (orange); parental β1/αv floxed cell (red).

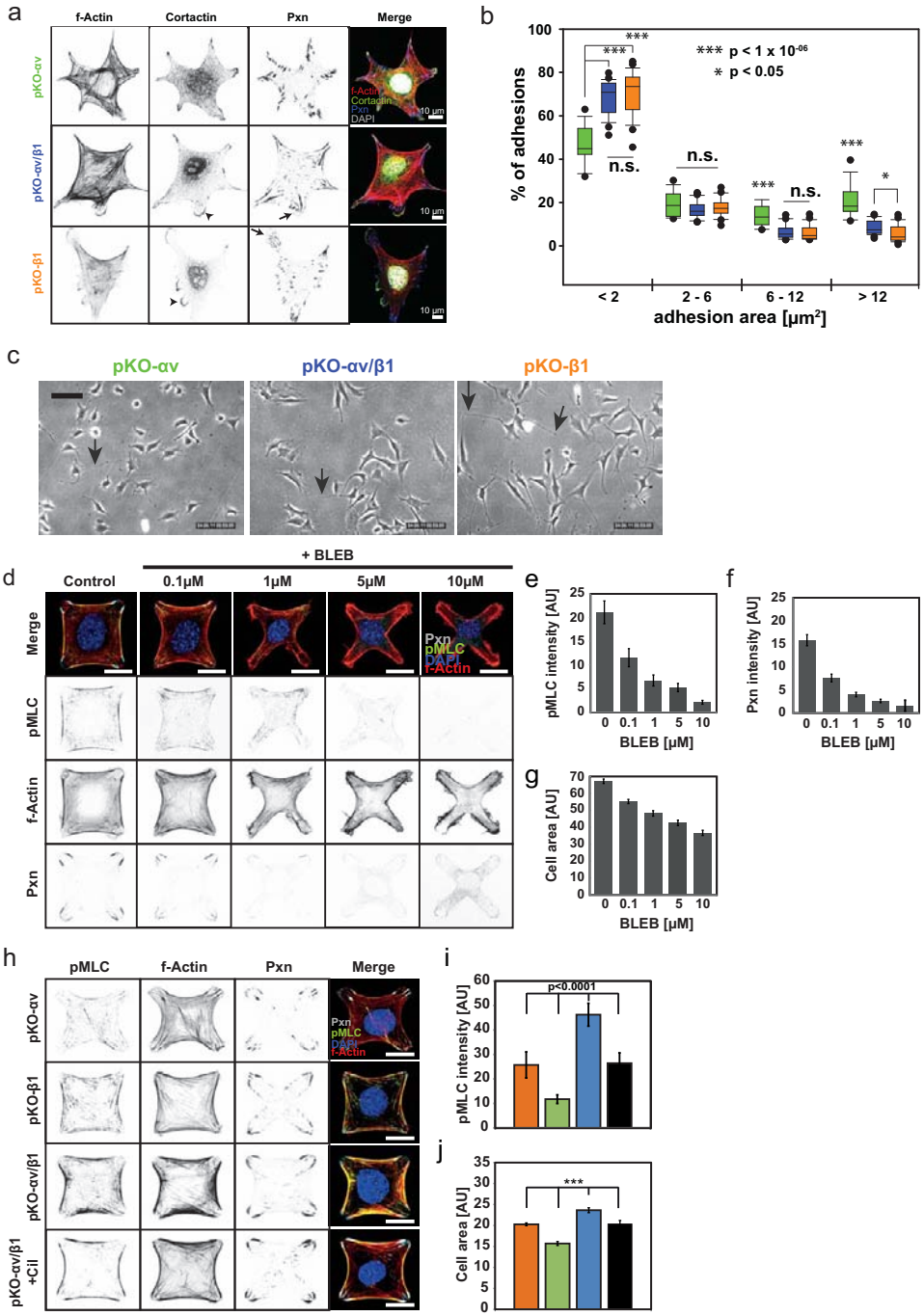

Figure S2 α5β1 and αv-class integrins induce different spreading areas, membrane protrusions and adhesion sites on FN. (**a**) Cells were plated on FN for 90 minutes and immunostained with the indicated antibodies. Arrowheads indicate cortactin-positive lamellipodia and arrows mark the small NAs in lamellipodia. Scale bar 10µm. (**b**) Size distribution of adhesive sites of cells stained with Paxillin calculated with the Metamorph software. Boxplots show the percentage of adhesions in the depicted size classes (pKO-αv n=15; pKO-αv/β1 n= 29; pKO-β1 n=23; one representative out of 2 independent experiments is shown). Boxplot whisker ends are at 1.5 interquartile range and outliers are shown as dots. Significance was calculated using a *t* test (*=p<0.05; ***=p<10 E-06). (**c**) Still pictures taken from supplementary movies S1-S3 showing trailing edge detachment defects indicated by the arrows. Scale bar 100 µm. (**d**) Floxed cells cultured 3 hours on FN-coated X-shapes treated for 1 hour with indicated concentrations of blebbistatin (BLEB), and then stained for Paxillin, pMLC and f-actin. Scale bar 10 µm. (**e**) Fluorescence intensities of pT18/S19-MLC, **(f)** Paxillin (Pxn) and **(g)** cell areas after blebbistatin treatment (n=20 cells; error bars represent s.e.m.). (**h**) Cells plated on FN-coated X-shapes and stained for pMLC, Paxillin and f-actin. Scale bar 10 µm. (**i**) Fluorescence intensities of pS18/T19-MLC and (**j**) cell areas (pKO-αV n=46, pKO-β1 n=46, pKO-αV/β1 n=21, pKO-αV/β1 +Cil n=10; one representative out of 3 independent experiments is shown; error bars represent s.e.m.). Cilengitide (Cil) was used to block αv-class integrins. Significance was calculated using a ttest. pKO-αv (green); pKOαv/β1 (blue); pKO-β1 (orange); pKOαv/β1 + 1 µM cilengitide (black).

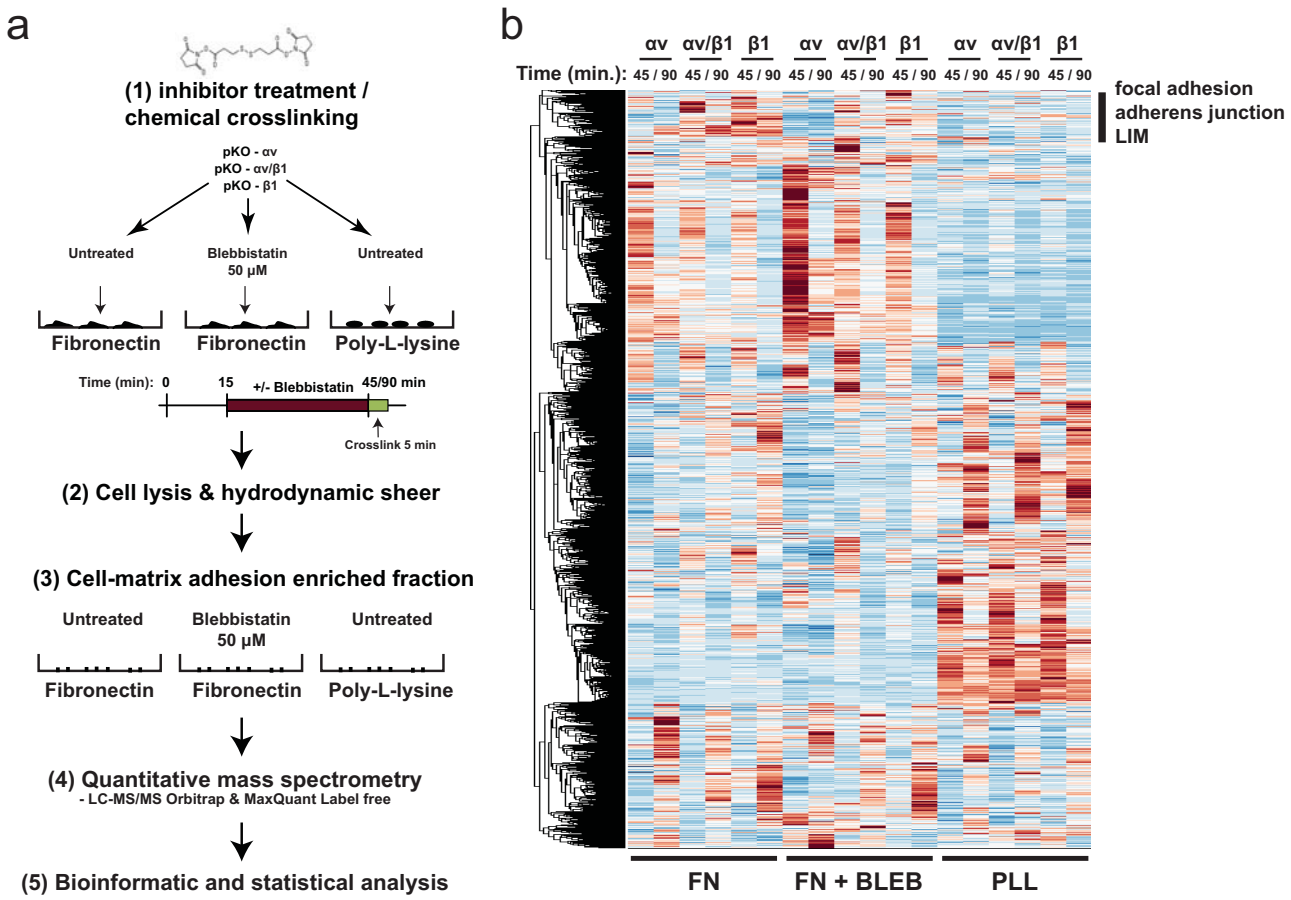

Figure S3 Adhesome analysis of pKO-αv, pKO-β1 and pKOαv/β1 cells. (**a**) Workflow for isolation of FA enriched fractions and analysis of adhesome components. (**b**) Adhesomes derived from cells plated on indicated substrates for 45 or 90 minutes were examined by non-supervised hierarchical cluster analysis of Z-scores of median MS intensities (n=3-4). The labels on the right indicate significantly enriched gene ontology (GO) terms.

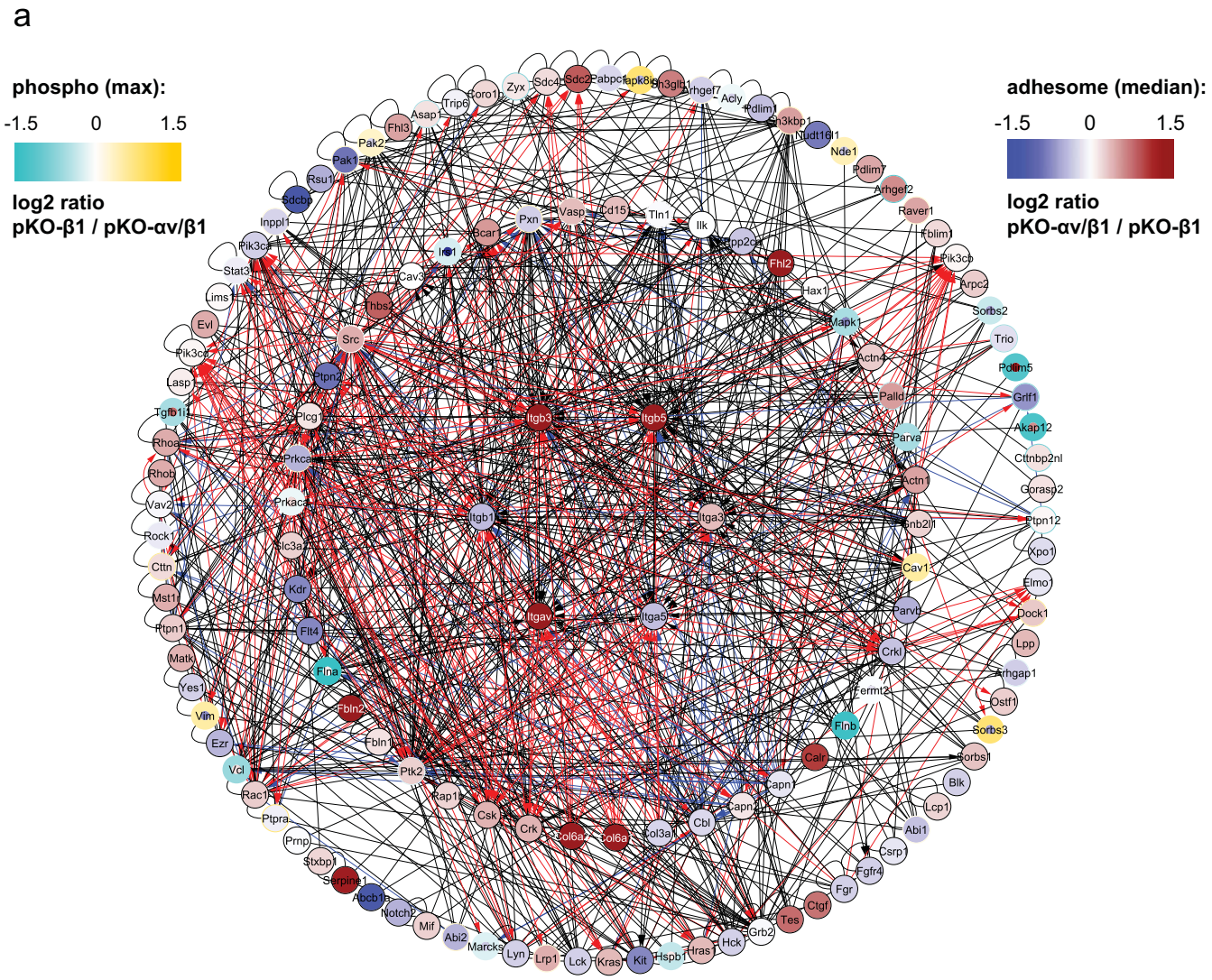

Figure S4 α5β1- and αv-class-specific PPIs and phosphosites. (**a**) The PPI network derived from FA-enriched samples. Integrin subunits are in the centre and their direct and indirect interactors are in the inner and outer circles, respectively. Black lines between nodes indicate high confidence PPI, red arrows indicate activating interactions and blue lines indicate inhibiting interactions. The nodes were labelled with gene symbols and colour-coded according to the MS intensity ratio of pKO-αv/β1 versus pKO-β1. Node edges were colour-coded according to the SILAC ratio of the maximally regulated phosphosite on each significantly regulated protein. (**b**) The PPI-network was derived as in (a). The nodes and node edges were colour-coded according to the MS intensity ratio of pKO-αv versus pKO-αv/β1. (**c**) The PPI-network was derived as described in (a). The nodes and node edges were colour-coded according to the MS intensity ratio of pKO-αv versus pKO-β1.

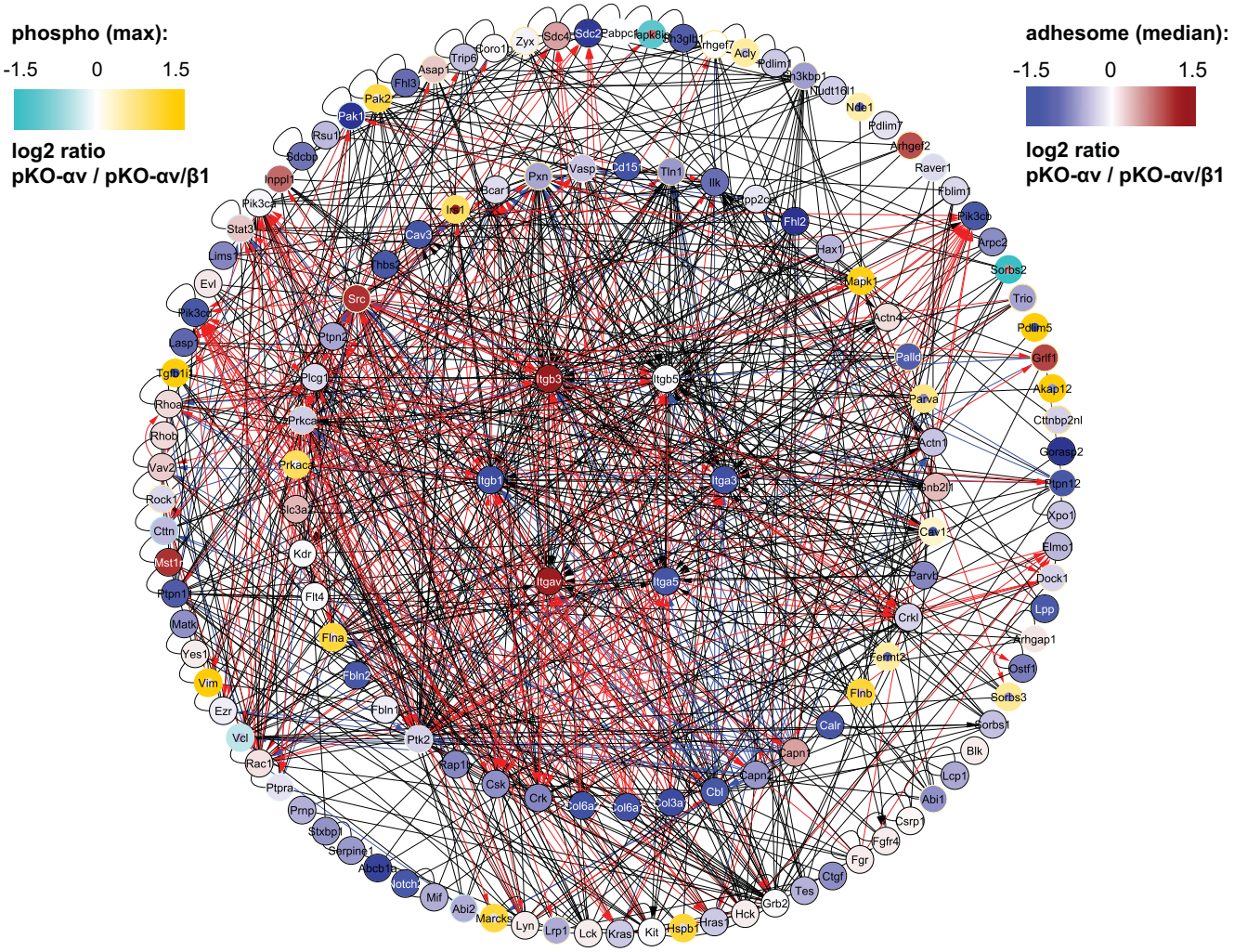

Figure S4 continued

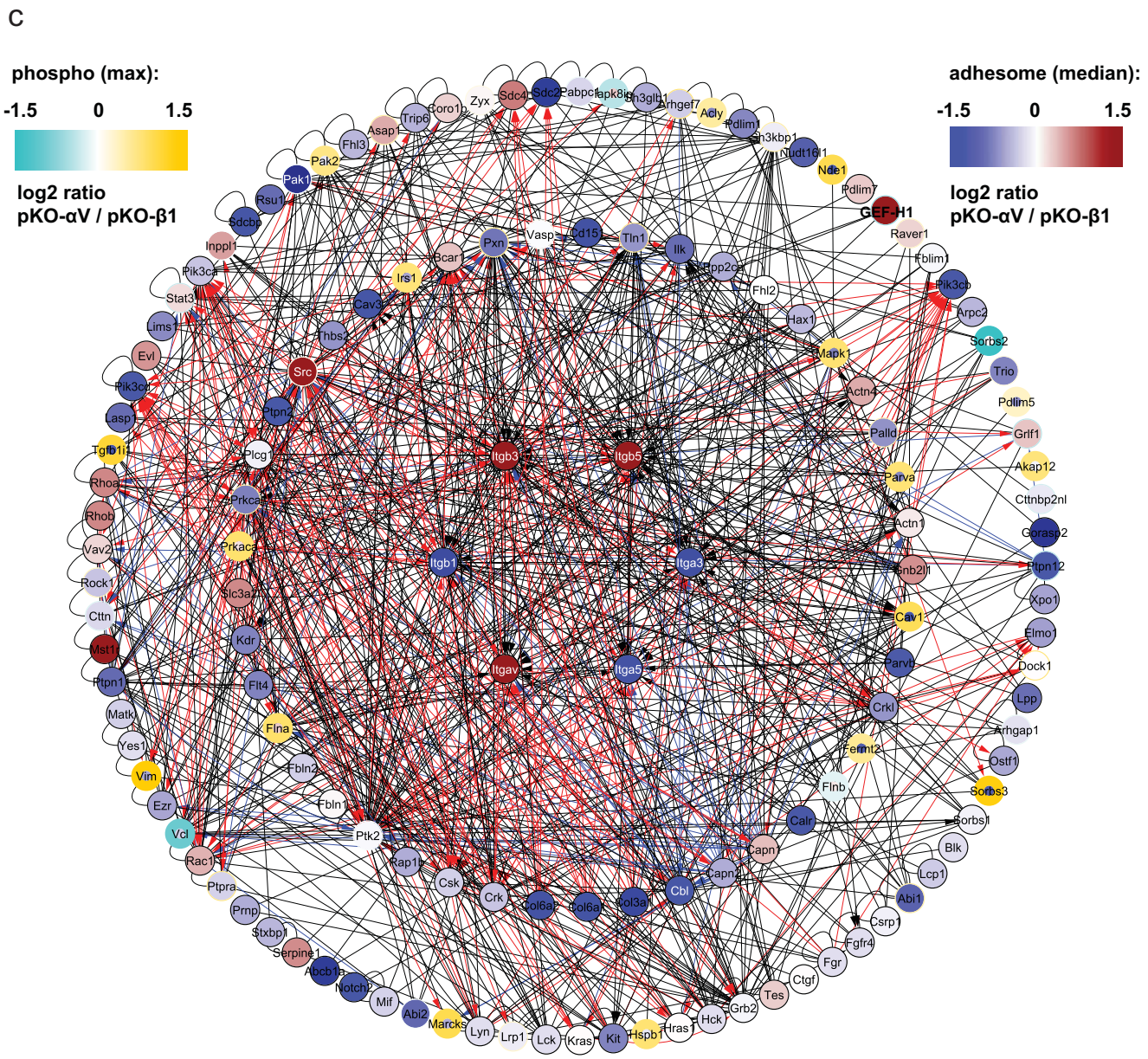

Figure S4 continued

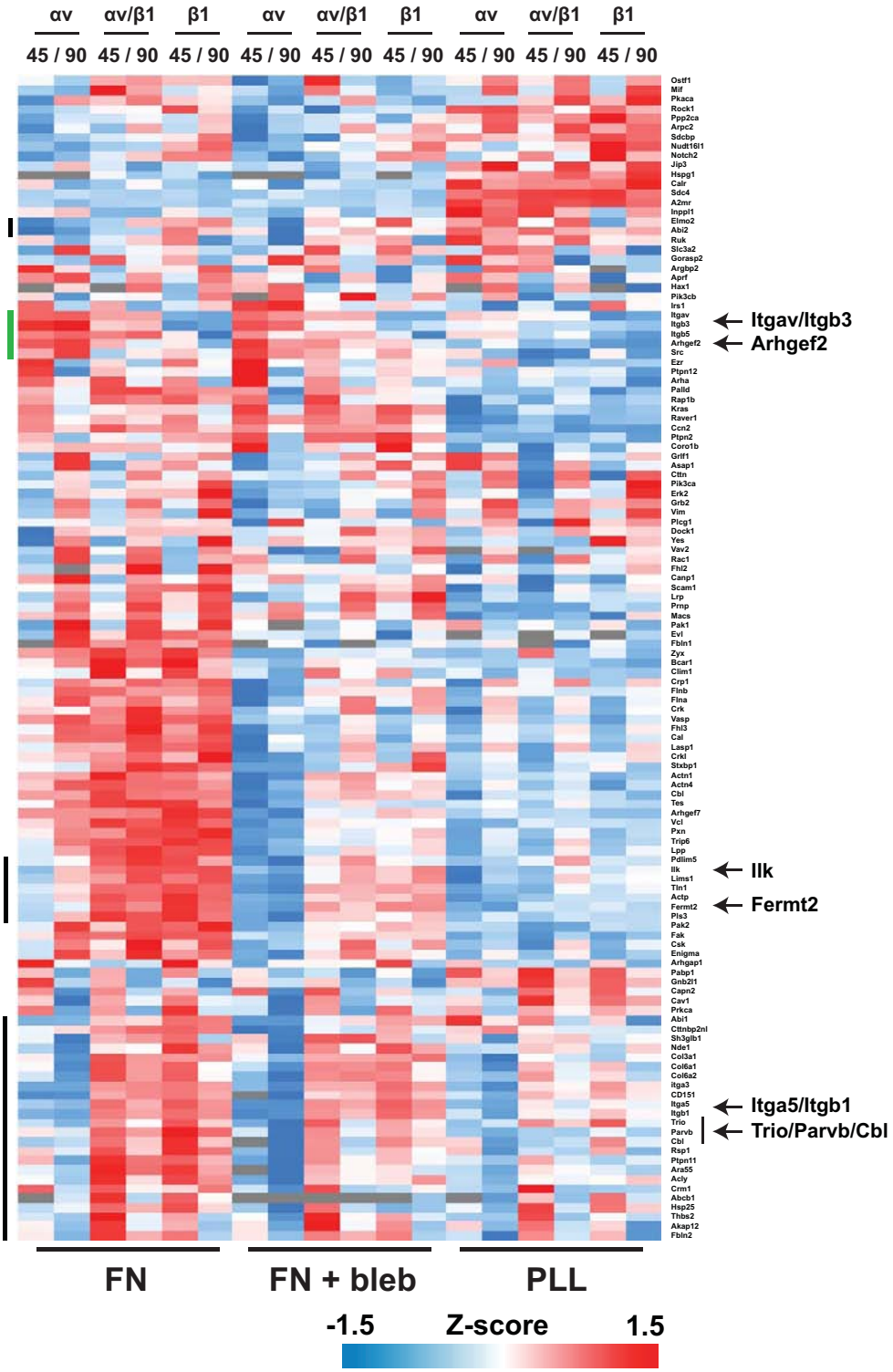

Figure S5 Integrin-specific differences in the "core integrin interactome". The Z-scores of median MS intensities (n=3-4) of the 125 core integrin-interactome proteins (Fig. S4) were subjected to hierarchical clustering. The black bars on the left indicate α5β1-dependent FA proteins, while the green bar indicates the αv-class integrin-dependent FA proteins selected for the clustering in Fig. 4c.

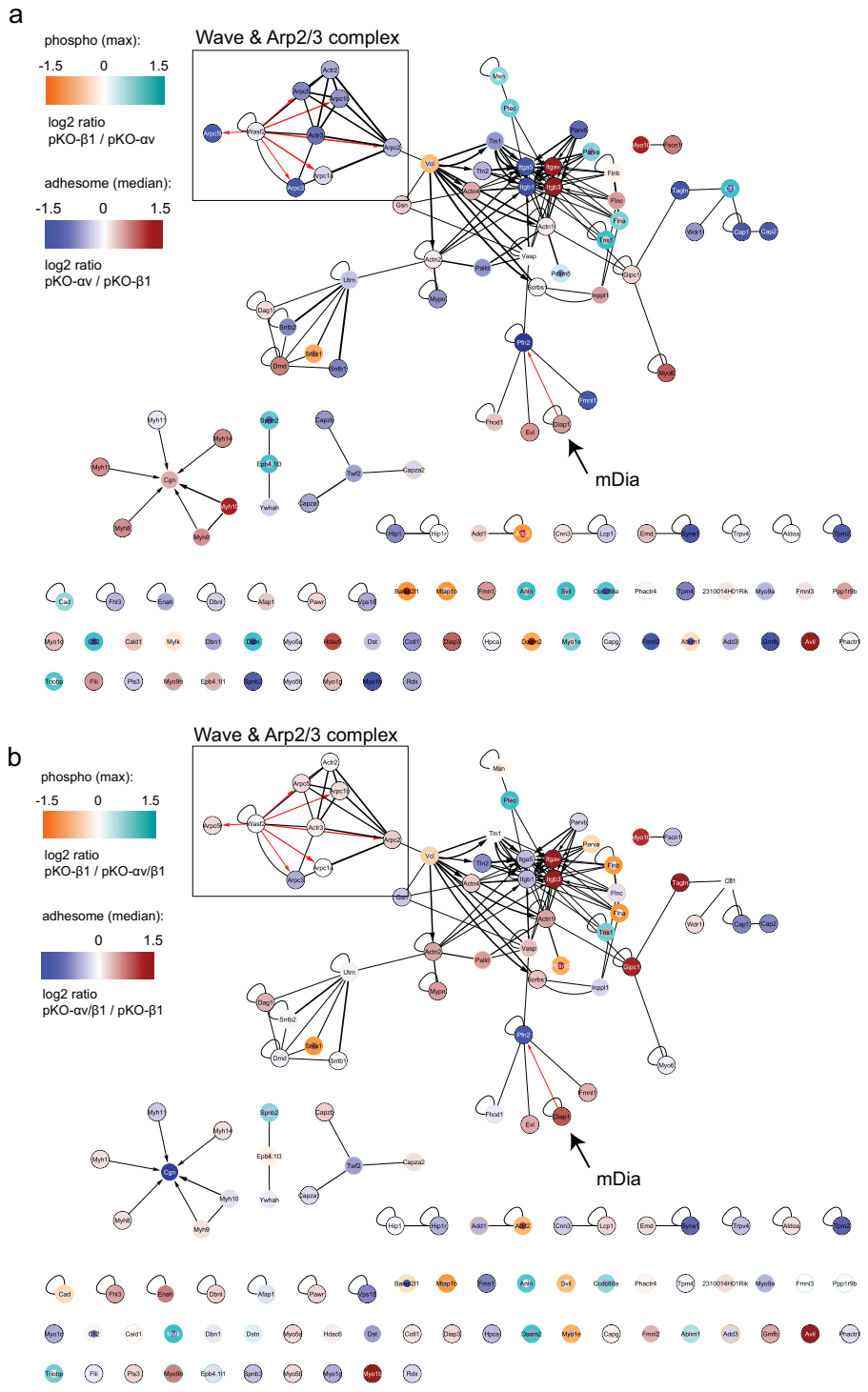

Figure S6 Network analysis of actin binding proteins enriched in the adhesome preparations. (**a**) Actin binding proteins were extracted from the adhesome dataset using gene ontology annotations. Black lines between nodes indicate high confidence PPI, red arrows indicate activating and blue lines indicate inhibiting interactions. The nodes were labelled with gene symbols and colour coded according to the log2 MS intensity ratio of pKO-αv over the pKO-β1 sample. Node edges were colour-coded according to the log2 SILAC ratio of the maximally regulated phosphosite on each significantly regulated protein. The box marks components of the WAVE and Arp2/3 complex, while the arrowhead marks the formin mDia. (**b**) The graph was generated as in (a), except that the nodes were colour-coded according to the log2 MS intensity ratio of pKO-αv/β1 over the pKO-β1 sample.

a

β1-tail:	Desthiobiotin - HDRREFAKFEKEKMNAKWDTGENPIYKSAVTTVVNPKYEGK - OH
β1-tail scr:	Desthiobiotin - ANYETKTNPKFKRAWKDNTKYEVVMSHAGFDIEVPREGKEK - OH
β3-tail:	Desthiobiotin - HDRKEFAKFEEERARAKWDTANNPLYKEATSTFTNITYRGT - OH
β3-tail scr:	Desthiobiotin - AETFLSRHYNKGFDKATKRPAEDRYWNTARENETAKTTIFE - OH

b

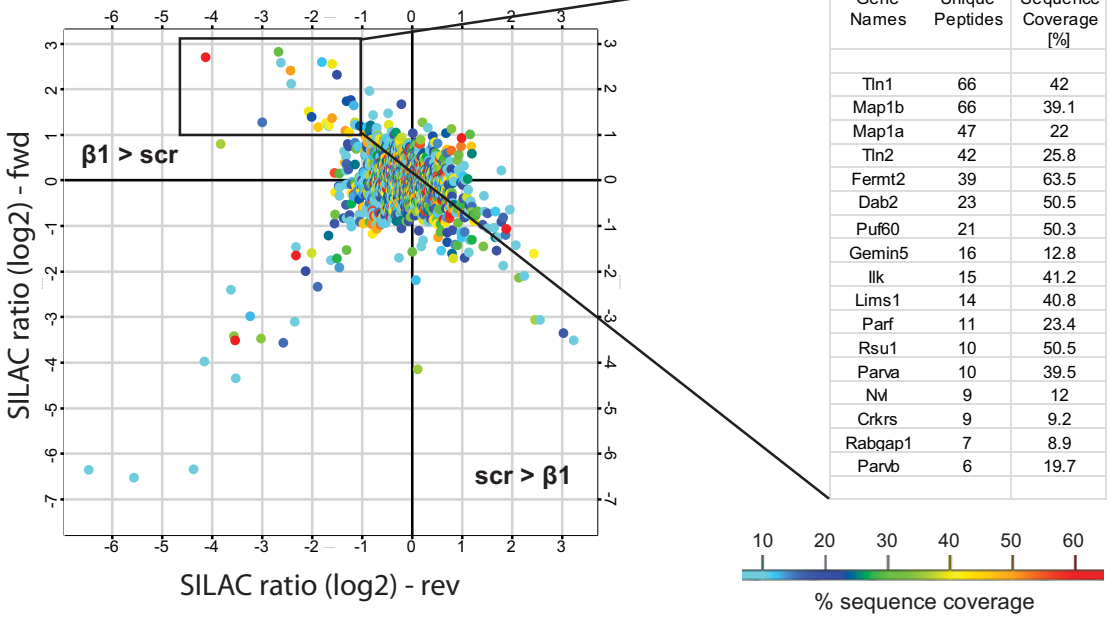

Gene Names	Unique Peptides	Unique Sequence Coverage [%]
Tln1	66	42
Map1b	66	39.1
Map1a	47	22
Tln2	42	25.8
Fermt2	39	63.5
Dab2	23	50.5
Puf60	21	50.3
Gemin5	16	12.8
Ilk	15	41.2
Lims1	14	40.8
Parf	11	23.4
Rsu1	10	50.5
Parva	10	39.5
Nvl	9	12
Crkrs	9	9.2
Rabgap1	7	8.9
Parvb	6	19.7

c

Gene Names	Unique Peptides	Unique Sequence Coverage [%]
Dync1h1	169	43.8
Iqgap1	91	67.2
Tln1	57	35.3
Iqgap2	50	41.1
Vim	49	85.6
Frap1	49	27.5
Usp9x	49	23
Lmo7	48	36.1
Ccdc88a	48	30.3
Fn1	46	29.9
Nes	44	33.4
Arhgef2	38	48.7
Svil	36	20.9
Cep170	35	31.4
Synj1	33	23.6
Hnrnpm	31	48.8
Rictor	31	24.4
Phldb1	31	26.7
KIAA1967	29	44.3

Gene Names	Unique Peptides	Unique Sequence Coverage [%]
Flnc	29	15.9
Irs1	29	34.4
Esf1	28	31.4
Fermt2	28	51
Spata5	27	44.2
Gigyf2	25	25.3
Lmna	25	39.8
Setd2	25	15
Cep55	25	45.2
Dab2	24	53.7
Rgnef	24	19.2
Mcm5	24	43.6
Pik3c2a	23	16
Ctnnd1	23	35.3
Jak1	23	28.6
Hadha	22	37
Dsp	22	9.1
Arhgef17	21	14.4
Rngtt	20	37.2
Dock7	20	11.5

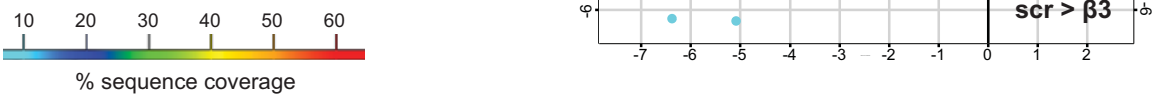

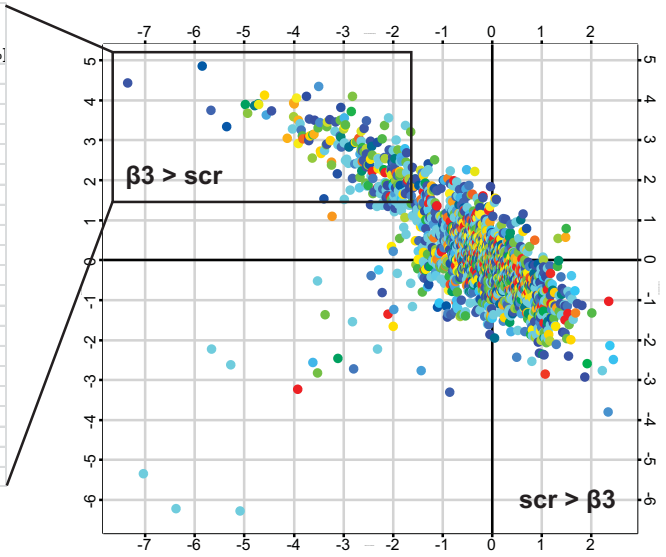

Figure S7 Integrin tail peptide pulldowns. (**a**) Sequence of synthetic desthiobiotinylated peptides used for the pull down experiments. (**b**) SILAC ratio plot from label inverted replicates (specific interactors have high SILAC ratio in the forward experiment and low SILAC ratios in the label swapped reverse experiment) comparing the β1-tail peptide with a scrambled control. The table shows the most intense β1-specific interactors with high sequence coverage that were reproducibly enriched versus the scrambled control peptide (scr) (n=4; 2 independent experiments). (**c**) SILAC ratios of proteins from inverted replicates comparing the β3-tail peptide with a scrambled control. The table shows the most intense β3-specific interactors with high sequence coverage that were reproducibly enriched versus the scrambled control peptide (scr) (n=4; 2 independent experiments).

a

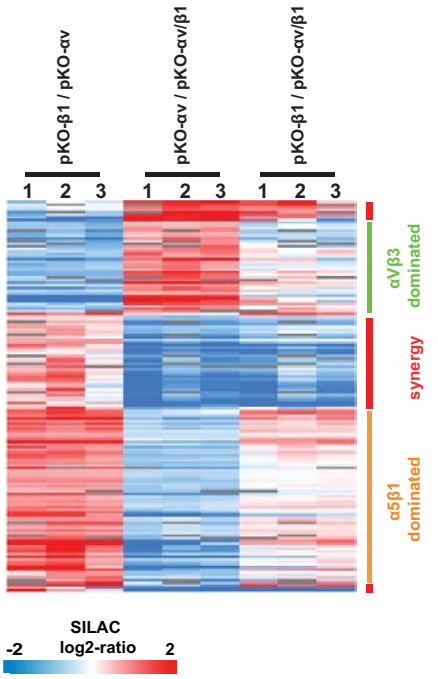

b

Synergy up/down	αvβ3 dominated	α5β1 dominated	α5β1 dominated
Actn1 *	AA881470	Acbd3	Lox
Adir	Abcc4	Acss2	Lxn
Apol9a	Add2	Ahnak2	Man2a1
Ass	Aif1l	Anx1	Mdh2
Bal	Aim1	Anx8	Me2
BC006779	Baiap2l1	Cap	Metap2
Bst2	Bckdha	Capn2	Mme
Clim1	Cadm1	Cav *	Mrc2
Cmpk2	Ctsl	Cdkn2a	Mre11
Ddx58	Daglb	Ckap4	Msra
Dtx3l	Dbt	Clp	Napg
Eif2ak2	Dcoh	Cnn2	Nudt9
G1p2	Dhx33	Col1a1	P4ha1
Galm	Eml2	Col1a2	P4ha2
Garg39	Enpep	Col3a1	Pea15
Garg49	Epb4.1l5	Col6a1	Pk3
Gbp2	Fam129a	Col6a2	Plod2
Gbp3	Fan1	Crabp1	Plod3
Gbp6	Fbxo2	Ctsb	Por
Gstm1	Gsta	D7Ertd671e	Ptmb4
Gstm2	Hist3h2bb	Dpysl3	Rad50
H2-D1	Hk2	Dsn	Rca1
Ifi1	Hmg2a	Ergic53	Rexo2
Ifi205b	Itgav	Fabp5	Rgc32
Ifi35	Jip3	Fam114a1	Sept5
Ifit1	Kiaa0193	Glud	Sparc
Ifitm3	Kiaa1102	H2-K	Svil *
Inf2	Nipsnap1	Igtp	Trp32
Kiaa2005	Polr1d	Ikbip	Tubb6
Mylk *	Ptplad1	Itga3	Ufc1
Nfkb2	Rpl5	Itgb1	Vcl *
Oasl2	Sp2	Kiaa1830	Wdr1
Parp12	Steap	Lamb-1	
Pdlim5	Tjp2	Lbr	
Pml	Wipi2	Lmp7	
Rnf213		Loh11cr2a	
RP23-399J8.4-002			
Sm22			
Stat1			
Tpm1			
Zfp185			

c

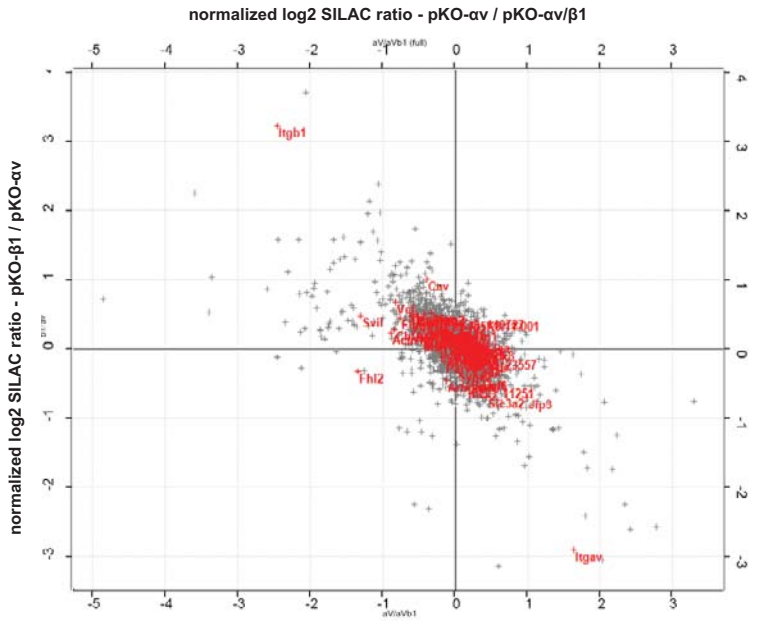

Figure S8 Cellular proteome of pKO-αv, pKO-β1 and pKO-αv/β1 cells. (**a**) SILAC labelled cells cultured on FN for several passages were analysed by MS. SILAC ratios of 150 significantly regulated proteins (ANOVA, Benjamini/Hochberg FDR) were subjected to non-supervised hierarchical cluster analysis and colour coded. The bars depict differentially regulated clusters of proteins. (**b**) Gene names of the 3 differentially regulated groups (a) are shown. Known FA proteins are marked with an asterisk. (**c**) Scatter plot showing SILAC ratios. Previously annotated FA proteins are labelled in red.

Figure 5c

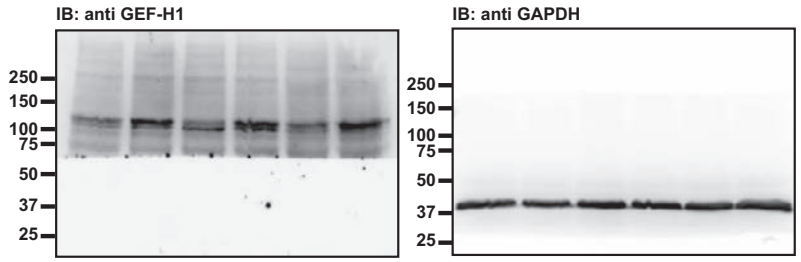

Figure 6d

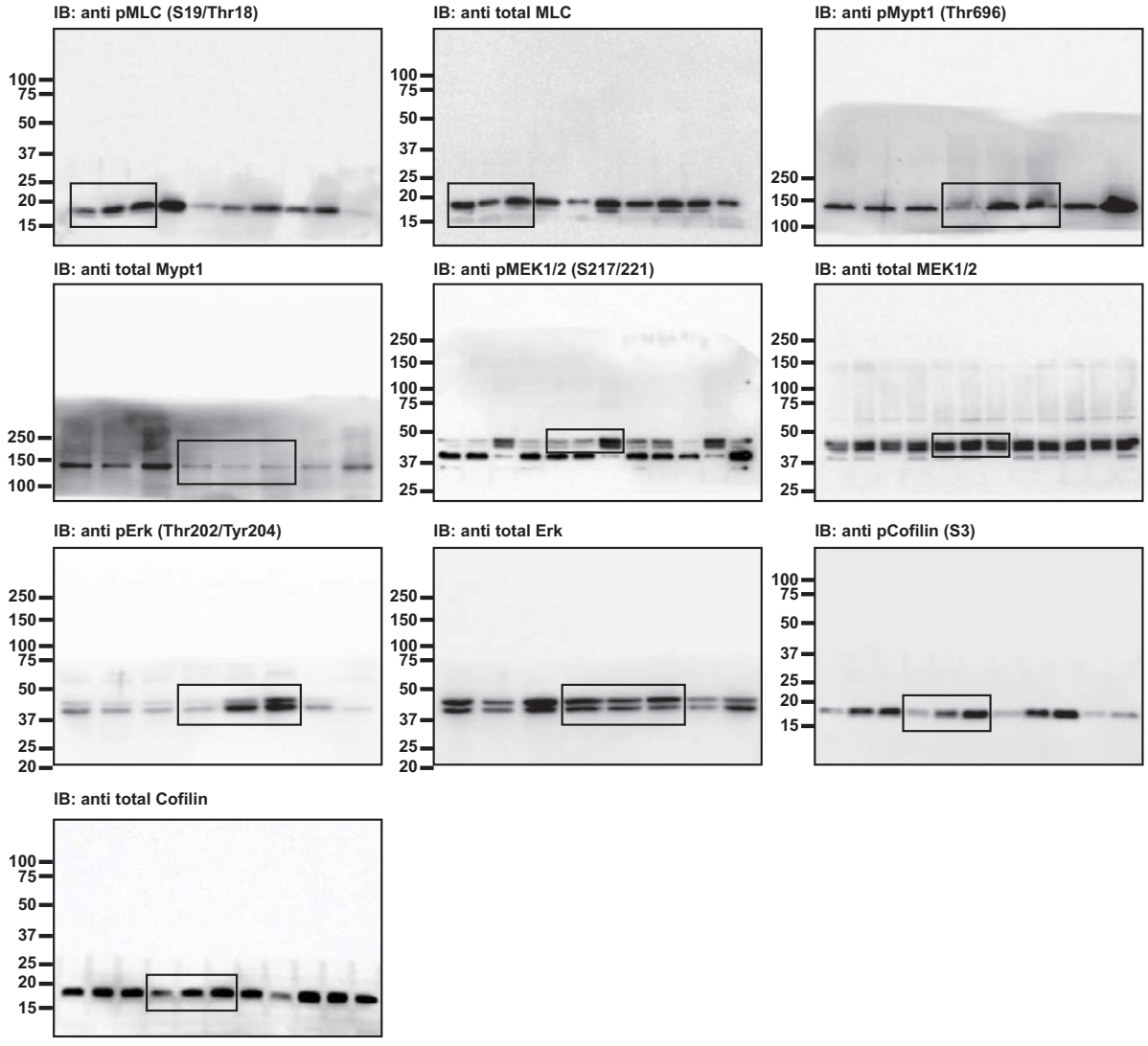

Figure S9 Uncropped western blots.

Figure 7c

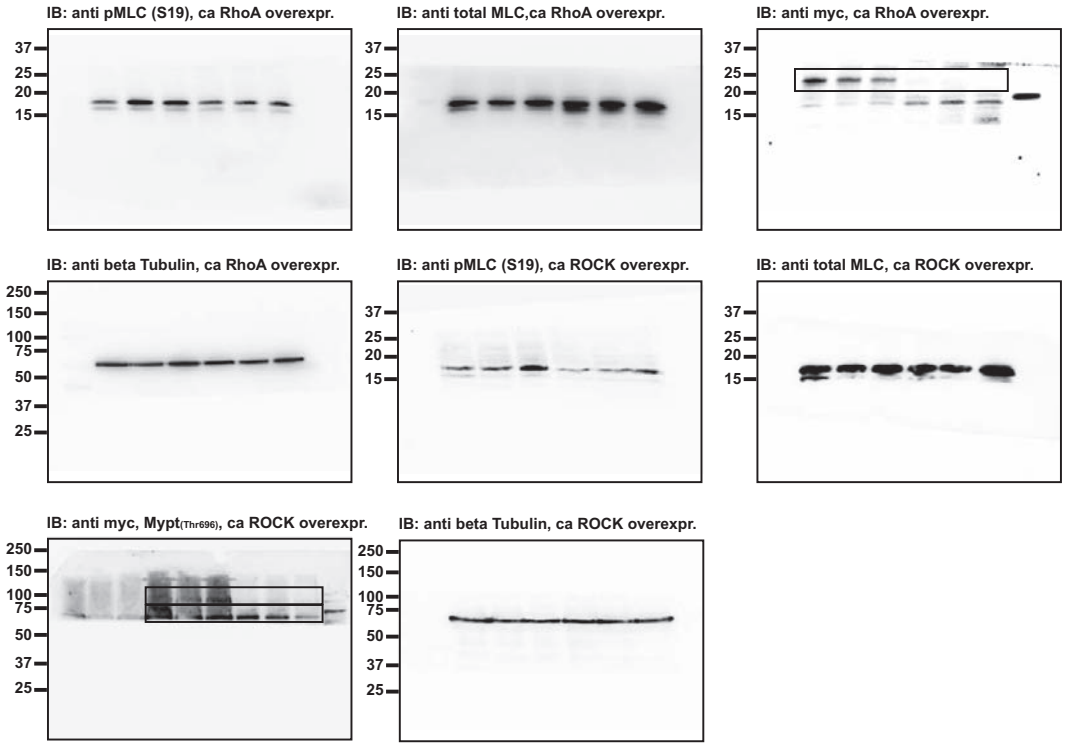

Figure S1f

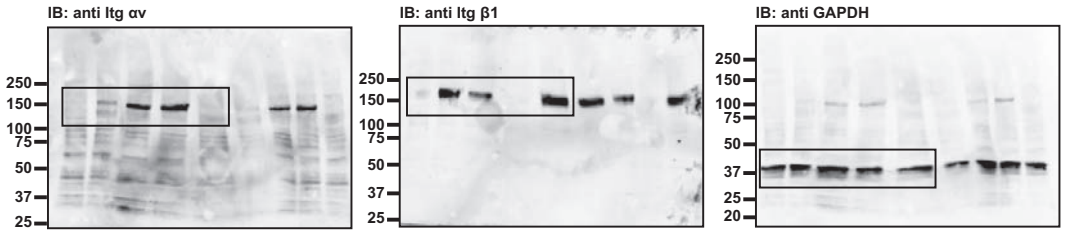

Figure S1g

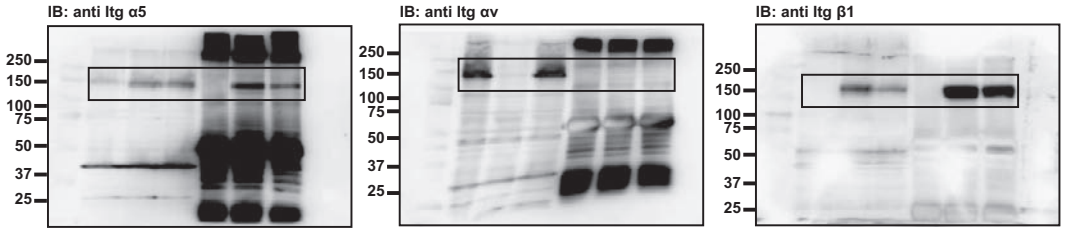

Figure S9 continued

Supplementary video legends

Video S1 Time-lapse movie of pKO-αv cells plated on FN. Cells were plated on FN coated (5 μg/ml; blocked with 1% BSA) tissue culture dishes in presence of 10% serum and video tracked over 20 hours with a frame rate of 1 picture every 4 minutes. Pictures were acquired with a phase contrast microscope at magnification 20x.

Video S2 Time-lapse movie of pKO-αv/β1 cells plated on FN. Cells were plated on FN coated (5 μg/ml; blocked with 1% BSA) tissue culture dishes in presence of 10% serum and video tracked over 20 hours with a frame rate of 1 picture every 4 minutes. Pictures were acquired with a phase contrast microscope at magnification 20x.

Video S3 Time-lapse movie of pKO-β1 cells plated on FN. Cells were plated on FN coated (5 μg/ml; blocked with 1% BSA) tissue culture dishes in presence of 10% serum and video tracked over 20 hours with a frame rate of 1 picture every 4 minutes. Pictures were acquired with a phase contrast microscope at magnification 20x.

Ma contribution à cette étude a été la réalisation des mesures de forces sur les 3 lignées cellulaires à différentes rigidités. J'ai également pu mettre en œuvre les techniques d'analyse d'image sur cellules patternées que j'ai développées pour mes propres expériences (génération des cartes moyennes d'intensité pour les immunomarquages, …). J'ai par ailleurs pris part aux discussions concernant l'interprétation des résultats et l'orientation de la discussion.

Cet article possède deux niveaux de lecture. Le premier niveau s'intéresse aux contributions respectives (spécifique, commune ou synergique) des deux intégrines dans des processus cellulaires clés : régulation de la taille des adhésions, étalement et migration cellulaire, modulation du niveau de forces en fonction de la rigidité de l'environnement, contribution à la régulation de la voie Rho – ROCK – mDia1. Le deuxième niveau considère cette étude comme un article de ressources fournissant de nombreuses données de protéomique à partir desquelles des hypothèses sur de nombreuses voies de signalisation ou le fonctionnement de telle ou telle partie précise du réseau pourront être formulées en fonction des domaines de prédilection de chacun.

Mise à jour du fonctionnement de la voie Rho dans le processus de mécano-transduction

Le rôle de RhoA dans le processus de mécano-transduction a été brièvement décrit en introduction (I-4-A). Rho joue un rôle prépondérant dans l'organisation du cytosquelette, de la taille des adhésions. Il permet de moduler ses deux effecteurs : mDia1 et ROCK.

L'inhibition spécifique de Rho et de ROCK a déjà permis de montrer que la formation de contacts focaux nécessitait mDia1 mais qu'un stimulus extérieur suffisait à remplacer ROCK dans ce mécanisme (Riveline, J. Cell Biol., 2001). Le schéma récapitulatif de ce travail suggérait déjà un découplage des actions de Rho sur ROCK et mDia1. (Figure 31).

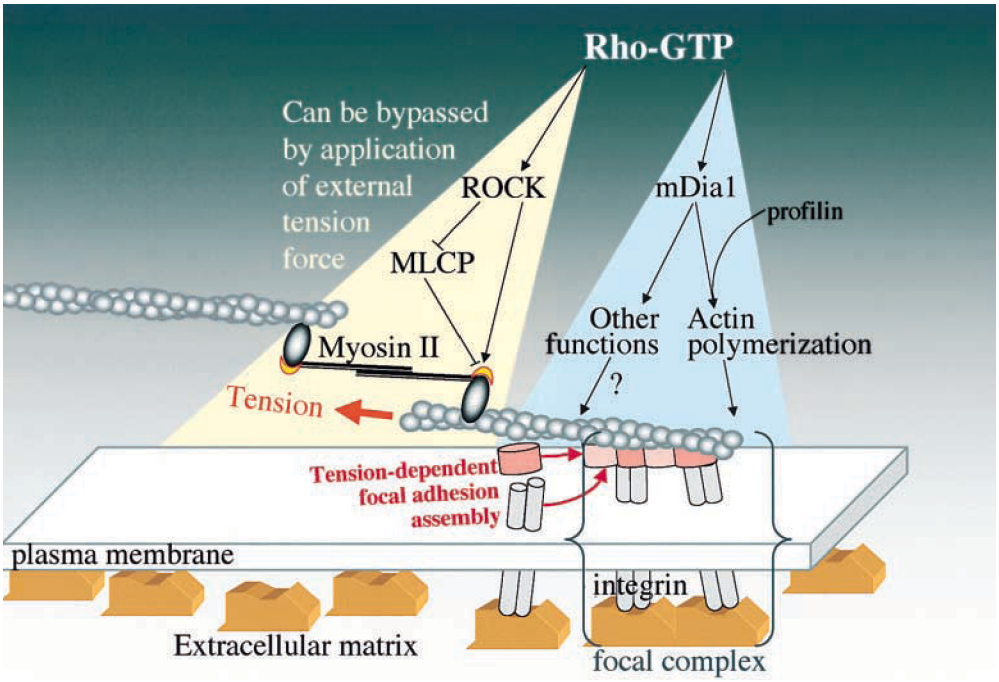

Figure 31 : Schéma décrivant le rôle de mDia1 et ROCK dans la formation des contacts focaux

Riveline, J. Cell Biol., 2011

A la lumière de nos résultats, ce schéma a pu être revisité et permet même de préciser la régio-sélectivité d'action au sein des adhésions (Figure 32). Différentes intégrines sont capables de réguler l'action de Rho vers l'un ou l'autre de ces effecteurs ce qui permet un couplage immédiat entre milieu extracellulaire et régulation de la signalisation intracellulaire.

αvβ3 est capable de générer de grandes adhésions sans pour autant permettre une adaptation de la force générée à la rigidité du substrat. Le faible niveau de contractilité constitutivement présent suffit à déclencher l'augmentation de la taille des adhésions. Ces observations sont concordantes, les travaux récents suggérant qu'un faible niveau de forces est suffisant pour permettre la croissance des adhésions (Stricker, Plos One, 2013). Par ailleurs, αvβ3 est le principal responsable de l'activation de Rho via GEF-H1. Cette régulation implique certainement les microtubules dont la stabilité aux sites d'adhésions est régulée par la rigidité du substrat et qui sont des inhibiteurs connus de GEF-H1 (Heck, Mol Biol. Cell, 2012). Ce type d'intégrine est donc responsable de la polymérisation de l'actine en réponse à la rigidité et joue un rôle dans l'augmentation de RhoA mais n'est pas capable seule d'augmenter la contractilité cellulaire au sein de la cellule.

α5β1 de son côté joue un rôle important dans la transmission du signal de RhoA vers ROCK pour permettre l'augmentation de la contractilité cellulaire. Cette intégrine actine Erk2, la kindline 2 et le complexe IPP et permet ainsi l'activation de la myosine mais également la régulation de protéines associées à l'actine comme la cofiline qui se retrouve phosphorylée et ne fragmente ainsi plus l'actine.

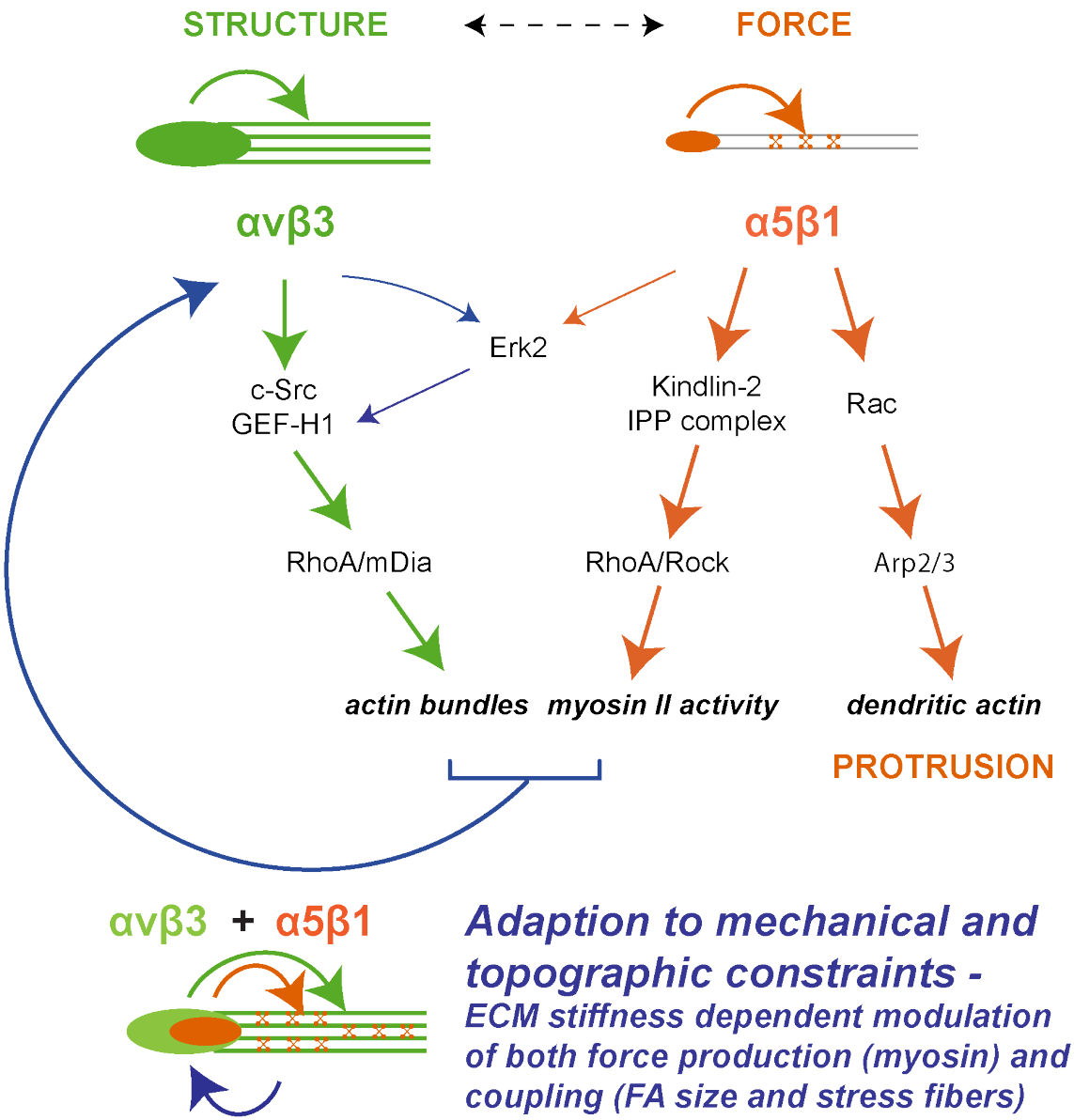

Figure 32 : Schéma récapitulatif du rôle de chaque intégrine dans la régulation de la signalisation par Rho.

Seul, ce type d'intégrine permet la génération d'une force plus importante qu' αvβ3 mais ne permet pas l'adaptation de la force à la rigidité.

L'action des ces deux intégrines de concert permet de changer la donne. αvβ3 permet une régulation de la quantité d'actine polymérisée et de la quantité de RhoA activée. α5β1 permettra alors l'orientation de RhoA vers la voie d'activation de ROCK et de la myosine. L'augmentation de la force ainsi générée par les fibres de stress permettra en retour une adaptation de la signalisation au site de l'adhésion pour permettre l'adaptation de la contractilité cellulaire à la rigidité.

Ce travail identifie ainsi l'actine comme plateforme d'intégration de ces deux signaux pour le processus de mécano-transduction. L'activation de la myosine par α5β1 sans augmentation de la

quantité d'actine par αvβ3 ne permet pas à la cellule d'adapter la force à son environnement, ce qui suggère que la régulation de la polymérisation de l'actine au sein de la fibre de stress concerné joue un rôle important dans la production de forces au sein de cette structure.

Enfin la ségrégation au sein de l'adhésion des deux types d'intégrines fait écho aux différences de mouvements identifiés par super-résolution au sein de l'adhésion (Rossier, Nat. Cell. Biol., 2012). Ces déplacements pourraient expliquer la ségrégation spatiale de ces deux intégrines au sein de l'adhésion permettant ainsi des signalisations distinctes. Ce mécanisme a sans doute son importance quand on voit la quantité impressionnante de protéines différentes capables d'interagir avec l'adhésion. La régulation de ces interactions pourrait passer par un niveau de ségrégation différent en fonction de la tension appliquée sur l'adhésion. Une force plus importante générée sur l'adhésion pourrait ainsi permettre une meilleure ségrégation et augmenter le niveau d'activation des voies de signalisation en augmentant la surface capable d'interagir avec les protéines du cytoplasme. Le couplage de la super-résolution à l'attachement des cellules sur des substrats de différentes rigidités devrait permettre de venir éclairer ces phénomènes dans les années à venir.

Après les adhésions, je vais maintenant m'intéresser à la régulation des forces cellulaires par l'architecture du cytosquelette d'actine et au fonctionnement de la production de forces au sein des fibres de stress.

IV. Fibres de stress et génération de forces

Chaque réseau d'actine possède des propriétés mécaniques différentes et des modes de production de forces différents. Dans cette partie, j'ai tenté de modifier le niveau des forces produites par la cellule en modifiant son architecture par l'utilisation des micropatterns.

1. ORGANISATION CELLULAIRE ET PRODUCTION DE FORCES : LE ROLE DES FIBRES DE STRESS

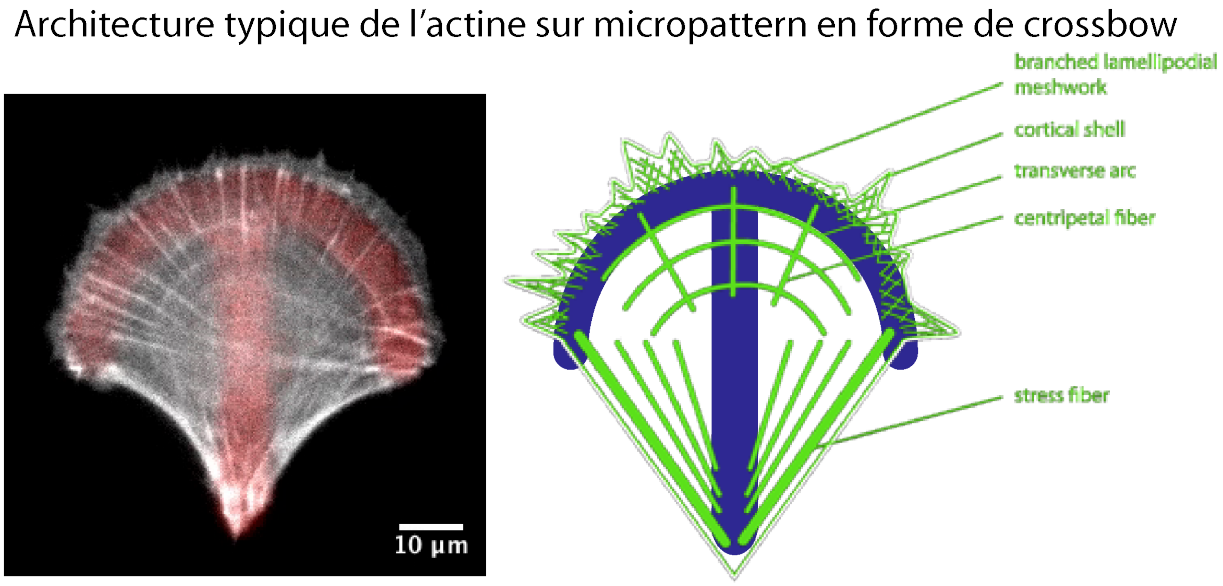

Figure 33 : Hypothèses de travail : régulation de la force produite en fonction de l'organisation du cytosquelette

Haut – description de l'architecture typique adoptée par une cellule sur un micropattern en

forme d'arbalète (crossbow). Tous les types de réseaux sont ici représentés. – Bas – l'hypothèse de travail considère que le micropattern pourra modifier l'importance de ces réseaux et le niveau des forces produites. Il sera ainsi possible de comprendre quel réseau participe le plus à la force. Les options suivies ont été les suivantes : modification de la courbure de la cellule pour modifier l'activité du lamellipode, épaississement ou élargissement de la zone d'interaction entre le flux rétrograde et le substrat.

L'hypothèse de travail était la suivante. La modification du micropattern permet de modifier l'architecture de la cellule. Chaque module d'actine composant ce réseau est responsable d'une partie de la production de forces par la cellule. La modification de l'architecture devrait donc permettre de modifier les forces générées. Des transformations progressives devraient ainsi fournir des tendances permettant d'identifier les déterminants de la production de forces, à surface d'étalement constante.

La courbure du bord de la cellule a été désignée comme un régulateur de son activité de protrusion (Parker, FASEB J., 2002), la modification de la courbure du front avant de la cellule est donc susceptible de modifier l'architecture et le niveau des forces cellulaires.

La corrélation entre flux rétrograde et forces au niveau des adhésions (Gardel, J. Cell Biol., 2008) suggère également que le confinement, par le pattern, des adhésions au front avant de la cellule pourrait diminuer les forces générées et minimiser la surface d'interaction entre le flux retrograde et l'adhésion. J'ai donc élargi ou épaissi la zone avant de l'arbalète pour tenter de modifier le niveau des forces générées par la cellule.

La modification de la courbure (figure 34) au front avant de la cellule permet de modifier de façon importante la répartition des forces. Dans la configuration rectiligne (C1) les forces sont localisées aux extrémités de la barre horizontale à l'avant de la cellule. Les zones de localisation des forces correspondent à la zone probable où se concentre la majorité de l'activité protrusive de la cellule. En augmentant progressivement la courbure, on va assister à une relocalisation progressive de forces, des parties latérales vers le centre du front avant de la cellule. La relocalisation des forces au front avant de la cellule pourrait ainsi s'expliquer par le rétablissement d'une activité protrusive à l'avant de la cellule.

Un autre mécanisme est également envisageable. La force serait plus importante dans les grandes fibres de stress. La courbure homogénéise la longueur des fibres joignant l'apex basal de la cellule à l'avant du micropattern et serait ainsi responsable de la re-répartition des forces au front avant de la cellule.

Cependant, malgré ces modifications importantes de la répartition des forces, aucun changement significatif de l'énergie mécanique de la cellule n'est identifiable dans ces conditions. La force serait alors conditionnée par la taille de la cellule et l'organisation du cytosquelette ne permettrait que l'adaptation des points d'application de ces forces en fonction de l'environnement ?

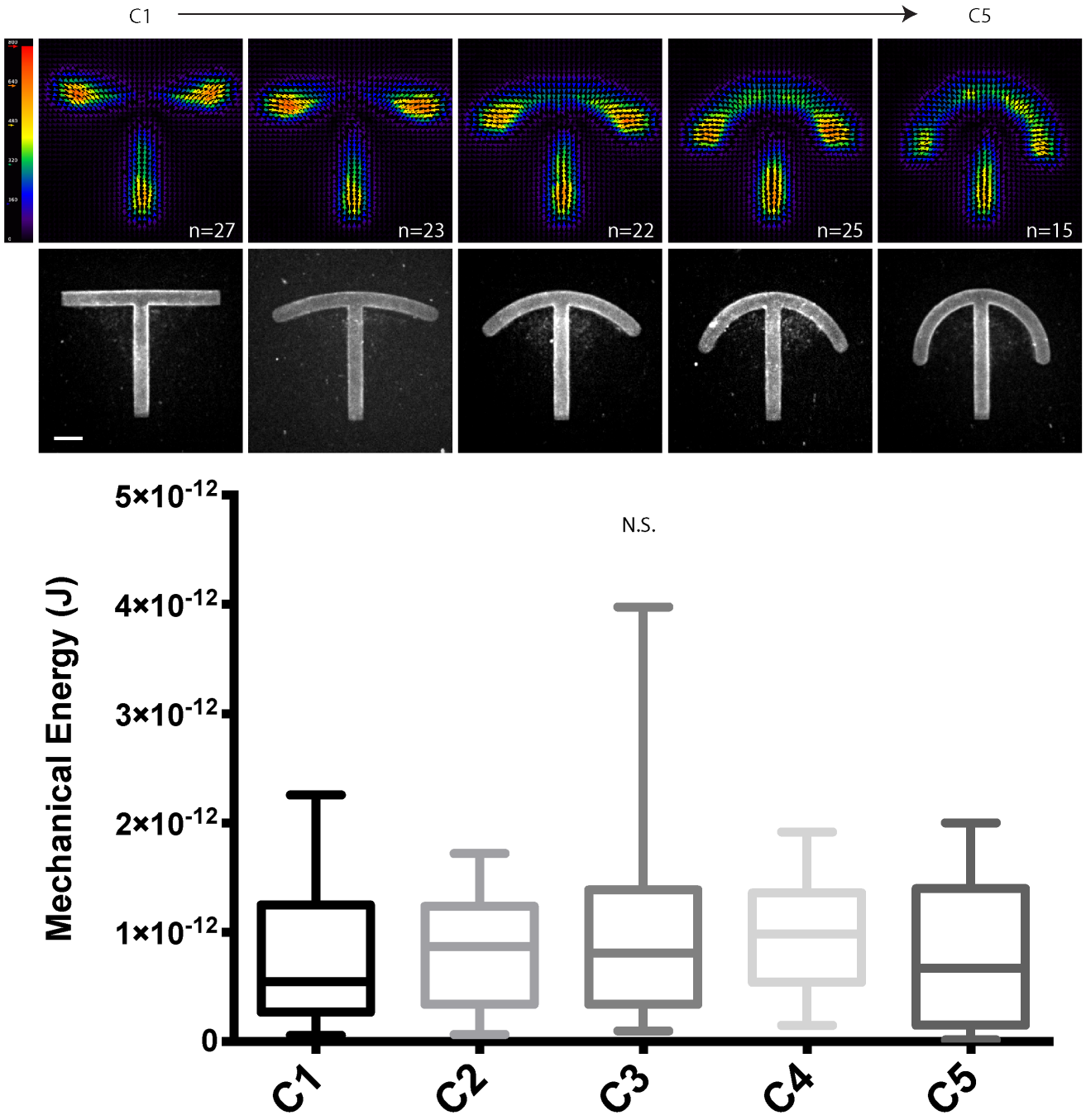

Figure 34 : Effet de la courbure sur la production de forces

Haut – carte moyenne des forces exercées par la cellule sur le micropattern – Milieu – Image moyenne du micropattern, la barre d'échelle représente 10 µm – Bas – Energie mécanique de la cellule en fonction des différents micropatterns. Aucune différence significative n'a pu être identifiée.

Pour aller plus loin dans mes observations, j'ai ensuite étudié l'effet de l'épaississement de la zone d'interaction entre le flux retrograde d'actine et le substrat adhérent (figure 35). Là encore, des modifications de la répartition des forces ont pu être mises en évidence. L'épaississement de la zone d'interaction permet une dilution des forces au front avant de la cellule mais pas une réelle

augmentation. La dispersion des adhésions sur une surface plus grande pourrait expliquer cette dilution des forces alors que dans le cas le plus fin, les adhésions sont contraintes au front avant de la cellule et la force y est précisément localisée.

Encore une fois, l'hypothèse de la longueur des fibres de stress est plausible. L'élargissement de la zone avant permet la génération de fibres de stress de longueur plus variée et une répartition de la force sur toute la surface du front avant.

De façon très intéressante, ces effets sont locaux et l'utilisation d'un pattern asymétrique récapitulant les propriétés de 2 micropatterns distincts permet de retrouver les deux phénotypes caractéristiques au sein de la même cellule (L7).

Cela encourage encore l'hypothèse du rôle du cytosquelette dans la régulation de la localisation de la transmission des forces à l'environnement.

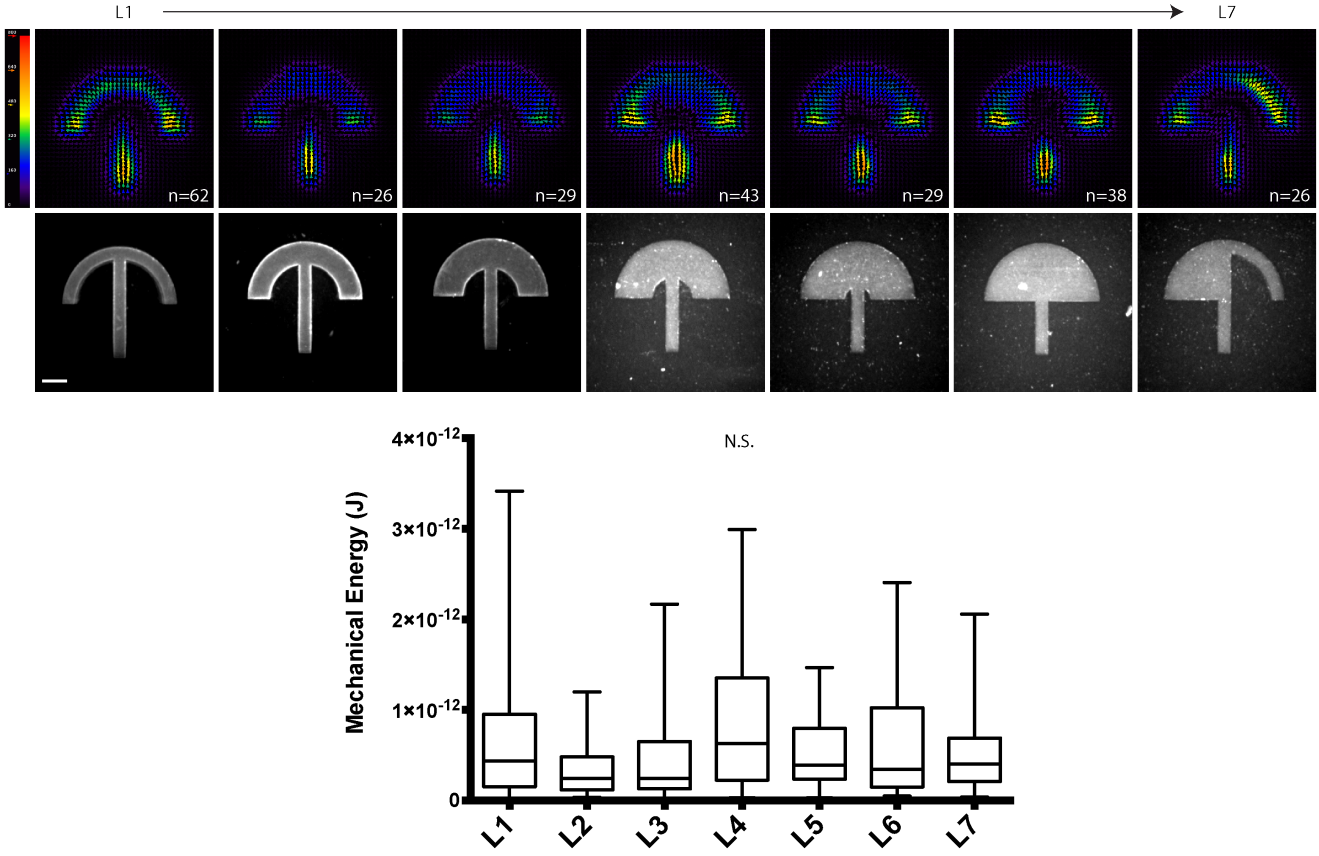

Figure 35 : Effet de l'épaisseur de la zone d'adhérence au front avant de la cellule

Haut – carte moyenne des forces exercées par la cellule sur le micropattern – Milieu – Image moyenne du micropattern, la barre d'échelle représente 10 µm – Bas – Energie mécanique de la cellule en fonction des différents micropatterns. Aucune différence significative n'a pu être identifiée.

Pour finir, j'ai fait varier la largeur de la zone d'interaction entre flux retrograde et zone

d'adhérence.

Une modification de la répartition des forces a encore une fois pu être mise en évidence. L'augmentation de la zone d'adhérence centre relocalise les forces à la périphérie de la cellule et la dilution des forces n'est pas observée dans cette situation. Cette fois-ci, il semble que les forces soient confinées aux zones où des fibres de stress vont être générées au dessus de la zone non adhérente du micropattern. Pour la première fois, une modification significative de l'énergie contractile est observée, entre le pattern totalement adhésif et le pattern présentant une grande surface non-adhésive dans sa partie centrale.

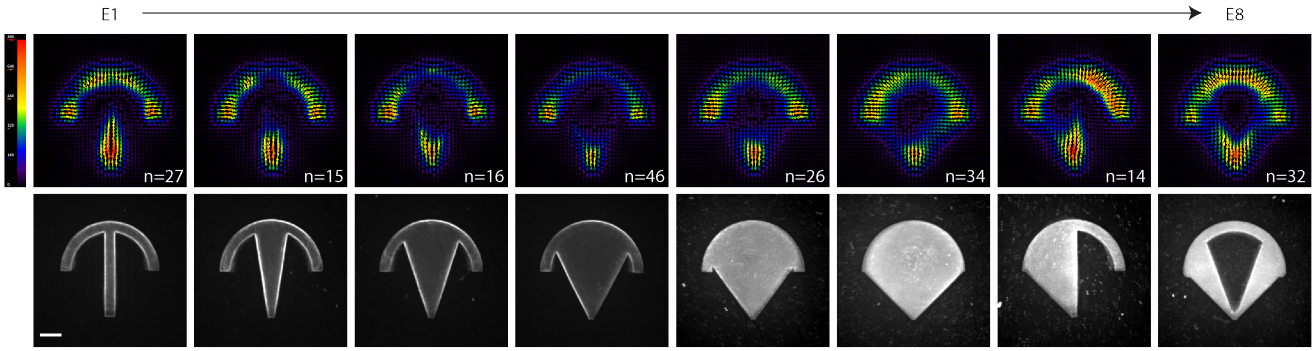

t-test P values summary

	E6	E7	E8
E5	0.36	0.14	0.01
E6		0.41	0.05
E7			0.56

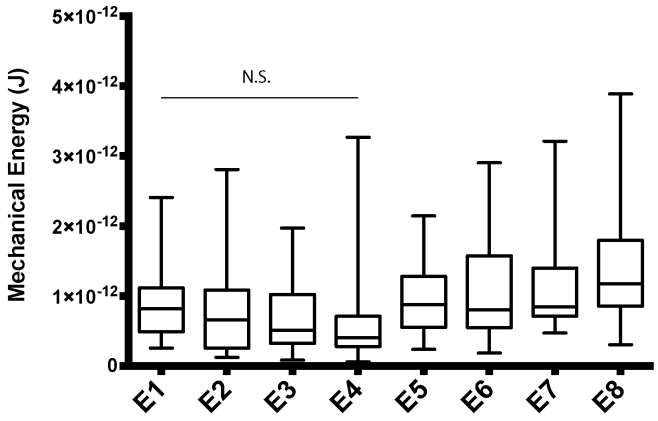

Figure 36 : Effet de la largeur de la zone d'adhérence sous la cellule

Haut – carte moyenne des forces exercées par la cellule sur le micropattern – Milieu – Image moyenne du micropattern, la barre d'échelle représente 10 µm – Bas – Energie mécanique de la cellule en fonction des différents micropatterns et récapitulatif des P values pour les mesures ayant montrée des écarts significatifs de leur moyenne après un test ANOVA (E1-E4 et E5-E8 ont été mesurés dans 2 expériences distinctes).

L'observation méticuleuse de l'organisation de l'actine au sein de ces cellules permet de mettre en avant la présence quasi-systématique de nombreuses fibres de stress parallèles dans la partie centrale de la cellule pour E8 alors que dans le cas E5, les fibres sont présentes de façon moins systématique et moins ordonnée. Ces observations suggèrent que la formation de fibres de stress permet de faire augmenter la force générée par les cellules, à surface d'étalement constant !

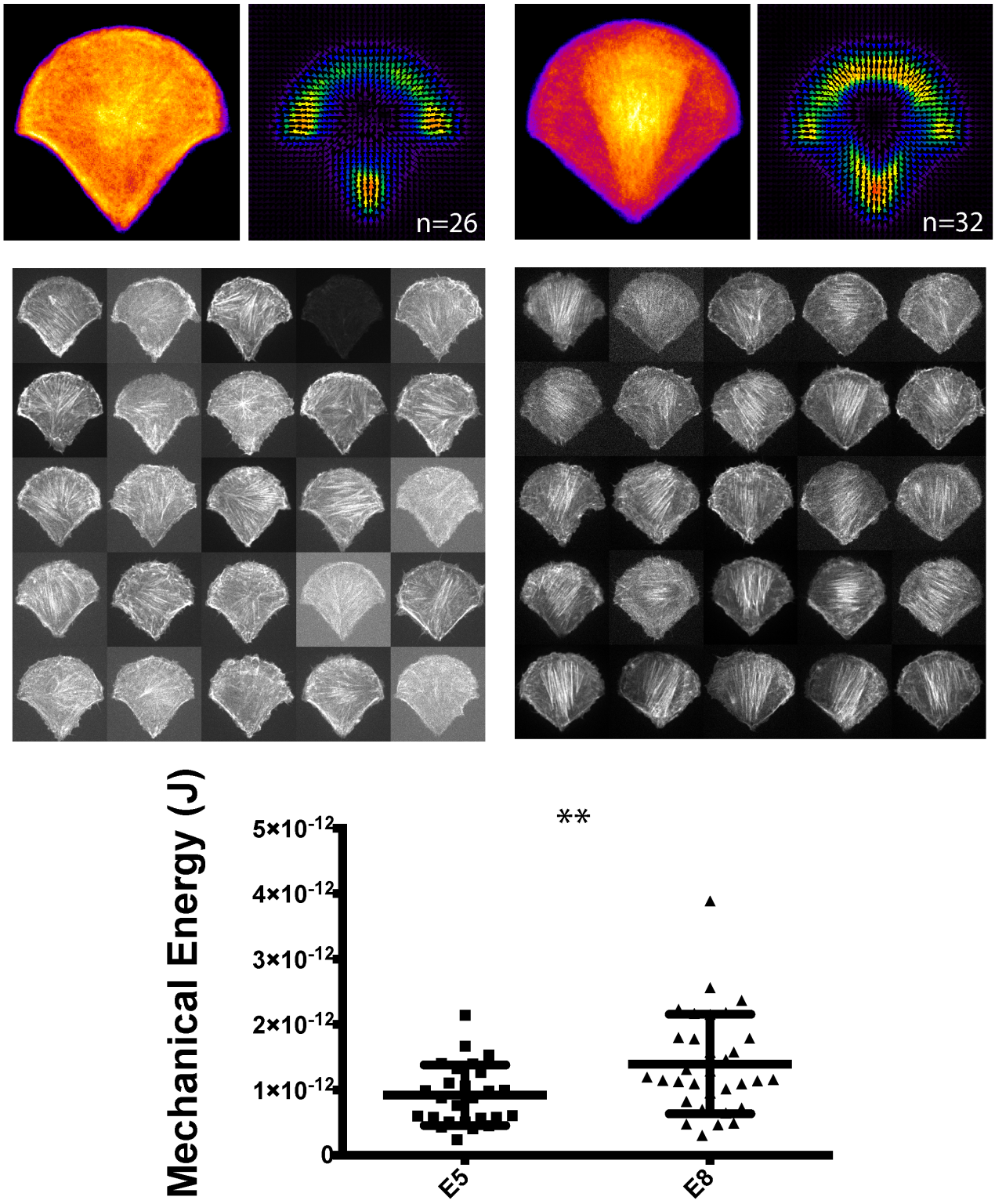

Figure 37 : L'augmentation de la force corrèle avec la formation de fibres de stress sous l'effet du micropattern adhésif.

Haut – Image moyenne de l'actine (Lifeact-GFP) et pattern de force correspondant – Milieu – montage représentant l'organisation de l'actine dans 25 cellules différentes – Bas – Energie contractile dans les deux situations. Les barres d'erreur représentent la déviation standard.

Ces observations m'orientent vers le rôle important des fibres de stress dans la régulation de la répartition des forces mais également dans leur production. Mes hypothèses peuvent se résumer sur le schéma suivant (figure 38).

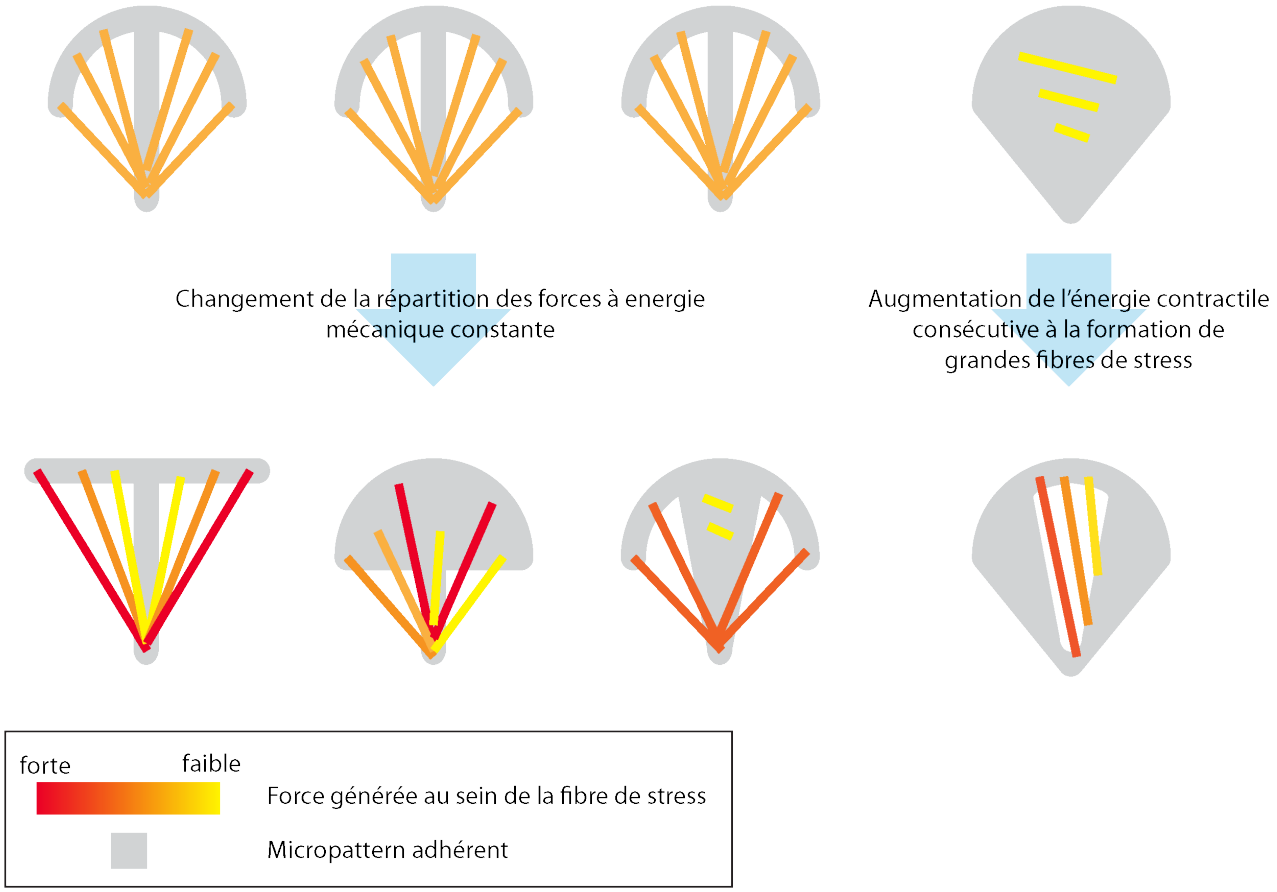

Figure 38 : Rôle de la longueur des fibres de stress dans la répartition des forces générées par la cellule

La modification de l'organisation des fibres de stress permet de modifier la répartition des forces avec des forces plus importantes aux zones où les fibres de stress sont les plus longues. L'énergie mécanique totale n'est pas pour autant modifiée, il s'agit d'un mécanisme permettant de réorganiser les forces sans nécessairement modifier le niveau contractile global. La formation de fibres de stress importantes permet également de faire augmenter le niveau de contractilité par rapport à une situation où celles-ci sont peu développées. Je vais maintenant tenter de caractériser de façon plus directe le niveau des forces générées au sein des fibres de stress en fonction de leur longueur

2. LONGUEUR DES FIBRES DE STRESS ET PRODUCTION DE FORCES (MANUSCRIT EN PREPARATION)

Critical length for force production within actin stress fibres defines the upper limit for cell length and contractility

Timothée Vignaud[1-4], Laëtitia Kurzawa[1-4], Benjamin Fogelson[5], Jonathan Arnaud[1-4], James Sillibourne[1-4], Magalie Prioux[1-4], Laurent Blanchoin[1-4], Alex Mogilner[5], Manuel Théry[1-4]

1 CNRS, Laboratoire de Physiologie Cellulaire & Végétale, UMR 5168, F-38054 Grenoble, France
2 Univ. Grenoble Alpes, LPCV, F-38054 Grenoble, France
3 CEA, DSV, iRTSV, LPCV, F-38054 Grenoble, France
4 INRA, LPCV, USC1359, F-38054 Grenoble, France
5 Department of Mathematics, Department of Neurobiology, Physiology and Behavior, University of California, Davis, One Shields Avenue, Davis, CA 95616

ABSTRACT

Regulation of traction forces by actin cytoskeleton plays a central role in key processes such as cell migration and differentiation. The positive feedback loop between adhesion signalling, myosin II activation and cytoskeleton reinforcement has been widely studied but no negative regulators have been found in these processes. Using TFM, acrylamide patterning and laser ablation, we showed that the force production within stress fibres follows a biphasic curve with respect to their length. After a critical length was reached, myosin/actin ratio and contractility were no longer correlated. We propose a negative feedback mechanism based on actin depletion or myosin mediated disassembly driving loss of mechanical connectivity within the fibre. This process provides the first mechanical negative signal in the process of adhesion-contractility reinforcement .

INTRODUCTION

Our body is under constant (re)construction. The cells are constantly renewed in most of the tissues of our organisms. Yet, the architectures of our organs display robust and well-defined organization. The cells are able to sense their environment and modify their behaviours accordingly, allowing for the maintenance of the overall tissue architecture. As an example, cell spreading has been shown to regulate cell fate[1] and cell contractility[2]. The mechanisms controlling the production of cellular forces are still not fully understood. The size of adhesions has been shown to correlate with traction forces [3] but this seems to be valid only at the front of the cell at the early stages of adhesions formation and maturation[4]. Recently, forces and adhesion sizes have even been decorrelated, showing that big focal adhesions could be formed at very low cellular contractility[5,6], under specific conditions. Mostly, only the positive feedback between cell adhesion and contractility has been studied and no clear mechanism has been shown to counteract this loop. β-Pix was shown to negatively regulate focal adhesion maturation in the context of myosin-II inhibition[7] but no negative feedback has been found in an active myosin II context.

Here we focus on the role of the structure responsible for force production: the actin cytoskeleton. Retrograde flow and actin fibres are the source of the force. Retrograde flow can be transmitted by friction to FA[8]. Actin fibres are anchored to adhesions and are another force generating structures[9,10]. Using micropatterned soft substrates, we identify stress fibres as the optimal structure for force production inside the cell. Increasing pattern length, we find that the forces produced by stress fibres first increase with their length before decreasing after a typical length is reached. This maximal tension length is insensitive to matrix rigidity and is identical to maximum cell extension on 2D substrate. Analysis of stress fibres composition shows that myosin/actin ratio is increasing with fibre length even when the forces are dropping. We propose a mechanism involving actin stress fibres disassembly by myosin above a critical myosin/actin ratio to explain our observations. This mechanism could be responsible for cell size regulation and the coupling between cell protrusion and retraction during migration.

RESULTS

Cell architecture modifies contractility of cells stably spread on micro-patterns

We first plated cells on 2D flat poly-acrylamide gel (PAG) and measured mechanical energy. Cell area and mechanical energy (ME) were significantly correlated (Fig 1b) as previously describe[2] whereas we found no correlation of ME with cell aspect ratio and cell major axis. When looking at individual cells, we found that high contractile cells often displayed stress fibres contrary to low contractile ones (Fig 1a). When then decided to investigate the contribution of stress fibres to the contractility of the cell. In order to avoid variability due to variations in adhesion maturation[4], we plated cells on fibronectin micro-islands of defined shape, so called micro-patterns, produced on PAG (Fig 1d). Cell ME was followed for several hours and compared between confined and unconfined cells

(Fig 1c). Contractility was quite stable in confined cell with a 26% ME mean variation coefficient whereas unconfined cells ME displayed high variability, probably due to protrusion-retraction cycle during cell movement.

We then removed the inside part of the micro-pattern (Fig 1d). This modification led to the formation of two big peripheral fibres over the non-adherent region of the micro-pattern, as previously described[11]. This modification of the micro-pattern was also accompanied by a doubling of ME. This suggested that the newly formed stress fibres were the structure responsible for this huge ME increase. The micro-pattern shape was then varied to vary the organization of stress fibres. Doubling of the area was achieved by doubling either its length or width (Fig 1e). In both cases, the ME increased but in different ways: in the doubling of the width, the maximal local traction force was not changed; we just saw forces of the same level but covering a higher area. Regarding the length, the situation was different. The maximal local traction was increased and spread over the same area as in the control case. At the same time, the doubling of the width increased the number of stress fibres en the same length as in control whereas doubling the width increased the length of the fibres without creating new ones. This suggested that the force produced by stress fibres is scaling with their length and that ME could increase either by creating more fibres or having longer fibres.

The scaling between cell length and ME has an upper limit, insensitive to substrate stiffness.

To assess the relationship between stress fibres length and contractility, we performed force measurements on micro-pattern of increasing length, from 22 µm to 82 µm (Fig 2a and b). The ME first displayed a regular increase with cell length until a 60 µm length was reached. For higher values, the ME energy then decreased. As substrate rigidity has been shown to regulate cell contractility[12], we performed the same measurements around the critical length but using a softer PAG (9.6 kPa vs. 35 kPa initially). The ME was slightly decreased but the transition was still occurring at the same length. To see if this limit in length was also relevant for unconfined cell, we looked at the distribution of cell major axis for cells on homogenous 2D substrate. Interestingly, the distribution dropped at 60 µm length, suggesting that this upper limit was also relevant for unconfined moving cells.

Actin stress fibres are the main contributors to cell ME.

The direct role of actin fibres for force production was still questionable because no direct measurement of force produced by single stress fibres was performed. We used a tightly focused pulsed UV laser to disrupt single fibres inside the cell[13]. The force released after fibre ablation was symmetric and well localized at both fibre ends (Fig 3a), consistent with force production and transmission within this structure. We then tested if stress fibres of increasing length were producing increased forces. The drop in ME after ablation was used to estimate the force released (Fig 3b). Fibres of length distributed around the critical value found previously (values of fibre length are shifted of 12 µm compared to cell length because of the width of the adherent region: a cell length of 59 µm correspond to a fibre length of 47 µm) were used to perform the experiment. Unexpectedly, the correlation was low between total and released ME (Fig 3d) and we saw no differences between ME released when values were sorted according to fibre length. Photo-bleaching the fibre before ablation (Fig 3e) allowed us to follow retraction within the fibre. All the marks moved after the initial cut but the contraction of the fibre was then only localized to region close to the ablation site (Fig 3f). We hypothesize that connectivity was rescued within the fibre and that a second cut was necessary to release all the forces produced by the fibre. Indeed, a second cut on the same fibre further decreased ME (Fig 3g-h). Released and total ME were then nicely correlated (Fig 3i) and the ME released by fibres of different sizes were following the same trend as total ME with respect to cell length (Fig 3j). Finally, the ME released corresponded on average to

37% of total ME when one of the two big peripheral stress fibres was ablated twice. This clearly showed that these two fibres were the main contributors to the ME.

Myosin/actin ratio is constantly increasing with fibre length

Stress fibres biochemical compositions were analysed by immuno-staining cells for actin, phospho-myosin and alpha-actinin (Fig 4a). Linescans were performed on fibres of different length. Average profile showed that actin density in the fibre was decreased whereas phospho-myosin was only slightly increased and alpha-actinin showed no clear trend (Fig 4b). Computing the myosin/actin ratio then showed a constant increase with stress fibre length, even when the ME was dropping. Myosin/actin ratio was thus decorrelated from ME after the critical length was reached. This suggested a physical limit in the force production process rather than a biochemical negative feedback loop.

Actin flow within the fibres correlates with ME

Movement of actin within intact stress fibres was then assessed by photo-bleaching. The marks were flowing at a certain speed toward a convergence point (Fig 5a). This convergence points were found on both ends of the fibre, with no systematic synchrony between two fibres inside the same cell (Fig 5b). Maximum actin flow speed within the fibre, when sorted according to fibre length, was following the same trend as both total and released ME. This suggested that connectivity within the stress fibres was lost after critical length was reached, thus preventing the transmission of forces and movement within the fibres. Stress fibres were also shown to be asymmetric flowing structures in these conditions.

DISCUSSION

We have used the combination of TFM, micropattern, laser-ablation and immuno-staining that to study the contractility of single actin fibres in their normal cytoplasm context.

Stress fibres were shown to be great contributors to the total ME of the cell. The ME of the cell was following a biphasic curve with decrease after a critical length of 60 µm. This loss of ME was also found in stress fibres. Immuno-staining showed that the myosin/actin ratio within these structures was constantly increasing, ruling out a potent biochemical feedback on myosin activity. Dynamic analyses of actin movement within the fibre were in agreement with these results, the maximum speed within the fibre being correlated with the ME of the cell.

Several mechanisms could explain our observations.

Myosin has been shown to be able to disassemble actin structures[14,15]. This could explain our observations. Increase in stress fibre length increased actin myosin ratio. Before the critical value, higher myosin/actin ratio is able to produce more forces. After the critical value is reached, the ratio between myosin and actin is too high and myosin is no longer able to trigger contraction. This hypothesis is in agreement of all of our results and should be testable by quantification of actin fibres turnover.

Another explanation could involve a limited amount of actin within the cell. After the critical length, the actin concentration won't be enough and the fibre won't be able to transmit and produce force anymore, due to the absence of actin for the action of myosin. This is consistent with all our data and should be tested by reproducing the measure in the presence of a very low concentration of an actin monomer-sequestrating agent (Latrunculin A). Decreasing the actin monomer concentration should then displace the critical value toward smaller length because available actin would be decreased.

In both cases, this would mean that the cell has a constitutive mechanical/physical negative feedback mechanism allowing for the decrease in force. Not enough actin or disassembly by myosin will protect the cell from too high contractility and extension. The limit in cell length has already been identified for fibroblast[16]where it was found to be around 50 µm, which is very close to our results (60 µm).

This mechanism would explain the coupling between protrusion and retraction during cell migration. During protrusion, cell will extend, build up strong adhesion and long fibres. When the critical length is reach, forces exerted on focal adhesion dropped. This triggers their disassembly [7] and retraction of the cell. The process can then start all over again.

Fluidization within tissues has also been described in the context of collective migration[17]. This process could indeed play a great role in the regulation of tension within tissues. For small deformation, the cells behave as elastic structures with higher reaction forces for higher deformation. If the deformation became too high, the cell will stop producing forces, thus limiting the tension within the tissue.

This work also gives great insight into the dynamic of stress fibres. They are shown to be asymmetric flowing structures with speed correlated to forces. This could be probably be explained by modelling of the constituent of the cytoskeleton or by higher scale theoretical concepts[18]

CONCLUSION

We have shown that stress fibres are responsible for the generation of strong contractile forces. The forces generated by stress fibres with respect to their length follow a biphasic curve. The existence of a critical fibre length provides a physical mechanism for negative feedback on the adhesion/myosin positive feedback loop. This process is likely to be very important in the regulation of key cellular process such as cell migration and mechanical equilibrium within tissues.

Online Methods

Lifeact molecular cloning, lentiviral expression and cell transduction

LifeAct-mGFP plasmids were kindly provided by Wedlich-Soldner [19]. The lifeact-mGFP fragment was amplified by PCR using primers flanked with specific restriction enzyme site (namely EcoR1 and Not1). This fragment was subsequently cut and ligated with the pLVX lentiviral vector (Dupont et al., 632153, Clontech, Japan) which was also cut with corresponding restriction enzyme. The viruses carrying the lifeact-mGFP were generated using the lenti-X packaging system (Dupont et al., 631247, Clontech, Japan). hTERT-RPE1 cells (infinity telomerase-immortalised Retinal Pigment Epithelial human cell line) were subsequently infected with those viruses followed by antibiotic selection, according to the manufacturer instructions (Clontech, Japan).

Cell culture

hTERT-RPE1 cells were cultured in DMEM F-12 (GIBCO) supplemented with 10 % Foetal Bovine Serum (A15-551, PAA, Germany), 50 Units/mL Penicillin and 50 µg/mL Streptomycin (15070-63, GIBCO). Cells were cultured in a 5% CO2 incubator at 37°C. Cells were trypsinised, centrifuged, resuspended in fresh medium and allow to spread on micropattern for 4 hours before the beginning of the experiment.

Image acquisition

Magnetic chambers containing the coverslips and filled with cell culture medium were put on the microscope in a stage incubator system at 37°C and 5% CO2 (Chamlide WP, Live Cell Instruments, Korea). Confocal acquisition was performed on an Eclipse TI-E Nikon inverted microscope equipped with a CSUX1-A1 Yokogawa confocal head and an Evolve EMCCD camera ; through a 100x CFI Plan Fluor oil objective or 60x CFI Apo TIRF oil objective (MRH02900 and MBH76162 respectively, Nikon, France) The whole system is controlled by Metamorph® software (Universal Imaging Corporation).

Micro-patterning on polyacrylamide gel

Micro-patterns were produced as previously described (Vignaud, Methods Cell. Biol., 2013). Briefly, quartz photomask was oxidized through oxygen plasma (FEMTO, Diener Electronics) for 3 min at100W before incubating with 0**:**1 mg ml 1 poly-**l**-lysine (PLL)_PEG (PLL20K-G35-PEG2K, JenKem) in 10mM HEPES, pH 7.4, for 30 min. After drying, uncoated photomask side was exposed to 165nm ultraviolet (UVO cleaner, Jelight) for 5 min. Then, the PLL-PEG coated side of the mask was incubated with 20 $mg.ml^{-1}$ of fibronectin (Sigma) and 2 mg ml^{-1} of rhodamine-labelled fibronectin (Cytoskeleton) in100mM sodium bicarbonate solution for 30 min. Acrylamide solution containing acrylamide and bis-acrylamide (Sigma) was degassed for 20 min under house vacuum and mixed with passivized fluorescent beads (Invitrogen) by sonication before addition of APS and TEMED. A 25 **µ**l drop of this solution was put directly on the micropatterned photomask. A silanized coverslip was placed over the drop and left polymerizing for 30 min (fluorescent beads passivation and glass silanization were performed as previously described[20]). The sandwich was then put in 100mM sodium bicarbonate solution and the gel was gently removed from the patterned glass coverslip while staying attached to the other coverslip owing to the silanization treatment. This process transferred the protein micropatterns onto the gel as previously described[21]. Two different solutions of 3%/0.225%, 5%/0.225%, 8%/0.264% acrylamide/bis-acrylamide were used. The corresponding Young's moduli of the gels were 9.6 and 34.8 kPa respectively as measured using AFM. Coverslips were mounted in magnetic chambers (Cytoo) and washed with sterile PBS before plating cells.

Traction Force Microscopy

Traction-force microscopy was performed as previously described28. Displacement fields describing the deformation of the polyacrylamide substrate are determined from the analysis of fluorescent bead images before and after removal of the adhering cell with trypsin treatment. Images of fluorescent beads were first aligned to correct experimental drift using the Align slices in stack ImageJ plugin. The displacement field was subsequently calculated by a custom-written particle image velocimetry (PIV) program implemented as an ImageJ (http://rsb.info.nih.gov/ij) plugin. The PIV was performed through an iterative scheme. In all iterations the displacement was calculated by the normalized correlation coefficient algorithm, so that an individual interrogation window was compared with a larger searching window. The next iteration takes into account the displacement field measured previously, so that a false correlation peak due to insufficient image features is avoided. The normalized cross-correlation also allowed us to define an arbitrary threshold to filter out low correlation values due to insufficient beads present in the window. The resulting final grid size for the displacement field was 2.67*2.67 µm. The erroneous displacement vectors due to insufficient beads present in the window were filtered out by their low correlation value and replaced by the median value from the neighbouring vectors. With the displacement field obtained from the PIV analysis, the traction-force field was reconstructed by the Fourier transform traction cytometry (FTTC) method with regularized scheme on the same grid (2.67*2.67 µm) without further interpolation or remapping. The regularization parameter was set at 8.10^{-11} for all traction-force reconstructions. The Fourier transform traction cytometry code was also written in Java as an ImageJ plugin, so that the whole traction-force microscopy procedure from PIV to force calculation could be performed with ImageJ. The entire package of traction-force microscopy software is available at https://sites.google.com/site/qingzongtseng/tfm. Contractile energy was then computed as the integral under the cell of the scalar product of force and displacement vectors using a custom-written code in MatLab.

Immuno-staining

Cells were briefly pre-permeabilize before fixation by a 15 s immersion in cytoskeleton buffer containing 0.1 % Triton X-100. RPE1 cells were fixed in 4% paraformaldehyde in cytoskeleton buffer, pH 6.1,for 15 min at room temperature without any prior PBS wash. They were then rinsed twice with PBS and incubated in 0.1 M ammonium chloride in PBS for 10 min. Primary polyclonal rabbit antibodies against phospho-myosin light chain 2 (1:100; Cell Signalling Technology), were added in blocking buffer (1.5% BSA) for 1 h at room temperature. The secondary antibodies Cy3- and Cy5-conjugated goat anti–mouse, goat anti–rat, and goat anti–rabbit (AffiniPure; Jackson ImmunoResearch Laboratories, Inc.) were used at a dilution of 1:500 in 1.5% BSA and incubated with 1 µg/ml FITC-conjugated phalloidin (Sigma-Aldrich) for45 min in the dark at room temperature. Cells were incubated in 0.2 µg/ml Hoechst for 5 min in PBS before mounting in Mowiol (Sigma-Aldrich).

Laser Ablation

Laser ablation was performed using of a Laser illuminator iLas2 (ROPER SCIENTIFIC, France) set up on an inverted microscope (Ti-E, Nikon, France). iLas2 is a dual axis galvanometer based optical scanner that focalizes the Laser beam on the sample (diffraction limited spot size) on the whole field of view of the camera. It includes a telescope to adjust Laser focalization with image focalization and a motorized polarizer to control beam power. The laser used is a passively Q-switched laser (STV-E, TeamPhotonics, France) that produces 300 picoseconds pulses at 355nm (Energy/Pulse 1.2µJ /Peak Power 4 kW/ Variable Repetition rate 0.01 to 2 KHz / Average power ≤ 2.4mW). Laser displacement, exposure time and repetition rate are controlled using Metamorph® software (Universal Imaging Corporation). The objective used is a 100x CFI S Fluor oil objective (MRH02900, Nikon, France). The point to cut was exposed for 12 ms

at a repetition rate of 7000 Hz. The polarizer was set to have energy per pulse of 300 nJ before the objective and going through the sample

REFERENCES

1. Chen, C. S., Mrksich, M., Huang, S., Whitesides, G. M. & Ingber, D. E. Geometric control of cell life and death. *Science* **276,** 1425–1428 (1997).
2. Califano, J. P. & Reinhart-King, C. A. Substrate Stiffness and Cell Area Predict Cellular Traction Stresses in Single Cells and Cells in Contact. *Cel. Mol. Bioeng.* **3,** 68–75 (2010).
3. Balaban, N. Q. *et al.* Force and focal adhesion assembly: a close relationship studied using elastic micropatterned substrates. *Nat. Cell Biol.* **3,** 466–472 (2001).
4. Stricker, J., Aratyn-Schaus, Y., Oakes, P. W. & Gardel, M. L. Spatiotemporal Constraints on the Force-Dependent Growth of Focal Adhesions. *Biophys. J.* **100,** 2883–2893 (2011).
5. Schiller, H. B. *et al.* β1- and αv-class integrins cooperate to regulate myosin II during rigidity sensing of fibronectin-based microenvironments. *Nat. Cell Biol.* **15,** 625–636 (2013).
6. Stricker, J., Beckham, Y., Davidson, M. W. & Gardel, M. L. Myosin II-Mediated Focal Adhesion Maturation Is Tension Insensitive. *PLoS ONE* **8,** e70652 (2013).
7. Kuo, J.-C., Han, X., Hsiao, C.-T., Yates, J. R. & Waterman, C. M. Analysis of the myosin-II-responsive focal adhesion proteome reveals a role for β-Pix in negative regulation of focal adhesion maturation. *Nat. Cell Biol.* **13,** 383–393 (2011).
8. Gardel, M. L. *et al.* Traction stress in focal adhesions correlates biphasically with actin retrograde flow speed. *J. Cell Biol.* **183,** 999–1005 (2008).
9. Kumar, S. *et al.* Viscoelastic retraction of single living stress fibers and its impact on cell shape, cytoskeletal organization, and extracellular matrix mechanics. *Biophysj* **90,** 3762–3773 (2006).
10. Colombelli, J. *et al.* Mechanosensing in actin stress fibers revealed by a close correlation between force and protein localization. *J. Cell. Sci.* **122,** 1665–1679 (2009).
11. Théry, M., Pépin, A., Dressaire, E., Chen, Y. & Bornens, M. Cell distribution of stress fibres in response to the geometry of the adhesive environment. *Cell Motil. Cytoskeleton* **63,** 341–355 (2006).
12. Lo, C. M., Wang, H. B., Dembo, M. & Wang, Y. L. Cell movement is guided by the rigidity of the substrate. *Biophysj* **79,** 144–152 (2000).
13. Colombelli, J., Reynaud, E. G. & Stelzer, E. H. K. Investigating relaxation processes in cells and developing organisms: from cell ablation to cytoskeleton nanosurgery. *Methods Cell Biol.* **82,** 267–291 (2007).
14. Reymann, A. C. *et al.* Actin Network Architecture Can Determine Myosin Motor Activity. *Science* **336,** 1310–1314 (2012).
15. Vogel, S. K., Petrasek, Z., Heinemann, F. & Schwille, P. Myosin motors fragment and compact membrane-bound actin filaments. *eLife* **2,** e00116–e00116 (2013).
16. Levina, E. M., Kharitonova, M. A., Rovensky, Y. A. & Vasiliev, J. M. Cytoskeletal control of fibroblast length: experiments with linear strips of substrate. *J. Cell. Sci.* **114,** 4335–4341 (2001).
17. Serra-Picamal, X. *et al.* Mechanical waves during tissue expansion. *Nat Phys* **8,** 628–634 (2012).
18. Hawkins, R. J. *et al.* Spontaneous Contractility-Mediated Cortical Flow Generates CellMigration in Three-Dimensional Environments. *Biophysj* **101,** 1041–1045 (2011).
19. Riedl, J. *et al.* Lifeact: a versatile marker to visualize F-actin. *Nat. Methods* **5,** 605–607 (2008).
20. Tseng, Q. *et al.* A new micropatterning method of soft substrates reveals that different tumorigenic signals can promote or reduce cell contraction levels. *Lab Chip* **11,** 2231–2240 (2011).
21. Rape, A. D., Guo, W.-H. & Wang, Y.-L. The regulation of traction force in relation

to cell shape and focal adhesions. *Biomaterials* **32,** 2043–2051 (2011).

Figure Legends

Figure 1: Cell architecture modifies contractility of cells stably spread on micro-patterns
a – Representative Lifeact-GFP pictures and traction maps for cells with low (left) high (middle) and elongated (right) spreading area
b – Mechanical Energy vs. Cell area (left), cell aspect ratio (middle) and cell major axis (right). Each data point corresponds to a different cell.
c – Mechanical energy vs. time (left) for a confined (doted line) and unconfined (plain line) cell. Quantification of variation coefficient over several cells from each condition. (right)
d-e From top to bottom: micropattern labelled with Fibronectin-Cy3, corresponding Lifeact picture of the cell, traction map for the same cell, average traction map over many cells. Comparison of total mechanical energy in each cases (scatter plot)

Figure 2: The scaling between cell length and ME has an upper limit, insensitive to substrate stiffness.
a – From left to right: micropattern labelled with Fibronectin-Cy3, corresponding Lifeact picture of the cell, traction map for the same cell, average traction map over many cells
b – Mechanical energy vs. cell length. Measurements performed on 35 kPa gel stiffness are represented by black dots, blue dots are used for 9.6 kPa experiments.
c – frequency distribution of cell length for unconfined cells plated on 2D soft substrate

Figure 3: Actin stress fibres are the main contributors to cell ME.
a – Lifeact-GFP picture of a cell on micro-pattern (up), overlay of traction released after ablation an Lifeact-staining (middle and bottom)
b – Mechanical energy vs. time during ablation. The arrow defines the amplitude that is defines as ME released
c – ME of cells with different lengths of stress fibres.
d – Released ME vs. cell ME. One dot corresponds to a single cell (up). The size of the stress fibres is colour coded (blue, green, orange, red for 25, 37, 47, 56 µm in length respectively. Released ME does not display the same trend as cell ME.
e – Lifeact-GFP actin fibres (up) were photo-bleached (middle) and the cut (down) to see the internal relaxation process
f – Kymograph of fibre retraction (left) and schematic representation of the localisation of the black marks on the fibres during retraction (right), red curves are moving regions whereas green lines are moving regions.
g – Top to bottom : sequential double ablation on stress fibre.
h – The second cut is also accompanied with a release of ME
i – Sum of amplitudes of first and second cut now correlated very well with cell mechanical energy and followed the same trend as cell mechanical energy (j)

Figure 4: Myosin/actin ratio is constantly increasing with fibre length
a – up: Immuno-staining pictures of actin (phalloidin) phospho-myosin and alpha-actinin (left to right). Linescans were performed according to doted red line on the picture. The profile of fluorescent was plot in each condition.
b – Actin density decreases with fibre length whereas phospho-myosin very slightly increased and alpha-actinin seemed unchanged.
c – Myosin/actin ratio is constantly increasing with fibre length

Figure 5: Actin flow within the fibres correlates with ME
a-Kymograph of bleached mark on stress fibres. Marks are moving toward a convergence points
b – Frequency distribution of converging points along fibres of different length
c – Maximum velocity within fibre was also following the same trend as released ME and cell ME.
In all figures, scale bars are 10 µm in length

Figure 1

a

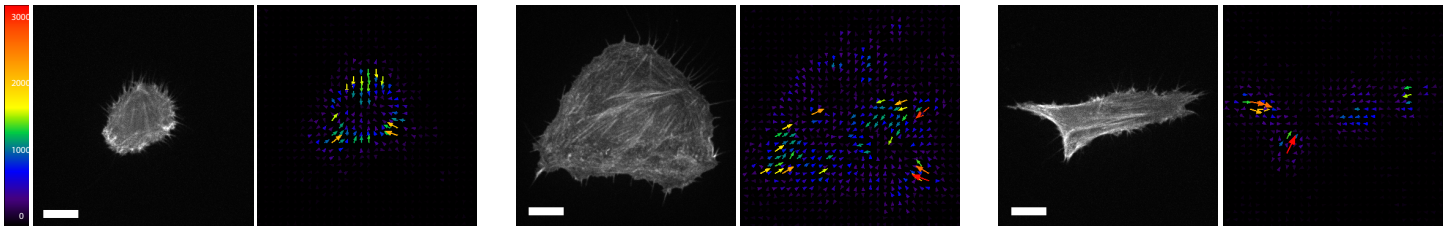

b

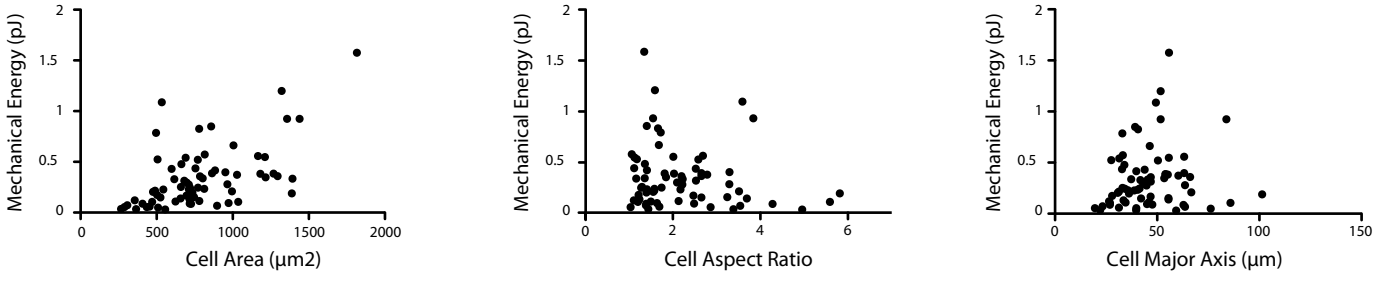

c

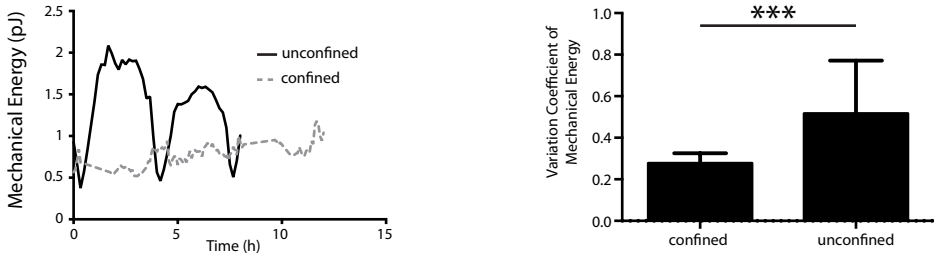

d

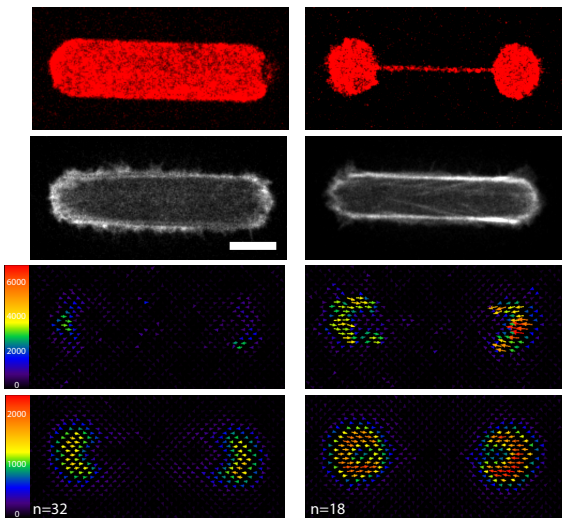

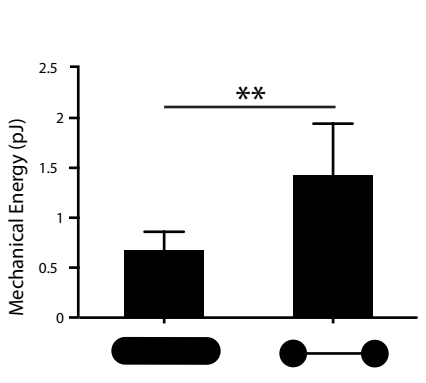

e

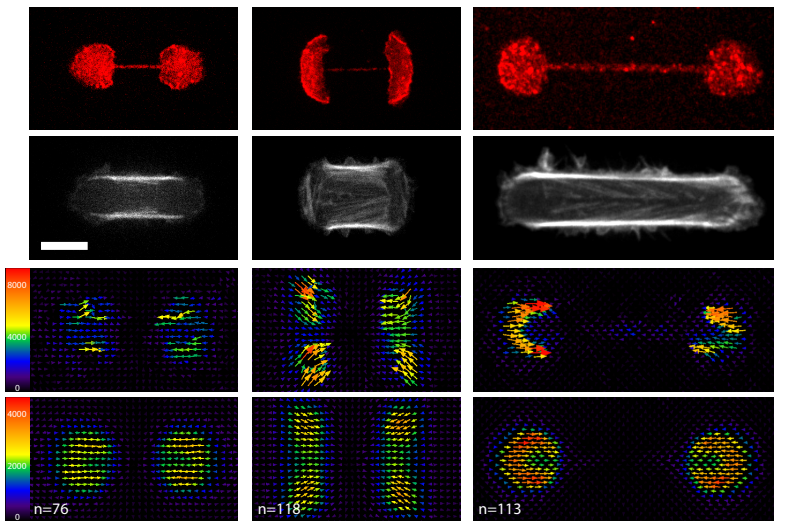

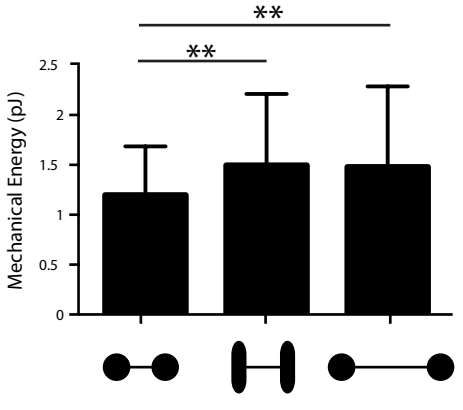

Figure 2

a

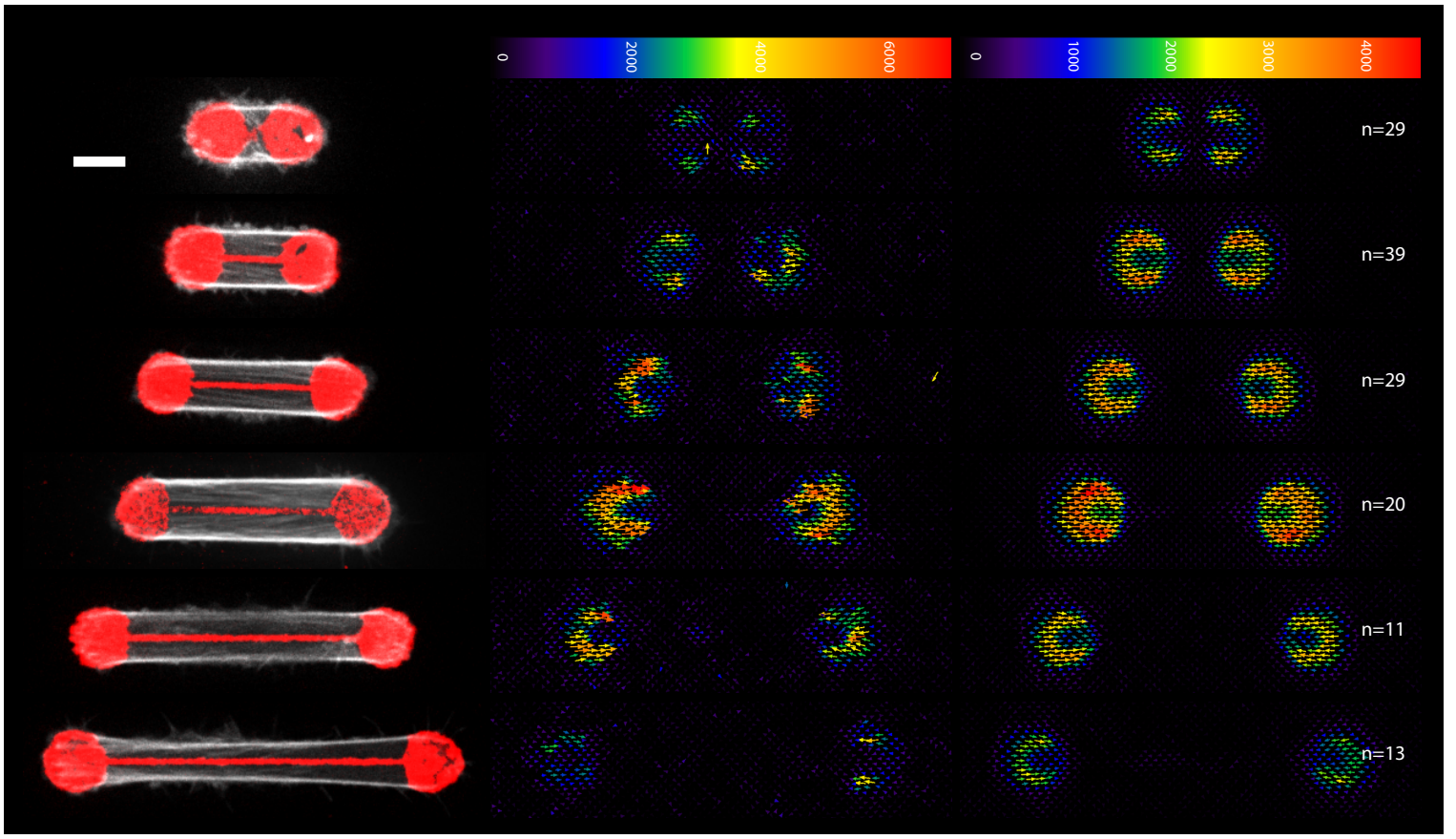
0
2000
4000
6000
0
1000
2000
3000
4000
n=29
n=39
n=29
n=20
n=11
n=13

b

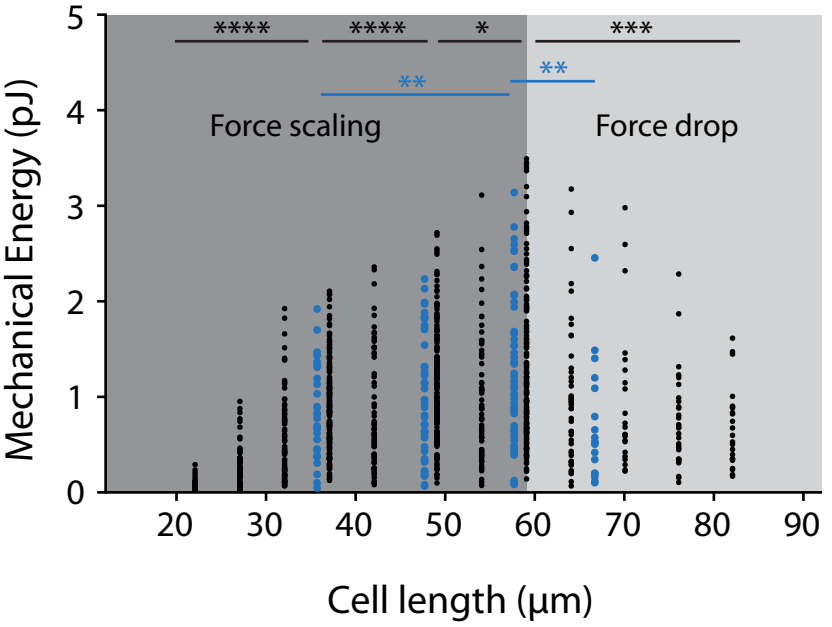
****
****
*
***
**
**
Force scaling
Force drop
Mechanical Energy (pJ)
0
1
2
3
4
5
20
30
40
50
60
70
80
90
Cell length (µm)

c

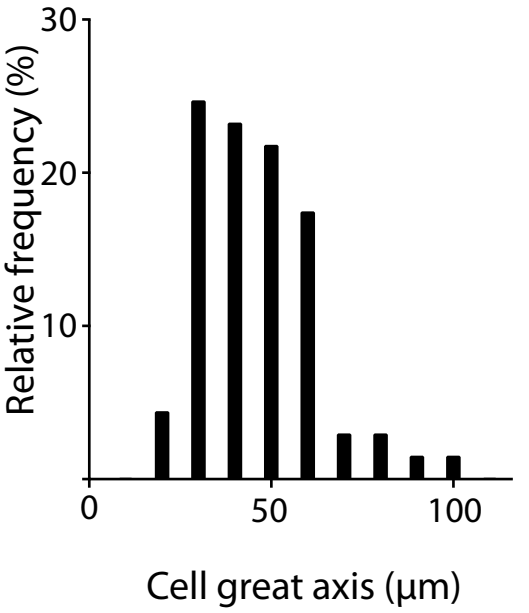
Relative frequency (%)
10
20
30
0
50
100
Cell great axis (µm)

Figure 3

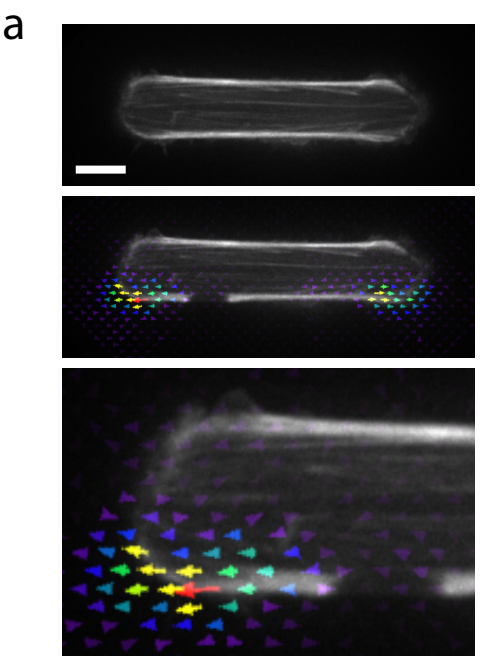
a

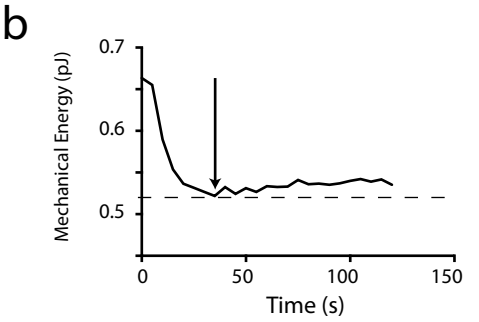
b
Mechanical Energy (pJ)
0.7
0.6
0.5
0
50
100
150
Time (s)

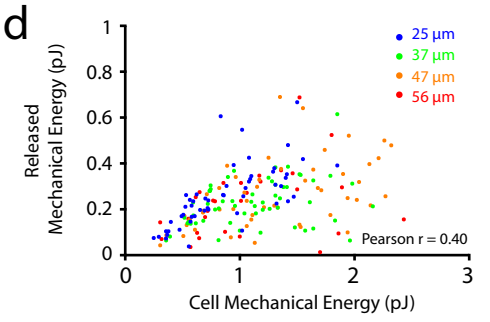
d
Released Mechanical Energy (pJ)
25 µm
37 µm
47 µm
56 µm
Pearson r = 0.40
Cell Mechanical Energy (pJ)

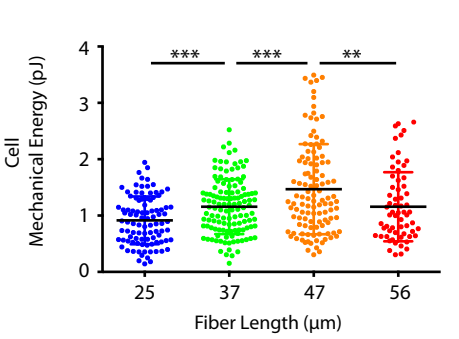
c
Cell Mechanical Energy (pJ)
***
***
**
25
37
47
56
Fiber Length (µm)

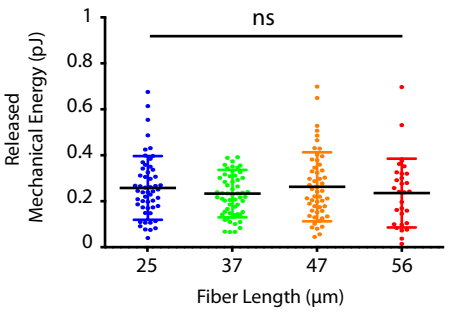
Released Mechanical Energy (pJ)
ns
25
37
47
56
Fiber Length (µm)

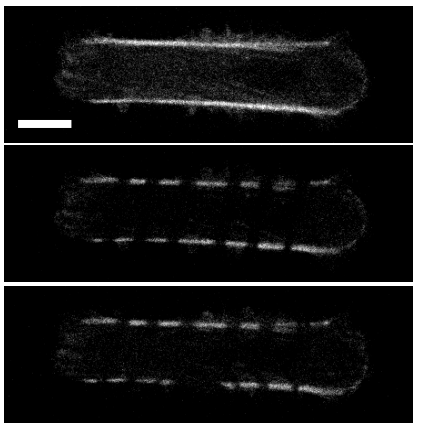
e

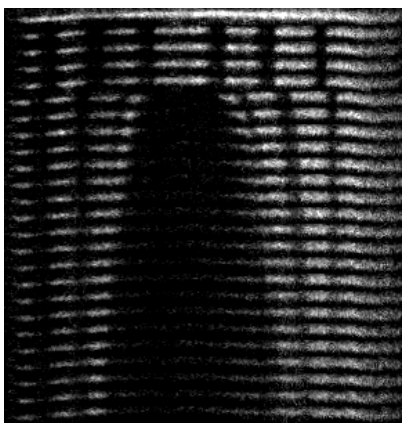
f

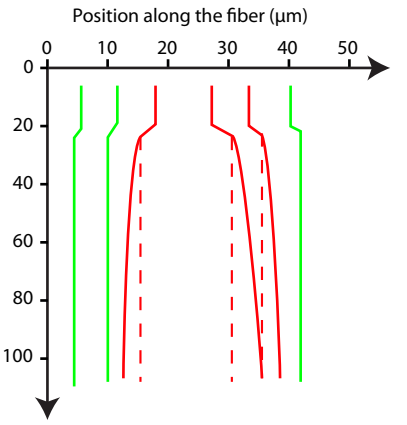
Position along the fiber (µm)
0
10
20
30
40
50
Time (s)
0
20
40
60
80
100

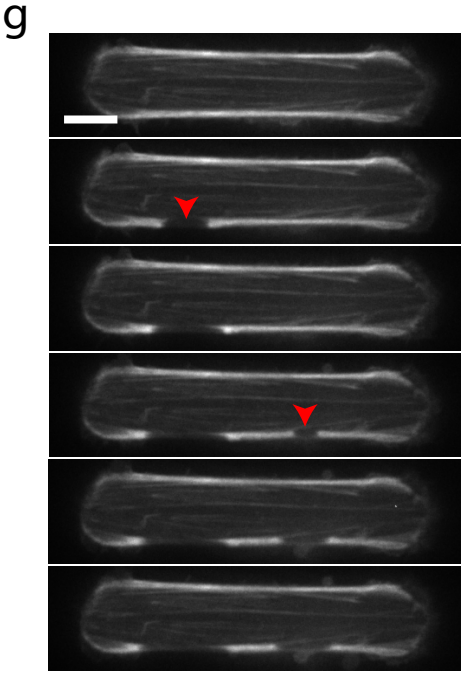
g

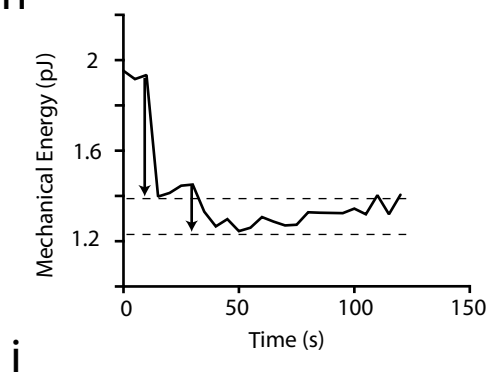
h
Mechanical Energy (pJ)
2
1.6
1.2
0
50
100
150
Time (s)

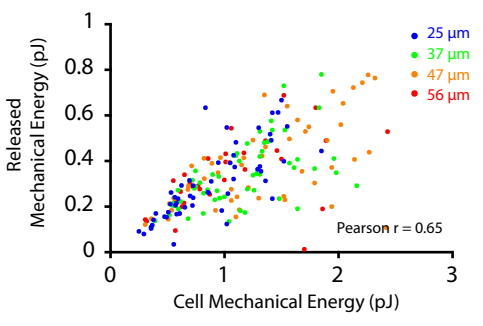
i
Released Mechanical Energy (pJ)
25 µm
37 µm
47 µm
56 µm
Pearson r = 0.65
Cell Mechanical Energy (pJ)

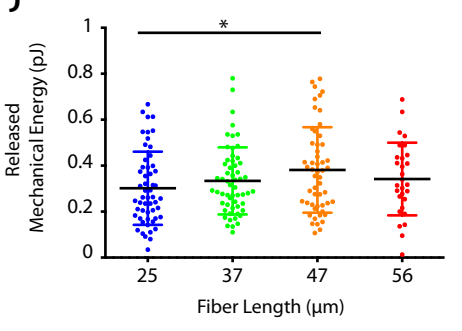
j
Released Mechanical Energy (pJ)
*
25
37
47
56
Fiber Length (µm)

Figure 4

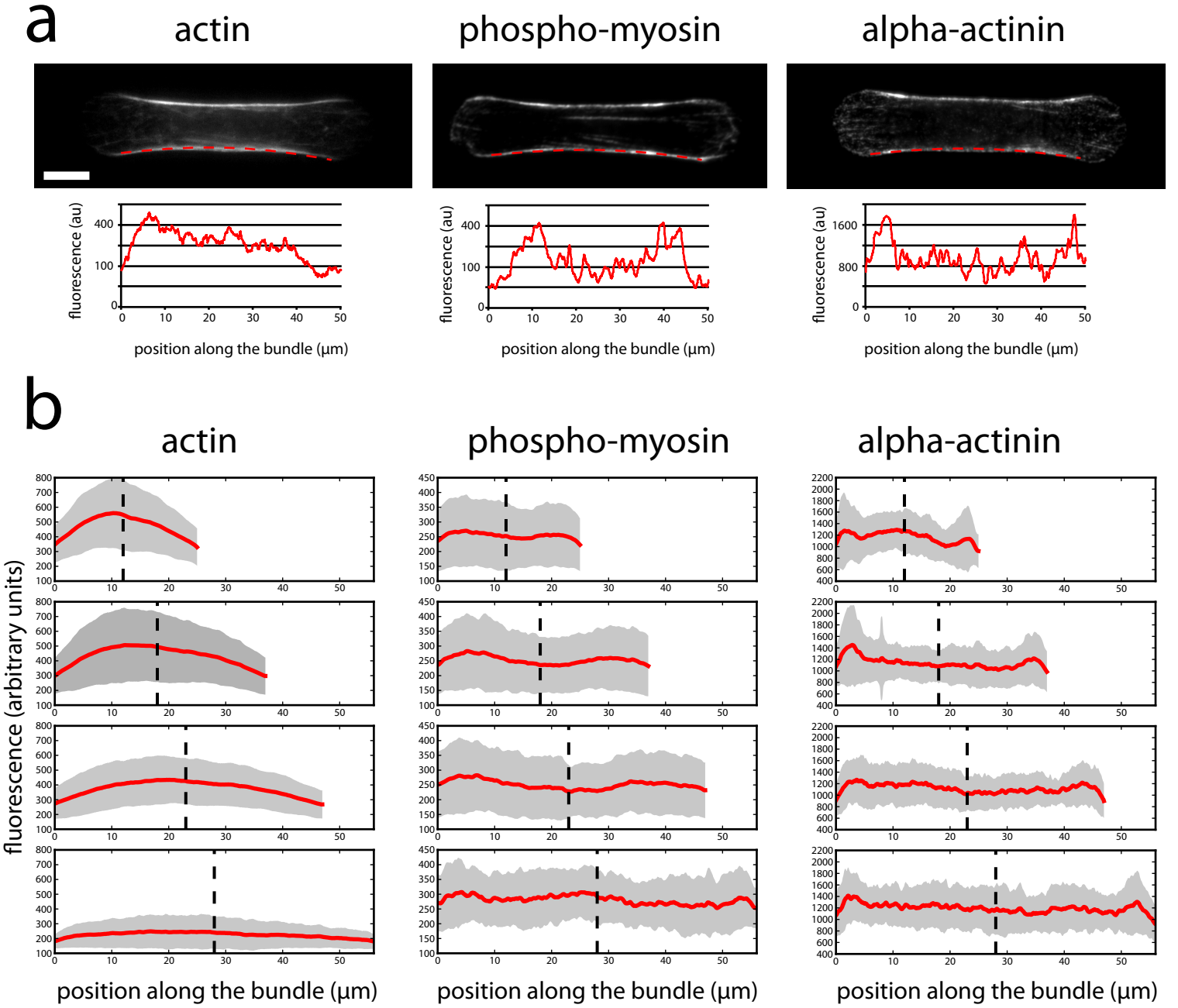
a
actin
phospho-myosin
alpha-actinin
fluorescence (au)
position along the bundle (μm)
b
actin
phospho-myosin
alpha-actinin
fluorescence (arbitrary units)
position along the bundle (μm)
C
myosin/actin ratio
Fluorescence ratio
Force drop
Force scaling
position along bundle length (μm)

Figure 5

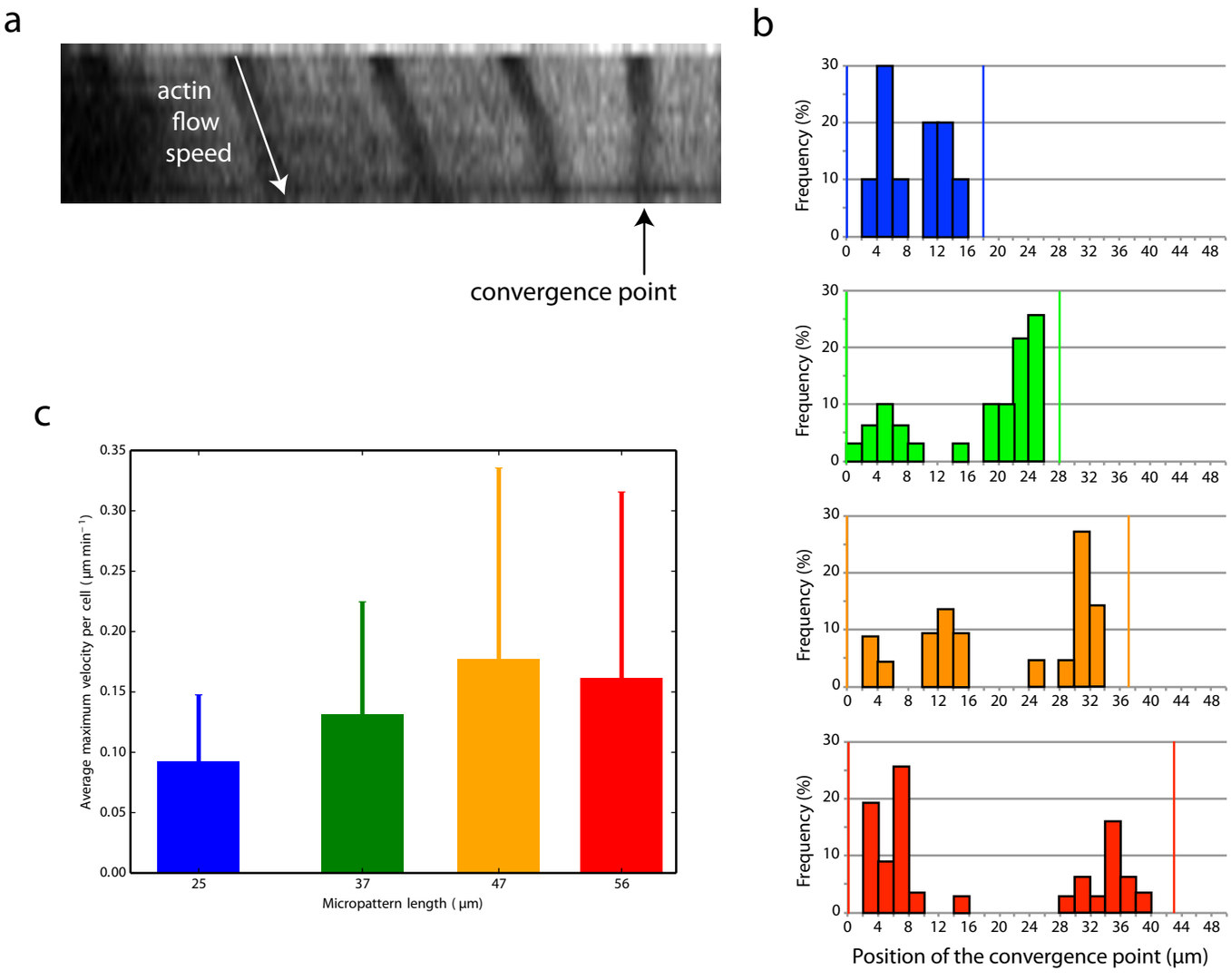
a
actin
flow
speed
convergence point
b
Frequency (%)
Position of the convergence point (μm)
c
Average maximum velocity per cell (μm min⁻¹)
Micropattern length (μm)
25
37
47
56

3. DISCUSSION

Le travail présenté met en avant le rôle des fibres de stress dans la régulation de la taille des cellules. Il propose que l'incapacité de la cellule à augmenter les forces qu'elle génère au delà d'une certaine longueur est à l'origine d'une déstabilisation des adhésions ce qui favorise une retraction de la cellule.

La question de la régulation de la longueur des cellules n'est pas nouvelle. Des observations étonnantes ont pu être faites à ce sujet, notamment grâce à l'utilisation de micropatterns en bandes (Levina, Journal of Cell Science, 2001) (Figure 38 A). L'étude consistait à mesurer le grand axe de cellules dans 2 situations : un substrat 2 dimensions et un substrat une dimension sous la forme de micropatterns en ligne. La question était de savoir si la taille du grand axe serait conservée entre les deux situations, ou si c'était l'aire d'étalement de la cellule qui resterait constante auquel cas la longueur devrait augmenter sur les lignes. Deux cas de figures ont été identifiés. Les cellules épithélioïdes ne possèderont pas de fibres de stress importantes et ne conserveront pas la même longueur entre les deux situations. Les cellules fibroblastiques formeront un cytosquelette polarisé avec d'importantes fibres de stress et conserveront la même longueur entre les deux situations (Kharitonova, Journal of Cell Science, 2004). Sans pousser plus avant les investigations, les auteurs suggèrent que la présence de fibres de stress est corrélée à l'existence de ce mécanisme de contrôle de la taille des cellules. (Figure 38 C)

L'utilisation de drogues perturbants les microtubules ou l'actine montre l'effet antagoniste de ces deux réseaux. L'altération de l'actine entraine une augmentation de la longueur de la cellule alors que l'atteinte des microtubules va la réduire. Ces observations sont cohérentes avec d'autres résultats. Les microtubules jouent un rôle dans la régulation de la stabilité des adhésions focales (Ezratty, Nat. Cell. Biol., 2005) et stimulent l'activation de Rac1 et la formation de lamellipode (Waterman-Storer, Nat. Cell Biol., 1999). Leur dépolymérisation augmente la contractilité cellulaire et le niveau de RhoA (Krendel, Nat., Cell Biol., 2002). L'inhibition du cytosquelette d'actine en revanche déclenche l'élongation de la cellule, sans doute à travers la diminution de la contractilité cellulaire. Les mêmes effets sont observés avec des inhibiteurs des myosines, ce qui va dans le même sens. (Figure 38 B)

Une étude (Picone, Plos Biology, 2010) suggère que les microtubules sont seuls responsables de la régulation de la longueur de la cellule car elle n'est pas modifiée par l'inhibition de l'actine. Cependant, les auteurs traitent leurs cellules seulement pendant une faible durée avec leur inhibiteur et il est probable que cela explique les différences de résultats observées par rapport à l'étude précédente (Levina)

On se retrouve ainsi avec un mécanisme dans lequel l'élongation de la cellule nécessite les

A - Cell length regulation in fibroblast like cell

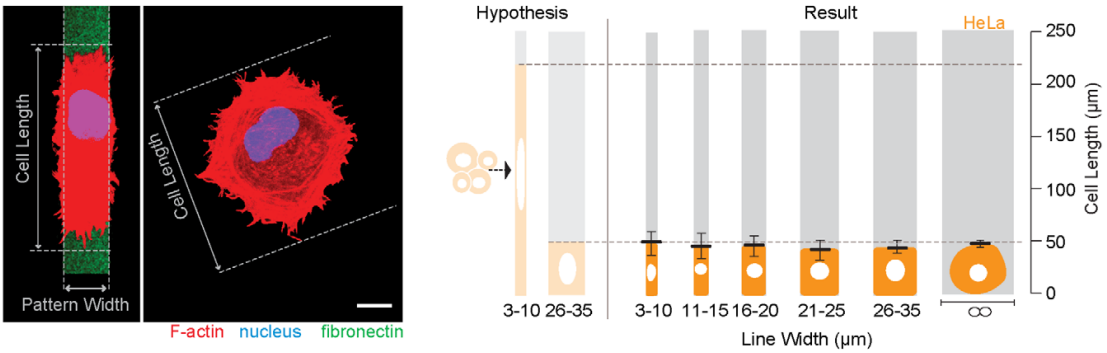

Picone, Plos Biology, 2010

B - Role of microtubules and actin in cell length regulation

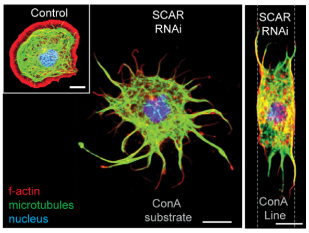

Table 2. Morphometric parameters of epitheliocytes

	Standard glass substrate				Substrate with narrow strips			
	Length (µm)	Area (µm²)	Dispersion	Elongation	Length (µm)	Area (µm²)	Dispersion	Elongation
				IAR2 EPITHELIOCYTES				
Control	63.6±2.2	2677.8±201.2	0.02±0.002	0.18±0.02	194.8±6.9	95.8±4.4	882.1±69.1	0.15±0.02
Colcemid	52.6±1.4	1733.5±97.0	0.02±0.002	0.18±0.02	160.0±4.4	77.5±1.8	851.5±33.6	0.06±0.01
Cytochalasin	55.6±2.8	1484.4±68.6	0.11±0.03	0.44±0.08	162.3±7.2	83.0±3.2	762.3±77.0	0.14±0.02
				MDCK EPITHELIOCYTES				
Control	21.1±0.3	296.5±8.3	0.08±0.02	0.18±0.02	44.8±1.6	419.2±16.2	0.03±0.004	1.67±0.07
				FBT EPITHELIOCYTES				
Control	42.08±0.7	1120.7±31.6	0.01±0.007	0.21±0.02	63.8±1.9	808.5±19.9	0.06±0.007	1.82±0.07

Mean ± standard errors are given. No less than 50 cell outlines from three experiments were used for the calculations in each group.

Levina, Journal of Cell Science, 2001

C - Role of actin phenotype in cell length regulation

Table 3. Reversibility of morphometric parameters of fibroblasts and epitheliocytes

Substrate with narrow strips				Standard glass substrate			
Length (µm)	Area (µm²)	Dispersion	Elongation	Length (µm)	Area (µm²)	Dispersion	Elongation
			HUMAN FIBROBLASTS M19				
124.5±5.0	1338.3±65.3	0.10±0.01	3.26±0.06	143.7±5.2	2675.6±159.9	0.34±0.04	2.37±0.10
			MDCK EPITHELIOCYTES				
43.0±2.2	393.6±19.2	0.05±0.009	1.43±0.11	20.4±0.3	243.8±7.8	0.008±0.0009	0.24±0.02

Mean ± standard errors are given. No less than 50 cell outlines from three experiments were used for the calculations in each group.
The cells were grown on the strips for 24 hours, then some cells were measured (left half of the table); other cells were removed from the strips, re-seeded on the planar glass and measured after another 24 hours (right half of the table).

Levina, Journal of Cell Science, 2001

D - Opposing mechanisms in cell length regulation

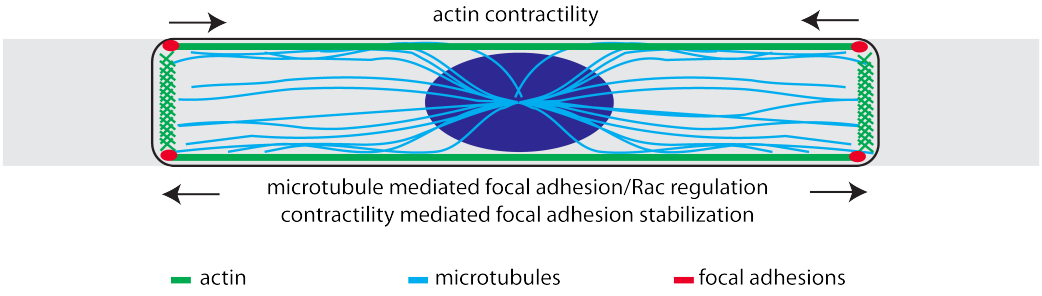

Figure 38 : Mécanisme de régulation de la longueur des cellules

microtubules et l'actine : les microtubules vont permettre d'activer Rac et de réguler les adhésions pour permettre l'élongation de la cellule et l'actine sera le moteur qui poussera la membrane. Ces mécanismes permettent l'élongation cellulaire mais pas la régulation de sa taille.

La contractilité du cytosquelette d'actine semble être le mécanisme qui limite l'élongation cellulaire, et nos observations placent les fibres de stress au centre de ce phénomène. L'augmentation de la force permet de limiter l'extension, et plus encore la chute brutale de force au delà d'une certaine longueur fournit un mécanisme pour la déstabilisation des adhésions et la rétraction de la cellule. La diminution du nombre de microtubules capables d'atteindre l'extrémité de la cellule joue sans doute également un rôle dans ce mécanisme (Picone, Plos Biology, 2010), probablement en diminuant l'activité de Rac et en favorisant ainsi également la retraction de la cellule. Cependant les quelques observations des microtubules effectuées dans nos conditions expérimentales ne montrent pas de diminution franche de la densité de microtubules avec l'allongement de la cellule.

Nous avons vu en introduction que l'existence de fibres de stress au sein des cellules n'est pas constante. Ces structures apparaissent dans des situations de stress cellulaires qui nécessitent la production de forces importantes (blessure, stress hydrodynamique, …). La régulation des forces générées par la cellule dans ces conditions est importante.

Dans le cas d'une blessure par exemple, sa fermeture va nécessiter que les cellules sur les deux berges produisent des forces pour combler l'espace qui les séparent. Si au cours de ce mécanisme, la cellule subit un étirement trop important, elle diminuera ses forces, et finira probablement par se diviser. Ce mécanisme permet de fermer la blessure en conservant un niveau de tension acceptable au sein du tissu et une densité cellulaire suffisante.

La contribution de ces mécanismes aux propriétés mécaniques des tissus « au repos » est moins évidente. Les fibres de stress y sont rarement observées et la réponse d'un tissu à une déformation rapide mettra plutôt en jeu l'architecture existante du réseau (cortex d'actine notamment) et ses filaments intermédiaires. En cas d'étirement prolongé, la formation de fibres de stress est probable et permettra de mettre en place un remodelage du tissu en réponse aux contraintes auxquelles il est soumis.

V. Conclusion Générale

Mes travaux se sont intéressés à deux versants de la régulation des forces produites par les cellules. Ils ont permis de montrer le rôle de la composition des adhésions dans le couplage entre contractilité et architecture du cytosquelette. La diminution spontanée de la force dans les fibres de stress au delà d'une certaine longueur impose quant à elle une limite à cette boucle de renforcement et

permet de faire diminuer les forces même en présence d'une forte concentration de moteurs. La rencontre de ces deux mécanismes permet de définir le champ des possibles pour la cellule en terme de contractilité.

Le mécanisme de chute de forces observé n'a pas pu être expliqué à ce jour mais nous travaillons activement pour qu'il le soit dans les mois à venir. Ce phénomène aura sans doute un grand rôle à jouer dans l'intégrité mécanique des tissus et les phénomènes de migration. La chute de force au delà de la longueur critique permet en effet de déstabiliser les adhésions et pourrait être à l'origine de la rétraction de la cellule dans la migration ou du détachement d'une cellule de ces voisines dans le cas d'un tissu sous forte contraintes. Ce détachement protégerait ainsi la cellule d'un déchirement sous l'effet de forces trop importantes.

Sur le plan méthodologique, le patterning laser en temps réel fournit un outil de choix pour de nombreuses applications, même si d'autres méthodes permettant de passer à volonté d'un état adhésif à non-adhésif du substrat, et inversement, semblent aujourd'hui plus prometteuses en terme de possibles. La technique développée ici permet la réalisation de ces expériences sans savoir-faire particulier en chimie, les réactifs étant tous disponibles commercialement.

L'amélioration de la technique de patterning d'acrylamide permet d'envisager des travaux à une échelle très réduite. L'utilisation de ces techniques en biochimie pour mesurer les forces générées par le cytosquelette in vitro est à portée de la main. Par ailleurs, l'étude des déterminants de l'organisation des cellules en réponse à l'environnement laisse espérer qu'une organisation fixe de la matrice puisse mener à une organisation contrôlée et précise d'un groupe multicellulaire, sans que soit forcément nécessaire une modification de l'organisation en temps réel.

Enfin, le couplage entre ablation laser, micropatterning et mesure de forces fournit une plateforme d'une rare puissance pour étudier la production et la propagation des forces au sein de la cellule (et demain peut-être des tissus), en fonction de l'organisation de son cytosquelette. Elle ne demande qu'à être utilisée.

VI. References

1. Achard, V. *et al.* A 'primer'-based mechanism underlies branched actin filament network formation and motility. *Curr. Biol.* **20,** 423–428 (2010).

2. Aratyn, Y. S., Schaus, T. E., Taylor, E. W. & Borisy, G. G. Intrinsic dynamic behavior of fascin in filopodia. *Mol. Biol. Cell* **18,** 3928–3940 (2007).

3. Balaban, N. Q. *et al.* Force and focal adhesion assembly: a close relationship studied using elastic micropatterned substrates. *Nat. Cell Biol.* **3,** 466–472 (2001).

4. Bantscheff, M., Lemeer, S., Savitski, M. M. & Kuster, B. Quantitative mass spectrometry in proteomics: critical review update from 2007 to the present. *Anal Bioanal Chem* **404,** 939–965 (2012).

5. Bement, W. M., Forscher, P. & Mooseker, M. S. A novel cytoskeletal structure involved in purse string wound closure and cell polarity maintenance. *J. Cell Biol.* **121,** 565–578 (1993).

6. Beningo, K. A., Dembo, M., Kaverina, I., Small, J. V. & Wang, Y. L. Nascent focal adhesions are responsible for the generation of strong propulsive forces in migrating fibroblasts. *J. Cell Biol.* **153,** 881–888 (2001).

7. Berg, J. S., Powell, B. C. & Cheney, R. E. A millennial myosin census. *Mol. Biol. Cell* (2001).

8. Besser, A. & Schwarz, U. S. Coupling biochemistry and mechanics in cell adhesion: a model for inhomogeneous stress fiber contraction. *New J. Phys.* **9,** 425–425 (2007).

9. Blanchoin, L., Boujemaa-Paterski, R., Sykes, C. & Plastino, J. Actin dynamics, architecture and mechanics in cell motility. *Physiological Reviews*

10. Burnette, D. T. *et al.* A role for actin arcs in the leading-edge advance of migrating cells. *Nat. Cell Biol.* **13,** 371–381 (2011).

11. Butcher, D. T., Alliston, T. & Weaver, V. M. A tense situation: forcing tumour progression. *Nat Rev Cancer* **9,** 108–122 (2009).

12. Byers, H. R., White, G. E. & Fujiwara, K. Organization and function of stress fibers in cells in vitro and in situ. A review.

. *Cell Muscle Motil.* 83–137 (1984).

13. Carlier, M. F. Control of actin dynamics. *Current Opinion in Cell Biology* (1998).

14. Colombelli, J. *et al.* Mechanosensing in actin stress fibers revealed by a close correlation between force and protein localization. *J. Cell. Sci.* **122,** 1665–1679 (2009).

15. Crackower, M. A. *et al.* Regulation of Myocardial Contractility and Cell Size by Distinct PI3K-PTEN Signaling Pathways. *Cell* **110,** 737–749 (2002).

16. Cramer, L. P., Siebert, M. & Mitchison, T. J. Identification of novel graded polarity actin filament bundles in locomoting heart fibroblasts: implications for the generation of motile force. *J. Cell Biol.* **136,** 1287–1305 (1997).

17. Deguchi, S., Matsui, T. S. & Sato, M. Simultaneous contraction and buckling of stress fibers in individual cells. *J. Cell. Biochem.* **113,** 824–832 (2012).

18. Doyle, A. D., Wang, F. W., Matsumoto, K. & Yamada, K. M. One-dimensional topography

underlies three-dimensional fibrillar cell migration. *J. Cell Biol.* **184,** 481–490 (2009).

19. Dumbauld, D. W. *et al.* How vinculin regulates force transmission. *Proceedings of the National Academy of Sciences* **110,** 9788–9793 (2013).

20. Echave, P., Conlon, I. J. & Lloyd, A. C. Cell Cycle: Report. *Cell Cycle* (2007).

21. Ehrlich, H. P. & Hembry, R. M. A comparative study of fibroblasts in healing freeze and burn injuries in rats. *Am. J. Pathol.* **117,** 218–224 (1984).

22. Engler, A. J., Sen, S., Sweeney, H. L. & Discher, D. E. Matrix Elasticity Directs Stem Cell Lineage Specification. *Cell* **126,** 677–689 (2006).

23. Eriksson, J. E. *et al.* Introducing intermediate filaments: from discovery to disease. *J. Clin. Invest.* **119,** 1763–1771 (2009).

24. Ezratty, E. J., Partridge, M. A. & Gundersen, G. G. Microtubule-induced focal adhesion disassembly is mediated by dynamin and focal adhesion kinase. *Nat. Cell Biol.* **7,** 581–590 (2005).

25. Fantes, P. A. Control of cell size and cycle time in Schizosaccharomyces pombe. *J. Cell. Sci.* (1977).

26. Fingar, D. C. Mammalian cell size is controlled by mTOR and its downstream targets S6K1 and 4EBP1/eIF4E. *Genes & Development* **16,** 1472–1487 (2002).

27. Franke, R. P. *et al.* Induction of human vascular endothelial stress fibres by fluid shear stress. *Nature* **307,** 648–649 (1984).

28. Friedrich, B. M., Fischer-Friedrich, E., Gov, N. S. & Safran, S. A. Sarcomeric pattern formation by actin cluster coalescence. *PLoS Comput. Biol.* **8,** e1002544 (2012).

29. Gabbiani, G., Ryan, G. B. & Majne, G. Presence of modified fibroblasts in granulation tissue and their possible role in wound contraction. *Experientia* **27,** 549–550 (1971).

30. Galbraith, C. G., Yamada, K. M. & Sheetz, M. P. The relationship between force and focal complex development. *J. Cell Biol.* **159,** 695–705 (2002).

31. Gao, F. B. Cell Size Control and a Cell-intrinsic Maturation Program in Proliferating Oligodendrocyte Precursor Cells. *J. Cell Biol.* **138,** 1367–1377 (1997).

32. Gardel, M. L. *et al.* Traction stress in focal adhesions correlates biphasically with actin retrograde flow speed. *J. Cell Biol.* **183,** 999–1005 (2008).

33. Geiger, B., Spatz, J. P. & Bershadsky, A. D. Environmental sensing through focal adhesions. *Nat. Rev. Mol. Cell Biol.* **10,** 21–33 (2009).

34. Goffin, J. M. *et al.* Focal adhesion size controls tension-dependent recruitment of alpha-smooth muscle actin to stress fibers. *J. Cell Biol.* **172,** 259–268 (2006).

35. Grashoff, C. *et al.* Measuring mechanical tension across vinculin reveals regulation of focal adhesion dynamics. *Nature* **466,** 263–266 (2010).

36. van der Gucht, J., Paluch, E., Plastino, J. & Sykes, C. Stress release drives symmetry breaking for actin-based movement. *Proc. Natl. Acad. Sci. U.S.A.* **102,** 7847–7852 (2005).

37. Heck, J. N. *et al.* Microtubules regulate GEF-H1 in response to extracellular matrix stiffness. *Mol. Biol. Cell* **23,** 2583–2592 (2012).

38. Herrmann, H., Strelkov, S. V., Burkhard, P. & Aebi, U. Intermediate filaments: primary determinants of cell architecture and plasticity. *J. Clin. Invest.* **119,** 1772–1783 (2009).

39. Hotulainen, P. & Lappalainen, P. Stress fibers are generated by two distinct actin assembly mechanisms in motile cells. *J. Cell Biol.* (2006).

40. Howard, J. Mechanics of motor proteins and the cytoskeleton. (2001).

41. Huber, F. *et al.* Emergent complexity of the cytoskeleton: from single filaments to tissue. *Advances in Physics* **62,** 1–112 (2013).

42. Hynes, R. O. Integrins: bidirectional, allosteric signaling machines. *Cell* **110,** 673–687 (2002).

43. Hytönen, V. P. & Vogel, V. How force might activate talin's vinculin binding sites: SMD reveals a structural mechanism. *PLoS Comput. Biol.* **4,** e24 (2008).

44. Jalili, N. & Laxminarayana, K. A review of atomic force microscopy imaging systems: application to molecular metrology and biological sciences. *Mechatronics* **14,** 907–945 (2004).

45. Kanchanawong, P. *et al.* Nanoscale architecture of integrin-based cell adhesions. *Nature* **468,** 580–584 (2010).

46. Keren, K. *et al.* Mechanism of shape determination in motile cells. *Nature* **453,** 475–480 (2008).

47. Kharitonova, M. A. & Vasiliev, J. M. Controlling cell length. *Seminars in cell & developmental biology* (2008).

48. Kharitonova, M. A. & Vasiliev, J. M. Length control is determined by the pattern of cytoskeleton. *J. Cell. Sci.* **117,** 1955–1960 (2004).

49. Kozma, S. C. & Thomas, G. Regulation of cell size in growth, development and human disease: PI3K, PKB and S6K. *Bioessays* **24,** 65–71 (2002).

50. Krendel, M., Zenke, F. T. & Bokoch, G. M. Nucleotide exchange factor GEF-H1 mediates cross-talk between microtubules and the actin cytoskeleton. *Nat. Cell Biol.* **4,** 294–301 (2002).

51. Kumar, S. *et al.* Viscoelastic Retraction of Single Living Stress Fibers and Its Impact on Cell Shape, Cytoskeletal Organization, and Extracellular Matrix Mechanics. *Biophys. J.* **90,** 3762–3773 (2006).

52. Lämmermann, T. *et al.* Rapid leukocyte migration by integrin-independent flowing and squeezing. *Nature* **453,** 51–55 (2008).

53. LATRONICO, M. V. G., COSTINEAN, S., LAVITRANO, M. L., PESCHLE, C. & CONDORELLI, G. Regulation of Cell Size and Contractile Function by AKT in Cardiomyocytes. *Annals of the New York Academy of Sciences* **1015,** 250–260 (2004).

54. Levina, E. M., Kharitonova, M. A., Rovensky, Y. A. & Vasiliev, J. M. Cytoskeletal control of fibroblast length: experiments with linear strips of substrate. *J. Cell. Sci.* **114,** 4335–4341 (2001).

55. Loisel, T. P., Boujemaa, R., Pantaloni, D. & Carlier, M. F. Reconstitution of actin-based motility of Listeria and Shigella using pure proteins. *Nature* **401,** 613–616 (1999).

56. Malek, A. M. & Izumo, S. Mechanism of endothelial cell shape change and cytoskeletal remodeling in response to fluid shear stress. *J. Cell. Sci.* **109 (Pt 4),** 713–726 (1996).

57. Marieb, E. N. & Hoehn, K. Human anatomy and physiology. (2007).

58. Mason, B. N., Califano, J. P. & Reinhart-King, C. A. Matrix Stiffness: A Regulator of Cellular Behavior and Tissue Formation. 19–37 (2012). doi:10.1007/978-1-4614-1080-5_2

59. Mitrossilis, D. *et al.* Real-time single-cell response to stiffness. *Proceedings of the National*

Academy of Sciences **107,** 16518–16523 (2010).

60. Mitrossilis, D. *et al.* Single-cell response to stiffness exhibits muscle-like behavior. *Proceedings of the National Academy of Sciences* **106,** 18243–18248 (2009).

61. Moffitt, J. R., Chemla, Y. R., Smith, S. B. & Bustamante, C. Recent Advances in Optical Tweezers. *Annu. Rev. Biochem.* **77,** 205–228 (2008).

62. Mseka, T., Coughlin, M. & Cramer, L. P. Graded actin filament polarity is the organization of oriented actomyosin II filament bundles required for fibroblast polarization. *Cell Motil. Cytoskeleton* **66,** 743–753 (2009).

63. Murrell, M. P. & Gardel, M. L. F-actin buckling coordinates contractility and severing in a biomimetic actomyosin cortex. *Proceedings of the National Academy of Sciences* **109,** 20820–20825 (2012).

64. Nemethova, M., Auinger, S. & Small, J. V. Building the actin cytoskeleton: filopodia contribute to the construction of contractile bundles in the lamella. *J. Cell Biol.* (2008).

65. Nobes, C. D. & Hall, A. Rho, rac, and cdc42 GTPases regulate the assembly of multimolecular focal complexes associated with actin stress fibers, lamellipodia, and filopodia. *Cell* **81,** 53–62 (1995).

66. Oakes, P. W., Beckham, Y., Stricker, J. & Gardel, M. L. Tension is required but not sufficient for focal adhesion maturation without a stress fiber template. *The Journal of cell …* (2012).

67. Otey, C. A. & Carpen, O. α-actinin revisited: A fresh look at an old player. *Cell Motil. Cytoskeleton* (2004).

68. Parker, K. K. *et al.* Directional control of lamellipodia extension by constraining cell shape and orienting cell tractional forces. *FASEB J.* **16,** 1195–1204 (2002).

69. Pellegrin, S. & Mellor, H. Actin stress fibres. *J. Cell. Sci.* **120,** 3491–3499 (2007).

70. Peterson, L. J. *et al.* Simultaneous stretching and contraction of stress fibers in vivo. *Mol. Biol. Cell* **15,** 3497–3508 (2004).

71. Picone, R. *et al.* A polarised population of dynamic microtubules mediates homeostatic length control in animal cells. *PLoS Biol.* **8,** e1000542 (2010).

72. Pollard, T. D. Rate constants for the reactions of ATP- and ADP-actin with the ends of actin filaments. *J. Cell Biol.* **103,** 2747–2754 (1986).

73. Pollard, T. D. & Borisy, G. G. Cellular motility driven by assembly and disassembly of actin filaments. *Cell* **112,** 453–465 (2003).

74. Prager-Khoutorsky, M. *et al.* Fibroblast polarization is a matrix-rigidity-dependent process controlled by focal adhesion mechanosensing. *Nat. Cell Biol.* **13,** 1–10 (2011).

75. Riveline, D. *et al.* Focal contacts as mechanosensors: externally applied local mechanical force induces growth of focal contacts by an mDia1-dependent and ROCK-independent mechanism. *J. Cell Biol.* **153,** 1175–1186 (2001).

76. Roca-Cusachs, P. *et al.* Integrin-dependent force transmission to the extracellular matrix by α-actinin triggers adhesion maturation. *Proc. Natl. Acad. Sci. U.S.A.* **110,** E1361–E1370 (2013).

77. de Rooij, J., Kerstens, A., Danuser, G., Schwartz, M. A. & Waterman-Storer, C. M. Integrin-dependent actomyosin contraction regulates epithelial cell scattering. *J. Cell Biol.* **171,** 153–164 (2005).

78. Rossier, O. *et al.* Integrins β. *Nat. Cell Biol.* **14,** 1057–1067 (2012).

79. Sabass, B., Gardel, M. L., Waterman, C. M. & Schwarz, U. S. High Resolution Traction Force Microscopy Based on Experimental and Computational Advances. *Biophys. J.* **94,** 207–220 (2008).

80. Schafer, D. A., Jennings, P. B. & Cooper, J. A. Dynamics of capping protein and actin assembly in vitro: uncapping barbed ends by polyphosphoinositides. *J. Cell Biol.* (1996).

81. Schiller, H. B. & Fässler, R. Mechanosensitivity and compositional dynamics of cell–matrix adhesions. *Nature Publishing Group* **14,** 509–519 (2013).

82. Schvartzman, M. *et al.* Nanolithographic Control of the Spatial Organization of Cellular Adhesion Receptors at the Single-Molecule Level. *Nano Lett.* **11,** 1306–1312 (2011).

83. Sjöblom, B., Salmazo, A. & Djinović-Carugo, K. α-Actinin structure and regulation. *Cellular and molecular life …* (2008).

84. Smith, M. B., Kiuchi, T., Watanabe, N. & Vavylonis, D. Distributed Actin Turnover in the Lamellipodium and FRAP Kinetics. *Biophysj* **104,** 247–257 (2013).

85. Stocker, H. & Hafen, E. Genetic control of cell size. *Current Opinion in Genetics & Development* **10,** 529–535 (2000).

86. Stricker, J., Beckham, Y., Davidson, M. W. & Gardel, M. L. Myosin II-Mediated Focal Adhesion Maturation Is Tension Insensitive. *PLoS ONE* **8,** e70652 (2013).

87. Stricker, J., Aratyn-Schaus, Y., Oakes, P. W. & Gardel, M. L. Spatiotemporal Constraints on the Force-Dependent Growth of Focal Adhesions. *Biophys. J.* **100,** 2883–2893 (2011).

88. Suarez, C., Roland, J., Boujemaa-Paterski, R. & Kang, H. Cofilin tunes the nucleotide state of actin filaments and severs at bare and decorated segment boundaries. *Current Biology* (2011).

89. Tan, J. L. *et al.* Cells lying on a bed of microneedles: an approach to isolate mechanical force. *Proc. Natl. Acad. Sci. U.S.A.* **100,** 1484–1489 (2003).

90. Tanner, K., Boudreau, A., Bissell, M. J. & Kumar, S. Dissecting Regional Variations in Stress Fiber Mechanics in Living Cells with Laser Nanosurgery. *Biophys. J.* **99,** 2775–2783 (2010).

91. Thoresen, T., Lenz, M. & Gardel, M. L. Thick Filament Length and Isoform Composition Determine Self-OrganizedContractile Units in Actomyosin Bundles. *Biophysj* **104,** 655–665 (2013).

92. Thoresen, T., Lenz, M. & Gardel, M. L. Reconstitution of Contractile Actomyosin Bundles. *Biophys. J.* **100,** 2698–2705 (2011).

93. Throm Quinlan, A. M., Sierad, L. N., Capulli, A. K., Firstenberg, L. E. & Billiar, K. L. Combining Dynamic Stretch and Tunable Stiffness to Probe Cell Mechanobiology In Vitro. *PLoS ONE* **6,** e23272 (2011).

94. Tojkander, S., Gateva, G. & Lappalainen, P. Actin stress fibers--assembly, dynamics and biological roles. *J. Cell. Sci.* **125,** 1855–1864 (2012).

95. Tseng, Q. *et al.* A new micropatterning method of soft substrates reveals that different tumorigenic signals can promote or reduce cell contraction levels. *Lab Chip* **11,** 2231–2240 (2011).

96. Tzur, A., Kafri, R., LeBleu, V. S., Lahav, G. & Kirschner, M. W. Cell growth and size homeostasis in proliferating animal cells. *Science* **325,** 167–171 (2009).

97. Vicente-Manzanares, M., Ma, X. & Adelstein, R. S. Non-muscle myosin II takes centre stage

in cell adhesion and migration. *Nature reviews …* (2009).

98. Vogel, S. K., Petrasek, Z., Heinemann, F. & Schwille, P. Myosin motors fragment and compact membrane-bound actin filaments. *eLife* **2,** e00116 (2013).

99. Watanabe, N., Kato, T., Fujita, A., Ishizaki, T. & Narumiya, S. Cooperation between mDia1 and ROCK in Rho-induced actin reorganization. *Nat. Cell Biol.* **1,** 136–143 (1999).

100. Waterman-Storer, C. M., Worthylake, R. A., Liu, B. P., Burridge, K. & Salmon, E. D. Microtubule growth activates Rac1 to promote lamellipodial protrusion in fibroblasts. *Nat. Cell Biol.* **1,** 45–50 (1999).

101. Wolfenson, H., Henis, Y. I., Geiger, B. & Bershadsky, A. D. The heel and toe of the cell's foot: A multifaceted approach for understanding the structure and dynamics of focal adhesions. *Cell Motil. Cytoskeleton* **66,** 1017–1029 (2009).

102. Yip, A. K. *et al.* Cellular Response to Substrate Rigidity Is Governed by Either Stress orStrain. *Biophysj* **104,** 19–29 (2013).

103. Yoshinaga, N. & Marcq, P. Contraction of cross-linked actomyosin bundles. *Phys Biol* **9,** 046004 (2012).

VII. Annexes

1. WORLD FIRST CELL RACE (ARTICLE)

confirming that their resources cannot be recycled.

Supplemental Information
Supplemental Information including experimental procedures, a figure and a table can be found with this article online at http://dx.doi.org/10.1016/j.cub.2012.064.038.

Acknowledgments
We thank The Smithsonian Tropical Research Institute for providing facilities in Gamboa that allowed us to collect ant colonies and conduct the behavioural assays, Luke Holman and two anonymous reviewers for helpful comments on an earlier version of the manuscript, and the members of the Centre for Social Evolution for creating a pleasant working environment. This study was supported by The Danish National Research Foundation (J.J.B.), the German Academic Exchange Service DAAD (V.N.) and a Freia grant from the Faculty of Science, University of Copenhagen (P.d.E.).

References

1. Strassmann, J.E., and Queller, D.C. (2007). Insect societies as divided organisms: The complexities of purpose and cross-purpose. Proc. Natl. Acad. Sci. USA *104*, 8619–8626.
2. Boomsma, J.J. (2009). Lifetime monogamy and the evolution of eusociality. Phil. Trans. Biol. Sci. *364*, 3191–3207.
3. Cornwallis, C.K., West, S.A., Davis, K.E., and Griffin, A.S. (2010). Promiscuity and the evolutionary transition to complex societies. Nature *466*, 969–972.
4. Leadbeater, E., Carruthers, J.M., Green, J.P., Rosser, N.S., and Field, J. (2011). Nest inheritance is the missing source of direct fitness in a primitively eusocial insect. Science *333*, 874–876.
5. Hart, A.G., and Ratnieks, F.L.W. (2005). Crossing the taxonomic divide: conflict and its resolution in societies of reproductively totipotent individuals. J. Evol. Biol. *18*, 383–395.
6. Gordon, D.M. (1996). The organization of work in social insect colonies. Nature *380*, 121–124.
7. Nielsen, M.G. (1978). Production of sexuals in nests of *Lasius flavus* (Forst.) (Hymenoptera: Formicidae). Nat. Jutl. *20*, 251–254.
8. Dijkstra, M.B., and Boomsma, J.J. (2007). The economy of worker reproduction in *Acromyrmex* leafcutter ants. Anim. Behav. *74*, 519–529.
9. Keller, L. (1991). Queen number, mode of colony founding, and queen reproductive success in ants (Hymenoptera, Formicidae). Ethol. Ecol. Evol. *3*, 307–316.
10. De Fine Licht, H.H., and Boomsma, J.J. (2010). Forage collection, substrate preparation and diet composition in fungus-growing ants. Ecol. Entomol. *35*, 259–269.

[1]Centre for Social Evolution, Department of Biology, University of Copenhagen, 2100 Copenhagen, Denmark. [2]Biology I, University of Freiburg, Hauptstraße 1, 79104 Freiburg, Germany. [3]Laboratoire d'Ethologie Expérimentale et Comparée (LEEC), Université Paris 13, 93430 Villetaneuse, France.
*E-mail: volker.nehring@biologie.uni-freiburg.de

The first World Cell Race

Paolo Maiuri[1], Emmanuel Terriac[1], Perrine Paul-Gilloteaux[1], Timothée Vignaud[2], Krista McNally[3], James Onuffer[3], Kurt Thorn[3], Phuong A. Nguyen[4], Nefeli Georgoulia[4], Daniel Soong[5], Asier Jayo[5], Nina Beil[6], Jürgen Beneke[6], Joleen Chooi Hong Lim[7], Chloe Pei-Ying Sim[7], Yeh-Shiu Chu[7], WCR participants[8], Andrea Jiménez-Dalmaroni[9], Jean-François Joanny[9], Jean-Paul Thiery[7], Holger Erfle[6], Maddy Parsons[5], Timothy J. Mitchison[4], Wendell A. Lim[3], Ana-Maria Lennon-Duménil[10], Matthieu Piel[1,*], and Manuel Théry[2,*]

Motility is a common property of animal cells. Cell motility is required for embryogenesis [1], tissue morphogenesis [2] and the immune response [3] but is also involved in disease processes, such as metastasis of cancer cells [4]. Analysis of cell migration in native tissue *in vivo* has yet to be fully explored, but motility can be relatively easily studied *in vitro* in isolated cells. Recent evidence suggests that cells plated *in vitro* on thin lines of adhesive proteins printed onto culture dishes can recapitulate many features of *in vivo* migration on collagen fibers [5,6]. However, even with controlled *in vitro* measurements, the characteristics of motility are diverse and are dependent on the cell type, origin and external cues. One objective of the first World Cell Race was to perform a large-scale comparison of motility across many different adherent cell types under standardized conditions. To achieve a diverse selection, we enlisted the help of many international laboratories, who submitted cells for analysis. The large-scale analysis, made feasible by this competition-oriented collaboration, demonstrated that higher cell speed correlates with the persistence of movement in the same direction irrespective of cell origin.

The race track consisted of 4 μm- and 12 μm-wide fibronectin lines printed in multi-well glass-bottomed cell-culture wells (see Supplemental Experimental Procedures and Figure S1A in the Supplemental Information available online); 54 different cell types from various animals and tissues were provided by 47 laboratories. Genotypically, cells were wild type, transformed or genetically engineered (Table S1). The cells were distributed to six organizing laboratories (two in the USA, and one each in the UK, France, Germany and Singapore), who prepared cell-culture stocks using the frozen samples received from participating laboratories and plated these onto the race tracks under identical culture conditions. Cells were allowed to adhere overnight and cell motility was recorded for 24 hours using an inverted video microscope (Figure 1B, Movie S1). Cell morphology (length, shape, symmetry, and nucleus position) varied greatly from one cell type to another (Figure 1A). Cell nuclei were stained by incubating live cells with 5 ng/ml Hoechst dye diluted in normal growth medium. Cell displacements were monitored every 10 minutes. Nuclei images were segmented and geometric centers were tracked with a global minimization algorithm in order to track automatically individual cell displacements (see Supplemental Experimental Procedures and Figure S1B). The motility of over 7,000 cells was compared, with an average of 130 cells analyzed per cell type. Detailed statistical analyses were used to characterize cell motility parameters for each cell type (see http://www.worldcellrace.com/ResultFiles).

The mean instantaneous speed of individual cells is computed by averaging the cell displacements between consecutive frames over time. The distribution of mean instantaneous speeds for each cell type was asymmetric (Figure 1C) and non-Gaussian (Figure S1C). Interestingly, we observed that a higher mean speed for a given cell type did not reflect a global shift of the speed distribution, but rather the spreading of the distribution due to the presence of faster moving cells (Figure 1C and Figure S1C). In order to identify the 2011 World Cell Race winner, only cells with an effective overall displacement of at least

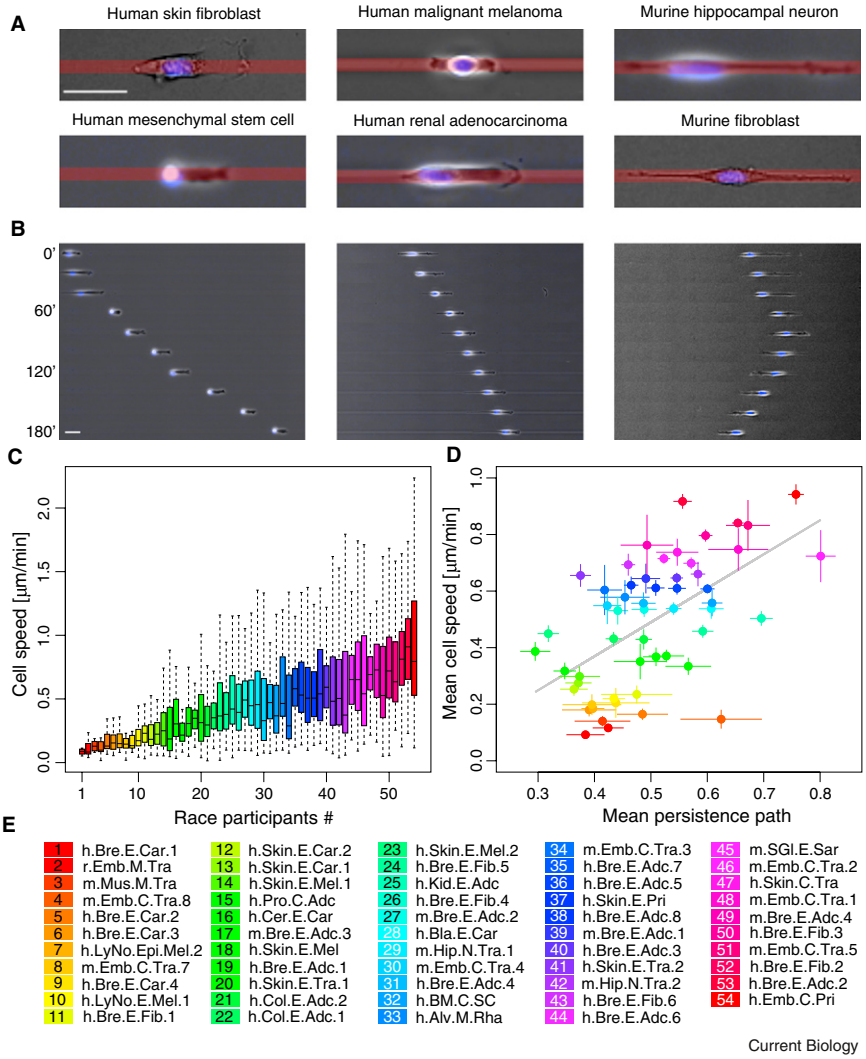

Figure 1. Cell speed and motion persistence on race tracks.
(A) Images illustrating cell shape variability on micropatterned tracks. (B) Kymographs illustrating different types of cell motility. Scales bars represent 50 µm. (C) Cell speed distributions represented with quartile diagrams for all participants. (D) Mean cell speeds plotted versus mean persistence . Bars correspond to standard deviation. Pearson correlation coefficient of the linear fit is 0.58. All cells analyzed are listed and color coded. (E) Color-coded participating cell types list: cell type – organism.source.tissue.tumor. Organisms: human (h), mouse (m), rat (r). Sources: embryo (Emb), alveola (Alv), bladder (Blad), bone marrow (BM), breast (Bre), cervix (Cer), colon (Col), hippocampus (Hip), kidney (Kid), lymph node (LyNo), muscle (Mus), prostate (Pro), salivary glands (SGl), skin. Tissues: epithelial (E), connective (C), muscle (M), nervous (N). Tumors: transformed (Tra), adenocarcinoma (Adc), carcinoma (Car), fibroma (Fib), melanoma (Mel), primary (Pri), rhabdomyosarcoma (Rha), sarcoma (Sar), stem cells (SC).

350 µm were considered. This cut-off was only reached by 26 of the 54 cell types. The highest migration speed was recorded at 5.2 µm/min by a human embryonic mesenchymal stem cell (Movie S2).

Cell displacements on lines can be described by a 1D correlated random walk [7], simply derived from the 2D model, in which cells are more likely to move in the direction of the immediately preceding movement conserving their polarity. This can be quantified by a *persistence probability* (p) for a cell to maintain its direction of motion and keep the same *front* and *rear*. For each cell type, we measured the number of cell steps between two motion reversals, i.e. the number of consecutive time intervals during which cells kept moving in the same direction (Figure S1E). To calculate p, histograms built from the number of cell steps were fitted to the 1D correlated random walk theory (Figure S1D). A persistence path, defined as the ratio of the effective maximum displacement to the actual trajectory length, was further calculated to obtain a macroscopic measure of p (Figure S1F). This ratio was strongly correlated with the persistence probability (Figure S1G). Persistence path distributions for the 54 cell types were typically non-Gaussian (Figure S1H). Strikingly, the overall mean speeds for all cell types correlated well with their mean persistence path (Figure 1D), implying that fast-moving cell types (mean cell speed >0.7 µm/min) displayed high mean persistence path (>0.5). Cells moving rapidly, but only backwards and forwards, were not observed.

Given the large and diverse sample of cell types, this result may reveal a conserved mechanism that allows the coupling of the machinery controlling cell polarity (responsible for persistent oriented motion) to the one regulating instantaneous cell speed. Future experiments aimed at unraveling the associated molecular mechanisms shall now be performed.

Together, the results generated by the first World Cell Race highlight how scientific games involving large-scale experiments can lead to the identification of novel and relevant biological processes, which may otherwise escape observation.

Supplemental Information

Supplemental Information includes experimental procedures, one figure, one table and two movies and can be found with this article online at http://dx.doi.org/10.1016/j.cub.2012.07.052.

Acknowledgments

We thank all the participants who sent cells to the inaugural World Cell Race (listed in Table S1). We thank the Société de Biologie Cellulaire de France for its financial support and the American Society for Cell Biology for the organization of the session dedicated to the race during the 2011 annual meeting. We thank our industrial partners, Cytoo and Nikon Instruments, who provided the micropatterned substrates and the imaging platforms, respectively.

P. Maiuri received a fellowship from the Fondation pour la Recherche Médicale, M. Parsons is funded by a Royal Society University Research Fellowship, H. Erfle and J. Beneke by the CellNetworks-Cluster of Excellence (EXC81), J. Onuffer, W.A. Lim and T.J. Mitchison by the NIH (PN2EY016546, GM23928), A. Lennon-Duménil and M. Piel by the ANR and Innabiosanté (09-PIRI-0027-PCVI and

MICEMICO), M. Théry by the INCA (PLBIO-2011-141).

References

1. Keller, P.J., Schmidt, A.D., Wittbrodt, J., and Stelzer, E.H.K. (2008). Reconstruction of zebrafish early embryonic development by scanned light sheet microscopy. Science *322*, 1065–1069.
2. Rembold, M., Loosli, F., Adams, R.J., and Wittbrodt, J. (2006). Individual cell migration serves as the driving force for optic vesicle evagination. Science *313*, 1130–1134.
3. Faure-André, G., Vargas, P., Yuseff, M.-I., Heuzé, M., Diaz, J., Lankar, D., Steri, V., Manry, J., Hugues, S., and Vascotto, F., *et al.* (2008). Regulation of dendritic cell migration by CD74, the MHC class II-associated invariant chain. Science *322*, 1705–1710.
4. Gligorijevic, B., Wyckoff, J., Yamaguchi, H., Wang, Y., Roussos, E.T., and Condeelis, J. (2012). N-WASP-mediated invadopodium formation is involved in intravasation and lung metastasis of mammary tumors. J. Cell Sci. *125*, 724–734.
5. Pouthas, F., Girard, P., Lecaudey, V., Ly, T.B.N., Gilmour, D., Boulin, C., Pepperkok, R., and Reynaud, E.G. (2008). In migrating cells, the Golgi complex and the position of the centrosome depend on geometrical constraints of the substratum. J. Cell Sci. *121*, 2406–2414.
6. Doyle, A.D., Wang, F.W., Matsumoto, K., and Yamada, K.M. (2009). One-dimensional topography underlies three-dimensional fibrillar cell migration. J. Cell Biol. *184*, 481–490.
7. Codling, E.A, Plank, M.J., and Benhamou, S. (2008). Random walk models in biology. J. R. Soc. Interface *5*, 813–834.

[1]Institut Curie, CNRS, UMR144, 75248, Paris, France. [2]Institut de Recherches en Sciences et Technologies pour le Vivant, CEA, UJF, CNRS, INRA, 38054, Grenoble, France. [3]Department of Cellular and Molecular Pharmacology, UCSF, San Francisco, CA 94158, USA. [4]Harvard Medical School, Systems Biology, Boston, MA 02115, USA. [5]Kings College London, SE1 1UL London, UK. [6]BioQuant, Heidelberg University, Germany. [7]Institute of Molecular and Cell Biology, A*Star, Proteos, 138673, Singapore. [8]World Wide, listed in Supplemental Information. [9]Institut Curie, CNRS, UMR168, 75248, Paris, France. [10]Institut Curie, INSERM, U639, 75248, Paris, France.
*E-mail: matthieu.piel@curie.fr, manuel.thery@cea.fr

Global distribution of a wild alga revealed by targeted metagenomics

Alexandra Z. Worden[1,*], Jan Janouskovec[2], Darcy McRose[1], Augustin Engman[1], Rory M. Welsh[1], Stephanie Malfatti[3], Susannah G. Tringe[3], and Patrick J. Keeling[2]

Eukaryotic phytoplankton play key roles in atmospheric CO_2 uptake and sequestration in marine environments [1,2]. Community shifts attributed to climate change have already been reported in the Arctic ocean, where tiny, photosynthetic picoeukaryotes (≤3 μm diameter) have increased, while larger taxa have decreased [3]. Unfortunately, for vast regions of the world's oceans, little is known about distributions of different genera and levels of genetic variation between ocean basins. This lack of baseline information makes it impossible to assess the impacts of environmental change on phytoplankton diversity, and global carbon cycling. A major knowledge impediment is that these organisms are highly diverse, and most remain uncultured [2]. Metagenomics avoids the culturing step and provides insights into genes present in the environment without some of the biases associated with conventional molecular survey methods. However, connecting metagenomic sequences to the organisms containing them is challenging. For many unicellular eukaryotes the reference genomes needed to make this connection are not available. We circumvented this problem using at-sea fluorescence activated cell sorting (FACS) to separate abundant natural populations of photosynthetic eukaryotes and sequence their DNA, generating reference genome information while eliminating the need for culturing [2]. Here, we present the complete chloroplast genome from an Atlantic picoeukaryote population and discoveries it enabled on the evolution, distribution, and potential carbon sequestration role of a tiny, wild alga.

We assembled a complete chloroplast genome from a coherent picoeukaryote population sorted from the Gulf Stream Current. The sorting step reduced bioinformatic complexity to a level where high quality *de novo* sequence assembly was possible. The resulting circular plastid genome was 91,306 bp, 35% G+C and encoded 106 proteins, 27 tRNAs, an rRNA operon as well as other features (Figure S1 in Supplemental Information, published with this article online). Multiple lines of evidence demonstrate this genome is from a member of the Pelagophyceae, a recently discovered phytoplankton class [4]. Complete plastid genomes are available from two cultured Pelagophyceae, the brown-tide forming *Aureococcus anophagefferens* and *Aureoumbra lagunensis*. Genome organization in the uncultured pelagophyte was similar to *Aureococcus*, and more divergent from *Aureoumbra* (Figure 1A), consistent with evolutionary relationships deduced from our 105 plastid-protein phylogeny (Figure S2). The uncultured pelagophyte encoded all *Aureococcus* genes plus one (*ycf45*) of *Aureoumbra*'s five additional proteins. All three Pelagophyceae encoded a 267 residue protein with multiple predicted transmembrane domains not seen in any other organisms based on tblastn and blastp against the full GenBank repository. Comparisons with the best-sampled protein-encoding pelagophyte plastid gene, *rbcL*, showed the uncultured population was most similar to *Pelagomonas calceolata* (99.0% nucleotide identity, ≤95.2% to other Pelagophyceae). The 16S rRNA gene, which is highly conserved across genera, had 100% identity to partial sequences available for *P. calceolata*. The uncultured population may therefore be *P. calceolata*, but based on extant sampling we call it 'wild *Pelagomonas*'.

With the plastid genome in hand, we addressed the distribution and ecological significance of this lineage. The complete set of coding regions from the chloroplast genome was compared with marine metagenomic samples using a cutoff of 97.0% nucleotide identity. We found that the wild *Pelagomonas*

Supplemental Information
The first World Cell Race

Paolo Maiuri, Emmanuel Terriac, Perrine Paul-Gilloteaux, Timothée Vignaud, Krista McNally, James Onuffer, Kurt Thorn, Phuong A. Nguyen, Nefeli Georgoulia, Daniel Soong, Asier Jayo, Nina Beil, Jürgen Beneke, Joleen Chooi Hong Lim, Chloe Pei-Ying Sim, Yeh-Shiu Chu, WCR participants, Andrea Jiménez-Dalmaroni, Jean-François Joanny, Jean-Paul Thiery, Holger Erfle, Maddy Parsons, Timothy J Mitchison, Wendell A. Lim, Ana-Maria Lennon-Duménil, Matthieu Piel, and Manuel Théry.

Supplemental Experimental Procedures

Participants sent frozen cells to one of the six organizing laboratories (two in the USA, and one each in the UK, France, Germany and Singapore) where they were thawed and maintained in culture in Dulbecco's Modified Eagle Medium supplemented with 10% fetal calf serum for one week. Cells were then trypsinized and plated in glass-bottomed multi-well video chambers at a low concentration of approximately 20 cells per mm , to avoid cell-cell contact wich could affect our analysis. The glass bottom of the video chamber was coated with alternate 4 and 12 micron-wide tracks of fibronectin by microfabrication (CytooChips *Motility*, Cytoo, France). Two line widths were produced to ensure the majority of cell lines provided would optimally adhere. It has been reported that the minimal width on which cells can bind might depend on cell type [6]. However, differences in the mean speed distribution between cell-types were larger than the spread of individual cell-types when including both line sizes, therefore we did not separate the two types of line in the analysis.

Cell nuclei were stained by incubating live cells with 5 ng/mL Hoechst dye diluted in normal growth medium. Cell displacements were monitored every 10 minutes with fluorescence and phase contrast microscopy for 24 hours using a humidity and temperature-controlled inverted wide-field microscope within an environmental chamber (Eclipse Ti, Nikon Instruments, USA) with a 10x objective.

Nuclei images were segmented and geometric centers were tracked with a global minimization algorithm. For this purpose a specific software in C++with the OpenCV [http://opencv.willowgarage.com/wiki/] and the GSL [http://www.gnu.org/software/gsl/] libraries was developed. The statistical analysis was performed by a C++ software coupled with R [www.R-project.org], using the RInside and Rcpp packages from Dirk Eddelbuettel [http://dirk.eddelbuettel.com/code/rcpp.html] and the Claudio Agostinelli CircStats package [http://cran.r-project.org/web/packages/CircStats/index.html].

We removed trajectories obtained from regions with locally high concentrations of cells that could clearly affect both cell speed and persistence. This was achieved by automatically filtering by cell/cell distance, removing all trajectories of cells closer than 10μm

for more than 20 min. This procedure should strongly reduces possible “traffic jam” effect on the final analysis.

To test that our time resolution, 10 min, was appropriated we computed the distribution of changes of direction frequency (data not shown) and we found that the maximum was a change of direction every 12 min and the peak of the distribution was around 20 min. It is possible that we miss some changes of direction on the less persistent cell-types, but this should not significantly affect our results.

Figure S1

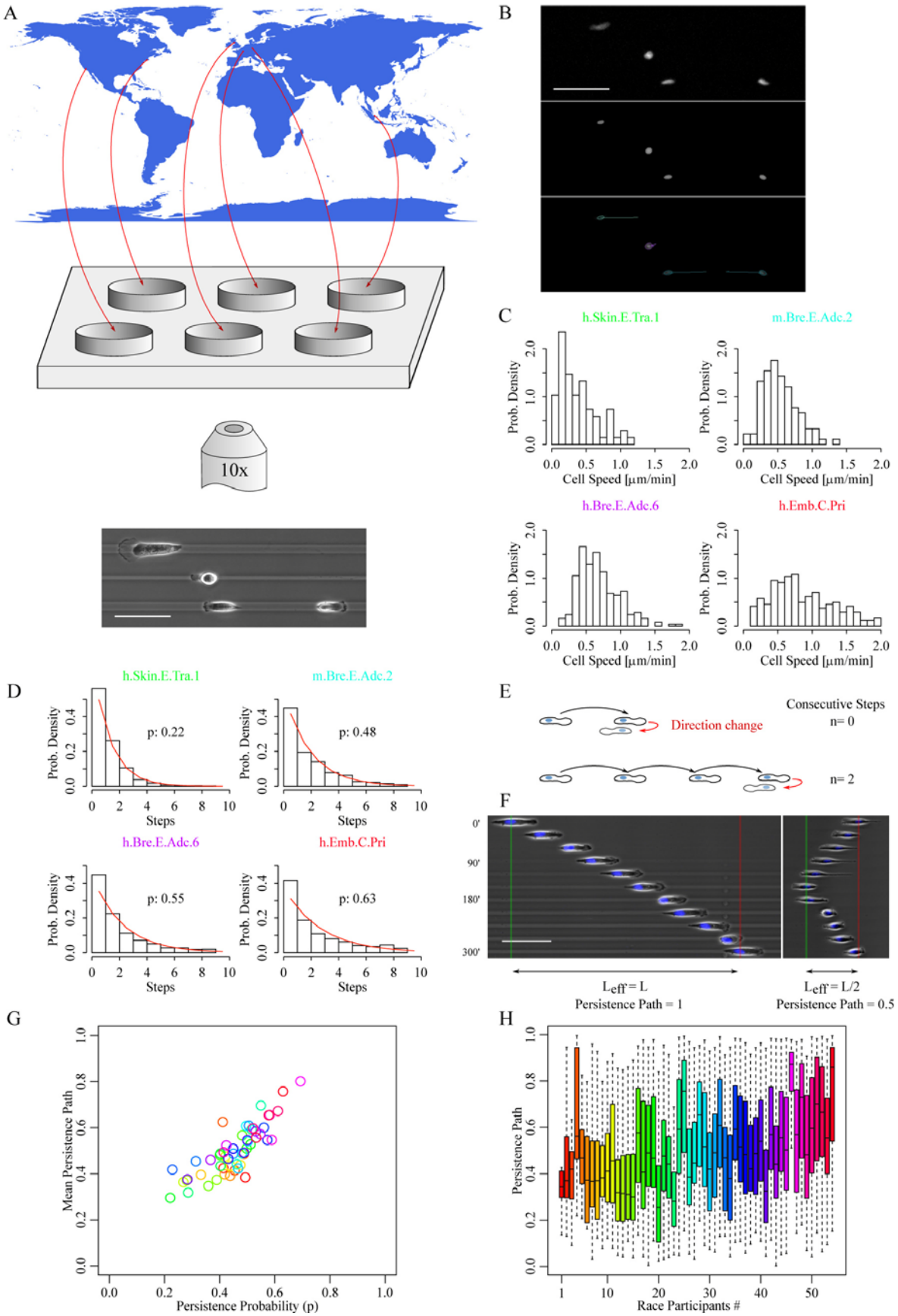
A
B
10x
C
h.Skin.E.Tra.1
m.Bre.E.Adc.2
h.Bre.E.Adc.6
h.Emb.C.Pri
Prob. Density
Cell Speed [µm/min]
D
p: 0.22
p: 0.48
p: 0.55
p: 0.63
Steps
E
Direction change
Consecutive Steps
n= 0
n= 2
F
0°
90°
180°
300°
Leff = L
Persistence Path = 1
Leff = L/2
Persistence Path = 0.5
G
Mean Persistence Path
Persistence Probability (p)
H
Persistence Path
Race Participants #

(A) Schematic representation of the race organization. In each organizing center, cells were plated in micropatterned multi-well plates and video-recorded at 10x magnification. (B) Example of fluorescent acquisition of nucleus staining (top), segmentation and detection of the signal (middle) and displacement tracking (bottom). Scale bars are 100 μm. (C) Examples of cell speed distributions in slow (top left) and fast (bottom right) moving cell-types, ordinate corresponds to probability density. (D) Examples of distributions of the number of steps performed by cells before changing directions for the same four cell-types as in (C). Ordinate corresponds to probability density. Distributions were fitted with a 1D correlated random walk model, in which the probability that a cell keeps its direction for n consecutive time points is $P(n)=(p^n)\cdot(1-p)$, to infer the persistence probability p. For very persistent cells, that never change their direction of motion, p will tend to 1; contrary it will tend to 0 far cells changing their direction at every time point. (E) Definition of n (consecutive steps) for the probability computation shown in (D). (F) Illustration of persistence path measurements as the ratio between the effective length and the total length the cell travelled/migrated. (G) Mean persistence path plotted versus the persistence probability (obtained in (D)) for all participants. Pearson correlation coefficient of the linear fit is 0.82. (H) Distributions of persistence path represented with quartile diagrams for all participants. Colour coding as detailed in Figure 1E.

Table S1

ID#	Cell Type Name	Participant		Cell Type description
33	h.Alv.M.Rha	Emilie Guillaume		Human Rhabdomyosarcoma
28	h.Bla.E.Car	Astrid Marx	astrid.marx@bioquant.uni-heidelberg.de	Human Bladder Carcinoma
32	h.BM.C.SC	Séverine Lecourt	severine.lecourt@sls.aphp.fr	Human Mesenchymal Stem Cell
9	h.Bre.E.Car.4	Hui Zhao	hzhao@fhcrc.org	Human Breast cancer cell line infected with cytoplasmic p27CK
19	h.Bre.E.Adc.1	Susana_Godinho	susana_godinho@dfci.harvard.edu	Human breast cancer, adenocarcinoma
53	h.Bre.E.Adc.2	Gilles Gadéa	gilles.gadea@crbm.cnrs.fr	Human breast cancer, adenocarcinoma, subcloned in mice for their metastatic properties
40	h.Bre.E.Adc.3	Asier Jayo	asier.jayo@kcl.ac.uk	Human breast cancer, adenocarcinoma, stably expressing GFP-lifeact
31	h.Bre.E.Adc.4	Asier Jayo	asier.jayo@kcl.ac.uk	Human breast cancer, adenocarcinoma, stably expressing RFP-Fascin
36	h.Bre.E.Adc.5	Alexis Gautreau	alexis.gautreau@lebs.cnrs-gif.fr	Human breast cancer, adenocarcinoma, tably expressing a shRNA targeting Arpin
44	h.Bre.E.Adc.6	Alexis Gautreau	alexis.gautreau@lebs.cnrs-gif.fr	Human breast cancer, adenocarcinoma, tably expressing a shRNA targeting Arpin
35	h.Bre.E.Adc.7	Alexis Gautreau	alexis.gautreau@lebs.cnrs-gif.fr	Human breast cancer, adenocarcinoma, tably expressing a shRNA targeting Arpin
38	h.Bre.E.Adc.8	Alexis Gautreau	alexis.gautreau@lebs.cnrs-gif.fr	Human breast cancer, adenocarcinoma, tably expressing a shRNA control
1	h.Bre.E.Car.1	Hui Zhao	hzhao@fhcrc.org	Human Breast cancer cell line
5	h.Bre.E.Car.2	Hui Zhao	hzhao@fhcrc.org	Human Breast cancer cell line infected with cytoplasmic p27
6	h.Bre.E.Car.3	Hui Zhao	hzhao@fhcrc.org	Human Breast cancer cell line infected with p27
11	h.Bre.E.Fib.1	Keiichiro Kushiro	k.kushiro@cell-engineering.org	Human Epithelial cell line
52	h.Bre.E.Fib.2	Odile Filhol-Cochet	odile.filhol-cochet@cea.fr	Human Epithelial cell line CK2beta knockdown transformed with RasV12
50	h.Bre.E.Fib.3	Odile Filhol-Cochet	odile.filhol-cochet@cea.fr	Human Epithelial cell line CK2beta knockdown transformed with RasV12
26	h.Bre.E.Fib.4	Yewchung Tang	yewchung.tang@duke-nus.edu.sg	Human Epithelial cell line with PTEN gene knocked out
24	h.Bre.E.Fib.5	Odile Filhol-Cochet	odile.filhol-cochet@cea.fr	Human Epithelial cell line CK2beta knockdown
43	h.Bre.E.Fib.6	Odile Filhol-Cochet	odile.filhol-cochet@cea.fr	Human Epithelial cell line CK2beta knockdown control
16	h.Cer.E.Car	Benjamin Flottmann	benjamin.flottmann@bioquant.uni-heidelberg.de	Human cervical cancer
22	h.Col.E.Adc.1	Vanessa Andries	Vanessa.Andries@dmbr.UGent.be	Human Colon Cancer cell line with inducible hECRep1 expression upon addition of doxycyclin
21	h.Col.E.Adc.2	Vanessa Andries	Vanessa.Andries@dmbr.UGent.be	Human Colon Cancer cell line with inducible hECRep1 expression upon addition of doxycyclin + doxycyclin
54	h.Emb.C.Pri		yuchun@nus.edu.sg	Human fetal bone marrow derived mesenchymal stem cells
25	h.Kid.E.Adc	Boston		Human Renal Adenocarcinoma
10	h.LyNo.E.Mel.1	Chung-Wei Lee	chungwei@alum.mit.edu	Human Malignant Melanoma lymph node metastasis of a 43 year old male A2058 with Nestin knockdown
7	h.LyNo.Epi.Mel.2	Chung-Wei Lee	chungwei@alum.mit.edu	Human Malignant Melanoma lymph node metastasis of a 43 year old male A2058 with vector control
15	h.Pro.C.Adc	Eric Sulpice	eric.sulpice@cea.fr	Human High Metastatic Prostate Cancer
47	h.Skin.C.Tra	Bruno Darocha-Azevedo	bruno.darocha-azevedo@utsouthwestern.edu	Human transformed skin fibroblasts (BR-5 Ras)
13	h.Skin.E.Car.1	Ester Martin	ester.martin@kcl.ac.uk	Human Cancer Squamous Cell Carcinoma
12	h.Skin.E.Car.2	Ester Martin	ester.martin@kcl.ac.uk	Human Cancer Squamous Cell Carcinoma
18	h.Skin.E.Mel	Zachary Pfeiffer	zachary_pfeiffer@brown.edu	Human Skin Melanoma
14	h.Skin.E.Mel.1	Gilles Weder	gilles.weder@csem.ch	Human Melanoma
23	h.Skin.E.Mel.2	JoseL uis Orgaz Bueno	jose_luis.orgaz_bueno@kcl.ac.uk	Human Melanoma
37	h.Skin.E.Pri	Stephen Britland	S.T.britland@Brad.ac.uk	Human Primary Keratinocytes
20	h.Skin.E.Tra.1	Rumena Begum	rumena.begum@kcl.ac.uk	Human Immortalised Keratinocytes from kindler syndrome patient
41	h.Skin.E.Tra.2	Rumena Begum	rumena.begum@kcl.ac.uk	Human Immortalised Keratinocytes from normal patient
39	m.Bre.E.Adc.1	Cristovao Sousa	Cristovao.sousa@curie.fr	Mouse 4T1 cell line stably transfected with mutant huntingtin m-Cherry.
27	m.Bre.E.Adc.2	Cristovao Sousa	Cristovao.sousa@curie.fr	Mouse 4T1 cell line stably transfected with mutant huntingtin m-Cherry.
17	m.Bre.E.Adc.3	Maria Molina Calavita	mailto:maria.molina-calavita@curie.fr	Mouse Striatal cell line, derived from a Huntington\'s Disease knock-in mouse model carrying 111 pathogenic poly-glutamine expantion.
49	m.Bre.E.Adc.4	Maria Molina Calavita	mailto:maria.molina-calavita@curie.fr	Mouse Striatal cell line, derived from a Huntington\'s Disease knock-in mouse model carrying 111 pathogenic poly-glutamine expantion.
48	m.Emb.C.Tra.1	Mickael Machicoane	machicoa@pasteur.fr	Mouse Embryonic Fibroblast
46	m.Emb.C.Tra.2	San Francisco		Mouse Embryonic Fibroblast
34	m.Emb.C.Tra.3	Frederique Gaits-Iacovoni	frederique.gaits@inserm.fr	Mouse Embryonic Fibroblast
30	m.Emb.C.Tra.4	Frederique Gaits-Iacovoni	frederique.gaits@inserm.fr	Mouse Embryonic Fibroblast stably transfected with a vector expressing the IpgD phosphatase
51	m.Emb.C.Tra.5	Taku Chibazakura	taku@nodai.ac.jp	Mouse Embryonic Fibroblast nullizygous for CDK inhibitors p21 and p107 and p27+/+
8	m.Emb.C.Tra.7	Krishnan Harini	krishnan.harini@gmail.com	Mouse Embryonic Fibroblast Podoplanin knockout overexpressing Podoplanin
4	m.Emb.C.Tra.8	Krishnan Harini	krishnan.harini@gmail.com	Mouse Embryonic Fibroblast Podoplanin knockout
29	m.Hip.N.Tra.1	Mengshyan Choy	mengshyan.choy@duke-nus.edu.sg	Mouse hippocampal neuronal cells over expressing GADD34
42	m.Hip.N.Tra.2	Mengshyan Choy	mengshyan.choy@duke-nus.edu.sg	Mouse hippocampal neuronal cells
3	m.Mus.M.Tra	Demorree	demorree@stanford.edu	Mouse (C57) primary myoblasts derived from a single fiber explant from EDL muscle
45	m.SGl.E.Sar	Chloe Sim	spy.chloe@gmail.com	Mouse Sarcoma
2	r.Emb.M.Tra	Setsuko Fujita-Becker	setsuko.fujita-becker@bioquant.uni-heidelberg.de	Rat smooth muscle Cells

Organim.Source.Tissue.Type

Organism	Source
h: human	Alv: Alveola
m: mouse	Bla: Bladder
r: rat	BM: Bone Marrow
	Bre: Breast
	Cer: Cervice
	Col: Colon
	Emb: Embryo
	Hip: Hippocampus
	Kid: Kidney
	LyNo: Lymph Node
	Mus: Muscle
	Pro: Prostate
	Sgl: Salivary Glands
	Skin: Skin

Tissue	Type
C: Connective	Adc: Adenocarcinoma
E: Epithelial	Car: Carcinoma
M: Muscle	Fib: Fibroma
N: Nervous	Mel: Melanoma
	Pri: Primary
	Rha: Rhabdomyosarcoma
	Sar: Sarcoma
	SC: Stem Cell
	Tra: Transformed

The table lists the cell types, the organizing center (city) where it was sent, the name and e-mail of the person who sent them and the description of the cell type.

Résumé

Les travaux présentés se sont intéressés à la régulation des forces produites par le cytosquelette d'actine. Le rôle primordial joué par le microenvironnement a été au centre de nos investigations.

L'étude de ces phénomènes a nécessité le développement de techniques innovantes.

La première permet le contrôle en temps réel de la forme de la cellule. Elle utilise un laser UV pulsé pour modifier le microenvironnement adhésif de la cellule et contrôler les zones disponibles pour son étalement.

La seconde est une amélioration d'une technique existante au sein du laboratoire. Il s'agit de produire des îlots de protéines d'adhésions, de forme contrôlée, sur un substrat déformable d'acrylamide. Ces supports permettent le contrôle de la taille de la cellule et de son organisation interne. En outre, l'élasticité de l'acrylamide permet la mesure des forces générées par la cellule.

La dernière technique a combiné le patterning sur acrylamide avec l'ablation laser. Les forces produites au sein d'une structure particulière du cytosquelette ont ainsi pu être estimées.

Deux grands mécanismes de régulation des forces ont pu être mis en évidence.

L'utilisation de techniques de spectrométrie de masse, de mesure de forces et de biologie moléculaire a permis de mettre en évidence les intéractions entre les différents types d'intégrines au niveau de l'adhésion cellulaire. Cette coopération permet un couplage entre l'architecture du cytosquelette et la quantité de moteurs moléculaires mettant en tension ces structures. Ces mécanismes sont primordiaux pour l'adaptation de la cellule à la rigidité de son environnement.

Ce sont les structures d'actine qui produisent les forces qui seront transmises au niveau des adhésions. La corrélation entre la taille de ces structures et les forces générées est encore mal caractérisée. La relation entre taille des fibres de stress et répartition des forces au sein de la cellule a pu être étudiée et suggère que la force produite par une fibre de stress augmente avec sa longueur.

Une étude systématique de la contractilité des cellules, sur des patterns de différentes tailles, a permis de montrer la relation entre la taille des fibres de stress et la force générée. Une relation biphasique a ainsi été mise en évidence. Quand la taille de la cellule augmente, la force générée au sein des fibres de stress commence par augmenter avant de diminuer au delà d'une longueur critique. Cette longueur correspond également à la taille maximale observée sur des cellules libres de s'étaler sans contraintes. Les résultats obtenus suggèrent que cette chute de force est liée à une augmentation excessive du ratio myosine/actine qui ne permet plus une production de force efficace. Le mécanisme pourrait faire intervenir le désassemblage des structures d'actine par la myosine ou la quantité insuffisante d'actine pour permettre un travail efficace des moteurs moléculaires.

La rencontre de ces deux mécanismes permet de définir le champ des possibles pour la cellule en terme de contractilité.

Le mécanisme de chute de forces observé n'a pas pu être expliqué à ce jour mais nous travaillons activement pour qu'il le soit dans les mois à venir. Ce phénomène aura sans doute un grand rôle à jouer dans l'intégrité mécanique des tissus et les phénomènes de migration. La chute de force au delà de la longueur critique permet en effet de déstabiliser les adhésions et pourrait être à l'origine de la rétraction de la cellule dans la migration ou du détachement d'une cellule de ces voisines dans le cas d'un tissu sous forte contraintes. Ce détachement protégerait ainsi la cellule d'un déchirement sous l'effet de forces trop importantes.

Abstract

Our work has been focused on the regulation of the forces generated by the actin cytoskeleton. We have more precisely studied the role of the cellular microenvironment in this process.

It was necessary to overcome some technical challenges to study these mechanisms. We developed two new techniques. The first one allows for the dynamic control of cell shape. A pulsed UV laser is used to modify the adhesive microenvironment around the cell and to create new area available for cell spreading.

The second technique is an improvement of an existing technique from the laboratory. It consists in producing ECM protein islands on a elastic acrylamide substrate. This substrate provides the control of cell shape and internal organization. Plus, the elasticity of the substrate is compatible with traction forces measurements.

The last technique combines acrylamide micropatterning and laser ablation of intracellular actin structures. Thus, the forces produced by a particular intracellular structure can be estimated.

Two keys mechanisms of force regulation were shown.

The use of mass spectrometry, traction force microscopy and molecular biology made it possible to study the interaction between different integrins in the adhesion complex. Cooperation was shown. It allows for the coupling between the architecture of the cytoskeleton and the amount of molecular motors in action. This process is necessary for the adaptation of cell forces to substrate stiffness.

Actin structures are the one responsible for force production. This force can then be transmitted to the environment through adhesions.. The link between the length of actin fibers and the force produced was more precisely studied. The results showed a correlation between stress fibers length and the force generated inside it. This was true only above a certain critical value. After that, the force was rather decreasing with increasing fiber length. This critical length corresponds to the maximal length of cell axis on infinite 2D substrate. Our main hypothesis is that a too high myosin/actin ratio will block the proper force production/transmission within the fiber. Disassembly of actin by myosin or limited pool of actin are the two explanations we are currently following.

The combination of these two-regulation process put brakes on force production by the cell. Above a certain length, the force produced is decreasing. This decreases in turn the strength of the adhesions anchored to these fibers. This will destabilize the adhesions and causes cell retraction

The interplay between the regulation by the adhesion and the production of forces within the fiber set some limits on the level of forces produced by the cell. These processes are likely to be modified in a pathological context and can lead to tumor formation. They also protect the cell from being destroyed by stretching. If the length/stretch is too high, the cell will decrease its forces and detach from neighboring cells. This provide a system protecting the cell from being destroyed by massive deformations within the body